LEABHARLANN CHOLÁISTE NA TRÍONÓIDE, BAILE ÁTHA CLIATH | TRINITY COLLEGE LIBRARY DUBLIN
Ollscoil Átha Cliath | The University of Dublin

Terms and Conditions of Use of Digitised Theses from Trinity College Library Dublin

Copyright statement

All material supplied by Trinity College Library is protected by copyright (under the Copyright and Related Rights Act, 2000 as amended) and other relevant Intellectual Property Rights. By accessing and using a Digitised Thesis from Trinity College Library you acknowledge that all Intellectual Property Rights in any Works supplied are the sole and exclusive property of the copyright and/or other IPR holder. Specific copyright holders may not be explicitly identified. Use of materials from other sources within a thesis should not be construed as a claim over them.

A non-exclusive, non-transferable licence is hereby granted to those using or reproducing, in whole or in part, the material for valid purposes, providing the copyright owners are acknowledged using the normal conventions. Where specific permission to use material is required, this is identified and such permission must be sought from the copyright holder or agency cited.

Liability statement

By using a Digitised Thesis, I accept that Trinity College Dublin bears no legal responsibility for the accuracy, legality or comprehensiveness of materials contained within the thesis, and that Trinity College Dublin accepts no liability for indirect, consequential, or incidental, damages or losses arising from use of the thesis for whatever reason. Information located in a thesis may be subject to specific use constraints, details of which may not be explicitly described. It is the responsibility of potential and actual users to be aware of such constraints and to abide by them. By making use of material from a digitised thesis, you accept these copyright and disclaimer provisions. Where it is brought to the attention of Trinity College Library that there may be a breach of copyright or other restraint, it is the policy to withdraw or take down access to a thesis while the issue is being resolved.

Access Agreement

By using a Digitised Thesis from Trinity College Library you are bound by the following Terms & Conditions. Please read them carefully.

I have read and I understand the following statement: All material supplied via a Digitised Thesis from Trinity College Library is protected by copyright and other intellectual property rights, and duplication or sale of all or part of any of a thesis is not permitted, except that material may be duplicated by you for your research use or for educational purposes in electronic or print form providing the copyright owners are acknowledged using the normal conventions. You must obtain permission for any other use. Electronic or print copies may not be offered, whether for sale or otherwise to anyone. This copy has been supplied on the understanding that it is copyright material and that no quotation from the thesis may be published without proper acknowledgement.

Intermolecular and Interlayer interaction in chiral smectic-C liquid crystals

by

Jang-Kun Song

A thesis submitted for the
degree of Doctor of Philosophy

in the

Advanced Electronic Materials Lab.
Department of Electronic and Electrical Engineering

TRINITY COLLEGE
THE UNIVERSITY OF DUBLIN

June 2008

TRINITY COLLEGE
05 AUG 2008
LIBRARY DUBLIN
THOSIS
8553

Declaration of Authorship

I, Jang-Kun Song, declare that this thesis titled, 'Intermolecular and Interlayer interaction in chiral smectic-C liquid crystals' and the work presented in it are my own. I confirm that:

- It has not been submitted as an exercise for a degree at this or any other University.
- It is entirely my own work, except where otherwise stated.
- I have quoted from the work of others, the source is always given. With the exception of such quotations, this thesis is entirely my own work.
- I agree that the Library may lend or copy the thesis upon request. This permission overs only single copies made for study purposes, subject to normal conditions of acknowledgment.

Signed: Jang Kun Song

Date: 13th Jun. 2008

"The silvery light was coming from the basin's contents, which were like nothing Harry had ever seen before. He could not tell whether the substance was liquid or gas. It looked like light made liquid - or like wind made solid -Harry couldn't make up his mind." (Harry's 4th year in Hogwart.)

"Silvery blue, neither gas nor liquid, it gushed from ...(syncopation)..., and Harry knew what it was, but did not know what to do-." (Harry's 6th year in Hogwart.)

from "Harry Potter and the Goblet of Fire" and
"Harry Potter and deadly hallow", J. K. Rowling

It was a great pleasure to deal with a magical substance, liquid crystals.

Acknowledgements

A long journey towards Ph.D degree started on September 2004 at age 33 when I moved to Ireland with my wife and two young children. In having decided on this voyage, I definitely needed encouragement, support and instruction. As a result, I feel I probably owe thanks to more people than many other Ph.D students.

I have been fortunate to have an excellent supervisor in **Prof. Jagdish K. Vij**. He regarded me as a coworker rather than a student, and supported me in all respects. I sincerely thank **Prof. Astuo Fukuda** for his valuable discussions, instructions, for providing samples of materials for these experiments, and for the hospitality during my visit to Tokyo Denki University. His discussions inspired me many times. I am also grateful to SFI (Science Foundation Ireland) for financially supporting the project that this thesis forms a major part of.

Prof. A. D. L. Chandani gave her gifted experimental skills freely, and also I thank her for the hospitality during sharing an office with her. The experimental data in Fig. 3.4 were obtained by her. **Dr. Vitaly Panov** taught me how to control many instruments in the lab. I thank **Dr. Gerard Power**, who is one of the most diligent and clever people in my awareness, for correcting my English many times, including this thesis. Theoretical discussions with **Dr. Micheal Lehanan** were a great pleasure for me. I also thank **Dr. Yuri Panarin** and **Dr. Olga Panarina** for their hospitality and assistance. It was very helpful and enjoyable to do experiments with and to discuss results with **Uttam Manna**, **Marcin Sufin** and **Dr. K. L. Sandhya**. Utam helped me carry out the dielectric measurements in Chap. 4, 8, and 11, and Marcin helped me for the electro-optic measurement in Chap. 7, and the experimental data in Fig. 10.3 were obtained by Dr. Sandhya. I also thank **Dr. V. Manjuladevi**, **Dr. A. Sigarev**, **Dr. Nick M. Shtykov**, **Prof. A. Kocot** for their helpful advice. **Dr. A. V. Emelyanenko** in Moscow State University is thanked for his contribution in carrying out the analytic calculation in Section 3.4.2.

Samsung Electronic company granted me a chance to study here and supported me financially as well. In particular, I sincerely thank Vice President **Dr. Sang-Su Kim** for recommending me for this program, and I also thank Vice President **Dr. June H. Souk** and Executive Director **Dr. Kyung-Hyun Kim** for their support and helpful advice. I would also like to thank to Executive Director **Dr.**

Sung-Tae Shin and **Prof. T. K. Lim** for their valuable advice and continuous concern for me. **Dr. S. S. Seomun** introduced me this lab and helped me to prepare the study. He also gave me many tips about how to survive and enjoy Ireland-(sorry I could not enjoy Golf.) I would like to express my sincere gratitude to all my colleagues in Samsung electronics for their encouragement and assistance.

I and my family owe alot to many Koreans in Dublin, without whom we might have endured many difficulties. **Mr. and Mrs. Delap** and their family, **Mr. Joo** and his family, **Mr. Y. K. Lee** at Korean Airline and his family, **Mr. J. H. Jeon** at KDB Ireland and his family, **Mr. C. Y. Kim** at DCU and his family, and **Dr. M. Hun** in TCD and his family *et al.* have made my family's living in Dublin homelike and fruitful. I could concentrate on my study by virtue of their help.

Lastly I come to my father, families, parents-in-law and families-in-law in Korea. I know that their thoughts and affection are always with me as mine is on them. This has been an endless strength for me and my family in Ireland. They have cared for and supported us in various ways including air transportation of Korean foods and supplies.

Finally, I thank my family for being always there with me.

To my Kyou-Lee,

Eun-Su,
& Min-Kyung. . .

Summary

The molecular and interlayer interactions in smectic-C phases have been investigated in detail. This topic is one of the less well established subjects in the field of liquid crystals.

Various new physical phenomena were observed and interpreted.

1. Molecular short axis ordering in the SmC^* phase is investigated by using a new experimental method, tilted conoscopy. It is found that the direction of the average molecular short axis is along the tilt direction in some liquid crystal materials and is normal to the tilt-plane in the other materials. The molecular ordering strongly affects the temperature dependence of the macroscopic biaxiality of the phase, and a sign reversal in the biaxiality as a function of temperature is found in those materials having the average molecular short axis normal to the tilt-plane.

2. The individual molecular motions and the collective motions in liquid crystals are investigated by the observation of the dielectric response. The sign reversal phenomena of the dielectric anisotropy as functions of the frequency and the temperature in the SmA^* phase are observed and analyzed. The frequencies of the antiferroelectric motion mode for the binary mixtures with a ferroelectric liquid crystal in various mixing ratios are investigated. The mixing ratio affects the frequency significantly, which is interpreted in terms of the interlayer interaction.

3. The solitary wave propagations in the field induced AF–F switching and in the temperature induced SmC_A^*–SmC^* transition are investigated. The mechanism of the solitary wave is found to arise from the quadrupolar term in the interlayer interaction. A new method to measure the interlayer interaction by observing the solitary wave is devised. The solitary wave propagation, a non-homogeneous transition, is found to be the only way for the SmC_A^*–SmC^* phase transition to occur. The solitary wave in SSFLC cells is also investigated for various surface conditions of the cell including asymmetric alignment layers.

4. The dependence of the stabilities of the smectic C phases on the surface confinement, the applied field, and the mixing ratio in the binary mixture

are investigated in detail. The suppression of the sub phases by the polar anchoring energy is modeled theoretically. Combined with the solitary wave model, the gradual phase transition between the SmC_A^*–SmC^* phases is demonstrated experimentally and explained theoretically. The coexistence of the two phases has frequently been misinterpreted as the frustration between them, but it is revealed to arise from the suppression of the phase transition rather than frustration between the two phases.

5. An explanation for the phase sequence reversal phenomenon is provided. This phenomenon can be explained by using the interlayer interaction energy.

6. The unwinding process of the helical structure in SmC^* is investigated. Helical fracture, which is a new concept in the helical unwinding process in liquid crystals, is introduced and modeled. The model implies that the interlayer interaction is the essential factor in the unwinding process. The helical fracture is rather similar to the helical unwinding of DNA from a topological view point.

For these observations, tilted conoscopic method is developed. This is a simple and a powerful method to measure the biaxiality of phases and to estimate the molecular distributions. Moreover, new simulation method based on the average refractive index approximation is suggested. This can expand the usage of the conoscopic method extensively.

New method to measure the interlayer interaction is also very useful for investigating the various physical phenomenon in smectic liquid crystals. The phase transitions, the stabilities of phases, the coexistence of antiferro- and ferroelectric phases are all observed, interpreted and characterized in this thesis using the method. The method can also be used to investigate the solitary waves in liquid crystals.

Contents

Declaration of Authorship iii

Acknowledgements v

Summary ix

Table of Contents xi

List of Figures xv

List of Tables xix

Abbreviations xxi

List of Publications xxiii

List of Presentations xxv

Part. I/ Introduction. 1

1 Introduction 3

1.1 Preface . . . 3
1.2 What is a Liquid Crystal? . . . 6
1.3 Order parameters . . . 8
1.4 Symmetry and Ferroelectric and Antiferroelectric Liquid Crystals . 11
1.5 Free energy expressions and phase transitions . . . 14
1.6 Physical properties of liquid crystals . . . 16

2 Experimental Method: Conoscopy 21

2.1 Introduction . . . 21
2.2 Conoscopy and analysis . . . 24
2.3 Tilted conoscopic method . . . 29
2.4 Verification of the approximations used in its analysis . . . 31
2.4.1 Single-biaxial-plate approximation . . . 31
2.4.2 Assumption of fixing one of the principal refractive indices . 38
2.5 Estimation of the molecular distribution using the conoscopic data . 40

2.5.1 Simulation method to estimate the molecular distribution . . 40
2.5.2 Simulation of the deformed helical structure 42
2.6 Conclusion 43

Part. II/ Molecular orderings and motions. 45

3 Molecular short axis orientations and biaxiality in SmC^* 47
3.1 Introduction 47
3.2 Experiment 51
3.3 Results 54
3.3.1 Correct assignment for the V-shaped switching materials . . 54
3.3.2 Temperature dependencies of biaxiality 57
3.3.3 Biaxiality as a function of enantiomeric excess ratios 61
3.4 Discussion 64
3.4.1 Effective polarizability tensor in SmC^* phase 64
3.4.2 Local field effect and the resulting positive biaxiality 66
3.4.3 The origins of the two types of temperature dependences . . 72
3.5 Conclusion 74

4 Dielectric response and Molecular motions. 77
4.1 Introduction 77
4.2 Sign reversal of dielectric anisotropy in SmA^* phase. 78
4.3 Dielectric response in the SmC^*_A phase 85

Part. III/ Interlayer interaction and the solitary wave propagations. 95

5 Interlayer interaction and field induced solitary wave in SmC^*_A. 97
5.1 Introduction to the field induced solitary wave in SmC^*_A phase. . . . 97
5.2 Experiment and discussion. 100
5.3 Conclusion 108

6 Dynamic Mechanism of SmC_A*–SmC* Phase Transition due to Solitary Wave Propagation. 111
6.1 SmC_A*–SmC* Phase Transition and the interlayer interactions. . . 111
6.2 Experiments and discussion. 115

7 Solitary Wave Propagation in Surface Stabilized Ferroelectric Liquid Crystal Cells. 123
7.1 Introduction to the solitary wave in SSFLC cells. 123
7.2 Model for the solitary waves in SSFLC cells. 125
7.3 Experimental results and discussion. 128

Part. IV/ Interlayer interaction and the stability of the subphases. 133

8 Cell thickness dependence of the stability of chiral smectic-C phases 135

8.1 Theory for the cell thickness dependent stability of the SmC^* phases 135
8.2 Comparison between experimental and simulation results. 146
8.3 Conclusion 148

9 Gradual phase transition between the SmC^*_A and SmC^* phase and the thresholdless antiferroelectricity; influences by confinement and binary mixture 149
9.1 Introduction to the thresholdless antiferroelectricity 149
9.2 Experiment 152
9.3 Results and Discussion 156
9.3.1 Phase diagram in a binary mixture and the gradual phase transition 156
9.3.2 Thresholdless antiferroelectric switching in the binary mixture 161
9.3.3 The mechanism of the frustration and the solitary waves . . 165
9.3.4 Surface effect: How does the interface induce the supercooling? 170
9.3.5 Ferroelectric V-shaped switching of bulk antiferroelectric mixtures 178
9.4 Conclusions 181

10 The SmC^*_A(1/3) - SmC^* Liquid Crystal Phase Sequence Reversal 183
10.1 Phase sequence reversal. 183
10.2 Simple phenomenological description for the phase sequence reversal. 191

Part. V/ Interlayer interaction and the unwinding process in the SmC^* phase. 195

11 Mechanism of field induced unwinding of SmC^* helix. 197
11.1 Topological problem in the helical unwinding 197
11.2 Dielectric response during the unwinding process. 206
11.3 Conclusion and Future works. 215

12 Interlayer interactions and the dependence of biaxiality of SmC^* on electric field in the helical unwinding process. 217
12.1 Introduction 217
12.2 Experiments and results 218
12.3 Simulation based on the narrow energy well model 226
12.4 Conclusion 235

Part. VI/ Conclusion and Appendix. 237

13 Conclusion and future works 239
13.1 Conclusion and Summary of this thesis 239
13.2 Future work 245

A Appendix 247
A.1 Materials used for fabricating cells 247

A.2 Apparatus 249
A.3 Softwares 250

Bibliography **251**

List of Figures

The captions listed here are not full captions but concise ones.

1.1 Schematic of phases 7
1.2 Examples of D_{nh} and C_n symmetry in nature and in liquid crystals. 12
1.3 Various smectic-C phases. 13

2.1 Schematic set-up for conoscopy and the chemical structure of liquid crystals used 26
2.2 Modified conoscopic method using a tilted cell. 30
2.3 Transmittances as a function of pitch in twisted nematic mode . . . 33
2.4 Simulated conoscopic images and experimentally obtained examples 35
2.5 Transmittance as function of the angle of light along the line passing the two optic axes 37
2.6 The transmittance as a function of angle at red and blue wavelengths 39
2.7 The director distribution estimated from the conoscopic image . . . 43

3.1 Schematics for orderings of molecular short axis. 48
3.2 Chemical structures of samples used. 52
3.3 Plots of the apparent biaxiality vs. applied field for MC452. 53
3.4 Experimental data of Y102 by using homeotropic cells. 56
3.5 Spectroscopic data for MC815. 57
3.6 Two types of temperature dependencies of biaxiality. 58
3.7 The observed biaxiality dispersions in MC452. 60
3.8 Experimental data for different enantiomeric excess ratios of MC815. 63
3.9 Numerically calculated results for the local field effect. 71

4.1 Chemical structure of MC881 and dielectric anisotropy. 79
4.2 Microscopic images of a MC881 cell 81
4.3 Relaxation frequency and dielectric stength. 83
4.4 Real part of the dielectric constant and dielectric anisotropy. 84
4.5 Schemetic of antiphase mode and antiferroelectric Goldstone mode. 86
4.6 Spontaneous polarization of MC881 and MC815. 88
4.7 Dielectric permittivity of MC881. 89
4.8 The relaxation frequency and the dielectric strength of MC881. . . . 90
4.9 Relaxation frequency of antiphase and molecular modes in various maxing ratio. 92

5.1 Microscopic images of the solitary waves in AFLC cell. 98
5.2 Chemical structure of MC881 and cell structure. 98
5.3 Spectroscopic experiment and fitting result. 101
5.4 Apparent tilt angle and retardation. 101
5.5 Measured P_s, E_{th} and $\delta\phi$ ($25\mu m$ planar cell) 105
5.6 Calculated V_0 and b, and interlayer interaction energy with $\Delta\phi$. . . 107
5.7 Measured velocity of the solitary wave and simulation result. 108

6.1 The Landau-de Gennes free energy and the interlayer interaction energy. 114
6.2 Experimental results for the interlayer interaction energy. 116
6.3 Microscopic images for the solitary waves. 119

7.1 Microscopy for the solitary wave in a SSFLC. 125
7.2 The velocity of the solitary wave for symmetric alignment layer. . . 129
7.3 The velocity of the solitary wave for various alignment layers. . . . 129
7.4 Optical transmittance vs. applied field. 131
7.5 E_s as a function of temperature. 132

8.1 Cell Structure. 140
8.2 Schematic diagram for director distribution in smectic C phases. . . 141
8.3 Example of simulation. 145
8.4 Comparison of experimental (a,b) and simulation results (c,d). . . . 147

9.1 The interlayer interaction energy represented by Eq. (9.1). $Q/D = 2$. 155
9.2 Bulk phase diagram of binary mixture system of MC881-MC452. . . 157
9.3 PEM data, indicating clearly the emergence of the subphase Sm$C^*_A(1/3)$. 157
9.4 Phase diagram using 2μm thick cells and dielectric measurement. . 158
9.5 Real part of dielectric permittivity measured at 1kHz. 159
9.6 Real part of dielectric permittivity after freezing the cell. 159
9.7 Apparent tilt angle Θ' as a function of the applied field. 162
9.8 The relative orientation of the **c** directors. 163
9.9 Apparent polarization as a function of applied field. 164
9.10 Free energy as a function of the azimuthal angle difference of the in-layer directors. 165
9.11 Free energy difference between SmC^*_A and SmC^* minima and its barrier height 167
9.12 Averaged $\langle\Delta\rangle$ and the absolute value of the slope near T_c. 168
9.13 Transmittance as a function of applied DC field. 171
9.14 Transmittance as a function of applied DC field. 172
9.15 Field induced transition from AF to F state. 173
9.16 Field induced transition from AF to F state. 175
9.17 Microscopy showing the solitary waves during the phase transition in a thin cell. 176

9.18 Spontaneous polarization of MC452 and its partially racemised mixture. . . . 178
9.19 Ferroelectric V-shaped switching. . . . 179

10.1 Chemical structure of 10OHF. . . . 184
10.2 Conoscopy for each phases. . . . 185
10.3 Schematic diagram for the direction of melatopes. . . . 189
10.4 Temperature dependence of dielectric permittivity for different mixtures. . . . 190

11.1 Schematics for the helical fracture and the diverging pitch. . . . 199
11.2 Microscopy (×200) for a homeotropic cell using 12OF1M7. . . . 201
11.3 Microscopy for a homeotropic cell using MHPOOCBC. . . . 202
11.4 Spectroscopy for a cell using 12OF1M7 with increasing applied field. 205
11.5 Schematic for the diverging force of the pitch. . . . 205
11.6 Director distributions for different DC fields. . . . 209
11.7 Plots for the normalized $\Delta\epsilon_G^* = Kq^2\Delta\epsilon_G/P_s^2$, and the normalized $\langle P_E \rangle$. . . . 211
11.8 Experimental data for 12OF1M7 and simulation results. . . . 212
11.9 Plots of theoretical E_t and E_c, and experimental E_t and E_c. . . . 215

12.1 Chemical structure of MHPOOCBC. . . . 219
12.2 Helical pitch as function of the e.e. value. . . . 219
12.3 Results of the conoscopic measurements. . . . 220
12.4 Micrographs (× 200) of a homeotropic cell with pure MHPOOCBC. 222
12.5 Micrographs (× 200) of a homeotropic cell with racemized MHPOOCBC. . . . 223
12.6 Dielectric permittivity with the increasing field. . . . 225
12.7 **c** directors and directors. . . . 227
12.8 Elastic energy between the adjacent layers in the conventional elastic model. . . . 230
12.9 Simulation of directors vs. applied field. . . . 231
12.10Simulation results for the biaxiality and the tilt-angle. . . . 232
12.11Comparison between the experimental data and the simulation. . . . 234

A.1 Liquid crystal materials used in this thesis. . . . 248
A.2 Simulation Programs using Visual Basic or MatLab. . . . 250

List of Tables

7.1 Surface conditions for each cells, and experimentally obtained Δw_p; For the strong rubbing condition, the surface was rubbed 4 times with the same rubbing strength as the weak rubbing process. . . . 128

8.1 A and F_s for lower temperature smectic C phases. 144
8.2 A and F_s for higher temperature smectic C phases. the values in ()s is approximated ones for simulation. 144

Abbreviations

LC	**L**iquid **C**rystal
LCD	**L**iquid **C**rystal **D**isplay
F	**F**erroelectric
AF	**A**nti-**F**erroelectric
FLC	**F**erroelectric **L**iquid **C**rystal
AFLC	**A**nti-**F**erroelectric **L**iquid **C**rystal
SSFLC	**S**urface **S**tabilized **F**erroelectric **L**iquid **C**rystal
SmA	**Sm**ectic **A** type phase (achiral)
SmC	**Sm**ectic **C** type phase (achiral)
SmA^*	chiral **Sm**ectic **A** phase (achiral)
SmC^*	chiral **Sm**ectic **C** phase
SmC^*_A	chiral **Sm**ectic $\mathbf{C}_A$ type phase
SmC^*_A**(1/3),Sm**C^*_γ	chiral 3-layer ferrielectric **Sm**ectic phase
SmC^*_A**(1/2),AF**	chiral 4-layer ferrielectric **Sm**ectic phase
SmC^*_α	chiral **Sm**ectic C^*_α phase
Cr.	**Cr**ystal phase
Iso.	**Iso**tropic phase
$^\circ C$	Degree Centigrade
ITO	**I**ndium **T**in **O**xide
dc, DC	**D**irect **C**urrent
ac, AC	**a**lternating **c**urrent
P_s	(**S**pontaneous) **P**olarization
E	**E**lectric field
T	**T**emperature

n	refractive index
S	S order parameter
D	D order parameter
P	P order parameter
C	C order parameter
PEM	**P**hoto **E**lastic **M**odulater
IR	**I**nfra **R**ed
C_n, C_2	n (2)-fold rotational symmetry group
C_{nh}	C_{nh} symmetry group
D_n, D_2	n (2)-fold rotational symmetry and flipping symmetry group
D_{nh}	D_{nh} symmetry group
PET	**P**oly**e**thylen **T**erephthalate
p	**p**itch
q	wave vector
α	polarizability, or an coefficient of the Landau expansion
ϵ, ϵ', ϵ''	dielectric susceptibility, real part, imaginary part of

List of Publications

1. J. K. Song, A. D. L. Candani, O. E. Panarina, A. Fukuda, J. K. Vij, V. Goertz and J. W. Goodby, *"Study of the SmC^*_α Phase in the Tokyo Mixture by Conoscopy Using Tilted Cell"*, **Ferroelectrics**, **344**, 41–47, (2006).

2. J. K. Song, J. K. Vij, and I. Kobayashi, *"Interlayer interactions and the dependence of biaxiality of the chiral smectic-C^* phase on electric field in the helical unwinding process"*, **Phys. Rev. E**, **75**, 051705, (2007).

3. J. K. Song, A. Fukuda, and J. K. Vij, *"Solitary wave propagation in antiferroelectric liquid crystal cells and the quadrupolar term in the interlayer interaction"*, **Phys. Rev. E**, **76**, 011708, (2007).

4. J. K. Song, A. D. L. Chandani, A. Fukuda, J. K. Vij, I. Kobayashi and A. V. Emelyanenko, *"Temperature-induced sign reversal of biaxiality observed by conoscopy in some ferroelectric Sm-C^* liquid crystals"*, **Phys. Rev. E**, **76**, 011709, (2007).

5. J. K. Song, U. Manna, A. Fukuda, and J. K. Vij, *"Sign reversals in the dielectric anisotropy as functions of temperature and frequency in SmA^* phase"*, **Appl. Phys. Lett.**, **91**, 042907, (2007).

6. J. K. Song, M. J. Sufin, and J. K. Vij, *"Solitary wave propagation in surface stabilized ferroelectric liquid crystal cells"*, **Appl. Phys. Lett.**, **92**, 083510, (2008).

7. J. K. Song, U. Manna, and J. K. Vij, *"Mechanism of field induced unwinding of SmC^* helix and bias field dependencies of dielectric permittivity and effective polarization"*, **Europhys. Lett.**, **82**, 26003, (2008).

8. J. K. Song, A. Fukuda, and J. K. Vij, *"Dynamic Mechanism of the SmC^*_A-SmC^* Phase Transition"*, **Phys. Rev. Lett.**, (submitted)

9. J. K. Song, J. K. Vij, and B. K. Sadashiva, *"Conoscopy of chiral smectic liquid crystal cells"*, **J. Opt. Soc. Am. A**, (accepted)

10. U. Manna, J. K. Song, Yu.P. Panarin, A. Fukuda, and J. K. Vij, *"Electro-optic and dielectric study of the de Vries–type smectic-A* phase exhibiting transitions to smectic-C_A^* and smectic-C* phases"*, **Phys. Rev. E**, **77**, 041707, (2008).

11. K. L. Sandhya, J. K. Song, Yu. P. Panarin, J. K. Vij, and S. Kumar, *"Experimental study of the high temperature smectic-C_{FI2}^* phase in chiral smectic liquid crystals that exhibit phase-sequence reversal"*, **Phys. Rev. E 77**, 051707, (2008).

12. U. Manna, J. K. Song, G. Power, and J. K. Vij, *"Effect of the cell surfaces on the stability of the chiral smectic-C phases"*, (submitted)

13. U. Manna, J. K. Song, and J. K. Vij, *"Observation of phase angle fluctuation in the de Vries-type SmA* phase possessing local orientational order with nano-scale correlation length"*, (submitted)

14. J. K. Song, U. Manna, A. Fukuda, and J. K. Vij, *"Antiferroelectric relaxation process in dielectric permittivity and the interlayer interaction in antiferroelectric liquid crystals"*, (submitted)

15. J. K. Song, A. Fukuda, and J. K. Vij, *"Gradual phase transition between the smectic-C* and smectic-C_A^* phases and the thresholdless antiferroelectricity"*, (submitted)

16. V. Manjuladevi, J. K. Song, Yu. P. Panarin, J. K. Vij, and B. K. Sadashiva, *"V-shaped electro-optic response observed in a chiral ferroelectric smectic liquid crystal"*, (in preparation)

17. J. K. Song, and J. K. Vij, *"Influences of confinement on the field induced sub-phases and the super-cooling for the antiferroferroelectric phase transition in chiral smectic liquid crystals"*, (in preparation)

List of Presentations

1. J. K. Song, A. D. L. Chandani, O. E. Panarina, A. Fukuda, J. K. Vij, V. Goertz and J. W. Goodby, *"Study of the SmC^*_α Phase in the Tokyo Mixture by Conoscopy Using Tilted Cell"*, **Proceedings of the 10th Conference On Ferroelectric Liquid Crystals, FLC05, in Stare Jablonki, Poland**, B39, p. 147, (2005).

2. J. K. Song, A. Fukuda, J. K. Vij, Y. Motoyama, and M. Johno, *"Temperature-induced sign reversal of biaxiality observed by conoscopy in so-called ferrielectric liquid crystals developed for V-shaped switching materials"*, **Proceedings of the 21st International Liquid Crystal Conference, ILCC06, in Colorado, USA**, FERRP-28, p. 612 (2006).

3. J. K. Song, J. K. Vij, and A. Fukuda, *"Field induced unwinding process of helix and inter-layer interaction in ferroelectric liquid crystals"*, **Proceedings of the 21st International Liquid Crystal Conference, ILCC06, in Colorado, USA**, FERRP-29, p. 613 (2006).

4. J. K. Song, A. D. L. Chandani, A. Fukuda, J. K. Vij, I. Kobayashi, and A. V. Emelyanenko, *"Temperature -induced sign reversal of biaxiality observed by conoscopy in some ferroelectric SmC* liquid crystals"*, **Proceedings of the 11th Conference On Ferroelectric Liquid Crystals, FLC07, in Sapporo, Japan**, O-04, p. 17 (2007).

5. J. K. Song, and J. K. Vij, *"Analysis of conoscopy of smectic liquid crystal cells"*, **Proceedings of the 11th Conference On Ferroelectric Liquid Crystals, FLC07, in Sapporo, Japan**, P1-47, p. 96 (2007).

6. J. K. Song, and J. K. Vij, *"Evidences of the existence of narrow energy well in synclinic ordering in SmC* phase"*, **Proceedings of the 11th Conference On Ferroelectric Liquid Crystals, FLC07, in Sapporo, Japan**, P2-17, p. 123 (2007).

7. J. K. Song, U. Manna, and J. K. Vij, *"High frequency collective mode of dielectric relaxation in antiferroelectric liquid crystal"*, **Proceedings of the 11th Conference On Ferroelectric Liquid Crystals, FLC07, in Sapporo, Japan**, P2-18, p. 124 (2007).

8. **(Awarded as 'Best Poster Presentation')** J. K. Song, and J. K. Vij, *"The solitary wave propagation in antiferroelectric liquid crystal cells"*, **Proceedings of the KSEAUK 33rd Anniversary Conference in Edinburgh, UK**, p. 21 (2007).

9. J. K. Song, U. Manna, and J. K. Vij, *"Mechanism of Field Induced Unwinding of SmC* Helix and Bias Field Dependencies of Dielectric Permittivity and Effective Polarization"*, **accepted in the 22nd International Liquid Crystal Conference, ILCC08, Jeju Island, Korea**, (2008).

10. J. K. Song, U. Manna, and J. K. Vij, *"Surface Confinement Effect in Various Smectic C Phases"*, **accepted in the 22nd International Liquid Crystal Conference, ILCC08, Jeju Island, Korea**, (2008).

11. U. Manna, J.-K. Song, and J. K. Vij, *"Investigation of the Electric Field Dependent Dielectric Response using 'Helical Fracture' Model and Effects of the Confinement in the Sm-Ca* Phase"*, **accepted in the 22nd International Liquid Crystal Conference, ILCC08, Jeju Island, Korea**, (2008).

12. U. Manna, J.-K. Song, J. K. Vij, and J. Naciri, *"Behavior of the Optical Birefringence and Electric Field Dependent Dielectric Response in the de Vries-type Sm-A* Phase possessing Local Orientational Order with Nanoscale Correlation Length"*, **accepted in the 22nd International Liquid Crystal Conference, ILCC08, Jeju Island, Korea**, (2008).

13. K. L. Sandhya, Yu. P. Panarin, J.K.Song, U. Manna, J. K. Vij, and S. Kumar, *"Electro-optics and Dielectric Studies Evidences the SmC^*_{FI2} - SmC* Liquid Crystal Phase Sequence Reversal"*, **accepted in the 22nd International Liquid Crystal Conference, ILCC08, Jeju Island, Korea**, (2008).

14. U. Manna, J.-K. Song, J. K. Vij, and J. Naciri, *"Behavior of Response time in an Electroclinic Liquid Crystal with Large induced Tilt and Polarization"*, **accepted in the 2nd International Conference on Liquid Crystal for Photonics, LCP-2008, University of Cambridge, UK**, (2008).

Part. I

Introduction and Experimental tools

Chapter 1

Introduction

"In this chapter, *the fundamentals of liquid crystals, and theoretical and mathematical tools required to realize the subject matter of this work are described.* "

1.1 Preface

Though most of the intense attention given to liquid crystals has been mainly due to their great success in the display industry, the physical characteristics of liquid crystals, themselves have also attracted many scientists' interest. As in all other areas of science, understanding and academic achievement in the liquid crystal field have been advanced originally by several pioneering scientists' inspirations, and subsequently by the contributions, small or large, of many other scientists inspired by previous discoveries.

This thesis also, building on the basis of the knowledge already established by other scientists, focuses on a small part of the liquid crystal field; Smectic liquid crystals, and in particular the intermolecular interaction and the interlayer

interaction between smectic layers. It is hoped that this work will inspire further development in the field. The subject, of smectic liquid crystals and their intermolecular and interlayer interactions, is quite broad and rather complicated. Moreover, the subject is one of the less well established parts of the liquid crystal field. This thesis reports a number of new physical observations, experimental methods and theoretical models.

The present thesis consists of thirteen chapters, and for convenience, the chapters are grouped into 5 parts.

Part. I (Chap. 1 and 2) provides an Introduction and describes the experimental methods used.

Chapter 1 is the introduction, which briefly outlines the basic concepts of liquid crystals and their various phases, the physical properties, and describes some mathematical tools required to realize the subject matter of this work. However, the reader should realize that this does not suffice either to give a full introduction to the field of liquid crystals or to provide the requisite mathematical and theoretical background for the subject matter described in this work. Those describing a broad overview of LCs or a deeper and more detailed discussion of the areas covered by this thesis are referred to [1] for a summarized review of general topics in liquid crystals, and to references [2] and [3] for a profound understanding of the topics, and to reference [4] for the specific field of ferroelectric and antiferroelectric liquid crystals.

Chapter 2 describes the experimental methods. In particular, the newly developed tilted conoscopic method and its usage are discussed in detail.

Part. II (Chap. 3 and 4) deals with the intermolecular interactions and the molecular distributions in smectic liquid crystals.

In **Chapter 3**, the orderings of the molecular short axis in the SmC^* are investigated by using the tilted conoscopic method. A temperature induced sign reversal of the biaxiality is found and explained theoretically. In **Chapter 4**, the molecular motions with the applied field in the SmA and SmC^*_A phases are investigated by

analyzing the dielectric permittivity.

In Part. IV (Chap. 5, 6 and 7), the interlayer interaction and solitary waves in smectic-C phases are investigated.

Despite the variety of solitary waves in the liquid crystal fields, this topic has not been received much attention to date. In **Chapter 5**, field induced solitary wave propagation in the SmC_A^* phase is investigated. A new method to measure the interlayer interaction in SmC_A^*, which is highly useful in the study of smectic liquid crystals, is reported as well. In **Chapter 6**, temperature induced solitary wave propagation in the SmC_A^* phase and the SmC^*-SmC_A^* phase transition accompanied by the solitary wave are investigated. In **Chapter 7**, the solitary wave in SSFLC cells is investigated.

In Part. V (Chap. 8, 9 and 10), the interlayer interaction and its consequences for the stabilities of the various tilted smectic phases are studied.

In **Chapter 8**, a new model for describing the cell thickness dependence of the stability of the subphases is suggested and compared with the experimental results. In **Chapter 9**, the so-called frustration between the ferroelectric and antiferroelectric states in binary mixtures of liquid crystalline materials is investigated. The interlayer interactions are revealed to play an important role in the stability of the phases. In **Chapter 10**, the phase sequence reversal phenomenon is dealt with shortly.

In Part. III (Chap. 11 and 12), the interlayer interaction and the unwinding process of ferroelectric liquid crystals is studied.

In **Chapter 11**, the unwinding process of the helical structure of ferroelectric liquid crystals is reexamined from the view points of the phase topology and the interlayer interaction. Though the conventional unwinding model explains nicely the basic properties of the helical unwinding, various contradictory experimental results have been reported. A new model, and the interpretation of various

physical properties based on the new model are described. In **Chapter 12**, a few experimental evidences for the new helical unwinding model are presented. In particular, the dependence of the biaxiality with the applied field during the helical unwinding is studied.

Finally, Part. VI (Chap. 13 and Appendix) are conclusion and appendix.
Chapter 13 contains the summary and the conclusion of this thesis. and in **Appendix A**, materials, apparatus and softwares used in this thesis are summarized.

1.2 What is a Liquid Crystal?

As might imagined from the name, "Liquid Crystal", the mechanical properties and the symmetry properties of liquid crystals are intermediate between those of an isotropic liquid and of a crystalline solid. Liquid crystal phases are called 'mesophase' or 'mesomorphic phases' (mesomorphic: of intermediate form) [2].

It is helpful to recall the distinction between a crystal and a liquid in order to understand the nature of liquid crystals. In crystals, the centers of mass of the molecules are located on a three-dimensional periodic lattice. In the liquid, the centers of mass are not ordered in this sense but are distributed isotropically. This fundamental difference results in different X-ray diffraction patterns; while X-ray diffraction patterns in crystals show sharp Bragg reflections characteristic of the lattice, those in liquids exhibit only diffuse peaks. In liquid crystals, some degree of anisotropy is present, and some sort of peculiar X-ray diffraction patterns appear though they are not so sharp.

The anisotropy in a liquid crystal, that is, the degree of ordering of the molecules, may vary depending on several factors. The first possibility is that there exists only orientational order, but no positional order, which corresponds to nematic liquid crystal phase. The second possibility is one-dimensional positional

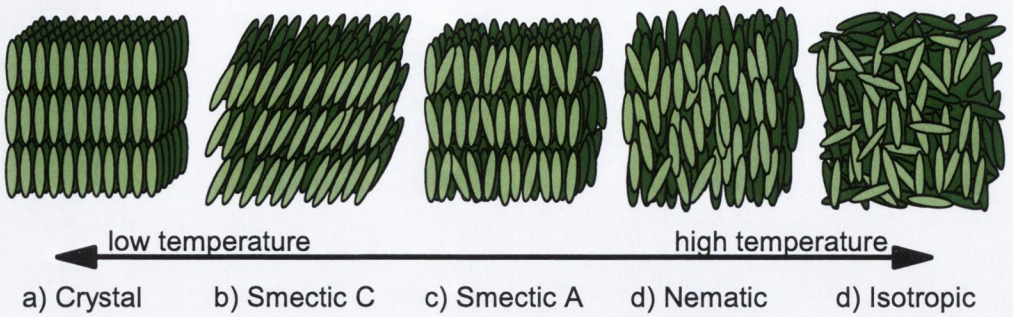

Figure 1.1: Schematic of phases

order, which means a two-dimensional freedom. The phase consists of a set of two-dimensional liquid layers stacked on each other. This corresponds to the case of smectic liquid crystals. The third possibility is two-dimensional ordering, which corresponds to columnar phases. Thus, in liquid crystals, the degree of ordering (as quantified by order parameters) is the most important property. Since columnar phases usually occur in materials with the disk-like liquid crystal molecules, except for a few large rod-like polymers [2, 3], only the nematic and smectic phases are commonly observed in materials with rod-like liquid crystalline molecules.

Fundamentally, there are two different types of liquid crystal; thermotropics and lyotropics. In the lyotropic liquid crystals, the order parameters depend on the concentration of the solution. On the other hand, in the thermotropic liquid crystals, the order parameters depend strongly on temperature. Therefore, in the thermotropic liquid crystals, the sequence of liquid crystalline phases is controlled by the temperature. The typical simplified phase sequence from high to low temperatures of thermotropic liquid crystals having rod-like molecular shape is isotropic - nematic - smectic A - smectic C - crystal as shown in Fig. 1.1. There are more phases such as hexatic smectics between smectic C and crystalline phase.

The word 'nematic' comes from the Greek word 'nema' meaning thread - referring to the typical type of defects visually observed in the nematic phase. Optically, nematic liquid crystals usually constitute a uniaxial medium with non-polar symmetry, but recently, a new type of nematic liquid crystals, biaxial nematic has been found [5]. The simple symmetry of nematics lends itself of easy alignment,

less defects and firm stability against the various external influences. Hence, nematics have had almost a monopoly in the various applications.

The word 'smectic' derives from the Greek 'smegma' meaning soap-like, or layered structures. Actually, soap itself has a thin layered structure and is a smectic liquid crystal.

Another important property in classifying liquid crystals is the chirality. A molecules is said to be chiral if it possesses no mirror plane or no center of symmetry. In order to distinguish a mesophase formed by chiral molecules, an asterisk(*) is usually added to its abbreviation. The chirality plays an important role in the properties as well as in the classification of liquid crystals, which will be partially explained in the next section.

The work described in this thesis is mainly focused on the thermotropic smectic A^* and smectic C^* phases only in cell geometries of planar and homeotropic alignments.

1.3 Order parameters

Axis of the preferred orientation of the molecules is usually characterized by a unit vector $\mathbf{n}$ known as the director. $\mathbf{n}$ has the usual vector properties except that it satisfies the physically reasonable condition $\mathbf{n} \equiv -\mathbf{n}$. The director determines only the axis of the preferred orientation of the molecules and has nothing to do with the degree of orientation.

The degree of orientation is described by the order parameter. The simplest form of order parameter is written as

$$S = \frac{1}{2}\left\langle 3\cos^2\theta - 1 \right\rangle, \tag{1.1}$$

where θ is the angle between the long axis of an individual molecule and the director. S represents the degree of orientation of the molecular long axis in

nematic ordering, and is suitable for representing the ordering of nematic liquid crystals.

The ordering of a biaxial phase or the ordering of impurity molecules in nematics cannot be represented by Eq. 1.1, and requires a tensor order parameter. The simplest second rank tensor order parameter in diagonalized form can be written as [6]

$$S_{ij} = \left\langle \frac{1}{2}(3l_i l_j - \delta_{ij}) \right\rangle, \tag{1.2}$$

where l_i is the direction cosine of the director with respect to a molecular axis i. Eq. 1.2 is referred to the Saupe ordering matrix.

The non-zero components of this tensor in polar coordinates are

$$\begin{aligned} S_{xx} &= \left\langle \frac{1}{2}(3\sin^2\theta\cos^2\phi - 1) \right\rangle, \\ S_{yy} &= \left\langle \frac{1}{2}(3\sin^2\theta\sin^2\phi - 1) \right\rangle, \\ S_{zz} &= \left\langle \frac{1}{2}(3\cos^2\theta - 1) \right\rangle, \end{aligned} \tag{1.3}$$

where θ and ϕ are the coordinates for the director in the x, y, z system. Eqs. 1.2 and 1.3 are sometimes useful to express the molecular distribution, but it also expresses only uniaxial orderings of each molecular axis. For example, S_{xx} represents the extent to which x axes of molecules are aligned along the same direction. However, with these order parameter, we cannot describe whether the fluctuation of the x axis of a molecule is isotropic or hindered. Therefore, we need a better expression of the order parameter for the biaxial phases.

The tensor representation can be extended to describe the orientational ordering of biaxial molecules in a biaxial phase by introducing a fourth rank ordering tensor [3, 7]. Following the notation used in reference [3],

$$S_{\alpha\beta,ij} = \left\langle \frac{1}{2}(3l_{i,\alpha}l_{j,\beta} - \delta_{ij}\delta_{\alpha,\beta}) \right\rangle, \tag{1.4}$$

where $l_{i,\alpha}$ is the cosine of the angle between the molecule axis α and the laboratory or phase axis i. By a suitable choice of coordinates without loss of generality, the 81 components of $S_{\alpha\beta,ij}$ can be reduced to nine such that $i = j$ and $\alpha = \beta$. This is equivalent to defining three diagonal Saupe ordering matrices, one for each of the three axes, $i = X, Y, Z$.

$$S_{\alpha\alpha}^{(i)} = \left\langle \frac{1}{2}(3l_{i,\alpha}^2 - 1) \right\rangle, \tag{1.5}$$

Taking the diagonal component of these three matrices allows the construction of a 3×3 matrix.

$$S_{\alpha\alpha}^{(i)} = \begin{pmatrix} S_{xx}^X & S_{yy}^X & S_{zz}^X \\ S_{xx}^Y & S_{yy}^Y & S_{zz}^Y \\ S_{xx}^Z & S_{yy}^Z & S_{zz}^Z \end{pmatrix}, \tag{1.6}$$

Note that x, y and z are the molecular axes, and X, Y and Z are the laboratory or phase axes. Hence, for example, S_{yy}^X represents the extent to which the y axis of molecules aligns along the X axis in the laboratory coordinate system.

The generalized biaxial order parameters can be defined as follows. The long axis ordering is described by $S = S_{zz}^Z$, which is the same as Eq. 1.1 and S_{zz} in Eq. 1.3. The phase biaxiality for a uniaxial molecule is given by $P = S_{zz}^X - S_{zz}^Y$, which represents the anisotropic fluctuation of the molecular long axis in the laboratory coordinate, hence it is connected to the macroscopic phase biaxiality. For biaxial molecules in a uniaxial phase the biaxial order parameter is $D = S_{xx}^Z - S_{yy}^Z$, which represents the anisotropic fluctuation of the molecular long axis in molecular coordinate. D does not represent the phase biaxiality. It is also possible to define a biaxial order parameter with respect to the X and Y axes, such that $D' = S_{xx}^X - S_{yy}^X$, and $D'' = S_{xx}^Y - S_{yy}^Y$. Another biaxial order parameter $C = D' - D''$ represents a phase biaxiality induced by the hindered rotation around the molecular long axis. Thus, S, P, D and C describe the full set of the order parameters for a biaxial molecule.

These order parameters are also defined using Euler angles as

$$\begin{aligned} S &= S_{zz}^{Z} = \left\langle \frac{1}{2}(3\cos^2\theta - 1) \right\rangle, \\ D &= S_{xx}^{Z} - S_{yy}^{Z} = \left\langle \frac{3}{2}(3\sin^2\theta\cos 2\psi) \right\rangle, \\ P &= S_{zz}^{X} - S_{zz}^{Y} = \left\langle \frac{3}{2}(3\sin^2\theta\cos 2\phi) \right\rangle, \\ C &= (S_{xx}^{X} - S_{yy}^{X}) - (S_{xx}^{Y} - S_{yy}^{Y}) \\ &= \left\langle \frac{3}{2}\left[(1+\cos^2\theta)\cos 2\phi\cos 2\psi - 2\cos\theta\sin 2\phi\sin 2\psi\right] \right\rangle, \end{aligned} \tag{1.7}$$

These order parameters are useful for connecting the microscopic molecular properties to the macroscopic phase properties.

1.4 Symmetry and Ferroelectric and Antiferroelectric Liquid Crystals

Ferroelectricity is an electrical phenomenon whereby certain materials may exhibit a spontaneous dipole moment, the direction of which can be switched between equivalent states by the application of an external electric field. Liquid crystal materials having the properties of ferroelectricity in one or more phases are referred to as the ferroelectric liquid crystals. Most liquid crystal molecules have permanent dipole moments, but only some of them shows ferroelectric phases because the permanent dipole moments of individual molecules are usually cancelled out through symmetrical alignment. Hence, the ferroelectricty in liquid crystals arises from the asymmetry of molecular alignments [8].

There are many mathematical groups in the rotational and the reflectional symmetry [9]. Here, a few cases following Schönflies notation, which are commonly found in liquid crystals, are introduced. Rotational symmetry of order n, also called n-fold rotational symmetry means that rotation by an angle of $360°/n$ (180°,

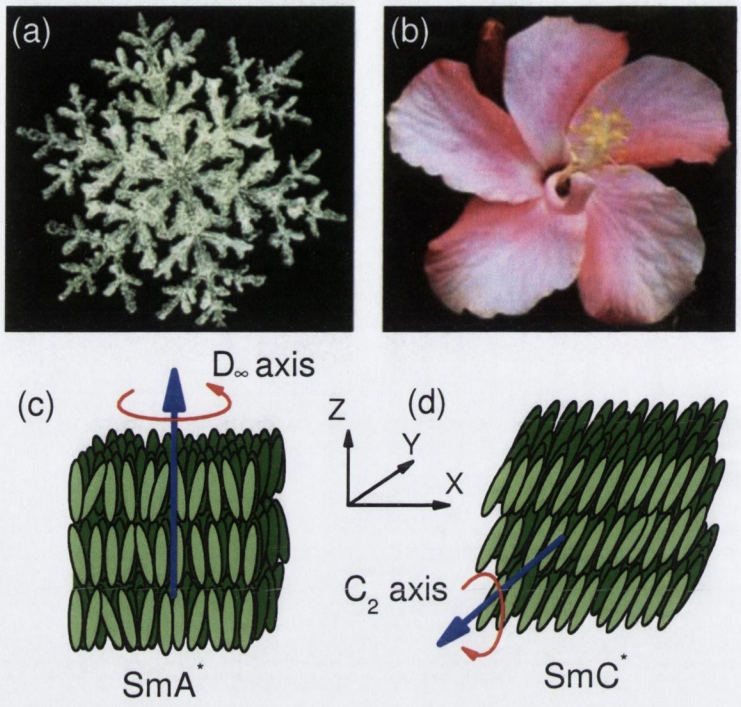

Figure 1.2: Examples of D_{6h} symmetry ((a): snowflake) and C_5 symmetry ((b): propeller-shaped flower) in nature; (c) D_∞ symmetry in SmA^* phase and (d) C_2 symmetry in SmC^* phase

120°, 90°, 72°, 60° *etc.*) does not change the object. Reflection symmetry, or mirror symmetry is a symmetry with respect to reflection.

The notation C_n corresponds to n-fold rotational symmetry along a fixed axis. D_n consists of the n-fold rotational symmetry in C_n together with the flipping symmetry along the axis perpendicular to the rotational symmetry axis, that is, the object having D_n symmetry is invariant under the up-side down flipping.

In addition to this, one may add a mirror plane perpendicular to the axis of rotational symmetry, which produces the additional groups C_{nh} and D_{nh} respectively. If the n-fold rotational symmetry axis also has n-mirror planes containing the axis, it produces C_{nv}. The D_{nd} or D_{nv} group has vertical mirror planes containing the main rotation axis, but instead of having a horizontal mirror plane it has an isometry which is the combination of a reflection in the horizontal plane and a rotation by an angle 180°/n.

Therefore, we find that nematic and SmA have a $D_{\infty h}$ symmetry since

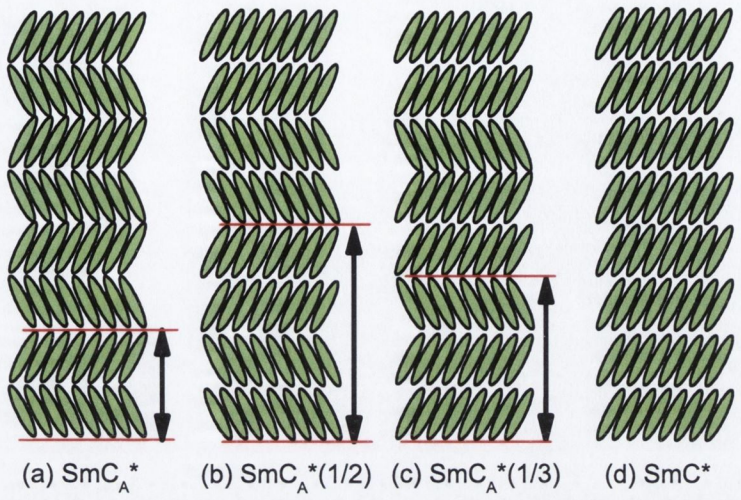

Figure 1.3: Various smectic-C phases; Arrows indicate the period for each structure.

these have a symmetry axis parallel to the director. SmC has two-fold rotational symmetry along the axis perpendicular to the tilt plane and the mirror plane perpendicular to the axis and this has C_{2h} symmetry. However, chiral SmC^* does not have a mirror plane perpendicular to the symmetry axis, hence the phase has C_2 symmetry. For the same reason, SmA^*, which consists of chiral molecules, belongs to the D_∞ point group.

The Neumann principle (named after Franz Neumann) states that any physical property of a medium must be invariant under the symmetry operations of the point group of the medium [9].

Therefore, we can conclude that the nematic and SmA^* phases cannot possess spontaneous polarization, because the polarization should be invariant under flipping or rotating with respect to the symmetry axes, and only zero polarization can be invariant under these symmetry operations. The SmC phase also cannot have a net polarization, since it has a C_{2h} symmetry and the physical property should be invariant under the 180° rotation and reflection operations. However, SmC^* has a C_2 symmetry, and the polarization cannot exist along x or z axes, but it can exist along y axis. Thus, the chirality actually breaks the mirror symmetry with respect to the tilt plane, and allowing spontaneous polarization, which was discovered by R. B. Meyer *et.al.* in 1975 [8].

On the other hand, the discovery of the antiferroelectric liquid crystal phase was made 15 year later by Chandani *et. al.* [10] who observed the tristable switching in MHPOBC. Later, at least two more sub-phases were identified between the ferroelectric SmC^* and the antiferroelectric SmC^*_A phases, and these were designated as Sm$C_A(1/2)$ and Sm$C_A(1/3)$ using qT notation denoting the number of synclinic ferroelectric orderings per one short period of a particular phase [11, 12]. qT varies from zero in SmC^*_A to one in SmC^*. These phases have the same symmetry, but the molecular tilting between neighboring layers is different.

Fig. 1.3 shows the schematics for the smectic-C phases. Typically, the phase sequence proceeding from low temperature is SmC^*_A–Sm$C_A(1/2)$–Sm$C_A(1/3)$–SmC^*. Sm$C_A(1/2)$ and Sm$C_A(1/3)$ are commonly called as AF and SmC_γ, respectively.

1.5 Free energy expressions and phase transitions

Landau theory [13] in physics was introduced by Lev Davidovich Landau (Soviet theoretical physicist, 1908 – 1968) in an attempt to formulate a general theory of second-order phase transitions. He was motivated to suggest that the free energy of any system should obey two conditions: that the free energy function is analytic, and that it obeys the symmetry of the Hamiltonian. Given these two conditions, one can write down a phenomenological expression for the free energy as a Taylor expansion in the order parameter. His theory has a universality, (*i.e.*, the theory can be applied in various fields of physics).

In liquid crystals, since de Gennes used the Landau theory to explain nematic-SmA transition, many attempts to explain various phase transitions in liquid crystals have been tried. For example, the free energy for describing the SmA^*–SmC^* transition can be written as [4]

$$G = \frac{1}{2}\alpha(T - T_0)\theta^2 + \frac{1}{4}b\theta^4 + \frac{1}{2\chi_0\epsilon_0}P_s^2 - c^*P_s\theta - PE, \tag{1.8}$$

where T_0 is the transition temperature in non-chiral system, θ is the polar tilt angle, P_s is the spontaneous polarization and E is the applied field. Simple calculations show that the transition temperature is determined by

$$T_c = T_0 + \frac{\chi_0 \epsilon_0 c^{*2}}{\alpha}. \tag{1.9}$$

When $T > T_c$, the minimum energy state is when $\theta = 0$, but when $T > T_c$, θ becomes that

$$\theta = \sqrt{\frac{\alpha(T_c - T)}{b}}. \tag{1.10}$$

As shown in these equations, the tilt angle θ is used for the order parameter to determine the temperature of the SmA^*–SmC^* transition. Thus, the landau expansion describes the phase transition reasonably.

Similar equations have been applied to the phase transitions between the various subphases. For example, in the discrete flexoelectric model, the free energy is written as [14]

$$\begin{aligned} F = \sum_{i=1}^{N} \Big[& \tilde{F}_0(\theta) - \tilde{a}\frac{\Delta T}{T^*}(\cos\varphi_{i-1,i} + \cos\varphi_{i,i+1}) - \widetilde{B}(\cos^2\varphi_{i-1,i} + \cos^2\varphi i, i+1) \\ & + \frac{1}{2\chi}\{\mathbf{P}_i^2 + g(\mathbf{P}_i\mathbf{P}_{i+1} + \mathbf{P}_i\mathbf{P}_{i-1})\} + c_s(\mathbf{P}_i\xi_{i+1}) \\ & + c_f \cos\theta(\mathbf{P}_i\Delta\mathbf{n}_{i\pm1})\Big], \end{aligned} \tag{1.11}$$

where $\tilde{F}_0(\theta)$ is the tilt angle dependent free energy part governing the non-tilted to tilted phase transition, that is the SmA^* – SmC^* phase transition, and the second and third terms are designed for expressing the synclinic phase to the anticlinic phase transitions, that is the SmC^* – SmC_A^* transition. The other terms in Eq. 1.11 are the spontaneous polarization terms including the flexoelectric polarization, which is believed to govern the generation of sub-phases between SmC^* and SmC_A^* in the model. In this case, the azimuthal angle ϕ is also used as an order parameter for describing the phase transitions.

1.6 Physical properties of liquid crystals

As a more complete description of the physical properties of liquid crystals is not possible here, only short introductions to the properties relevant to the work in this thesis are give.

■ Electric properties: Polarization and dielectric anisotropy

When an external field E is applied to a medium, the total polarization (P_t) in the medium is written as

$$\vec{P}_t(E) = \vec{P}_s + \epsilon_0 \chi_{\alpha\beta} \vec{E}, \tag{1.12}$$

where $\vec{P}_s$ is spontaneous polarization, and $\chi_{\alpha\beta}$ is the second rank of the susceptibility tensor.

Therefore, when the applied field is parallel to y axis in Fig. 1.2, the electric potential energy is written as

$$\begin{aligned} U &= -\vec{P} \cdot \vec{E} = \vec{P}_s \cdot \vec{E} - (\epsilon_0 \chi_{\alpha\beta} \vec{E}) \cdot \vec{E} \\ &= -P_s E \cos\phi + \epsilon_0 \Delta\epsilon' \cos^2\phi E^2 + const., \end{aligned} \tag{1.13}$$

where ϕ is the angle between x axis and **c** director, $\Delta\epsilon' = \sin^2\theta \Delta\epsilon$, θ is the tilt angle, and $\Delta\epsilon$ is the dielectric anisotropy.

Therefore, in the static case, the coupling of liquid crystals with the applied field is determined by P_s and $\Delta\epsilon$. In the liquid crystals having no spontaneous polarization such as Nematic and SmA^*, the dielectric anisotropy $\Delta\epsilon$ is the most important parameter in the electric coupling. In the liquid crystals having spontaneous polarization, P_s is the major coupling factor, because $\epsilon_0 \Delta\epsilon$ is much smaller than P_s usually.

■ Optical properties and anisotropy

According to Vuks isotropic local field model [15], the principal refractive indices can be written as

$$\frac{n_i^2 - 1}{n^2 + 2} = \frac{N\alpha_i}{3\epsilon_0}, \tag{1.14}$$

where α_i is the average value of the polarizability along the direction of the principal refractive index n_i, and $n^2 = (n_1^2 + n_2^2 + n_3^2)/3$ is a mean refractive index.

Therefore, the anisotropy of the polarizability induces the macroscopic anisotropy of the refractive index. The anisotropy of the polarizability Using the order parameters in section 1.3, we can express the eigen values α_i, $i = X, Y,$ or Z as

$$\left.\begin{aligned} \alpha_X &= \bar{\alpha} - \tfrac{1}{3}\left[\Delta\alpha\,(S+P) + \Delta\alpha_\perp \tfrac{(D+C)}{2}\right] \\ \alpha_Y &= \bar{\alpha} - \tfrac{1}{3}\left[\Delta\alpha\,(S-P) + \Delta\alpha_\perp \tfrac{(D-C)}{2}\right] \\ \alpha_Z &= \bar{\alpha} + \tfrac{2}{3}\left[\Delta\alpha S + \Delta\alpha_\perp \tfrac{D}{2}\right], \end{aligned}\right\} \tag{1.15}$$

where $\bar{\alpha}$ is the average polarizability, $\Delta\alpha$ and $\Delta\alpha_\perp$ are the anisotropy, and the transverse anisotropy of the molecular polarizabilities, respectively [3].

Thus, the molecular ordering is the basic origin of the macroscopic refractive index anisotropy in liquid crystals. For better description, see chapter 3.

■ Elastic property and continuum theory

The elasticity is a macroscopic property of matter defined as the ratio of an applied static stress to the strain or deformation produced in the material. The mechanical stability of liquid crystals is described in terms of elastic properties. In the absense of flow, ordinary liquids cannot support a shear stress, while solids will support compressional, shear and torsional stresses. The elastic properties of liquid crystals are intermediate between those of liquids and solids, and depends on the symmetry and phase type.

Free energy density induced by distortion can generally be written as

$$g = \frac{1}{2}\left[K_1(\nabla \cdot n)^2 + K_2(n \cdot \nabla \times n)^2 + K_3(n \times \nabla \times n)^2\right], \tag{1.16}$$

where K_1, K_2 and K_3 are the elastic coefficients for the splay, the twist and the bend deformation, respectively. Thus, elastic energy is determined by the deformation of the directors. The energy expression can be simplified or be complicated according to the deformation structure.

■ Viscosity

The viscosity of a fluid is an internal resistance to flow, defined as the ratio of shearing stress to the rate of shear. It arises from the intermolecular forces in the fluid. The viscous behavior has a profound effect on the dynamical behavior of liquid crystals.

■ Flexoelectric effect

Elastically deformed structure induces the ordering of the molecules, which influences the polarization. This is the flexoelectric polarization. Therefore, the flexoelectric polarization depends on the deformation. The flexoelectricity is supposed to be responsible for the emergence of various subphases.

■ Chirality

Molecular symmetry is used to describe the spacial configuration of a single molecular structure, inasmuch as it describes the geometric, conformational and cofigurational properties of the material. On the other hand, optical activity or chirality is simply the property of the molecules of an enatiomer to rotate the polarization plane. Such molecules are said to be optically active. The molecular chirality induces the helical structure in the phases. As explained in section 1.4, it also reduce the symmetry of smectic C phase from C_{2h} to C_2, and as a result, the spontaneous polarization appears.

■ Surface and anchoring effect

This will be dealt with in chapter 10.

■ Optical calculation in a liquid crystal cell

Many birefringent optical systems including liquid crystal cells are made of anisotropic layered media that consist of a train of polarizers and crystal plates. The effect of

each individual element on the polarization state of the light beam can be easily pictured without the aid of any matrix algebra. However, when an optical system consists complex structures of optical components such as a twisted or deformed liquid crystal cell, the calculation of the transmission becomes complicated and is greatly facilitated by a systematic approach.

Jones matrix algebra is a powerful 2×2 matrix method in which the electric field vector (or state of polarization) is represented by a two-element column vector, while each crystal plate or polarizer is represented by a 2×2 matrix. The whole optical system is represented by a 2×2 matrix obtained by the multiplication of all the matrices in sequence. The transmission of light is thus described by the multiplication of the input vector with the matrix. The Jones matrix method is suitable far carrying out the optical calculation only in the case of normal incidence of light.

In 1982, Pochi Yeh [16] developed an Extended Jones matrix method to calculate the transmission characteristics of a birefringent network for off-axis light. This new 2×2 matrix is still easy to manipulate algebraically and accounts for the effects of the Fresnel refraction and single refraction at the interface. However, this method neglects multiple reflections, so it is not suitable for dealing with reflections. For example, Bragg reflection and selective reflection cannot not be modelled using the Extended Jones matrix method.

The 4×4 matrix method by Berreman [17] is a general approach for finding the eigenwaves. This method explains reflection as well as transmission. Yeh [18] developed another 4×4 matrix method, which is similar to that of Berreman [17], but is based on the Jones matrix platform and so, is easy to understand for those who have studied the Jones matrix method previously.

The optical simulations in this thesis are based on the 4×4 matrix method by Yeh [18]. The details of the method are not given here. The reader is referred to articles [17, 18] and books [19, 20] for full details on programming the simulation.

Chapter 2

Experimental Method: Conoscopy

"**In this chapter,** *conoscopy is investigated in detail including i) a novel method using tilted samples, ii) limitations of conoscopy and solutions of these, and iii) a new simulation method for estimating the molecular distribution from conoscopic data.* "

2.1 Introduction

The experimental methods used in this thesis are listed as belows;

i) Conoscopy,

ii) Microscopy and electro-optic measurement including the measurement of spontaneous polarization and an apparent tilt angle [21],

iii) IR and Visual Spectroscopy for measuring helical pitches and birefringence [22, 23],

iv) PEM (photo-elastic modulator) system for measuring birefringence [24,

25],

v) Dielectric response measurement using a broadband high resolution dielectric spectrometer (Novocontrol GmbH, Germany) [26, 27],

vi) Raman, (the data of which are not included in this thesis.)[28]

and softwares for analyzing and simulating the experimental data and for verifying models are listed as;

vii) Visual Basic 6.0, for simulating various intermolecular interaction, interlayer interaction, director distribution, and conoscopic analysis,

viii) Matlab 6.1, for optical simulation including the 4×4 matrix method,

ix) Origin 7.5, for fitting Raman data and analyzing usual experimental data.

These tools are very useful to investigate the properties of liquid crystals, but the detail of these does not present in this thesis and only brief summary will be given in Appendix. In this chapter, only the conoscopic method, which the author contributed significantly to improve, is dealt with in detail.

Conoscopic method is an optical technique to investigate an optically transparent specimen placed in a cone of the converging rays of light placed within the crossed polarizers. This technique has been used extensively for investigating the properties of liquid crystals. The method is also used widely in the liquid crystal display industry for measuring the viewing angle properties of displays and for determining the image quality from oblique directions of the incidence of light. For the latter, the various commercial measurement systems have been developed [29]. Scientifically, the method has been found to be an extremely powerful tool for investigating and modeling the various properties of liquid crystals. The method is used in determining the eigen refractive indices of refractive index ellipsoid of liquid crystal cells. Here a cell is considered as an optically single-biaxial plate having three principal refractive indices n_{o1}, n_{o2} and n_e. Galerne obtained the biaxiality ($\Delta n = n_{o2} - n_{o1}$) and the apparent tilt angle (Θ, the angle between the directions of n_e and the normal to the cell) of achiral liquid crystal material in its various phases using conoscopic experiments [30]. Gorecka *et al.* carried out similar experiments by applying electric field across ferroelectric liquid crystal

cells, where helical structure may be formed [31]. Fujikawa *et al.* observed the dynamic behavior of conoscopic image by using the CCD camera [32], and Song *et al.* contributed to enlarging the observable range of the tilt angle of chiral smectics by developing the tilted conoscopic system [33, 34].

As stated above, conoscopy has been used for various scientific and technological applications including those for determining the refractive index ellipsoid [30–34], in estimating the molecular distribution [33–36] and in identifying the liquid crystalline phases [12, 31, 32]. Due to the sub-structure of a few layers periodicity and of a longer helical structure, each phase shows a special characteristic behavior during the field induced unwinding process of the helix, hence the values of the biaxiality ($\Delta n = n_{o2} - n_{o1}$) and the apparent tilt angle (Θ) under low electric fields have been used for identifying the phases. For example, the melatopes parallel to the applied field in conoscopic images have been used for assigning the phase as SmC^*_γ (or Sm$C^*_A(1/3)$) [12, 31, 32], but it has been reported that such a qualitative identification technique can in some cases lead to incorrect conclusions [34, 36]. Melatopes parallel to the applied field can appear not only in SmC^*_γ phase but also in SmC^* and SmC^*_α phases [33, 34, 36], and so, we can not state with certainty that directions of the melatopes in the conoscopic image relative to the low external electric field do correctly identify the phase. For a clear identification of the phase, it is required to calculate the exact values of the biaxiality and the apparent tilt angle and to estimate the molecular distribution in a cell accurately. Therefore, an accurate and a quantitative method of the analysis of conoscopy is required. Furthermore, conoscopy has mostly been used as a qualitative auxiliary technique in the study of liquid crystals and the quantitative analysis has been rarely made. This is presumably due to the fact that despite a simplicity involved in carrying out the conoscopic experiments and obtaining the data, analysis of the results and their meaningful interpretations are quite complicated. Furthermore, the quantitative method for analyzing the conoscopic image contains a number of approximations, and their validity and the errors in obtaining the results have not been explored as yet. Therefore, to expand the usage of the conoscopic method, it is required to improve the analyzing

method as well as the experimental method.

In section 2.2, we summarize the conoscopic set-up and analyzing method, and in section 2.3, we suggest a novel experimental method using a tilted cell, and in section 2.4, we investigate the method of the analysis of the conoscopic data and find that there exist two approximations in the analysis: (i) a single-biaxial-plate assumption in helical phases and (ii) a choice of one of the principal refractive indices with a view to using the technique. In section 2.5, we suggest a better utilization of the technique of conoscopy for the study of liquid crystals, and develop an effective simulation method to determine the molecular distribution from the measured conoscopic results based on using the average-refractive index method.

2.2 Conoscopy and analysis

We briefly explain the conoscopic experiment and the procedure for the analysis of the conoscopic images [31, 37, 38]. The schematic is shown in Fig. 2.1. Conoscopic method consists of the two cross polarizers and the use of at least two optical lenses. The screen and the sample cell are placed at the focal planes of the objective lens. The light passing through the sample along each direction gives rise to a distribution of the intensity on the screen, independently of all other directions. Each point on the image projected on the screen (*i.e.* the x'–y' plane in Fig 2.1) corresponds to a certain direction of the incident light into the cell, and the direction is determined by a simple geometric calculation; The direction of light outside the cell can be represented as the polar angle ϑ' and the azimuthal angle φ', where ϑ' is the angle of incidence with respect to the normal to the cell and φ' is the angle of the projection of light on the cell plane with respect to the x axis. The center point of the image corresponds to the direction $(\vartheta',\varphi')=(0,0)$, and the maximum observable polar angle is determined by the value of numerical aperture (NA $= \sin\vartheta'$ in air) of the lens and so, ϑ'_{max} at the boundary of the image is given as $\vartheta'_{max} = \sin^{-1}(\mathrm{NA})$. Hence, a point $(x',y')=(x'_0,y'_0)$ on the screen corresponds

to the direction $(\vartheta',\varphi')=(\tan^{-1}[\tan(\vartheta'_{max})(x'^2_0+y'^2_0)^{1/2}/x'_{max}],\tan^{-1}(y'_0/x'_0))$, where x'_{max} is the radius of the image. The intensity projected on the screen reflects the phase difference or the retardation that the light experiences in passing through the sample. Therefore, the two dimensional pattern on the screen contains the information about the refractive index ellipsoid of the sample. This can be extracted from the conoscopic pattern through a series of calculations. Conoscopic observations can be made by using a specially designed conoscopic instrument or by using a polarizing microscope equipped with a Bertrand lens. A Bertrand lens in a polarizing microscope is placed between the objective and the ocular lenses for making the observations of the so-called directional image, or the conoscopic image. The conoscopic images shown in this thesis were obtained by using an optical polarizing microscope (Olympus BX-52). We used lenses with large numerical aperture (NA) both for the objective (Olympus, LM PlanFI; 50 , 0.5 NA) and the condenser (Instech; 0.65 NA) for maximizing the observable range. Homeotropically aligned liquid crystal cells each of 100 μm cell thickness were prepared by using a homeotropic alignment agent, carboxylatochromium complexes (chromolane). The liquid crystals used are (R)(1-methylheptyloxycarbonyl)phenyl-4'-carboctyloxy-biphenyl-4-carboxylate (MHPOOCBC), 3.b.5 and Felix018. Chemical structures of MHPOOCBC and 3.b.5 are shown in Fig. 2.1. Felix018 is a commercial ferroelectric liquid crystal mixture synthesized by HOECHST AG, and the chemical structure of it is unknown.

Conoscopic images captured using a digital camera (Leica DFC480) mounted on the microscope head were fed to a computer for the analysis of results. Conoscopic image produced by a biaxial plate consists of concentric elliptic dark rings and the two parabolic dark lines as shown in Fig. 2.1, where only a half of the conoscopic image is shown. The vertices of the parabolas correspond to the optic axes of the biaxial plate. Hence, one can obtain an approximate information about the refractive index ellipsoid that mimics the cell qualitatively from the shape and the direction of the parabolas.

A brief procedure for obtaining the biaxiality and the apparent tilt angle of the liquid crystalline compound confined in the cell is detailed here. The two

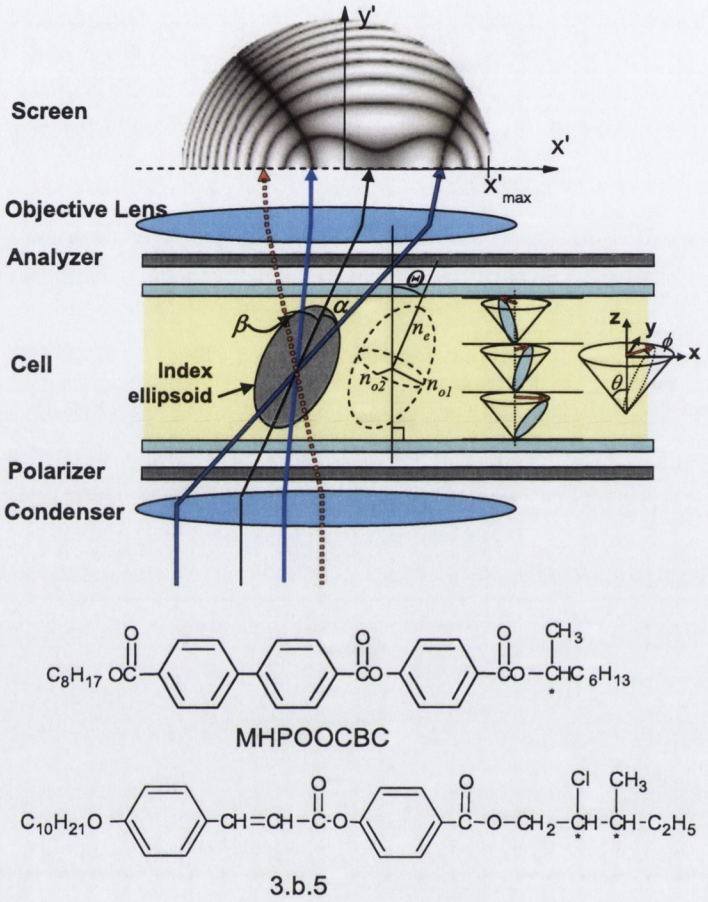

MHPOOCBC

3.b.5

Figure 2.1: Schematic set-up for conoscopy (Top) and the chemical structure of liquid crystals used (bottom); The x'–y' plane is the screen plane, and the x, y and z coordinate system is for the cell. The directions of two optic axes (blue thick lines), a dark line (red dashed line) and the tilt direction of the refractive index ellipsoid (black thin line) are required for calculating the biaxiality and the apparent tilt angle, Θ. Homeotropically aligned Smectic C liquid crystals have a layered structure. In each smectic layers, the average direction of molecules is tilted from normal to the cell by θ, called the tilt angle, and the tilting direction, ϕ, varies vertically layer by layer and forms a helical structure. α and β are the angles of the optic axes and the N-th dark ring from the major axis of the index ellipsoid, respectively (N can be chosen arbitrararily, and here, $N = 2$).

optic axes and a dark point on the concentric elliptic rings are used for calculating the biaxiality and the apparent tilt angle of the LC in the cell. The angle of the incident light outside the cell for the two optic axes (blue thick lines), for a dark point (red dashed line) and for the apparent tilt direction (black thin line) can be obtained by the simple geometric calculation explained above, and the directional information can easily be transformed to the approximate directions of light inside the cell using Snell's law and an approximate value of the refractive index ($\tilde{n} = 1.5$) in the geometry shown in Fig. 2.1 [34]. In this way, the apparent tilt angle, Θ, is obtained directly from the calculation. Similarly, angles of the optic axes and the n-th dark point from the major axis of the refractive index ellipsoid, which are denoted as α and β, respectively, are obtained. Incident light is separated into two paths inside the biaxial cell; the path is determined by the two eigen refractive indices for the direction. When the light propagates in the plane including the two optic axes of the refractive index ellipsoid of the cell, the two eigen refractive indices are n_{o2} and $n_{o1'}$ if $n_{o2} > n_{o1}$. However, if $n_{o2} < n_{o1}$, the two eigen refractive indices are n_{o1} and $n_{o2'}$. The eigen refractive index, $n_{o1'}$ is found as

$$n_{o1'} = \left[\left(\frac{\cos\zeta}{n_e} \right)^2 + \left(\frac{\sin\zeta}{n_{o1}} \right)^2 \right]^{-\frac{1}{2}}, \tag{2.1}$$

where ζ is the angle of the light path from the direction of n_e inside the cell. No transmission of the incident light corresponding to the dark point on the screen means that the phase difference of the two beams that have been split by the birefringent medium after passing through it, is an integral multiple of the wavelength, λ. For the optic axes and the dark lines on the screen, therefore one can write a simple equation as

$$n_{o1'} l_{o1'} - n_{o2} l_{o2} = m\lambda, \quad (m = 0, 1, 2...), \tag{2.2}$$

where $l_{o1'}$ and l_{o2} are the geometrical path lengths of the two split beams, and are found as $l_{o1',o2} = d \cdot n_{o1',o2} / \sqrt{n_{o1',o2}^2 - \sin^2(\vartheta)}$, where d is the cell thickness and ϑ is the polar angle of the incident light outside the cell with respect to the normal

to cell. Hence, eq. 2.2 can be rewritten as

$$d\left[\frac{n_{o1'}^2}{\sqrt{n_{o1'}^2-\sin^2\vartheta}}-\frac{n_{o2}^2}{\sqrt{n_{o2}^2-\sin^2\vartheta}}\right]=m\lambda,\quad(m=0,1,2...). \tag{2.3}$$

In eqs. 2.1 and 2.3, d and λ are given from the experimental conditions, and ϑ is measured from the conoscopic image. When $\zeta=\alpha$, that is, the light propagates along the optic axes, $m=0$, and when $\zeta=\beta$, that is, the light propagates along the direction corresponding to the N-th dark line, $m=N$ (in Fig. 2.1, $N=2$). Each of these conditions produces one set of equations from eqs. 2.1 and 2.3, and these equations can be used to find the principal refractive indices of the ellipsoid. By assuming one of the values of the principal refractive indices (for example, $n_{o1}=1.5$), the other two principal refractive indices are obtained numerically from eqs. 2.1 and 2.3. The obtained values of principal refractive indices are used to recalculate α, β and Θ and in order to improve the accuracy of the obtained values, the same procedure is iterated several times, when the calculated principal refractive indices converge quickly. Finally, the biaxiality is calculated as $(n_{o2}-n_{o1})$. This is an explicit method to find the biaxiality, but eqs. 2.1–2.3 can be further simplified to obtain analytic equations, which enable us to find the other two principal refractive indices analytically, by using further approximations so that $l_{o1'}\approx l_{o2}$ in eq. 2.2 [31, 38].

In these calculations, the two approximations are made. Firstly, the cell is considered as a single-biaxial-plate as shown in Fig. 2.1, and secondly one of the values of the principal refractive indices is assumed, for example, $n_{o1}=1.5$. We examine these two assumptions in the next section.

If the optical properties of a sample are known, the conoscopic image can be simulated conversely. The 4×4 Matrix method [17, 18] is useful for this purpose. When a polarized light passes through a single or multi-layered biaxial plates, one can calculate the polarization and the amplitude of the transmitted and the reflected lights accurately using the 4×4 Matrix method. In particular, when a sample is placed between the two polarizers, the transmittance of the incident

light can be calculated for any direction of the incident light. For simulating the conoscopic image, one need to decide the resolution of the image and the range of the polar angle. Once the resolution and the range are determined, the screen is divided in to a number of square grids to represent the resolution. Positional information of each point of the grids on the screen is changed into the polar angle and the azimuthal angle of the light. By using the 4×4 Matrix method, the transmittance is calculated for each direction of light, and is plotted for each point of the screen corresponding to the direction of the incident light. In this way, one can obtain a two dimensional conoscopic pattern for a given stack of biaxial plates.

2.3 Tilted conoscopic method

All conoscopic observations were made using an optical polarizing microscope (Olympus BX-52) having large numerical aperture (NA) lenses both for the objective (Olympus, LM PlanFI, 50X / 0.5NA) and the condenser (Instech, 0.65 NA). NA=0.5 corresponds to an angular field extending from $-30°$ to $30°$ in air, and extending from $-19.5°$ to $19.5°$ in a liquid crystal cell with $n_{\mathrm{lc}} = 1.5$ placed horizontally. Consequently, the melatopes of liquid crystals having tilt angles of larger than $\sim 20°$ are out of the field of view, so that we could not determine the biaxiality.

By sandwiching the cell between a pair of prisms (Fig. 2.2) made of heavy optical glass SF11 (index of refraction of 1.82) and having an apex angle of 30°, we attained an angular field that extends from 17° to 60.6°, so that a large tilt angle and large biaxiality could be measured. Index-of-refraction matching oil was used to reduce the reflection arising from the air gaps between the glass plates and the prisms. Sometimes the prism was replaced with a conventional cell and its metal attachments slanted by 30° with respect to the microscope stage so that the angular field in the liquid crystalline sample extends from 0° to 35.3°. By combining the two methods, we can use conoscopy for measuring the biaxiality when the tilt angle is as large as 45°. The sample was heated in an oven.

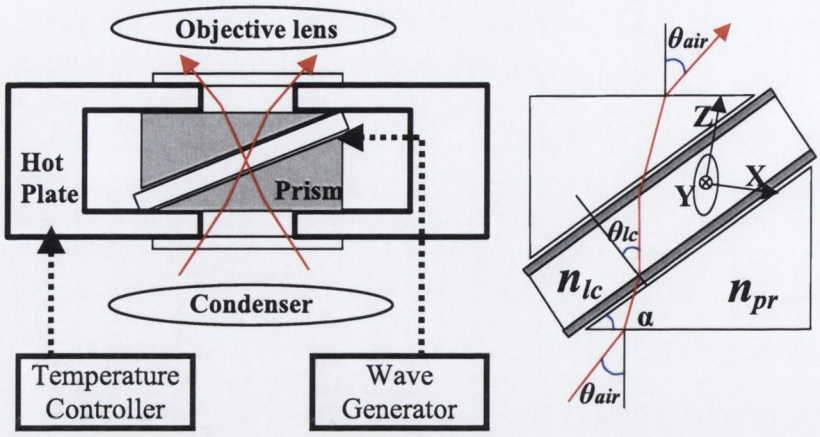

Figure 2.2: Modified conoscopic method using a tilted cell (left) and a cell sandwiched with prisms (right). X, Y and Z axes are the eigen axes of the refractive index ellipsoid in the cell.

Snell's law assures that a ray traveling in air at an angle of θ_{air} with respect to the microscope optical axis makes an angle θ_{lc} with the smectic layer normal given by

$$\theta_{\text{lc}} = \sin^{-1}\left[\sin\left\{\sin^{-1}\left(\frac{\sin\theta_{\text{air}}}{n_{\text{pr}}}\right) + \alpha\right\}\frac{n_{\text{pr}}}{n_{\text{lc}}}\right]. \tag{2.4}$$

Here n_{pr} and α are the index of refraction of the prism and its apex angle, and n_{lc} is the index of refraction of the liquid crystalline sample. This equation obtained for the prism-sandwiched cell is also applicable to a slanted cell and a conventional cell placed horizontally on the microscope stage, where α is 30° and zero, respectively, and $n_{\text{pr}} = 1$ for both cases.

Thus, the tilted conoscopic method enlarges the observable range of the conoscopy, and since most of the ferroelectric liquid crystals have larger tilt angle than 20°, the tilted conoscopic method is highly useful.

2.4 Verification of the approximations used in its analysis

2.4.1 Single-biaxial-plate approximation

Since Gorecka *et al.* measured the biaxiality and the apparent tilt angle as a function of the applied field using conoscopy for a chiral smectic liquid crystal in its various phases such as SmC^*, SmC^*_A, SmC^*_γ phases [31], this method adopting more or less the same procedure has frequently been used by a number of authors [30–33, 35–37]. In those works, the cells were considered as single-biaxial-plates. The cells of achiral SmC and SmA phases in reality are single biaxial plates and the tilt angle and biaxiality are reasonably defined. However, the cell containing the chiral smectic in its various phases is not a single biaxial plate, and strictly speaking, the biaxiality cannot be defined in the cell having a helical structure. We pose the fundamental question: what is the meaning of the biaxiality obtained using conoscopy in chiral smectic phases? In chiral smectic phases, each layer has its own refractive index ellipsoid, and the directions of the principal axes vary gradually from the layer to layer. Hence, the biaxiality and the apparent tilt angle estimated from conoscopic experiments can only represent the average properties of the various layers.

In the approximation of the isotropic local field, the principal refractive indices (n_i) of the uniform media can be written as [7, 39]

$$\frac{n_i^2 - 1}{< n^2 > +2} = \frac{4\pi N < \alpha_{ii} >}{3} \tag{2.5}$$

where the average square of refractive index, $< n^2 >= (n_1^2 + n_2^2 + n_3^2)/3$. The polarizability component $< \alpha_{ii} >$ is the average value along the direction of the principal refractive index n_i, and N is the number of molecules per unit volume. The principal refractive indices of the average refractive index ellipsoid consisting

of m layers can be expressed from eq. 2.5 as

$$\begin{aligned} n_i^2 &= \frac{1}{m} \sum_{j=1,2,\ldots,m} \left[\frac{4\pi}{3} N < \alpha_{ii} >_j (< n^2 > +2) + 1 \right] \\ &= \frac{4\pi N (< n^2 > +2)}{3} \left[\frac{1}{m} \sum_{j=1,2,\ldots,m} (< \alpha_{ii} >_j) \right] + 1 \\ &= \frac{4\pi N < \alpha_{ii} > (< n^2 > +2)}{3} + 1 \end{aligned} \tag{2.6}$$

Thus, eq. 2.6 is identical to eq. 2.5. This implies that the average refractive index can be defined by averaging the polarizability component over the layers. By assuming

$$n_{ij}^2 \approx \frac{4\pi}{3} N < \alpha_{ii} >_j (< n^2 > +2) + 1, \tag{2.7}$$

where n_{ij} is the refractive index value along the i-th direction of the j-th layer, we can define the average refractive index along the arbitrary direction ($\hat{\varphi}$) of the layered structure as

$$n_{\hat{\varphi}}^2 \approx < n_{\hat{\varphi}j}^2 >_{j=1,2,\ldots,m} . \tag{2.8}$$

Equation 2.8 defines average value of the refractive index over all the layers, and this may not always be valid. However, if the single-biaxial-plate approximation is only applicable, eq. 2.8 is valid, that is, the single-biaxial-plate approximation is identical to the average-refractive index approximation given by eq. 2.8. If the thickness of a single period in a periodic structure is much less than the wavelength of light, incident light will experience the average refractive index, and eq. 2.8 is therefore valid. However, if the thickness of a single period is larger than the wavelength, eq. 2.8 may not be valid. For example, when the helical pitch of a smectic C liquid crystal is larger than the wavelength of the incident light, the average-refractive index approximation is not supposed to be valid and the liquid crystal cells cannot be considered as a single-biaxial-plate. In this case, the cell should be considered as a stack of a number of biaxial plates and each layer should be accounted for separately. However, the approximation in the literature

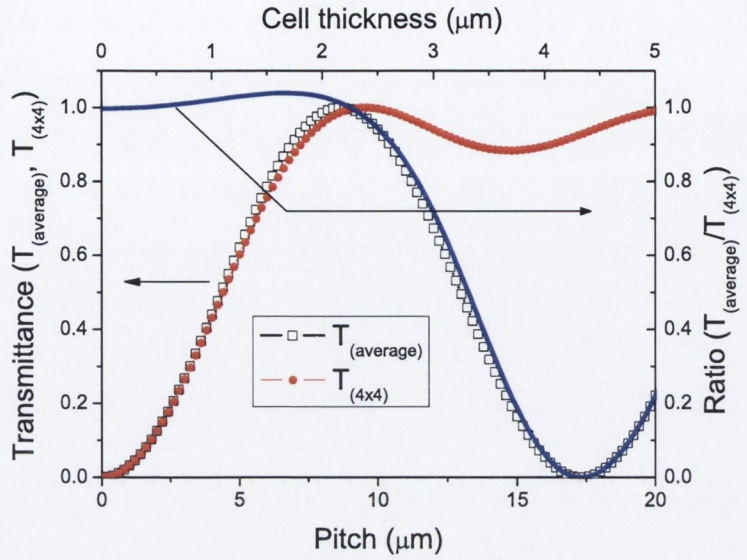

Figure 2.3: Simulated transmittances as a function of pitch or the cell thickness in twisted nematic mode (TN) by using 4×4 matrix method ($T_{(4\times4)}$) and average-refractive index method ($T_{(average)}$). Simulation condition: 90° twist nematic, $n_o = 1.5$, $n_e = 1.7$.

has been used even for the phase having a long helical structure without confirming its validity. For example, the structures of SmC_A^* and SmC_γ^* phases of 4-(1-methylheptyloxycarbonyl)phenyl 4'-octyloxybiphenyl-4-carboxylate (MHPOBC), a prototype antiferroelectric liquid crystalline compound, were determined by observing the conoscopic images [12, 31, 32], and the pitch of MHPOBC is reported to be approximately 670 nm in the SmC_A^* phase and much larger in the SmC_γ^* phase. In the SmC_γ^* phase, the selective refraction band does not appear for wavelengths shorter than 2.5 μm, which means that the pitch is longer than $(2.5/n)\mu$m (where n is the refractive index of liquid crystal). However, the biaxiality and the apparent tilt angle of MHPOBC in the SmC_γ^* phase were measured and the SmC_γ^* phase was characterized based on a single-biaxial-plate approximation.

Thus, in general it is required to test the validity of the average-refractive index method for helical structures in order to arrive at correct conclusions. Firstly, we shall test the validity of the approximation in a twisted nematic (TN) mode. TN mode has been used in a majority of the commercial liquid crystal displays, and the optical properties of TN mode have been investigated in greater detail [20]. Hence, TN mode is suitable for determining the validity of the approximation.

The transmittances of TN mode are calculated as a function of the cell thickness as shown in Fig. 2.3 using the two methods: 4×4 Matrix method [17, 18] and the average-refractive index method defined in eq. 2.8. The 4×4 matrix method gives an accurate value of the transmittance, whereas the average-refractive index method provides an approximated value. By comparing the results from these two methods, we can find the range of validity of the average-refractive index method. Since TN mode has 90° twisted directors, the pitch p is proportional to the cell thickness d ($p = 4d$). The results from the two methods show good agreement with each other for the short range of the helical pitches as shown in Fig. 2.3, while the difference between these significantly increases sharply for $p > 8\mu m$. Thus, the average-refractive index approximation is not valid for structures with longer helical pitches, but we can see that the method is applicable reasonably for the samples having short helical pitches up to several times the wavelength of light.

Now, we shall confirm the validity of this method for the smectic phases with a longer helical pitch. For this, we obtained an accurate conoscopic image by using the 4×4 matrix simulation, and compare it with the result simulated by using the single-biaxial-plate approximation. Uniform helical structure produces a symmetric shape of the conoscopic image, where both the apparent tilt angle and the biaxiality are zero. So, for obtaining non-zero values of these two parameters, we need to use a deformed helical structure. Since a helical structure is a periodic structure, the azimuthal angle ϕ of the average direction of molecules, defined in Fig. 2.1, in a deformed helical structure under the application of field can be written using Fourier expansion as [40]

$$\phi(z) \approx qz + \phi_0 \sin qz + \phi_1 \sin(2qz) + ..., \tag{2.9}$$

where the wave vector q and the pitch p are related to each other as $q = 2/p$. Considering that the purpose of this simulation is to verify the average-refractive index approximation by using an assumed helical structure of the smectic liquid crystalline compound, we do not need to use a number of terms in eq. 2.9, and first we shall use up to the second term and the director distribution when $\phi_0 = -1$.

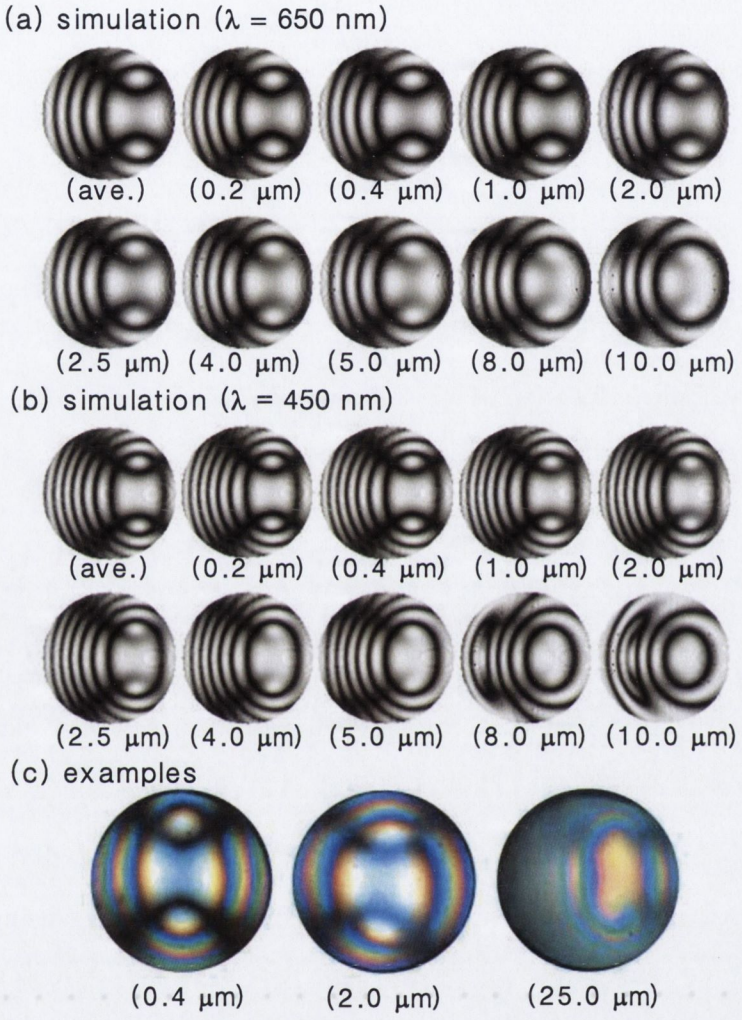

Figure 2.4: Simulated conoscopic images (a, b) and experimentally obtained examples (c). The first images indexed by (ave.) in (a) and (b) were obtained by the average refractive method, and all the others were from the 4 × 4 matrix method. The numbers in parentheses are the length of the pitch for the simulation condition of the 4 × 4 matrix method. The first two images in (c) were taken by using pure (R)MHPOOCBC ($p \sim 0.4\mu$m), and a racemic mixture ($p \sim 2\mu$m) of (R)MHPOOCBC 65% and (S)MHPOOCBC 35%, respectively, and the last one was taken by using Felix018 ($p \sim 25\mu$m).

The simulation conditions are: 40 μm cell thickness, 4 nm layer thickness, $\theta = 25°$ and $n_e = 1.7$, $n_o = 1.5$ and $\lambda = 450$ nm and 650 nm. The simulation result is shown in Figs. 2.4 (a) and (b), where the first two images in (a) and (b) are obtained using the average-refractive index approximation, and the others are obtained using the 4×4 matrix simulation method. The number in inset in Figs. 2.4 for each conoscopic image corresponds to a value of the helical pitch. As shown in Figs. 2.4 (a) and (b), the simulation result using the average-refractive index approximation finds good accord with those obtained using the 4×4 matrix method for short helical pitches. However, as the pitch increases, the optic axes become obscured and the shapes of the melatopes get deformed. The deformation for the incident light of wavelength $\lambda = 450$ nm is much greater than for $\lambda = 640$ nm. The transmittances along the line passing the two optic axes are plotted in Fig. 2.5. The optic axes are marked by the blue arrows, the transmittances at the optic axes points should be zero in the ideal case, but the transmittances at the points increase with increase in the helical pitch. The positions of the optic axes and dark lines also move with the pitch. These give rise to an error in the value of the biaxiality using this method for the analysis of conoscopy. We can see that the shift of the optic axes and the dark lines is much greater for $\lambda = 450$ nm than for $\lambda = 650$ nm.

It is very interesting that the simulated conoscopic images using the 4×4 matrix method do not change significantly for $p < 5$ μm at $\lambda = 650$ nm and for $p < 3$ μm at $\lambda = 540$ nm from those simulated using the averaged refractive index method. This means that the average refractive index approximation is valid up to a pitch of roughly 7 times λ. It has been reported [41] that for a homogeneous approximation, where a non-homogeneous medium containing microstructure is approximated as a homogeneous medium, is valid for a periodic nanoarray structure placed perpendicular to the direction of light if the periodicity of the structure is few times less than the wavelength of light. However, as shown above, in the helical structure of liquid crystal cells, where the periodic structure is placed parallel to the direction of light, the homogenization approach using the average-refractive

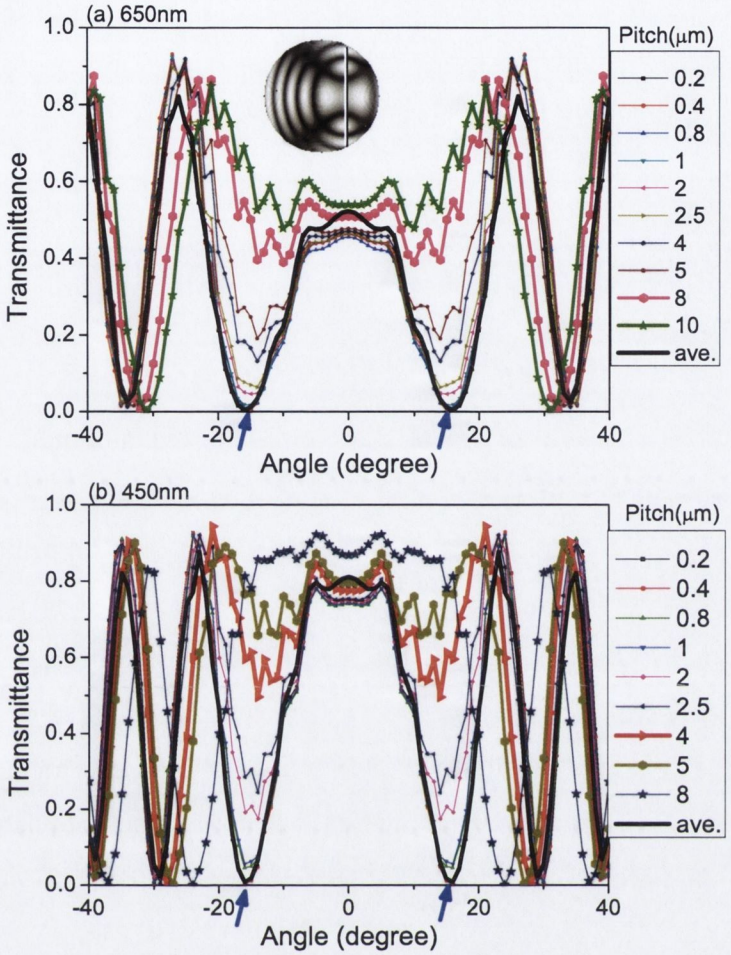

Figure 2.5: Simulated transmittance as function of the angle of light with respect to n_e along the line passing the two optic axes in the simulated conoscopic images in Fig. 2.4 (see the inset image in (a)). The pitches in the insets are the simulation condition for the 4×4 matrix method, and (ave.) indicates the average-refractive index method. Points marked with blue arrows are optic axes.

index approximation is valid up to much longer helical pitch than the wavelength of light.

To date, it has been accepted [36] that the use of a shorter wavelength is a more accurate conoscopic method in LCs, because it has the advantage of showing up more rings in the image, and this may thus reduce the error arising from mis-assignment of the optic axes. However, the use of a longer wavelength leads to lower errors induced by the average refractive index approximation and also enlarges the observable range of the pitch of the materials that can be investigated

using this technique. Figure 2.4 (c) shows experimentally observed conoscopic images for different helical pitch values, where a similar tendency predicted from the simulation results is observed.

2.4.2 Assumption of fixing one of the principal refractive indices

Usually, the main advantage of the conoscopic technique is a determination of the biaxiality ($n_{o2} - n_{o1}$) but not of determining the absolute values of the refractive indices. By taking an approximate value for one of the principal refractive indices, the other two values can reasonably be calculated. As has already been pointed out by Gorecka *et al.* [31], when n_{o1} is incorrectly chosen as 1.45, a value less than the real value of say 1.5, an error in the biaxiality caused by this incorrectly chosen value was found to be less than 1%, which can be neglected. However, an error in the apparent tilt angle found from conoscopy is rather large compared to that for the biaxiality. The light path in the cell can be calculated using Snell's law.

$$\vartheta = \sin^{-1}[\sin(\vartheta')/n_0], \tag{2.10}$$

where ϑ and ϑ' are the angles of the incident light inside and outside the cell respectively. The tilt angle also is calculated using eq. 2.10. According to eq. 2.10, an error in the tilt angle caused by the same incorrectly chosen n_{o1} is found to be 3.5–4%, which is rather large. The error caused by this effect can also be a problem when conoscopy is carried out on a sample for various wavelengths of the light. Fig. 2.6 shows a typical conoscopic image of a ferroelectric liquid crystal, 3.b.5, and a halogen lamp as the source of light. The transmittance curves along the line across the two optic axes for blue (450 nm) and red (650 nm) wavelengths clearly show different positions of the optic axes.

One of the optic axes close to the center of the image is in the same position in the two curves, while the second away from the center appears in different

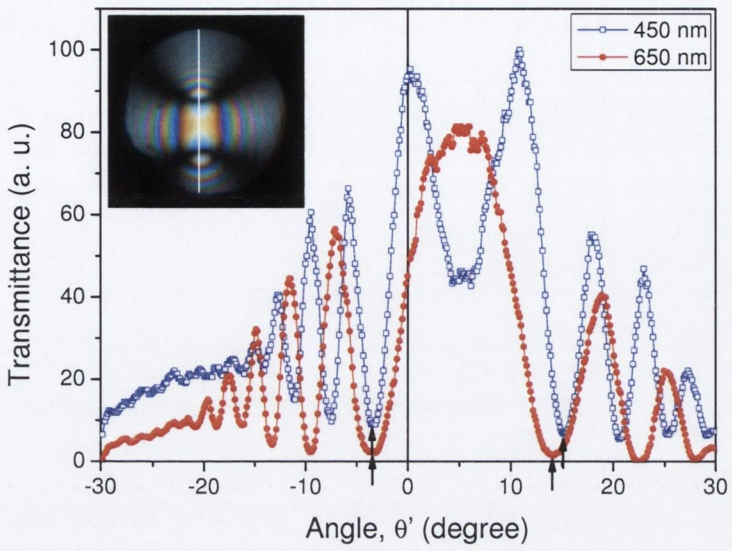

Figure 2.6: The transmittance along the line passing between the two optic axes at red and blue wavelengths obtained by using 3.b.5. (experimental conditions: $E = 200\text{V/mm}$, 40°C)

positions. According to Fig. 2.6, the apparent tilt angle found appears to be dispersive with λ. This may have been thought to have been induced by the local field effect [34]. We measured the apparent tilt angle as a function of the applied field using a different method on a planar cell (data not shown here). However we could not find any change in the apparent tilt angle as a function of λ. The apparent tilt angle dispersion caused by the local field effect may be too small to detect using the usual optical method. Thus, the shift of the optic axis observed in Fig. 2.6 does not arise from the dispersion of the apparent tilt angle. The shift actually arises from eq. 2.10, where n_{o1} varies with λ and hence, ϑ is found to be dispersive with λ which is not the case in reality. We therefore find the effect of choosing an incorrect value of n_{o1} gives rise to incorrect results for the apparent tilt angle, especially when a number of wavelengths of the incident light are used. The dispersion of the position of the optic axis in the conoscopic images can be used to determine the dispersion of the refractive index of liquid crystals.

2.5 Estimation of the molecular distribution using the conoscopic data

2.5.1 Simulation method to estimate the molecular distribution

As explained in the introductory part, we can estimate the director distribution in a cell from the results of a conoscopic experiment. In the earlier papers [12, 30–32], the distribution was estimated qualitatively and intuitively. For example, in the antiferroelectric phase, the tilting direction (ϕ in Fig. 2.1) of molecules in smectic layers are supposed to align parallel to the applied field and the angle difference ($\phi_i - \phi_{i+1}$) between the adjacent layers is almost π, that is, the tilting directions are in the opposite directions to each other. This results in a large positive biaxiality and a small apparent tilt angle as already explained [12]. Later, Suwa *et al.* [35, 36] estimated the director distribution in the deformed helical structure of a ferroelectric liquid crystal by using 4×4 matrix simulation, where more precise quantitative estimation was tried for the first time. Though their method using the 4×4 matrix simulation is quite interesting, it showed apparent limitations.

Basically, the procedure of determining the director distribution from the conoscopic data is the same as the procedure of finding the optimized fitting parameters from the experimental data. In this procedure, the experimental data are compared with the simulation results by varying the fitting parameters in order to find the optimized condition where the differences between the simulation and the experiment are minimized. For this fitting, a proper model for the director distribution in the cell need to be found. This model may vary depending on the application, liquid crystalline phase and the cell structure. Fourier expansion shown in eq. 2.9 can be a simple but a good model, or a theoretical molecular distribution function can be obtained by minimizing the total free energy containing the elastic and the electric energy [37]. Suwa *et al.* [36] used a much simplified

model for the director distribution. Once the model is established, we should decide what physical properties are compared between the model and the experiment to optimize the fitting parameters. A direct comparison of the conoscopic images obtained by experiment and simulation creates various difficulties, because the two dimensional transmittance patterns in the conoscopic images are significantly complicated and these contain narrow rings, which turns the quantitative comparison into a difficult task. Therefore, the biaxiality and the apparent tilt angle are used for drawing a comparison [36, 37], since the biaxiality and the apparent tilt angle actually contain most of the information about the conoscopic image. Then, a considerable iteration is required for finding the optimum condition.

For this iteration procedure, the approach using the 4×4 matrix method has limitations. One of such limitations is that the 4×4 matrix calculation requires a long time to iterate many times [17, 18, 42], though the calculation time has significantly been reduced by simplifying the matrix method [43]. Note that the simulation of the conoscopic image requires to produce two dimensional conoscopic pattern and each point of the two dimensional image requires the 4×4 matrix calculation to be carried out independent of another point. Another limitation lies in the difficulty of extracting the biaxiality information from the simulated conoscopic images. The 4×4 matrix calculation gives only the transmittance information, that is, the conoscopic image. However, the physical property to compare with the experimental data is the biaxiality and the apparent tilt angle. Hence, we need to extract the biaxiality from the simulated conoscopic image. Due to the complexity of the conoscopic image, however it is not easy to find the positions of the optic axes automatically. As a result, it is difficult to iterate the simulation automatically.

Meanwhile, the method using the average-refractive index defined by eq. 2.8 can be used for solving this problem. As shown in section 2.B, the average-refractive index approximation is valid for a relatively wide range of helical pitch values and it gives values of the apparent tilt angle and the biaxiality directly. This means that the average-refractive index method is suitable for carrying out iteration in the simulation, and is much faster than the 4×4 matrix method. Therefore,

we can easily find the optimum director distribution using the experimental values of the apparent tilt angle and the biaxiality.

2.5.2 Simulation of the deformed helical structure

As an example of the estimation of the molecular distribution along the cell thickness direction, i.e., along the normal to the smectic layers, we shall simulate a deformed helical structure of a common ferroelectric liquid crystalline material. We used a racemic mixture of (R)MHPOOCBC 65% and (S)MHPOOCBC 35%, where (R) and (S) indicate the handedness of chiral group (R: *rectus* or right, S:*sinister* or left). The racemic mixture showed a typical continuous unwinding process over a wide rage of applied fields and is suitable for this simulation, while pure (R)MHPOOCBC showed an irregular non-homogeneous helical fracture [34]. It is difficult to find a molecular distribution function for the irregular structure. The conoscopic image in Fig. 2.7 was obtained under the application of 27 V/mm at 70°C. From the conoscopic image, the following values are found: biaxiality = -0.00101; the apparent tilt angle = 14.7 °. By applying a large field of (say 250 V/mm), the conoscopic image in the helical unwound state was obtained. Since the tilting directions are the same for all of the smectic layers in the unwound state, the optical properties of the unwound cell is identical to the properties of a single smectic layer. In this way, we find that the principal refractive indices of each layer as 1.65, 1.501 and 1.05 respectively, and the tilt angle, θ is found to be 27°. Based on these data, we carry out the simulation to find the molecular distribution of a deformed helical structure at an electric field of 27 V/mm. We use the Fourier expansion as shown in eq. 2.9 for the molecular distribution function along the cell thickness direction, z. When we used up to the second term of eq. 2.9, we could not satisfy perfectly both the biaxiality and the apparent tilt angle values obtained experimentally using any value of ϕ_0. By using up to the third term of eq. 2.9, we can find the optimized values of ϕ_0 and ϕ_1 for having the same tilt angle and the biaxiality as the experimental results; ϕ_0 = -0.8775 and ϕ_1= 0.151. The director

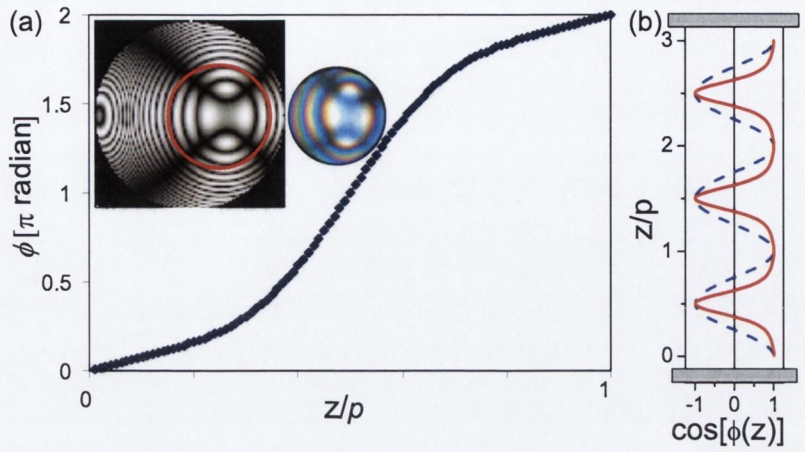

Figure 2.7: (a) The director distribution estimated from the conoscopic image using a racemic mixture of MHPOOCBC (right inset image), and the reproduced conoscopic image from the calculated director distribution (left inset image). The experimental conoscopic image was obtained by using the tilted method, so the center point is shifted. The circle in the simulated conoscopic image denotes the observable range in the actual experiment. (b) helix distortion by the applied field in the cell. Initial uniform helix (blue dash line) changes to the distorted helical structure (red solid line) by the field.

distribution for this is shown in Fig. 2.7. Thus, the director distribution can be estimated simply by using the average-refractive index approximation.

2.6 Conclusion

We have investigated the procedure of analyzing the conoscopic image on chiral smectic liquid crystals, which basically assumes two approximations in the calculation procedure. We find that the single-biaxial-plate approximation for helical structures is valid for the pitch up to several times the wavelength of the incident light. Using a long wavelength of light can enlarge the observable range of the helical pitch of the materials in the cell to be investigated. The arbitrarily chosen value of one of the principal refractive indices gives rise to the wavelength dispersion in the apparent tilt angle. This can make the refractive index dispersion appear as the dispersion of the apparent tilt angle with wavelength. We suggest a new simulation method for determining the molecular distribution function in

liquid crystal cells of using the average-refractive index method, given as eq. 2.8. This is a better and a faster method for carrying out a automatic simulation that uses the iterative process.

In this way, the conoscopic method, which has been used mainly for an auxiliary technique, can be used for finding quantitative molecular distributions even for materials having large tilt angles and large biaxiality. Considering that the conoscopic method is rather simple and easy, the suggested methods can extensively expand the usage of the conoscopy.

Part. II

Molecular Orderings and Motions

Chapter 3

Molecular short axis orientations and biaxiality in SmC^*

"In this chapter, *the distribution of the molecular short axis in the SmC* phase is investigated by measuring the biaxiality. Two types of liquid crystal groups showing different orientational distributions of molecular short axis are found, and the temperature induced sign reversal of the biaxiality is observed."*

3.1 Introduction

The molecular ordering in liquid crystals is originated or affected by various intermolecular interactions such as the dipole-dipole interactions, the steric interaction by direct contacts between molecules, and thermal fluctuation. Hence, the molecular distributions, which have been studied extensively over a long time, actually reflect whether the various intermolecular interactions are strong or weak, and whether they are cooperative or competitive with each other, and so on. As already explained in Chapter 1, the basic molecular ordering for each phase has

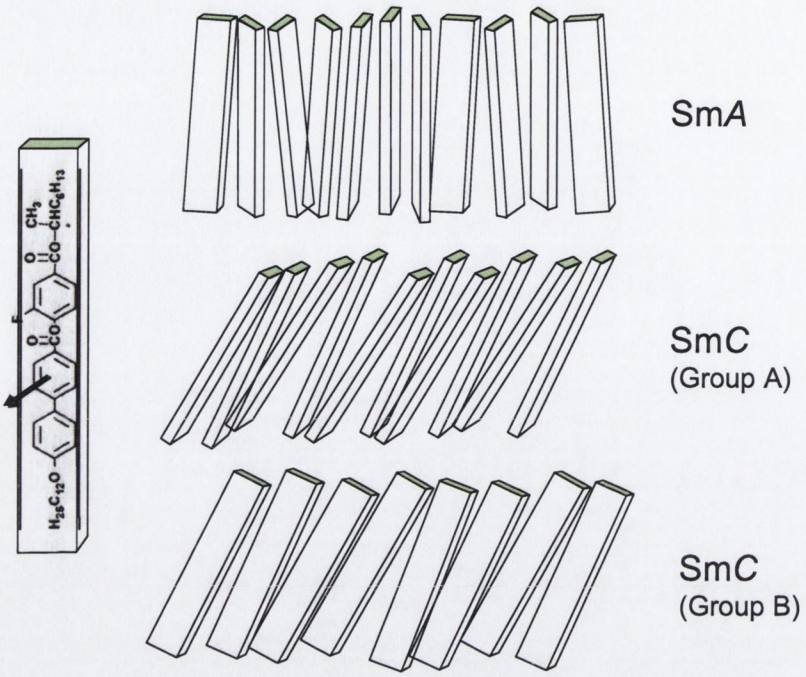

Figure 3.1: Schematics for the orderings of molecular short axis. The plot in the left-hand side shows the schematic of a biaxial molecule, where the minimum axis of the polarizability corresponds to the normal to the flat core part of the molecule. SmA phase is uniaxial due to the random rotational distribution (top), and SmC phase is biaxial and the minimum direction of the refractive index may depend on the average direction of molecular short axis (middle and bottom).

been well studied and well published in the literature. However, the ordering of molecular short axis is still not clear. In this chapter, the ordering of the molecular short axis in the SmC^* phase is investigated by measuring biaxiality using conoscopy.

The biaxiality of calamitic mesogenic molecules is mainly determined by their flat hard cores. In the smectic-A phase (Sm-A), the molecular long axes are ordered along the director which is parallel to the smectic layer normal, while the molecular short axes specifying the core orientation are randomly distributed around the normal as shown schematically in Fig. 3.1; hence the Sm-A phase itself is uniaxial in spite of the biaxiality of the constituent molecules. In the smectic-C phase (Sm-C), on the other hand, the molecular long axes are ordered along the director which is tilted from the layer normal by the director tilt angle Θ. The

right-handed Sm-C phase coordinate system is usually specified by fixing the Z axis parallel to the director, the Y axis is perpendicular to the director tilt plane, and the X axis is normal to both Y and Z. The molecular short axes must also be ordered to a certain extent due to the phase biaxiality. This quadrupolar ordering of molecular hard cores is not determined by chirality and hence is considered to be higher than the dipolar ordering of transverse molecular dipoles in the chiral ferroelectric smectic-C phase (Sm-C^*). Based on the assumption that the quadrupolar ordering of the molecular short axes in Sm-C is sufficiently high, Osipov and Pikin [44] developed the general phenomenological and molecular-statistical theory of Sm-C^*. They considered the influence of the quadrupolar ordering on the ferroelectric properties of Sm-C^*, and analyzed the temperature variation of spontaneous polarization, dielectric constant, and the helical pitch. Osipov and Pikin reasonably concluded: "The general situation can be clarified only after new systematic experimental investigations of the nonpolar ordering of the molecular short axes both in chiral and nonchiral smectic-C systems are carried out."

So far as the authors are aware of, no direct measurement of refractive indices has proven the quadrupolar ordering of the molecular short axes in Sm-C and Sm-C^*. The SmC phase has been confirmed to be biaxial as pointed out by Saupe [45] based on symmetry considerations. Let us designate the eigen axes of the dielectric permittivities as X', Y', and Z', with the Z' axis along the largest permittivity and the $Y' \equiv Y$ axis perpendicular to the director tilt plane. Note that, in principle, the Z' and X' axes are rotated by $\delta\Theta$ about the $Y' \equiv Y$ axis with respect to the Z and X axes. Taylor *et al.* [46, 47] observed $n_{Y'} > n_{X'}$ (hereafter designated as positive biaxiality) in Sm-C of all the four compounds investigated by conoscopy; three of them show a first-order phase transition from isotropic to Sm-C with an almost constant tilt angle as large as 45° and the last one apparently exhibits a second-order transition from Sm-A to Sm-C with a continuous change in the tilt angle from 0°. They concluded that at least a part of the positive biaxial character may be due to an anisotropic fluctuation of the molecular long axis, assuming molecular free rotation about this axis. Later Galerne [30] measured all

the three principal refractive indices in Sm-C as well as Sm-A of another liquid crystal compound, which shows a second-order phase transition from Sm-A to Sm-C, and again confirmed that $n_{Y'} > n_{X'}$. This positive biaxiality was also interpreted on the basis of the molecular anisotropic fluctuations.

More recently, so many Sm-C^* compounds and mixtures have been extensively developed for FLCD (Ferroelectric Liquid Crystal Display) applications [48]. All of their observed melatopes in the completely unwound state emerge in the tilt plane perpendicularly to the applied field and indicate that $n_{Y'} > n_{X'}$. In this way, the previously observed biaxiality was always positive; hence no one was sure whether the short-axis-ordering contribution was really observed by clearly distinguishing it from the long-axis-fluctuations. Anyway, it seems to have simply been anticipated that the short axis ordering always occurs in such a way that the biaxiality of Sm-C and completely unwound Sm-C^* is positive ($n_{Y'} > n_{X'}$), i.e. that the melatopes in conoscopy appear parallel to the tilt plane. This anticipation is due to several facts: (i) The spontaneous polarization inevitably emerges along the C_2 axis (the Y axis) perpendicularly to the tilt plane [8]; (ii) The molecular transverse dipoles must also align quadrupolarly [44]; and (iii) The most polarizable molecular short axis of the molecular core is usually considered to be rather parallel than perpendicular to the averaged direction of transverse dipoles responsible for the spontaneous polarization.

This naive belief of positive biaxiality in Sm-C^* made it easier to identify the *ferrielectric* Sm-$C^*_A(1/3)$ subphase, which shows negative biaxiality due to the special molecular ordering, at the early stages of the investigations of the subphases (the Sm-C^* variants) [12, 31, 49, 50]. At the same time, it appeared to promote an incorrect phase identification of compounds and mixtures developed for the smectic liquid crystal display with gray scale (the so-called V-shaped switching materials) [51–53]. These materials were assigned to be "*ferrielectric*" by simply observing the electric field dependence of their conoscopic figures, i.e. by confirming negative biaxiality in the completely unwound state. The "*ferrielectric*" temperature range is as wide as 100°C or more in some of these compounds and mixtures. This fact indicates that the assignment is unacceptable, because the only *ferrielectric*

phase, whose existence is well established, is the Sm-$C^*_A(1/3)$ subphase produced by the frustration between ferro- and antiferro-electricity and it can emerge in a temperature range as narrow as 10°C or less. Moreover, there is no reason that Sm-C^* could not show the melatopes parallel to an applied electric field in its completely unwound state [36]. In other words, the structural symmetry of Sm-C^* allows either of the two cases: where the melatopes appear parallel or perpendicular to the field, whereas the parallel melatopes inevitably appear in the *ferrielectric* Sm-$C^*_A(1/3)$ subphase.

This chapter has a triple experimental purpose as described in Section 3.3. The first is to show that no discrepancy exists in assigning the above V-shaped switching materials as ferroelectric instead of as "*ferrielectric*", by observing the temperature variations of Bragg reflection bands due to the helical structure [22, 23, 54]. The second is to study the temperature dependence of biaxiality rather systematically using various compounds and mixtures including the V-shaped switching materials. We will notice that all of them show the positive biaxiality at high temperatures just after the phase transition to Sm-C^*, which is probably due to the fluctuations of molecular long axis, and that some materials do exhibit a temperature-induced sign reversal of biaxiality. Thus, surprisingly two kinds of the temperature dependence of the biaxiality are observed. Finally, the third purpose is to give a new result which shows that the observed biaxiality scarcely depends on the enantiomeric excess (optical purity) of the sample compounds. On the basis of these three experimentally observed facts, as discussed in Section 3.4, we model for the molecular distribution actual considering molecules as biaxial ones. We can conclude that the negative biaxiality unambiguously results from the negative C order parameter.

3.2 Experiment

Samples used are listed in Fig. 3.2. The V-shaped switching was first observed in Inui mixture (sometimes also called Tokyo mixture) [55, 56], which was

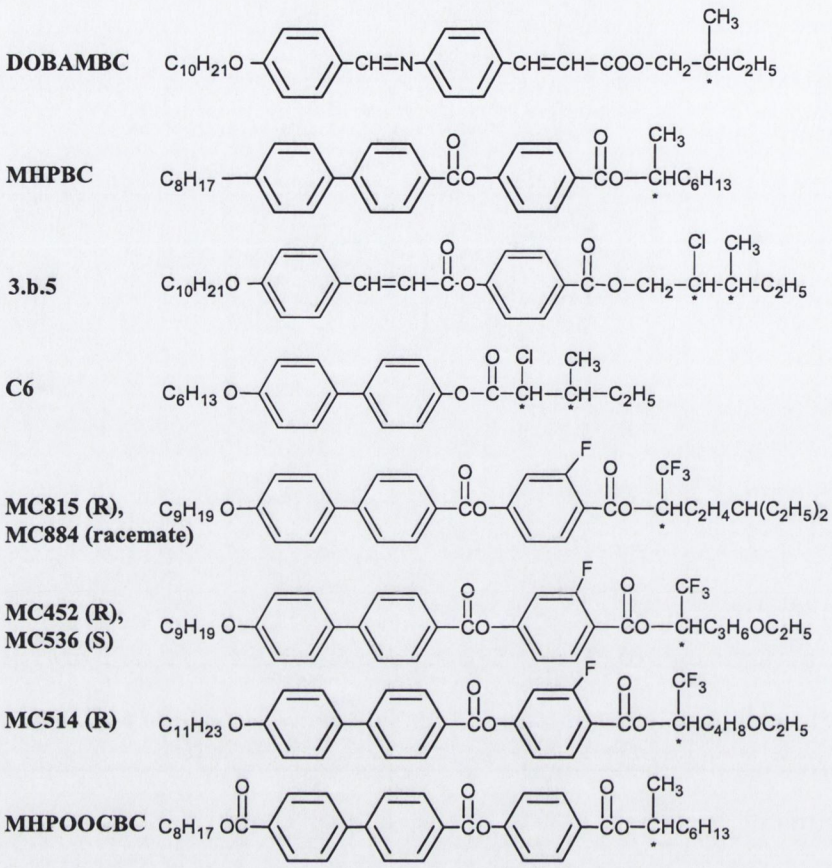

Figure 3.2: Chemical structures of samples used. We also measured the temperature dependence of biaxiality in three mixtures, i.e. Tokyo mixture, Y102, and Felix18. MC815 (*R*-moiety), MC-884 (racemate of MC815), MC452 (*R*-moiety), MC536 (*S*-moiety of MC452), MC514 (*R*-moiety).

initially considered to be antiferroelectric but later was regarded to be ferroelectric though some questions have been raised regarding the assignment. Mitsubishi Gas Chemical Company, Inc. (MGC) developed MC815 and MC452 compounds and Y102 mixture for the V-shaped switching materials and considered them to be "*ferrielectric*" [51–53]. Note, however, that these are ferroelectric as explained in detail in the following.

Homeotropically aligned, 50 $\sim$ 150 μm thick cells, of the samples listed in Fig. 3.2, were prepared by using two glass plates coated with a Dow Corning silane coupling agent, (72% 3-(trimethoxysilyl)propyldimethyloctadecyl-ammonium-chloride and 28% MeOH) for spectroscopy and conoscopy measurements. Free-standing

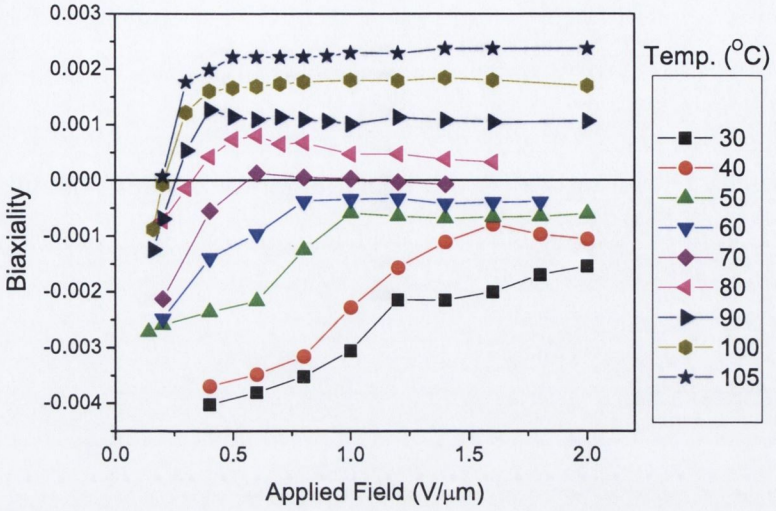

Figure 3.3: (Color online) Plots of the apparent biaxiality vs. applied field measured by conoscopy for MC452 at various temperatures.

films, ranging from 30 to 50 μm thick, were drawn across a 2 mmϕ hole drilled on a 300 μm thick steel plate for spectroscopically observing Bragg reflection bands due to the helical structure. These films were used conveniently to see the existence of reflection bands but the observed band shape may usually be disturbed by inhomogenuity in film thickness. Consequently, Bragg reflection bands were observed with a spectrometer (Perkin Elmer, Lambda 900) by using carefully prepared homeotropically aligned cells of 50 $\sim$ 100 μm thickness. Biaxiality was studied by conoscopy [33] using the tilted conoscopic method. The details of this method is explained in Chapter 2. The sample is carefully insulated thermally with glass windows. To unwind the helical structure completely, we applied an electric field using PET spacers covered with gold foils and these are separated 300 μm apart. A wave generator and an amplifier allowed us to apply a maximum voltage of 600V DC or AC to the sample cell, which equates to the maximum electric field of 2000 V/mm. The conoscopic image quality deteriorated seriously when some LC flow occurred. To minimise the flow effect, we were very careful in sample handling and utilized a 1 Hz square wave field instead of a DC signal. The obtained conoscopic images were analysed to get the biaxiality ($n_{Y'}$ - $n_{X'}$). We plotted apparent biaxiality vs applied field for MC452 as illustrated in Fig. 3.3 and confirmed the complete unwinding of the helical structure. As seen in Fig 3.3, the

biaxiality at low applied fields is quite low and increases rather rapidly with electric field and then saturates to a constant value at high fields. This is commonly observed during the unwinding process of SmC^* phase [33]. The observation of the positive biaxiality as the saturated value for the unwound SmC* is quite normal, whereas the negative biaxialty is an unusual but interesting observation.

3.3 Results

3.3.1 The correct assignment of ferroelectric Sm-C^* for the V-shaped switching materials

Y102 is a mixture developed by MGC for the V-shaped switching, which was used by Casio to prototype a 5.5 inch, full-color, video rate LCD [51]. Although the ingredients of Y102 are propriety to the company, an MGC patent Gazette [53] appears to indicate that the two main components are MC815 and an antiferroelectric compound (MC881), and that the mixing ratio is close to the critical concentration where the "*ferrielectric*" and the antiferroelectric phases have equal free energies. Note that this critical concentration scarcely depends on the temperature as illustrated in Fig. 1 of Ref. [53]. Since MGC considered Y102 to be "*ferrielectric*" and moreover since this assignment must be inappropriate as pointed out in Section 3.1, we first studied the Bragg reflection of Y102 in detail as a function of temperature. Only one peak is observed in the wavelength region of 350 nm–2.5 μm over a wide temperature range from below 0° to 68°C and the band shape is ideally bell-shaped as illustrated in Fig. 3.4 [1] (a). The band peak changes smoothly with temperature as shown in Fig. 3.4 (b). No jump in the wavelength of the Bragg reflection occurs which suggests no phase transition is observed, except for the very steep decrease of helical pitch at high temperatures just below Sm-A. The steep decrease in the wavelength of the selective reflection (a measure of the helical pitch) suggests the existence of Sm-C^*_α in a narrow temperature region just

[1] All data shown in Fig. 3.4 were obtained by prof. A.D.L. Chandani.

below Sm-A [57]. In fact, the birefringence contour lines drawn in the E–T space using a PEM (Photo-Elastic Modulator) clearly proves its existence of Sm-C^*_α as shown in Fig. 3.4 (c). Aside from this narrow temperature range, it is natural to consider that Y102 shows a single phase in a wide temperature range and that this phase should be assigned as ferroelectric Sm-C^*.

Now let us examine whether the Bragg reflection due to the helical structure can reasonably be understood by identifying this phase as ferroelectric Sm-C^*. The dispersion relation for Sm-C^*, as studied in detail by Ouchi *et al.* [22], naturally depends on the director's tilt angle and the light propagation direction specified by an oblique angle from the helical axis, i.e. the smectic layer normal. The first order reflection, which is called the full pitch band, shows total reflection. It emerges at about the wavelength equal to twice of the optical helical pitch (mechanical pitch times average refraction index, $\bar{n}p$) when the light is incident almost normally to the smectic layer and propagates nearly parallel to the helical axis. Note that the reflection intensity becomes zero and the full pitch band is not observed for the exact normal incidence. The second order reflection called the characteristic band corresponds to the first order reflection in the chiral nematic (cholesteric) phase, and it has much more complicated dependence on the tilt angle and on the oblique propagation (incidence angle) direction. It is generally a triplet, with a central total reflection band and characteristic selective reflection bands appear on both sides of it. For normal incidence, these three bands coalesce, the central band becomes infinitesimally narrow, and the second order reflection is circularly polarized.

The single reflection band observed in Y102 must be the full pitch band in Sm-C^* because its intensity is much stronger than 50%, and the reflected light is not circularly polarized. The second order characteristic reflection band must be hidden in the opaque intrinsic absorption region of the liquid crystal mixture, Y102. In the case of MC815, the appropriateness of identifying the phase as ferroelectric Sm-C^* is much clearer. Figure 3.5 shows wavelength of the reflection peaks vs. temperature. Two reflection bands are observed at higher temperatures; with decreasing temperature, the second reflection band gets buried in the opaque

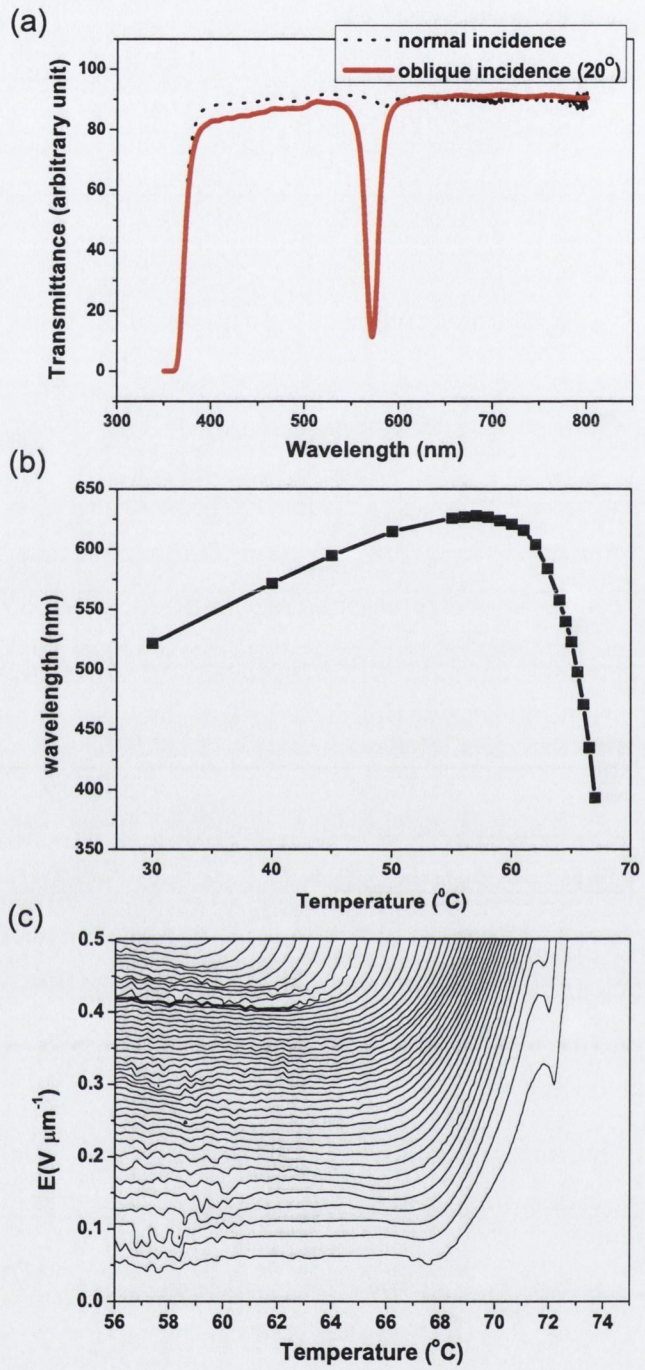

Figure 3.4: Experimental data of Y102 by using homeotropic cells. (a) Reflection band at $40°C$ (100 μm homeotropic cell) for normal and oblique incidence of light. (b) Temperature dependence of the peak of the full-pitch reflection band (100 μm homeotropic cell). (c) Field-induced birefringence contour lines in $E - T$ space obtained by using PEM. Lines shown are those of constant birefringence $\Delta n \cdot 10^{-3}$. This shows SmC^* phase up to a temperature of $68°C$ followed by Sm$C_\alpha{}^*$ from 68 to $72°C$ and SmA phase at higher temperatures.

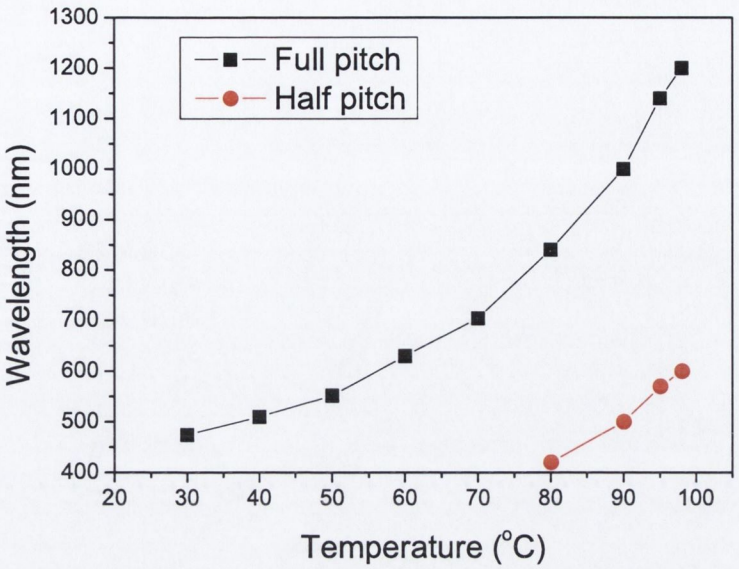

Figure 3.5: The observed temperature dependencies of the peak of the two reflection bands of MC815.

intrinsic absorption region. The first reflection band peak varies smoothly with temperature; no jump in the wavelength of the reflected light occurs which suggests no phase transition is observed over a wide temperature range from below room temperature up to 100°C where the phase transition to isotropic occurs. Therefore, it is quite reasonable to conclude that MC815 exhibits Sm-C^* over a wide temperature range. Contrary to the case for Y102, there exists neither Sm-C^*_α nor Sm-A in MC815 just below isotropic. For normal incidence, the first order reflection is practically zero, but the second order one shows a saturation at 50% and is polarized circularly with right handedness for R moiety.

3.3.2 Temperature dependencies of biaxiality

Figure 3.6 summarizes the results for the temperature dependence of the observed biaxiality in the unwound Sm-C^* of the various compounds and mixtures listed in Fig. 3.2. Two types of temperature dependencies are observed; the biaxiality decreases with temperature in Fig. 3.6(a), while it increases with temperature in Fig. 3.6(b), sometimes, except for a narrow high temperature region of Sm-C^*. For example, MHPBC, Felix18, C6 *etc.* (let us designate these materi-

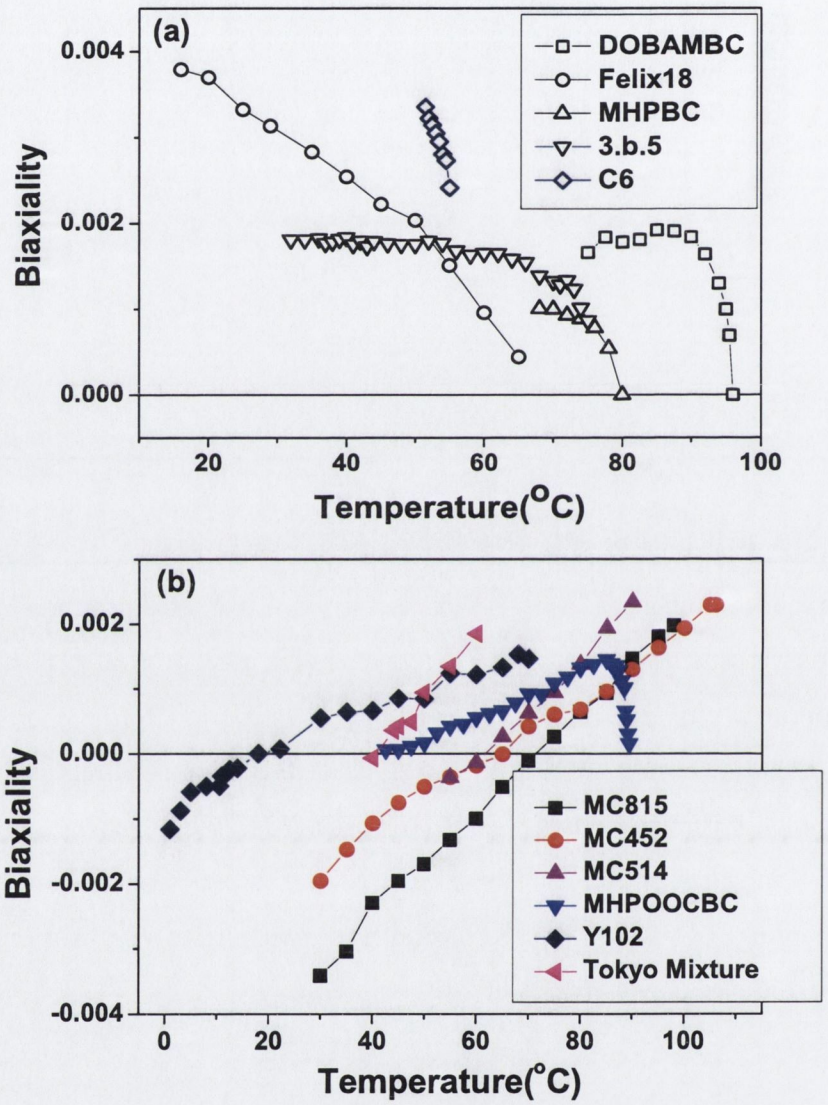

Figure 3.6: Two types of temperature dependencies of biaxiality; (a) decreasing biaxiality with temperature for compounds given in the inset, (b) increasing biaxiality with temperature and temperature induced sign reversal of biaxiality for a different set of compounds given in the inset.

als as group A for convenience) have biaxiality that decreases with temperature, and MHPOOCBC, Y102, MC815 *etc.* (designated as group B) show an increasing trend excluding in a narrow temperature region. The group B has negative biaxiality values at low temperatures with a change in the sign of the biaxiality above a certain temperature. So, they become uniaxial at a certain intermediate temperature depending on the wavelength of the light used for conoscopy. That is also seen in Fig. 3.7, which shows conoscopic images, where the melatopes in conoscopy change from a horizontal direction (parallel to the electric field) to a vertical direction (normal to the electric field) with increasing temperature. We also note that this sign reversal of the observed biaxiality in the group B occurs without the sign reversal of the spontaneous polarization or of the helical pitch divergence happening. Thus, it's quite interesting to elucidate what causes those kinds of behaviors, considering that SmC phase is believed to have only positive biaxiality which decreases with temperature increasing.

It is also meaningful to investigate the color dispersion of the biaxiality. Fig. 3.7 shows the conoscopic images of the compound MC452 (belonging to group B) at various temperatures under a blue light (average wavelength: 450nm) and a red light (average wavelength: 600nm) respectively. Uniaxiality appears at a different temperature for each wavelength, which indicates the biaxiality is determined by two or more different physical origins. In other words, if the zero biaxiality or uniaxiality is due to a perfectly random rotation around the molecular long axis and a perfectly isotropic fluctuation of the long axis, the uniaxiality should not exhibit color dispersion. The existence of the color dispersion of biaxiality at the cross-over of the uniaxiality indicates that there exist at least two or more physical origins and these compete with each other to produce the zero value of biaxiality.

Three different physical mechanisms have been considered for the emergence of the biaxiality and these may be superimposed.

(i) The molecular long axis thermally fluctuates anisotropically. The stronger azimuthal fluctuations project the largest polarizability along the molecular long

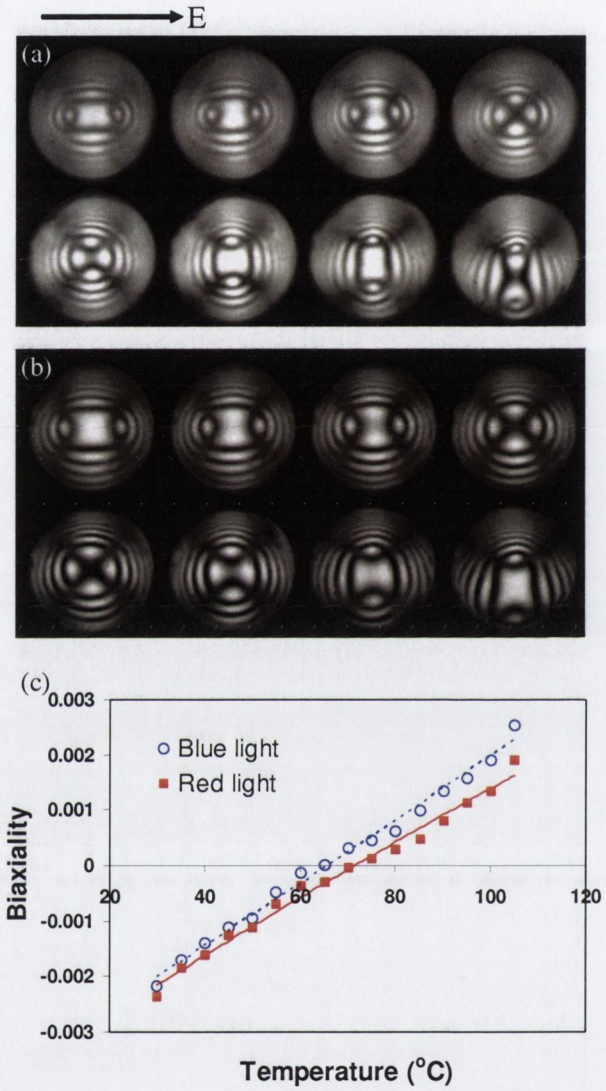

Figure 3.7: The observed biaxiality dispersions in MC452 for blue and red wavelengths; (a), (b) conoscopic images under blue light (~450nm) and red light (~600nm) (MC452, Temperature: 35°C, 45°C, ..., 105°C (from upper left side), (c) biaxiality as a function of temperature for blue and red wavelengths. In figures (a) and (b), the tilt plane is in the vertical direction, whereas the direction normal to the cell is not at the center of the images but is directed at the bottom part of the images.

axis onto the $Y' \equiv Y$ direction, while the weaker polar fluctuations project it onto the X' axis. Consequently, this mechanism predicts $n_{Y'} > n_{X'}$ [30, 46, 58].

(ii) The molecular environment is monoclinic and the molecular rotation around its long axis is biased, giving rise to the phase biaxiality, i.e. *the quadrupolar ordering* of the short axes which characterizes the molecular biaxiality. When the constituent molecules are chiral and the compound is not racemic, such biased rotations also produce spontaneous polarization in the chiral smectic-C phase (Sm-C^*), i.e. *the dipolar ordering* of the short axes characterizing the molecular transverse dipole moments. The chirality reduces the C_{2h} symmetry of Sm-C to the C_2 symmetry of Sm-C^*. As a necessary consequence, the transverse molecular dipoles align at least partially so that the spontaneous polarization emerges along the polar direction which is parallel to the Y axis [8, 30, 44].

(iii) The induced dipoles in the tilted molecules may not polarize symmetrically because of their particular arrangement in Sm-C^*, and hence the local field may not be parallel to the applied electric field. The tensors of dielectric polarizability and permitivity do not need to have the same eigen axes, which can cause the biaxiality in liquid crystal systems, except for the Y axis. In the monoclinic symmetry, the Y axis is fixed, while the other two are color dispersive.

The mechanism (i) and (ii) are connected to each other. One mechanism could affect the other more and less. The main purpose is to examine the sign of the order parameter concerning the mechanism (ii), and the temperature dependences of the order parameters for mechanisms (i) and (ii).

3.3.3 Observation of biaxiality apparently not dependent on the enantiomeric excess ratios

As already pointed out in Section 3.1, it has not so far been known whether the short-axes-ordering was really observed from results on biaxiality by clearly distinguishing this contribution from those by the long-axes-fluctuations, because all the biaxiality observed so far is only positive. The negative biaxiality now

observed in Fig. 3.6 appears to result from the ordering of the short axes. In order to confirm it, let us first experimentally show that, in Sm-C^*, the quadrupolar ordering of the molecular hard cores is sufficiently large as compared with the dipolar ordering of the transverse molecular dipoles. For our experiments, we chose the compound MC815 which is a nominally pure R-moiety and shows the negative biaxiality, and its racemate MC884. These two compounds are mixed to obtain different enantiomeric excess ratios. Figure 3.8 (a) illustrates the biaxiality vs temperature obtained in several sample compounds with the same chemical structure but different enantiomeric excess ratios, *e.e.* $= ([R] - [S])/([R] + [S])$, where $[R]$ and $[S]$ represent the amounts in weight of R- and S-moieties of the compounds contained in the mixture. Surprisingly in Fig. 3.8 (a), the biaxiality is found to hardly depend on the enantiomeric excess (optical purity) of the sample compounds. The corresponding data on the measured values of the tilt angle and the spontaneous polarization vs temperature are given in Figs. 3.8 (b) and (c). The tilt angle is found to be independent of the *e.e.* ratio. The accuracy in measuring the biaxiality of unwound Sm-C^* of nominally optically pure compound was of the order of $\pm$ 0.0001. When the enantiomeric excess is small, the accuracy in measuring the biaxiality was somewhat reduced by the occurrence of flow due to the applied electric field particularly. We are in the process of improving the accuracy by using a magnetic field instead of an electric field so that we can align even the racemate compounds.

The biaxiality measured by conoscopy does not appear to depend on the enantiomeric excess, *e.e.*, ratio not only in the high temperature region where the biaxiality is positive but also in the low temperature region where it is negative. Sigarev *et al.* [59] analyzed the dependence of the IR absorption of the chiral carbonyl band on the cell rotational angle in terms of its theoretical angular dependence [60] in Sm-C^* of the compound M5POBC and obtained the distribution function of the biased rotation of the short axis around the long molecular axis in the unwound state. They concluded that the result can be reproduced by assuming its dipolar ordering alone. When Kim *et al.* unambiguously showed the biased rotation of the carbonyl groups in MHPOBC, they noticed the difference in

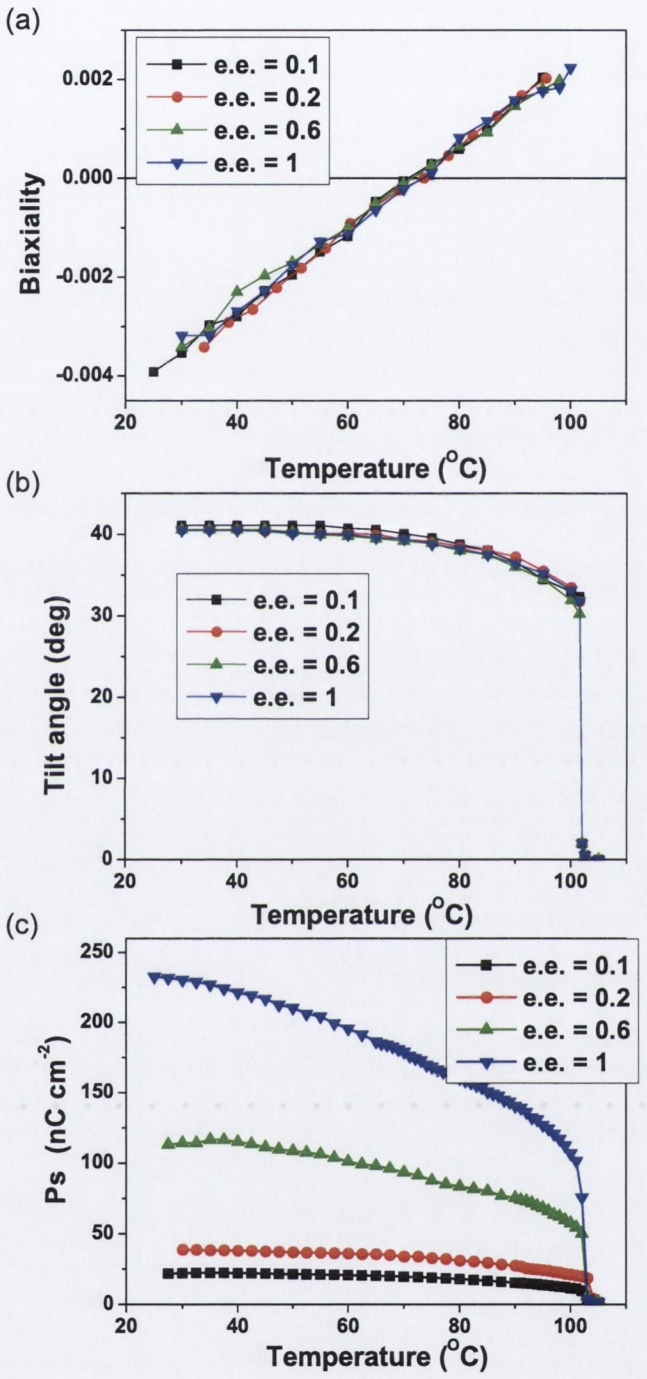

Figure 3.8: Experimental data for different enantiomeric excess ratios of MC815(R) and MC884(racemate) of the same compound. (a) The observed biaxiality as a function of temperature, (b) the tilt angle as a function of temperature, (c) the spontaneous polarization, P_S as a function of temperature.

the angular dependencies between the chiral carbonyl and the core one [61]. They considered that some part of the difference may result from the dipolar ordering of the chiral carbonyl and the quadrupolar ordering of the carbonyl group in the core part of the molecule. Polarized IR absorbance and Raman scattering investigations for a variety of samples of different enantiomeric excess ratios, including those on racemates, must be interesting and valuable works in elucidating the ordering of the transverse dipoles responsible for an emergence of the spontaneous polarization. Thus, the ordering of the molecular short axis in the SmC^* phase has been proven to be highly dipolar. However, the optical biaxiality measured by conoscopy does not distinguish the dipolar ordering from the quadrupolar ordering. In other words, the dipolar ordering and the quadrupolar ordering produces the same biaxiality. Our experimental results implies that the intermolecular interactions producing the quadrupolar ordering do not depend on the the values of *e.e.* ratio. That is, though the phase spontaneous polarization decrease with mixing [R] and [S] compounds, the strength of the intermolecular interactions does not decrease.

To detect the dipolar ordering directly, we suggest the use of the non-linear optical techniques, such as the coherent Raman scattering and the vibrational sum-frequency generation spectroscopy.

3.4 Discussion

3.4.1 Effective polarizability tensor in SmC^* phase

We define the right-handed molecular coordinate system with the maximum polarizability z axis which can also be regarded as the molecular long axis, the minimum polarizability x axis, and the y axis perpendicular to both z and x.

Then the molecular polarizability tensor is written as

$$\hat{\boldsymbol{\alpha}}_{\mathrm{mol}} = \begin{pmatrix} \alpha_x & 0 & 0 \\ 0 & \alpha_y & 0 \\ 0 & 0 & \alpha_z \end{pmatrix}. \tag{3.1}$$

On the other hand, the right-handed Sm-C phase director coordinate system was defined in Section 3.1 by the Z axis parallel to the director, the Y axis perpendicular to the director tilt plane and the X axis normal to both Y and Z. As explained in Introduction of this thesis, the ordering of the molecules in Sm-C with the phase symmetry of C_{2h} can be specified by four independent order parameters,

$$\left.\begin{aligned} S &= S_{zz}^{Z} \\ P &= S_{zz}^{Y} - S_{zz}^{X} \\ D &= S_{yy}^{Z} - S_{xx}^{Z} \\ C &= \left(S_{yy}^{Y} - S_{xx}^{Y}\right) - \left(S_{yy}^{X} - S_{xx}^{X}\right). \end{aligned}\right\} \tag{3.2}$$

Here $S_{\alpha\beta}^{i} = \langle 1/2(3l_{i,\alpha}l_{i,\beta} - \delta_{\alpha\beta})\rangle$ is one of the three diagonal Saupe ordering matrices, where $l_{i,\alpha}$ is the cosine of the angle between the phase coordinate $i = X, Y,$ or Z and the molecular coordinate $\alpha = x,\ y,$ or z [3, 62]. In Eq. 3.2, we defined the P order parameter as $S_{zz}^{Y} - S_{zz}^{X}$, where the Y and X axes are exchanged compared to the reference [3]. This is because we defined the biaxiality as $n_Y - n_X$, which is positive when P is positive. This consideration is required for easily connecting the order parameters to the biaxiality. Note that P order parameter represents physical mechanism 1, the anisotropic thermal fluctuation of molecular long axis and C order parameter corresponds to physical mechanism 2 or the biased rotation around the molecular long axis.

After averaging the molecular orientation, we can consider that each molecule has, at the center of gravity, the effective polarizability tensor,

$$\hat{\boldsymbol{\alpha}} = \begin{pmatrix} \alpha_X & 0 & 0 \\ 0 & \alpha_Y & 0 \\ 0 & 0 & \alpha_Z \end{pmatrix}. \tag{3.3}$$

The eigen values α_i, $i = X, Y,$ or Z, are given by

$$\left.\begin{aligned} \alpha_X &= \bar{\alpha} - \tfrac{1}{3}\left[\Delta\alpha\,(S+P) + \Delta\alpha_\perp \tfrac{(D+C)}{2}\right] \\ \alpha_Y &= \bar{\alpha} - \tfrac{1}{3}\left[\Delta\alpha\,(S-P) + \Delta\alpha_\perp \tfrac{(D-C)}{2}\right] \\ \alpha_Z &= \bar{\alpha} + \tfrac{2}{3}\left[\Delta\alpha S + \Delta\alpha_\perp \tfrac{D}{2}\right], \end{aligned}\right\} \tag{3.4}$$

where $\bar{\alpha}$ is the average polarizability, $\Delta\alpha$ and $\Delta\alpha_\perp$ are the anisotropy, and the transverse anisotropy of the molecular polarizabilities, respectively [3]. These are given by

$$\left.\begin{aligned} \bar{\alpha} &= (1/3)(\alpha_x + \alpha_y + \alpha_z) \\ \Delta\alpha &= \alpha_z - (1/2)(\alpha_x + \alpha_y) \\ \Delta\alpha_\perp &= (\alpha_y - \alpha_x). \end{aligned}\right\} \tag{3.5}$$

In fact, Isaert and Billard obtained Eq. (2.3) of Ref. [58] when they examined the anisotropic thermal fluctuations of the molecular long axis. Similarly, we can take the biased rotation around the molecular long axis into account and obtain the effective polarizability tensor in the same form as given in Eq. 3.3. If we assume the perfect nematic order of the long axis, the single order parameter $\langle\cos(2\psi)\rangle$ is needed to calculate α_X, α_Y and α_Z from α_x, α_y and α_z. Here ψ denotes the angle between the X axis and the x axis. In the case of perfect nematic order of the long axis, out of the three biaxial order parameters, only C is finite.

3.4.2 Local field effect and the resulting positive biaxiality

[2] The anisotropic fluctuation of the molecular long axis and the biased rotation of the molecular short axis around the molecular long axis are the two molecular motions that may primarily cause the emergence of biaxiality in Sm-C. Even if we assume the perfect nematic order and the free rotation, however, the characteristic layered structure with the tilted director in Sm-C may also produce the biaxiality due to the local or the effective field effect. We now examine the relation between the effective polarizability tensor with the eigen axes (X, Y, Z)

[2] Analytical calculations in Section 3.4.2 were carried out by Dr. A. V. Emelyanenko in Moscow State University, in discussion with prof. Fukuda and author.

and the dielectric permittivity tensor with the eigen axes (X', Y', Z') by considering the local field effect. In general, Z' and X' are not parallel to Z and X, respectively, since these are color dispersive; whereas we can always take $Y' \equiv Y$, since this is fixed. In the approximation of the isotropic local field which was introduced by Vuks about four decades ago [15, 39], we can take $Z' \equiv Z$ and $X' \equiv X$ in addition to $Y' \equiv Y$, and the principal refractive indices can be expressed in terms of polarizabilities

$$\frac{n_i^2 - 1}{n^2 + 2} = \frac{4\pi N \alpha_i}{3}. \tag{3.6}$$

Here α_i and n_i with $i = X, Y, \text{or } Z$ are the eigen values of Eq. (3.3) and the approximate refractive indices along the $i = X, Y, \text{or } Z$, respectively, and $n^2 = (1/3)(n_X^2 + n_Y^2 + n_Z^2)$ is the mean square refractive index. N is the number of molecules per cm^3.

The self-consistency of the Vuks equations, Eq. (3.6), was studied in detail for the uniaxial case and its validity was established with an accuracy of 0.5 % in the uniaxial liquid crystalline materials with refractive indices, $n_{\parallel}$ and $n_{\perp}$, ranging from ~1.46 to ~1.86 [39]. Since the anisotropy Δn is usually much larger than 1 %, it is reasonable to assume the isotropic-local-field approximation and to use the Vuks equations in the nematic and Sm-A phases. In the biaxial case of Sm-C under consideration, the transverse anisotropy $\Delta n_{\perp}$ is of the order of 0.1 % and we are not sure whether the isotropic-local-field approximation can quantitatively hold in accuracy of this level. In order to prove that the negative biaxiality experimentally observed inevitably results from the molecular short axes ordering, we now show that the biaxiality due to the local field effect must be positive. Let us use a reasonably simplified model, i.e. the Sm-C phase with the perfect nematic order and the perfect smectic layer order consisting of circular-cylindrical hard-rod molecules with length l and diameter a and with the uniaxial effective polarizability tensor $\hat{\boldsymbol{\alpha}}$ at the center of gravity of the molecules, which is

written in the (X, Y, Z) coordinate system as

$$\begin{pmatrix} \alpha_\perp & 0 & 0 \\ 0 & \alpha_\perp & 0 \\ 0 & 0 & \alpha_\parallel \end{pmatrix}. \tag{3.7}$$

Suppose N is the number of molecules per unit volume and $\mathbf{E}'(\mathbf{r}, t)$ the local field acting on a particular molecule located at a point $\mathbf{r}$ and at a time t. Then the polarization $\mathbf{P}(\mathbf{r}, t)$ is given by

$$\mathbf{P}(\mathbf{r}, t) = N\mathbf{p} = N\hat{\boldsymbol{\alpha}}\,\mathbf{E}'(\mathbf{r}, t). \tag{3.8}$$

Polarization is also written in terms of the mean or observed field $\mathbf{E}(\mathbf{r}, t)$ and the dielectric permittivity tensor $\hat{\boldsymbol{\epsilon}}$ as

$$\mathbf{P}(\mathbf{r}, \mathbf{t}) = \frac{1}{4\pi}(\hat{\boldsymbol{\epsilon}} - \hat{\mathbf{1}})\,\mathbf{E}(\mathbf{r}, \mathbf{t}). \tag{3.9}$$

Now we consider a sphere whose center is located at the center of gravity of the particular molecule and whose radius ρ is sufficiently large compared with the dimensions of the molecule and small enough compared with the wavelength of the incident light. The local field acting on the molecule located at the center of the sphere consists of the sum of two contributions [38, 58, 63, 64]: one from the outside of the sphere, $\mathbf{E} + (4\pi/3)\mathbf{P}$, and the other from the inside of the sphere, and is written as

$$\mathbf{E}'(\mathbf{r}, t) = \mathbf{E}(\mathbf{r}, t) + \frac{4\pi}{3}\mathbf{P}(\mathbf{r}, t - \rho/c) + \frac{1}{N}\sum_i \nabla \times \nabla \times \frac{\mathbf{P}(\mathbf{r}_i, t - R_i/c)}{R_i}. \tag{3.10}$$

Here $R_i = \mid \mathbf{r} - \mathbf{r}_i \mid$ and the summation is performed over the molecules inside the sphere. Because of the chosen size of the sphere, we can neglect the retardation effect, replace the summation by the integration, and obtain

$$\mathbf{E}'(\mathbf{r}, t) = \mathbf{E}(\mathbf{r}, t) + \frac{4\pi}{3}(\hat{\mathbf{1}} + \hat{\mathbf{T}})\,\mathbf{P}(\mathbf{r}, t) \tag{3.11}$$

with

$$T_{\alpha\beta} = T_{\beta\alpha} = \frac{3}{4\pi} \int \frac{3R_{i\alpha}R_{i\beta} - \delta_{\alpha\beta}R_i^2}{R_i^5} \mathrm{d}V', \tag{3.12}$$

where $R_{i\alpha} = r_\alpha - r_{i\alpha}$ and the integration is to be made by taking into account the excluded volume of the particular molecule located at the center of the sphere. By eliminating $\mathbf{E}'$ and $\mathbf{P}$ with the help of Eqs. (3.8), (3.9) and (3.11), we finally obtain

$$\hat{\boldsymbol{\epsilon}} = \left\{ \hat{\mathbf{1}} - \frac{4\pi N}{3} \hat{\boldsymbol{\alpha}} (\hat{\mathbf{1}} + \hat{\mathbf{T}}) \right\}^{-1} \left\{ \hat{\mathbf{1}} + \frac{4\pi N}{3} \hat{\boldsymbol{\alpha}} (\hat{\mathbf{2}} - \hat{\mathbf{T}}) \right\}. \tag{3.13}$$

In this way we can calculate $\hat{\boldsymbol{\epsilon}}$ as a function of $N\hat{\boldsymbol{\alpha}}$ [38, 58].

Concerning the integration given by Eq. (3.12) in the isotropic case, it is assumed, as may actually be shown for a number of important special cases, that they do not produce any resulting field at the central molecule. In the case of Sm-C, on the other hand, the integration plays an essential role for the emergence of biaxiality and how to determine it is the main issue. Isaert and Billard [58] made the integration using the reasonably simplified model described above Eq. (3.7). Since the uniformly distributed dipoles within the smectic layer of perfect order produce the electric field only in the layer [65, 66], as in the case of a plane parallel condenser, we can integrate the field and obtain

$$\hat{\mathbf{T}} = \begin{pmatrix} H & 0 & 0 \\ 0 & G & 0 \\ 0 & 0 & -G - H \end{pmatrix}. \tag{3.14}$$

Here G and H are the elliptic functions and are given in Appendix A in [37] in the expanded form as a function of l/a and Θ. The integration is performed in the laboratory coordinate system with the axis 3 parallel to the smectic layer normal, the axis 2 perpendicular to the director tilt plane, and the axis 1 normal to both 2 and 3. Accordingly we inversely transform Eq. (3.7) written in the director

coordinate system (X, Y, Z) into

$$\hat{\mathbf{R}}^{-1} \begin{pmatrix} \alpha_\perp & 0 & 0 \\ 0 & \alpha_\perp & 0 \\ 0 & 0 & \alpha_\parallel \end{pmatrix} \hat{\mathbf{R}}, \quad \text{where } \hat{\mathbf{R}}(\Theta) = \begin{pmatrix} \cos\Theta & 0 & -\sin\Theta \\ 0 & 1 & 0 \\ \sin\Theta & 0 & \cos\Theta \end{pmatrix}. \tag{3.15}$$

Inserting Eqs. (3.15) and (3.14) into Eq. (3.13), we obtain

$$\hat{\epsilon} = \begin{pmatrix} \epsilon_{11} & 0 & \epsilon_{13} \\ 0 & \epsilon_{22} & 0 \\ \epsilon_{31} & 0 & \epsilon_{33} \end{pmatrix}, \tag{3.16}$$

where $\epsilon_{\alpha\beta}$ is given in Appendix B in [37] as a function of $G, H, N\alpha_\parallel, N\alpha_\perp$, and Θ.

It should be noted that, in the laboratory frame, the director tilt produces the non-zero non-diagonal elements of the dielectric permittivity tensor, which may be diagonalized by a rotation of the coordinate system in the director tilt plane by an angle of Θ'. The angle Θ' is given by

$$\tan 2\Theta' = \frac{\tan 2\Theta}{1 - \frac{1}{3}(G + 2H)\varkappa}, \tag{3.17}$$

with

$$\varkappa \equiv \frac{N\alpha_\parallel \alpha_\perp}{(\alpha_\parallel - \alpha_\perp)\cos 2\Theta}, \tag{3.18}$$

and the relations between the eigenvalues of tensor $\hat{\epsilon}$ and its elements in the laboratory frame are given by

$$\begin{aligned} n^2_{X'} &= \varepsilon_{X'} = \frac{1}{2}\left\{\varepsilon_{33} + \varepsilon_{11} - \frac{(\varepsilon_{33} - \varepsilon_{11})}{\cos 2\Theta'}\right\}, \\ n^2_{Y'} &= \varepsilon_{Y'} = \varepsilon_{22}, \\ n^2_{Z'} &= \varepsilon_{Z'} = \frac{1}{2}\left\{\varepsilon_{33} + \varepsilon_{11} + \frac{(\varepsilon_{33} - \varepsilon_{11})}{\cos 2\Theta'}\right\}. \end{aligned} \tag{3.19}$$

Note the relation that exists between the principal refraction indices and the eigenvalues of the dielectric permittivity tensor.

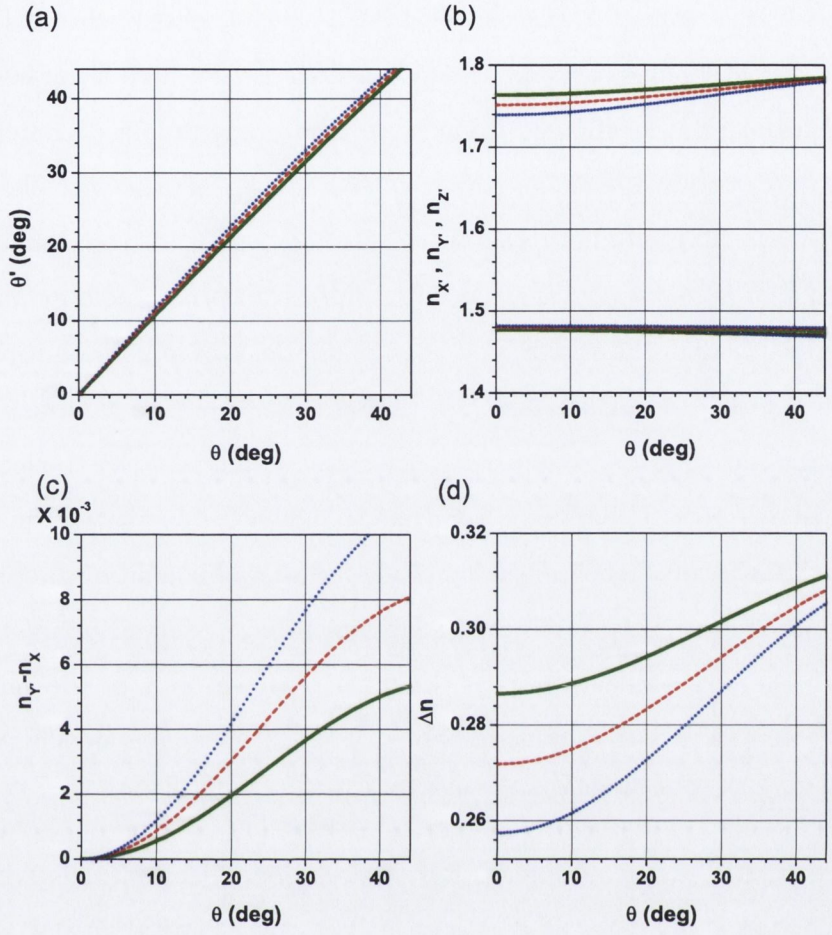

Figure 3.9: Numerically calculated results of Θ' (a); $n_{X'}$, $n_{Y'}$, and $n_{Z'}$ (b); $n_{Y'} - n_{X'}$ (c); and $\Delta n = n_{Z'} - (n_{X'} + n_{Y'})/2$ as a function of Θ. Parameter values used are $N\alpha_{\parallel} = 0.0669$, $N\alpha_{\perp} = 0.1011$, $l/a = 2$, 3 and 4 (for green solid line, red dash and blue dot, respectively), and one fiftieth of the value in Eq. (3.12).

When we numerically obtain the refractive indexes, n'_X, n'_Y and n'_Z, for suitably assumed parameter values, $N\alpha_{\parallel} = 0.0669$, $N\alpha_{\perp} = 0.1011$, $\Theta = 35°$ and $l/a = 2 \sim 4$, we notice that the model by Isaert and Billard [58] clearly overestimates the Sm-C anisotropy and that one fiftieth of the value in Eq. (3.12) reproduces $\sim 10^{-3}$ level biaxiality actually observed as shown in Fig. 3.9. Note that the assumed values of $N\alpha_{\perp}$ and $N\alpha_{\parallel}$ are obtained from Eq. (3.6) using the typical values of $n_{\perp} = 1.5$ and $n_{\parallel} = 1.7$. Because of the simplified assumption of the point dipole moment approximation as well as the perfect nematic orientational and smectic layer order, the overestimation of the Sm-C anisotropy is naturally

anticipated. Vuks assumed a isotropic local field, which is possible in the isotropic state. The reason why his assumption is valid with a quite high accuracy is that real molecules are quite different from those of a point dipole. The charge is complicatedly distributed over the entire volume of the molecule with the dipoles distributed over the molecule. This is more closer to an isotropic state. Our assumption, that is, molecules are just point dipoles and the dipole moments are located at the center of the smectic layers in the absence of any fluctuations gives rise to this overestimation of biaxiality. Even though our calculations cannot yield the quantitative value of the contribution to the biaxiality by the local field, the calculation process is correct conceptually and yields important qualitative information. Sm-C anisotropy always produces positive biaxiality, $n'_Y > n'_X$. So, we are sure that the negative biaxiality experimentally observed unambiguously results from the molecular short axis ordering, because both of the remaining causes for the emergence of the biaxiality, i.e. the molecular long axis fluctuations and the local field effect, always causes the positive biaxiality.

Moreover, the contribution for $\Delta n_\perp$ by the local field effect is around 10 times smaller than that for Δn, as shown in Fig. 3.9. The validity of Vuks assumption was established with an accuracy of 0.5 % for Δn, which implies that it is also valid with an accuracy of 0.05 % for $\Delta n_\perp$. Consequently, we keep using the approximation of the isotropic local field for qualitatively analyzing the biaxiality in the following.

3.4.3 The origins of the two types of temperature dependences and the sign reversal of the biaxiality

In the approximation of the isotropic local field, we can write the biaxiality by using Eqs. (3.3)–(3.6) as

$$\begin{aligned} n_Y - n_X &= \frac{4\pi N}{3}\frac{n^2+2}{2n_\perp}(\alpha_Y - \alpha_X) \\ &= \frac{4\pi N}{9}\frac{n^2+2}{2n_\perp}(2\,\Delta\alpha\, P + \Delta\alpha_\perp\, C), \end{aligned} \tag{3.20}$$

where $n_\perp = (n_Y + n_X)/2$ is the averaged transverse refractive index. Thus, the biaxiality for biaxial molecules can be described as the sum of the mechanisms (i) and (ii), that is, P and C. As explained in the previous section, the mechanism (iii) can be ignored by adopting Vuks approximation. The order parameter P represents the anisotropic thermal fluctuations of the molecular long axis and is always positive as already pointed out above; hence the first term in the last line of Eq. (3.20) is positive because $\Delta\alpha > 0$ by its definition. Since α_x is the minimum polarizability, $\Delta\alpha_\perp$ is also positive as is clear from Eq. (3.5). Consequently, to get negative biaxiality, the order parameter C should be negative, which is related with the biased molecular rotation around the long axis. Moreover, considering that the coefficent $2\Delta\alpha$ of the P order parameter is one order of magnitude higher than the coefficient $\Delta\alpha_\perp$ of the C order parameter, we can conclude that the absolute value of the C order parameter may be at least 10 times larger than that of the P order parameter at low temperatures. This conclusion is consistent with the results obtained by Ossowska-Chrusciel *et al.* [67] in Sm-C^* of MHOBS5 using polarized IR absorbance. Furthermore, they showed that the C order parameter decreases linearly with temperature in Sm-C^* to almost zero near the transition temperature to Sm-A and that the P order parameter stays almost constant and very small. Thus we can conclude that the temperature dependence of the biaxiality is determined mainly by a change in the C order parameter, except for the rather steep increase observed in the high temperature region just below Sm-A. This appears to result from a change in the P order parameter, which is shown clearly in the data of MHPOOCBC of Fig. 3.6.

The materials having the order parameter C positive exhibit biaxiality decreasing with increasing temperature, because C is positive and deceases with increasing temperature. On the contrary, the materials having the order parameter C negative exhibit biaxiality increasing with increasing temperature, because the absolute value of C deceases with increasing temperature, i.e. the negative order parameter C increases with temperature. The sign reversal of the biaxiality observed in materials having negative C is easily explained. At high temperatures, the positive P contribution is larger than the C contribution so that the apparent

biaxiality is positive. However, at low temperatures, the C contribution is larger than the P contribution, so the biaixiality is negative. At a certain temperature, the two contributions cancel out with each other and the biaxiality becomes zero.

Thus, the biassing direction of the short axis in the molecular distribution can be $\psi = 0$ (x is directed along the X axis) or $\pi/2$ (x is directed along the Y axis). When the X axis is the biassing direction, the biaxiality is positive; whereas it is negative at least at low temperatures when the biassing occurs along the Y axis. Since all of the compounds investigated must have the more or less flat hard cores as the molecular structures listed in Fig. 3.2 indicate, it is natural to expect that the biassing direction of the flat hard core part corresponds to the biassing direction of the biaxiality. Some materials show the positive biaxiality due to perpendicular biassing, while some others show the negative one due to parallel biassing. Some materials show very steep dependence of biaxiality, whereas the others (for example, 3.b.5) show a linear increase or decrease with temperature.

3.5 Conclusion

Using conoscopy and the tilted cell geometry, two types of temperature dependencies of biaxiality have been observed in the perfectly unwound state of the helix in the ferroelectric phase: one decreasing and the other increasing with increasing temperature. In the second class of compounds, the biaxiality at low temperatures is negative and the sign reversal of this was also observed. To find the origin of these behaviors, we have combined the three physical mechanisms that are the conceivable origins for the emergence of biaxiality in a model liquid crystal system composed of rigid calamitic biaxial molecules with the eigen axes of the molecular polarizabilities as the long and the short axes [30]. We show that the fluctuations of the long axes and the local field effect can give rise to only one type of biaxiality. By means of a simple theoretical investigation, we find that the average direction of the shortest axis of molecular polarizability, either perpendicular or parallel to the tilt plane, determines the temperature dependence

of the biaxiality. If the biassing of the shortest axis is normal to the tilt plane, the biaxiality is negative and if it is in the tilt plane, it is positive. The short axes ordering is determined by the C order parameter. MHPBC, Felix 18, 3.b.5, C6 and DOBAMBC belong to the positive C order parameter group (positive biaxiality), while MC815, MC452, MC514, MHPOOCBC, Y102 and Tokyo Mixture to the negative C order parameter group (negative biaxiality).

In actual molecules, a number of conformations of the core part must be possible and their population may influence the overall biaxiality. Intuitively, however, we can envisage that the central phenyl ring plane of molecules on the average tends to align close to the tilt plane in the latter while out of the tilt plane in the former. The shortest axis normal to the plane of the central phenyl rings in the axis of minimum polarizability. As a result of the competition between the anisotropic fluctuations of the molecular long axis and the biased rotation around the molecular long axis, the unexpected temperature-induced sign reversal of biaxiality observed in the latter group of compounds is explained.

Until now, we do not know what determines whether a liquid crystal material has positive or negative C order parameter. For example, it is quite interesting to note that all molecules having 'F' lateral part among the materials we used in this experiment, have negative C order parameter. The molecular structure surely affects the orientation of the short axis of the molecule in the smectic phase, but the details still remain to be elucidated in a future work. We also conclude that no discrepancy in assigning the V-shaped switching materials, as Sm-C^* phase rather than ferrielectric phase assigned initially, exists. In the unwound Sm-C^* phase, the melatopes in conoscopy can appear parallel or perpendicular to the tilt plane.

More recently, Osipov and Pikin [44] theoretically considered the influence of the molecular biaxiality on the ferroelectric properties of Sm-C^* in detail. By using the two order parameters: the molecular long axis and the short axis, they successfully showed that the short molecular axis ordering as well as long axis ordering are both equally important for the phase biaxiality and for a determination of the various ferroelectric properties.

Chapter 4

Dielectric response and Molecular motions.

"In this chapter, *sign reversals in the dielectric anisotropy as functions of the temperature and the frequency in SmA* phase are found and their mechanisms are suggested. The fastest collective motion of liquid crystal molecules is discussed. The antiferroelectricity and the relaxation frequency of the antiphase mode is discussed."*

4.1 Introduction

Dielectric permittivity reflects various molecular motions, and has been used to study the dynamics of molecular motions. The molecules in a liquid crystal cell fluctuate individually or collectively, though they bind each other through intermolecular interactions. The fluctuations are coupled with the electric field, and affect the dielectric permittivity. Therefore, the study of the dielectric permittivity allow us to have an insight of the molecular interactions, molecular fluctuations,

and molecular collective motions. In the first section, the dielectric response and special phenomenon in the SmA^* phase are described, and in the second section, these in the SmC^*_A phase are given. The dielectric response in the SmC^* phase is mostly influenced by the helical unwinding process, which is dealt with in next chapter.

4.2 Sign reversal of dielectric anisotropy in SmA^* phase.

The dielectric response of liquid crystals shows complex behavior as functions of both frequency and temperature [26, 27, 68]. For rod-like liquid crystalline molecules, the optical anisotropy Δn ($\equiv n_{\parallel} - n_{\perp}$) is always positive, because the central core part of the molecules mostly affects the optical response. However, the dielectric anisotropy, $\Delta\epsilon'$ ($\equiv \epsilon'_{\parallel} - \epsilon'_{\perp}$) at low frequencies does not follow it. This could be positive or negative and sometimes shows complex behavior, one example of which is the dual frequency nematic liquid crystal response [69, 70]. The dual frequency nematic liquid crystals have attracted attention for their potential to overcome the slow-response of the conventional nematic displays [71, 72]. The dual frequency phenomenon observed in special nematic liquid crystals arises from the molecular dielectric relaxation having the relaxation frequency of a few decades of kHz; the rotation around their short axes. The sign of the dielectric anisotropy as function of frequency changes near the relaxation frequency. Therefore, by changing the frequency of the applied field, the direction of the director can be controlled by the coupling torque of the applied field with the dielectric anisotropy in both cases of rising and of falling signals.

Meanwhile, smectic liquid crystals have additional relaxation processes which include collective modes, thus a complicated dielectric response could ensue. Although extensive studies about the dielectric anisotropy of the nematic liquid crystals have been carried out, a little is known about the dielectric anisotropy in

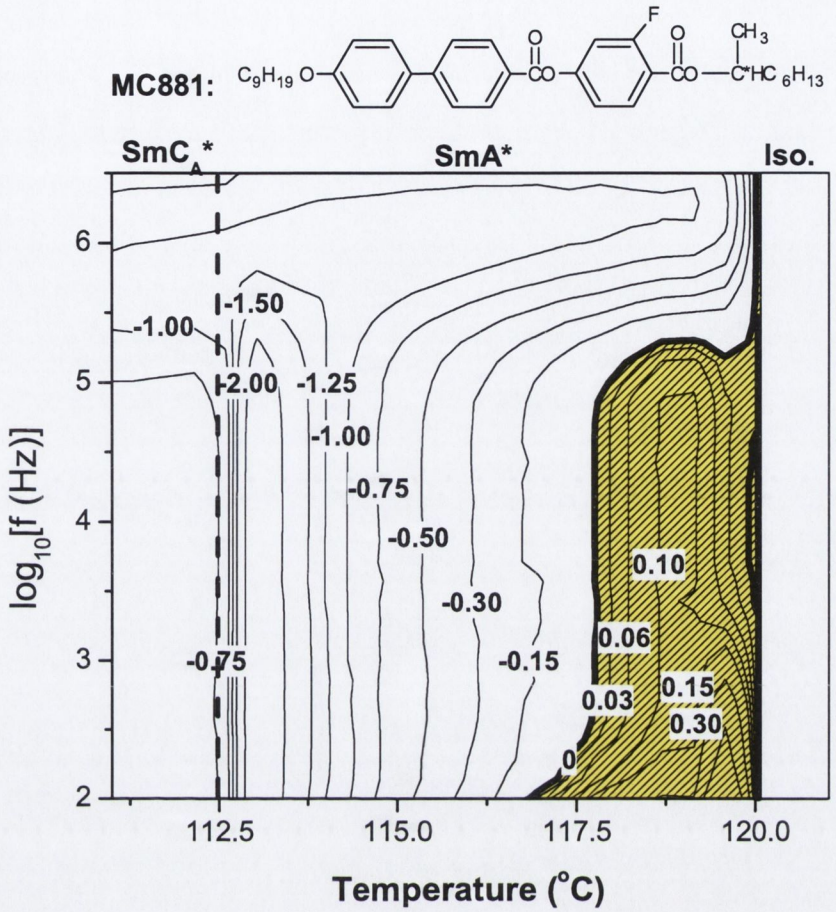

Figure 4.1: Chemical structure of MC881; and the dielectric anisotropy ($\epsilon'_{\parallel} - \epsilon'_{\perp}$). The shaded area has positive dielectric anisotropy. Contour lines marked values of dielectric anisotropy are shown on the plot.

smectic phases [68, 73]. In this paper, we find that the sign reversal in the dielectric anisotropy could appear as function of temperature and of frequency in SmA^* phase due to the involvement of at least two different relaxation mechanisms, while the sign reversal with frequency has only been reported in nematics [69, 70]. SmA^* has zero net tilt angle in the absence of the external field, hence the director is parallel to the long axis of the optical ellipse, similar as in nematics except for the translational order parameter in SmA^*. Therefore, the dielectric anisotropy in SmA^* phase can easily be understood in terms of different physical mechanisms.

The sample used is MC881 shown in Fig. 4.1, and the phase sequence is SmC^*_A (112.5°C) SmA^* (120°C) Isotropic (I) phase. The dielectric permittivity

of MC881 was investigated in both homeotropic and planar cells using broad-band high resolution dielectric spectrometer (Novocontrol Gmbh, Germany). Dielectric/optical cells each of 20 μm thickness were prepared by using two low resistance-ITO glass plates (20 $\Omega/\square$) coated with an alignment layer. RN-1175 (Nissan Chemical Co.) for a planar cell and Dow Corning 9-6346 Silane (72% 3-(trimethoxysilyl)propyldimethyloctadecylammonium-chloride and 28% MeOH) for a homeotropic cell were used to obtain a planar alignment and a homeotropic alignment of the cells respectively.

The dielectric anisotropy of smectic phases having helical layer structure can be written as

$$\Delta\epsilon = \epsilon'_{\parallel} - \epsilon'_{\perp} = \frac{2(\epsilon'_H - \epsilon'_P)}{3\cos^2\theta - 1}, \tag{4.1}$$

where θ is the tilt angle, and ϵ'_H and ϵ'_P represent the real parts of the dielectric permittivities of the homeotropic and the planar cells, respectively [74]. In the SmA^* ($\theta = 0$), the dielectric anisotropy reduces to a simple form, $\epsilon'_H - \epsilon'_P$, since the electric field is parallel to the molecular long axis in the homeotropic cell ($\epsilon'_H = \epsilon'_{\parallel}$) and is perpendicular to that in the planar cell ($\epsilon'_P = \epsilon'_{\perp}$). Fig. 4.1 shows the result, where the positive area of the dielectric anisotropy is shaded to make it easily recognizable. As shown in Fig. 4.1, the positive area appears at the high temperature and low frequency region of the SmA^* phase, while in the other region, the dielectric anisotropy is negative. Thus, the dielectric anisotropy exhibits the sign reversal with frequency when the temperature lies in the range from 117.5 ^{o}C to 120 ^{o}C rather close to the SmA^* to I transition temperature, and it also shows the sign reversal with temperature when the frequency is below 100 kHz. In order to confirm the sign reversal phenomenon, a planar cell was investigated using polarising microscopy. The cell was cooled from isotropic to SmA^* phase (118^{o}C), 2^{o}C below I-SmA^* transition temperature and the texture confirms that liquid crystals are aligned homogeneously as shown in Fig. 4.2 (a) and (b), where changes in the luminance are seen by the rotation of the cell under the crossed polarizers. By applying a rectangular shaped field (20 kHz, 12 V/μm) to the cell,

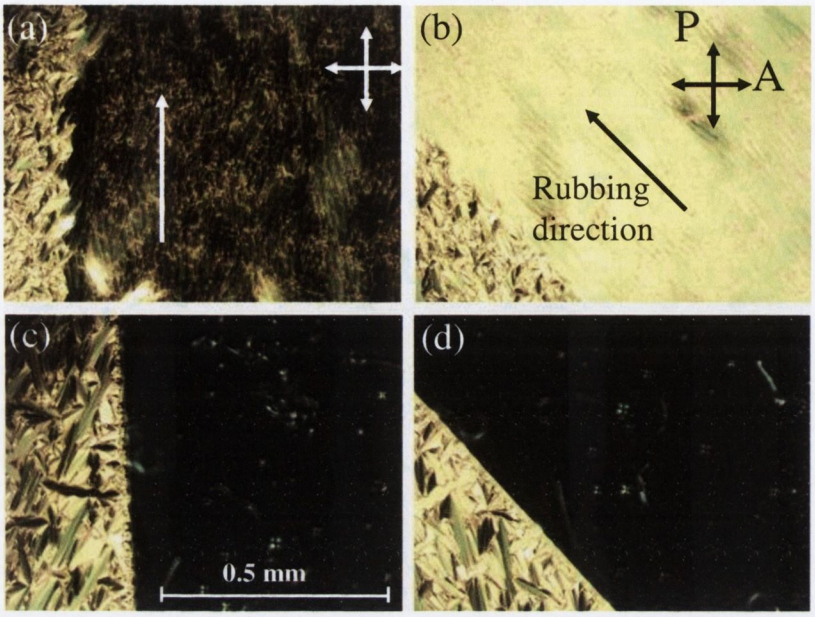

Figure 4.2: Microscopic images of a cell using a planar alignment layer after cooling from the isotropic phase to the SmA^* phase (118^{o}C). (a) and (b) were taken after cooling without fields; (c) and (d) were taken after cooling with a rectangular shaped field (20 kHz, 12V/μm) and turning off the fields; P and A denote the directions of the polarizer and the analyzer, respectively.

we could obtain a homeotropically aligned state, which implies that the dielectric anisotropy is positive at 118 ^{o}C. However, the aligned state in the homeotropic state was not perfect after removing the field because the layer structures of the SmA^* phase in a planarily aligned cell had significantly been distorted by the field. Again, the cell was cooled from isotropic state to 118^{o}C with applying the same rectangular shaped field. We obtained a nice homeotropic alignment as shown in Fig. 4.2 (c) and (d), where the cell stays dark while it is rotated. Surprisingly, the homeotropic state was preserved after removing the field and even after cooling to room temperature in the absence of the field. It is an interesting phenomenon that we could obtain a nice homeotropic texture, even though a planar alignment layer is used in the cell. Thus, we could control the alignment on applying or removing fields during the cooling from the isotropic phase.

However, when we cooled the cell having the homeotropic state from 118 ^{o}C to 114 ^{o}C with the field applied, the homeotropic state was not preserved, but the cell recovered its planar alignment. This implies that the sign in the dielectric

anisotropy is reversed during cooling and the applied field induces the planar alignment. The same phenomenon happened when the frequency of the applied field is increased up to $\sim$ 500 kHz at 119 °C. Thus, these microscopic observations confirm the sign reversals as function of temperature and of frequency in the SmA^* phase.

Measured dielectric response can be fitted to the Havriliak-Negami (H-N) equation for the frequency dependent complex permittivity $\epsilon^*(\omega)$ [75].

$$\epsilon^*(\omega) = \epsilon' - i\epsilon'' = \epsilon_\infty + \sum_{j=1}^{n} \frac{\delta\epsilon_j}{[1 + (i\omega\tau_j)^\alpha]^\beta} \quad , \tag{4.2}$$

where ϵ_∞ is the high-frequency permittivity, j is a variable denoting the number of the relaxation processes up to n, τ_j is the relaxation time of jth relaxation process, α and β are the fitting parameters and $\delta\epsilon_j$ is the dielectric relaxation strength for the jth process.

Fig. 4.3 shows the relaxation frequency and the dielectric strength obtained by fitting the measured permittivity data of the planar cell (solid data) and the homeotropic cell (open data) of MC881 to the H-N equation. While only the molecular mode induced by the rotational fluctuation along the molecular short axis is possible in the isotropic phase, the soft mode arises from the fluctuation of the tilt angle (θ) in the SmA^* phase [26, 27, 68], and is observed in the planarily aligned cell. The molecular mode is maximized and the soft mode is suppressed in the homeotripic cell, and the opposite is true in the planar cell because of the directions of the dipole moments with respect to the applied field. Therefore, the relaxation in the homeotropic cell arises mostly from the molecular mode, and that in the planar cell does from the soft mode in SmA^* phase.

The strength of the soft mode increases dramatically on approaching the transition temperature to the SmC_A^* phase, while the strength of the molecular mode is weakly temperature dependent in the entire range of temperatures in the SmA^* phase as shown in Fig. 4.3. This temperature dependence explains the sign

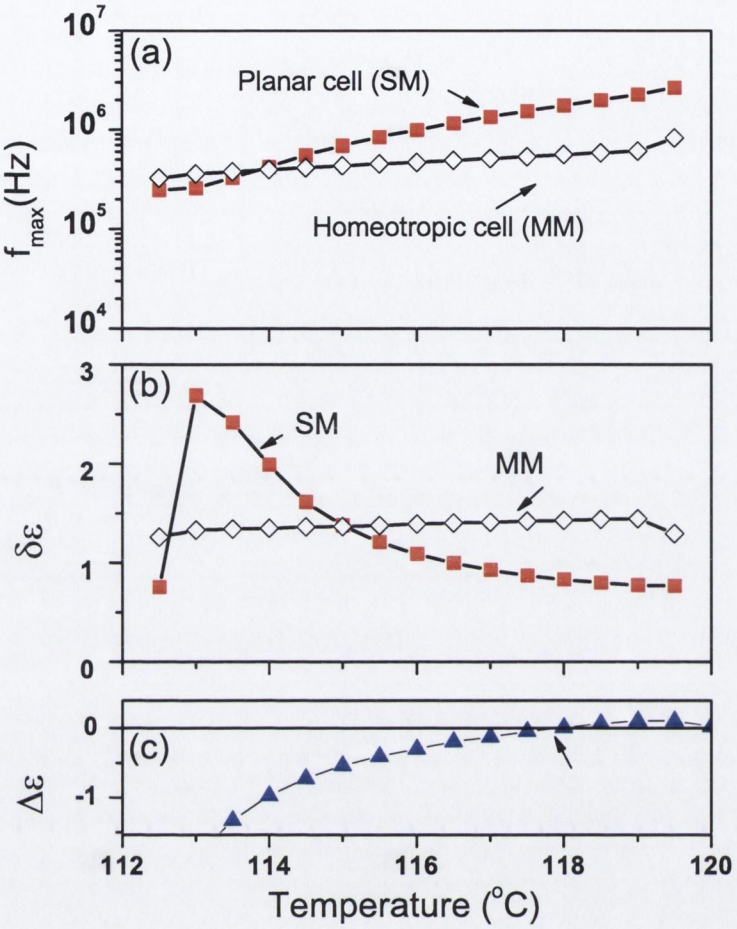

Figure 4.3: Relaxation frequency ($f_{max} \approx (2\pi\tau)^{-1}$, when $\alpha, \beta \approx 1$) (a) and the dielectric strength ($\delta\epsilon$) (b) [76] in the homeotropic cell (open data points) and the planar cell (solid data points), and the dielectric anisotropy ($\Delta\epsilon$) (c) at 12 kHz as a function of temperature in the SmA^* phase. SM and MM denote the soft and the low frequency molecular modes, respectively.

reversal of the dielectric anisotropy with temperature as shown in of Fig. 4.3 (c). The strong temperature dependence of the soft mode induces the sign reversal with temperature. In Fig. 4.4, the real part of the permittivity is plotted as a function of the frequency in SmA^* phase at 113 °C and 119 °C close to SmC_A^* and I transition temperatures respectively. At 119 °C, while the soft mode is very weak, the molecular mode generates a large value of the permittivity along the molecular long axis ($\epsilon'_{\|}$), and causes a positive value in the dielectric anisotropy in the low frequency region. The negative value of the dielectric anisotropy at high frequencies at 119 °C is due to the high-frequency relaxation process, which is a second molecular mode due to the rotation along the molecular long axis (this

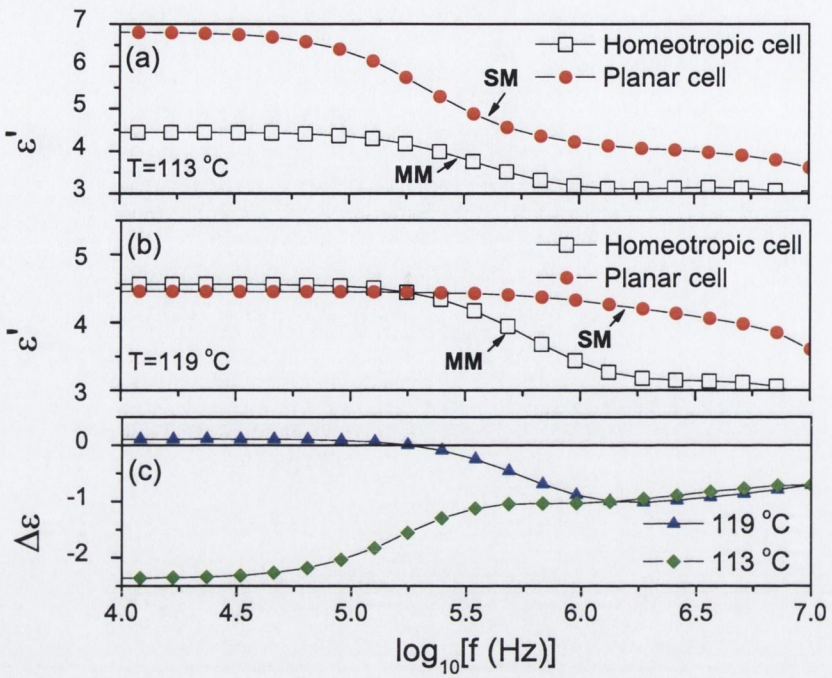

Figure 4.4: The real part of the dielectric constant as function of the frequency at 113 °C (a) and 119 °C (b), and the dielectric anisotropy (c). The decrease of ϵ' near 10 MHz arises from the resistance of ITO on the windows of the experiment and not from the material property of the liquid crystal.

high-frequency mode is beyond the experimental window). However, at 113 °C, the permittivity along the molecular short axis ($\epsilon'_{\perp}$) magnified by the soft mode surpasses $\epsilon'_{\parallel}$ governed by the molecular mode so that the dielectric anisotropy becomes negative in the entire frequency range.

Thus, we can see that the sign reversal with frequency at high temperatures is due to the molecular mode, which is the same as the case in the dual frequency nematics, and the sign reversal with temperature in low frequency is due to the competition between the soft and the molecular modes. This implies that the strong soft mode of the SmA^* phase decreases the dielectric anisotropy so it is likely to induce the negative value of $\Delta\epsilon$, but the soft mode is suppressed at high temperatures and the positive dielectric anisotropy can appear.

We have reported the sign reversals of the dielectric anisotropy as functions of temperature as well as frequency in the SmA^* phase for the first time. These arise from the competition between the soft mode and the low-frequency molecular

mode. We also found that the alignment of the cell can be controlled by applying a proper field at certain temperatures. The method is quite effective and we can obtain a homeotropic alignment with a cell having a planar alignment layer.

4.3 Dielectric response in the SmC_A^* phase

The dielectric permittivity of liquid crystal cells reflects the molecular motions induced by applied fields, and so, the dielectric response of liquid crystals has been studied widely to obtain an understanding of the dynamics of liquid crystal molecules. So far, various dielectric relaxation processes have been found in liquid crystal cellss. These dielectric processes can be broadly classified as the molecular processes and the collective processes [26, 27, 68]. The molecular processes correspond to the independent motions of individual molecules, where the macroscopic change of the average alignment of molecules is not detected, while the collective processes result from the collective motion of molecules.

The molecular processes affect physical properties of liquid crystals such as dielectric anisotropy. For example, the molecular process of reorientation around the molecular short axis induces a dual frequency phenomenon in some nematic and smectic liquid crystals as explained in the previous section. Meanwhile, the collective processes are directly related to the electro optical properties of liquid crystals such as the apparent tilt angle, birefringence and spontaneous polarization etc., since the collective processes involve the macroscopic changes of directors.

Each process has its own relaxation frequency, which reflects the rate of the motions. Usually, the molecular processes appear at higher frequency than the collective processes, implying that the individual molecular motions are faster than the collective motions. However, this is not always the case. The fastest collective mode is found in the antiferroelectric phase. Hiraoka et.al. reported that the antiphase process, which is a collective mode as explained schematically in Fig. 4.5(a), is faster than the reorientation around the molecular short axis in MHPOBC[77]. The relaxation frequency was reported to reach up to 0.9 MHz at

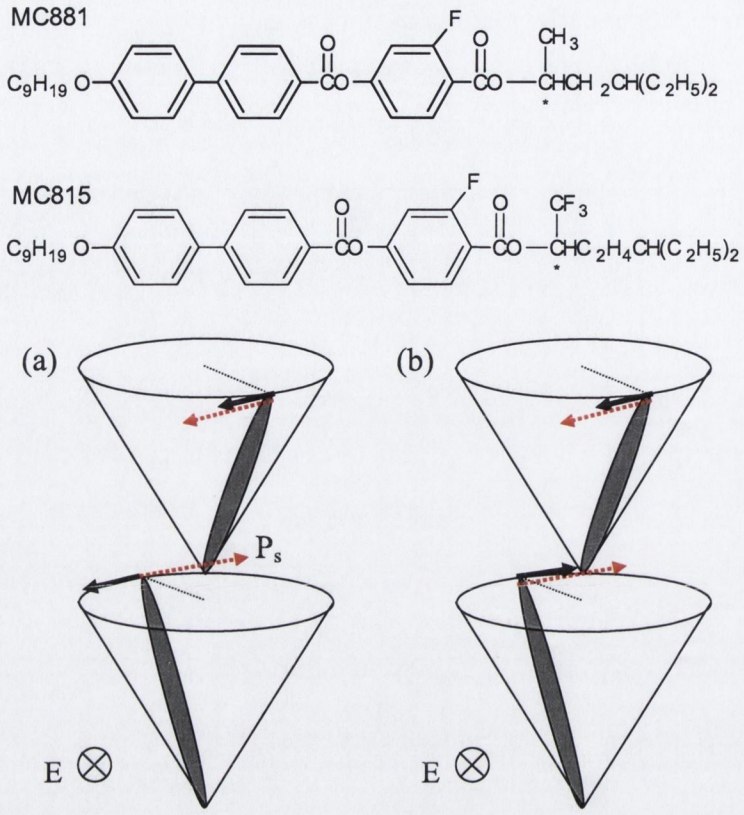

Figure 4.5: Chemical structure of MC881 (antiferroelectric liquid crystal) and MC815 (ferroelectric liquid crystal), and the antiphase mode (a), and the antiferroelectric Goldstone mode in the dielectric relaxations of antiferroelectric phase.

high temperature, though it is less than 10kHz at low temperature. It is worth while to investigate the high frequency collective modes, since it is helpful to predict the limitation of the response time of the material for various liquid crystal applications such as liquid crystal displays. There exist two collective modes in the chiral smectic liquid crystals; the Goldstone mode associated with the fluctuation of the azimuthal angle (ϕ) around the helical axis and the soft mode corresponding to the fluctuation of the molecular tilt angle (θ) [26, 27, 68]. However, this definition becomes insufficient in the antiferroelectric phase, since two types of the fluctuation of the azimuthal angle (ϕ) may exist in this phase. One of these is the antiferroelectric Goldstone mode. This is similar to the Goldstone mode in the SmC^* phase and represents the unwinding of the long helical structure of the SmC_A^* phase as explained in Fig. 4.5(b). The other consists of the opposite motion of two adjacent layers as shown in Fig. 4.5(a), and was referred to as the

antiphase motion in references [78, 79]. This mode can cause a field induced phase transition from the antiferro- to the ferroelectric state, and so, it is not adequate to designate as a Goldstone mode. Usually, the antiphase mode appears in the frequency range 10 kHz - 1 MHz, which may be one of the fast collective mode [77, 79].

Here, we report that an antiferroelectric liquid crystal, MC881 shows a very high relaxation frequency antiphase mode. We also show that the relaxation frequency of the antiphase motion is decreased by mixing a ferroelectric liquid crystal into the antiferroelectric liquid crystal.

An antiferroelectric liquid crystal MC881 and a ferroelectric liquid crystal MC815 synthesized by Mitsubishi Gas Chemical Company, Inc., were investigated using dielectric measurements [80]. The chemical structures of MC881 and MC815 shown in Fig. 4.5 are quite similar. The tilt angle and the spontaneous polarization of the two materials do not differ much either as shown in Fig. 4.6. However, the phase sequence of MC881 is SmC_A^* (112.5°C) SmA^* (120°C) Isotropic (I) phase, while that of MC815 is SmC^* (102°C) I. Thus, MC881 is an antiferroelectric liquid crystal, and MC815 is a ferroelectric liquid crysal. The dielectric permittivity of MC881 was investigated in both homeotropic and planar cells using a broadband high resolution dielectric spectrometer (Novocontrol GmbH, Germany). Dielectric/optical cells of 20 μm thickness each were prepared by using two low resistance indium tinoxide (ITO) glass plates (20 $\Omega/\square$) coated with an alignment layer. RN-1175 (Nissan Chemical Co.) and Dow Corning 9-6346 Silane (72% 3-(trimethoxysilyl)propyldimethyloctadecylammonium-chloride and 28% MeOH) were used to obtain a planar alignment and a homeotropic alignment of the cells, respectively. The experiments were performed on cooling the sample from 120°C to 80°C. Mixtures of MC881 and MC815 are also investigated using the same procedure.

Fig. 4.7 shows the dielectric permittivity of MC881 as function of frequency at 85°C. Fig. 4.7(a) and (b) are the real part (ϵ') and the imaginary part (ϵ'') of the dielectric permittivity. The solid points and the open points represent the data

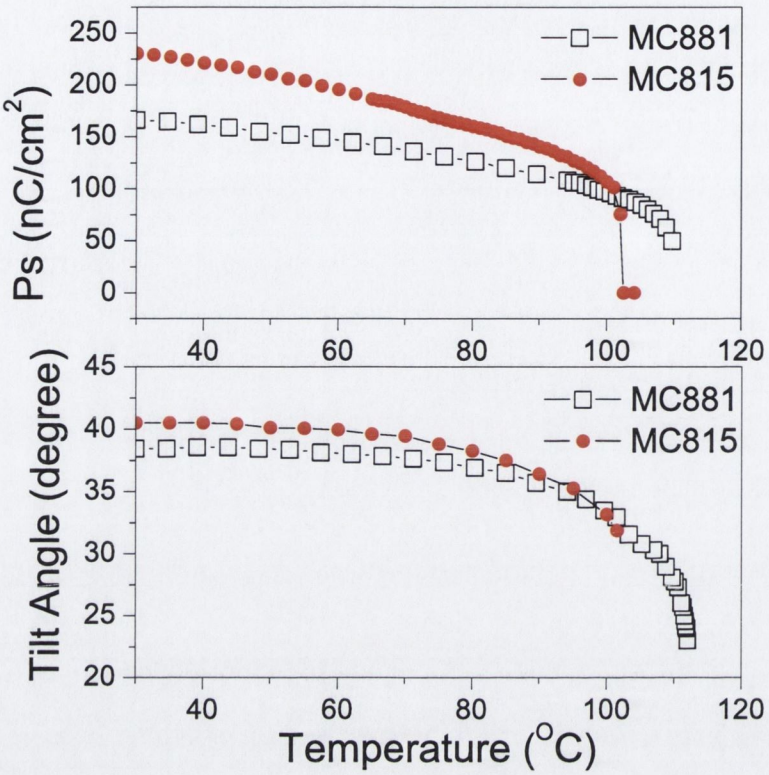

Figure 4.6: The spontaneous polarization (top), and tilt angle (bottom) of MC881 and MC815.

for the planar cell and the homeotropic cell respectively. As shown in Fig. 4.7, the planar cell shows two relaxation processes (excluding the cell relaxation process induced by the electrical resistance of ITO layer) while the homeotropic cell displays only a single relaxation process. To extract the parameters characterizing the relaxation processes, the experimental data were fitted to a Harvriliak-Negami expression.

$$\epsilon''(f) = \frac{\sigma}{2\pi\epsilon_0 f^m} + \mathrm{Im}\left[\frac{\Delta\epsilon}{\{1+(if/f_{HN})^\alpha\}^\beta}\right], \tag{4.3}$$

where f is the measuring frequency, σ is the conductivity of the material, ϵ_0 is the vacuum permittivity, $\Delta\epsilon$ and f_{HN} are the dielectric strength and Harvriliak-Negami relaxation frequency respectively. The parameters α and β describes the shape of ϵ'' with frequency profile. α=1 and β=1 represent the shape for a debye type of relaxation. We found that β=1, and α is larger than 0.8 in entire range

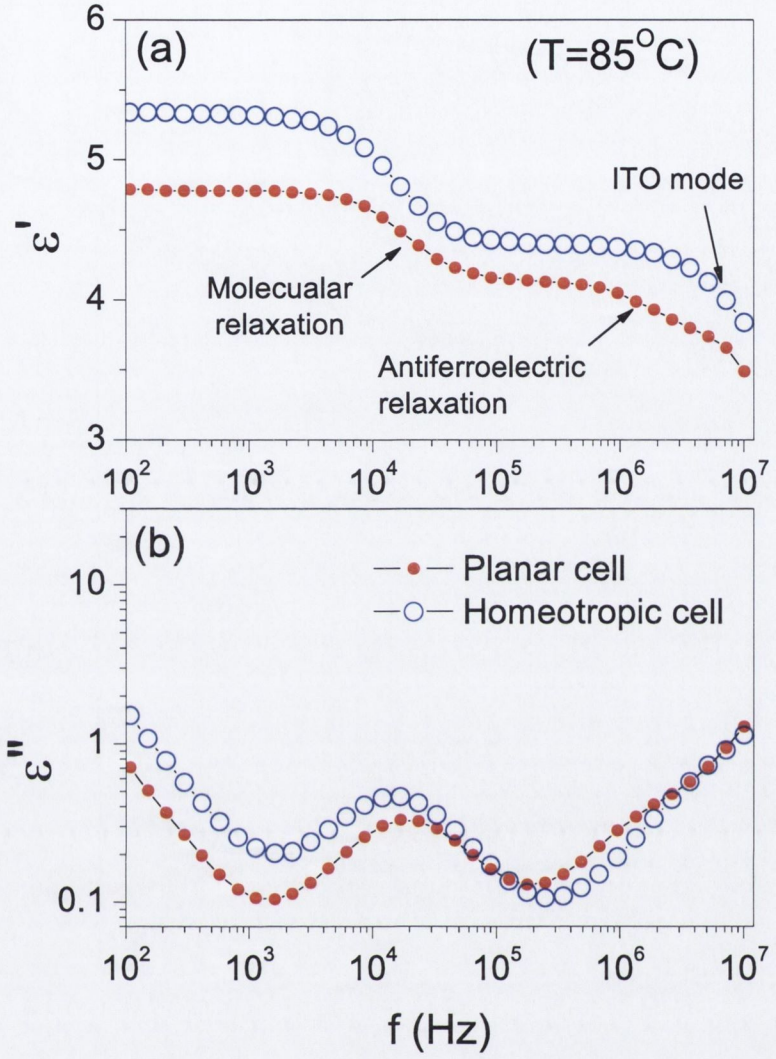

Figure 4.7: The real part (a) and the imaginary part (b) of the dielectric permittivity of pure MC881 at 85°C.

of temperature, indicating that the profiles are symmetric about the maximum in the dielectric loss factor and the distribution of the relaxation times is narrow.

Fig. 4.8 (a) and (b) shows the maximum relaxation frequency and the dielectric strength respectively, and solid and open points are for the planar and the homeotropic cell respectively. From 10kHz to 10MHz, two relaxation processes are found in the planar cell in Fig. 4.8 as was also shown in Fig. 4.7. It is reported that usually four different processes are observed in antiferroelectric phase. The highest frequency process is assigned to the molecular relaxation around the long molecular axis, which appears roughly in the ~1GHz range and is beyond our

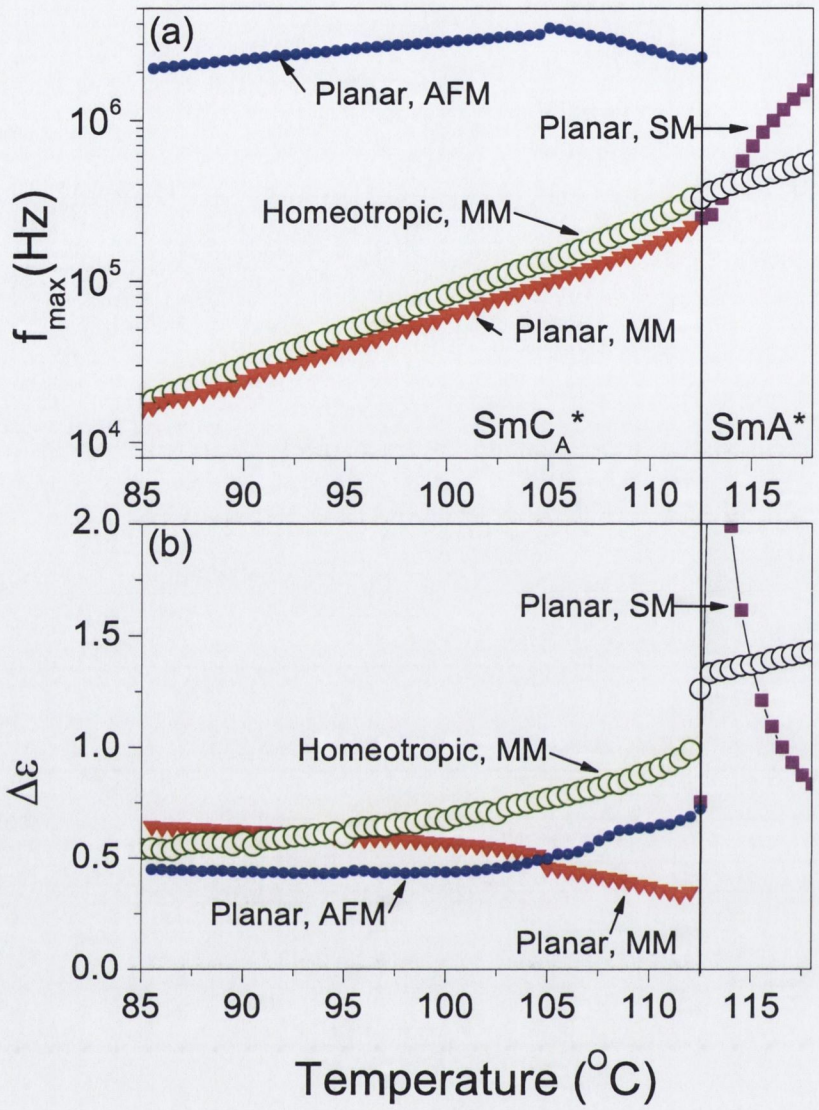

Figure 4.8: The relaxation frequency (a) and the dielectric strength (b) of pure MC881 as function of temperature.

experimental range [81]. The lowest frequency process is the helical unwinding process or the antiferroelectric Goldstone process, which appears at frequencies of less than 1kHz in MC881 and is overlapped by conductivity processes due to ion impurity *etc.* so that it is not easy to separate the Goldstone mode. The antiferroelectric Goldstone mode is not plotted in Fig. 4.8. The other two processes are the molecular relaxation around the molecular short axis, which appears in lower frequency range than the high frequency molecular relaxation around the molecular long axis, and the antiphase process induced by oppositely rotating motion of

spontaneous polarizations of neighboring layers. Therefore, the two processes observed in the planar cell in Fig. 4.8 are the low frequency molecular relaxation and the antiferroelectric mode. As an aid for identifying the two relaxation processes of the planar cell, we compare the results for the planar and the homeotropic cells. In Fig. 4.8 (a), the homeotropic cell shows a single relaxation process, which is continuous from the SmA^* phase to the SmC^*_A phase. This implies that the relaxation process in the homeotropic cell is the molecular process along molecular short axis. Note that the antiferroelectric Goldstone mode and the antiphase mode can not appear in the homeotropic cell, because the field direction is perpendicular to smectic layers and the applied field cannot induce any azimuthal motion of directors. The molecular process observed in the homeotropic cell has almost the same frequency as the low frequency process observed in the planar cell. This means that this low frequency relaxation in the planar cell is the molecular process. Therefore, the remaining high frequency process in the planar cell must be the antiphase process [78, 79]. As shown in Fig. 4.7(a), the frequency of the antiphase mode is about 2-4 MHz, which as far as we are aware is the fastest such collective process reported to date [77–79].

It is also interesting to investigate the behavior of the mixtures of MC881 and MC815. We added 12% and 20% by weight of MC815 into MC881 to make two mixtures of 88% and 80% MC881. By adding MC815 into MC881, a SmC^* phase appears in the temperature interval between the SmA and SmC^*_A phases. The phase sequence of the 88% MC881 mixture is SmC^*_A (110°C) SmC^* (114°C) SmA^* (120°C) Isotropic phase, and that of 80% MC881 mixture is SmC^*_A (105°C) SmC^* (112°C) SmA^* (120°C) Isotropic phase. Fig. 4.9 shows the relaxation frequency of the antiphase mode and the molecular mode in the mixtures in the antiferroelectric phase. The frequency of the molecular mode is not affected by the mixing of two liquid crystals (Fig. 4.9(b)), whereas the frequency of the antiferroelectric mode varies with the mixing ratio (Fig. 4.9(a)). An appreciation of the difference in the origins of the two relaxation processes allows one to deduce the difference of the dependencies of the relaxation frequency on the mixing ratio. The molecular

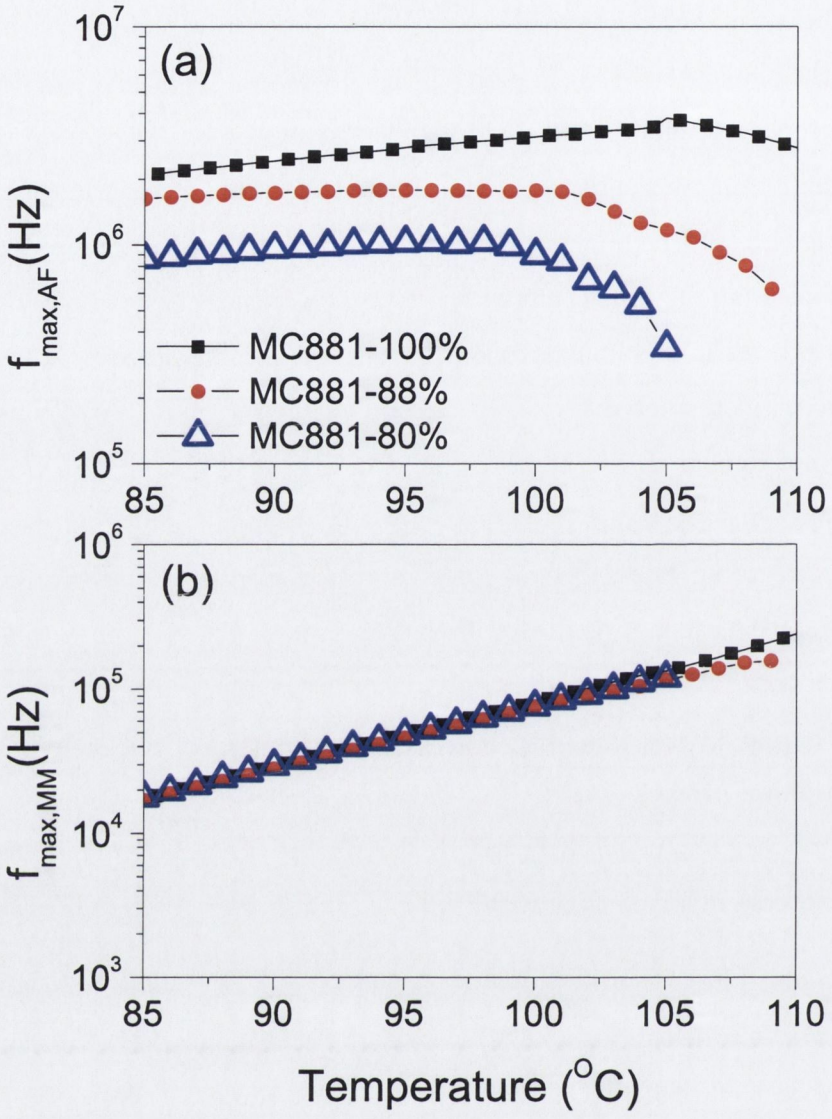

Figure 4.9: The relaxation frequency of the antiphase mode and the molecular mode as function of temperature with varying maxing ratio of MC881 and MC815.

mode arises from individual molecule's fluctuations, so it is related to the inter-molecular interactions between molecules. However, the antiphase mode results from the motion of smectic layers, and is related to the interlayer interactions between neighboring layers. As explained in the previous section, MC815 is a ferroelectric liquid crystal having a quite similar chemical structure to MC881. The negligible dependence of the relaxation frequency of the molecular mode on the mixing ratio may be due to the similar chemical structures of two liquid crystal components, that is, the strength of inter-molecular interactions may not vary

so much on mixing a small amount of MC815 into MC881. This rapid fall in the frequency of the antiphase mode with addition of ferroelectric liquid crystal implies that the interlayer interaction depends rather sensitively on the mixing ratio. Though a more accurate calculation may be required to obtain an exact expression for the frequency of the antiphase mode, we can estimate intuitively that the frequency of the antiphase mode is proportional to the elastic constant (K) between two adjacent layers [78].

$$f_{max} \approx \frac{K}{\gamma}, \tag{4.4}$$

where γ is rotational viscosity between layers.

According to the phenomenological theory for antiferroelectric phases [14, 82], the interlayer interaction between two adjacent layers has a dipolar term and a quadrupolar term, which is also well confirmed experimentally [83, 84]. By ignoring the flexoelectric polarization term, which may be small in spite of its essential role in sub-phases [14], and ignoring the tilt angle dependent term based on a constant tilt angle approximation, we can simplify the free energy in terms of the azimuthal angle (ϕ) of between **c** directors of two neighboring layers as

$$F = \sum -a(T - T_0)\cos\phi_{i,i+1} - B\cos^2\phi_{i,i+1}, \tag{4.5}$$

where the positive coefficient a represents the antiferroelectric interaction and positive coefficient B makes the molecules in two adjacent layers placed in one plane, and T_0 is the transition temperature from SmC_A^* to SmC^*. In the SmC_A^* phase, $\Delta T \equiv (T - T_0)$is negative so that anticlinic ordering is more stable. Larger a means a more stable antiferroelectric state. The elastic constant between layers can be defined as $K \equiv \frac{\partial F/\partial\phi_{i,i+1}}{\delta\phi}(\phi_{i,i+1} = \pi + \delta\phi)$ at anticlinic order. Therefore, we find for the elastic constant between layers

$$K = a(T - T_0) + 2B\ . \tag{4.6}$$

Thus, the elastic constant is proportional to the antiferroelectric coefficient

a, which means that strong antiferroelectric interaction is likely to increase the elastic constant at anticlinic ordering. It is reasonable to assume that the antiferroelectric coefficient a of an antiferroelectric liquid crystal may decrease upon mixing with a ferroelectric liquid crystal. Therefore, we can deduce that the elastic constant decreases with increasing percentage of the added ferroelectric liquid crystal, which causes the decrease of the relaxation frequency of the antiphase mode.

We measured the dielectric permittivity of MC881, an antiferroelectric liquid crystal and MC815, a ferroelectric liquid crystal mixture system. Pure MC881 exhibits very large values of the relaxation frequency of the antiphase mode, about 2-4 MHz, which is supposed to be the fastest collective process reported so far. The relaxation frequency decreases with the increasing ratio of MC815 in the mixture of MC881 and MC815. By adding a ferroelectric liquid crystal, the antiferroelectric coefficient a in Landau free energy expression of antiferroelectric phase is supposed to decrease and so, the elastic constant in the anticlinic order decreases as well. We suggest that the decrease of the elastic constant by mixing a ferroelectric liquid crystal is the origin of the phenomenon whereby the relaxation frequency of the antiphase mode decreases by increasing the ferroelectric component in the mixture.

Part. III

Interlayer interaction and The solitary wave propagations

Chapter 5

Interlayer interaction and field induced solitary wave in SmC_A^*.

"In this chapter, *mechanism of the field induced solitary waves in the SmC_A^* phase is investigated. New method to measure the interlayer interaction is suggested."*

5.1 Introduction to the field induced solitary wave in SmC_A^* phase.

Antiferroelectric liquid crystals (AFLCs) have attracted many researchers interest due not only to scientific [74, 85] but also for display applications [12, 82, 86, 87]. Especially, the field driven phase transition from antiferroelectric (AF) state to ferroelectric (F) state, that is, the switching of AFLC cells has been studied in detail [83, 85, 88, 89] for application purpose. The switching of AFLC cells shows various interesting phenomena (threshold, hysteresis, fast response, continuous grayscale, etc.) useful in applications.

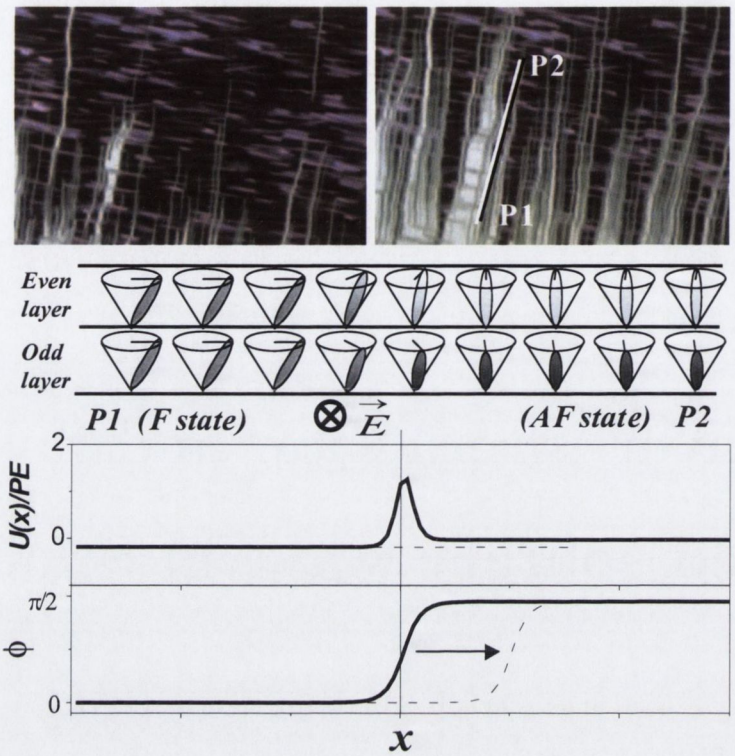

Figure 5.1: Microscopic images of the solitary waves in AFLC cell using MC881 (upper); Director distributions near the boundary for the two states P1 and P2 (middle); The potential energy U and the angle ϕ calculated from Eq. 5.3 and Eq. 5.10 (lower).

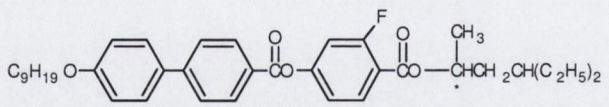

MC881: SmC_A^* (119.5 °C) SmA^* (127 °C) Iso.

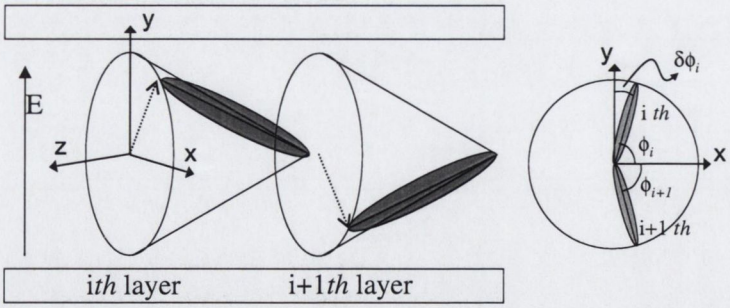

Figure 5.2: Chemical structure of MC881. Molecular and **c** directors in the intermediate unwound antiferroelectric state (VAF state) in a cell.

The solitary wave propagation [90, 91], which is a consecutive transition of the anticlinic orders to the synclinic orders occurring as dominoes, is the most crucial aspect of the switching in AFLC cells. As shown in the microscopic images in Fig. 5.1, the solitary wave propagation is usually observed in the antiferroelectric cells under DC or alternating rectangular field as propagating boundaries of finger domains. A domain propagation observed in a surface-stabilized ferroelectric liquid crystal cell is induced by the special cell structure [48] and the surface interaction between liquid crystals and alignment layers. However, the solitary wave propagation in a AFLC cell is an intrinsic property of the phase. Hence, the physics in both cases is quite different in spite of the similarity of the behavior. So far, the solitary wave phenomenon has been studied mainly for understanding the switching properties of AFLC cells from the viewpoint of applications [87, 89]. However, the solitary wave itself has rarely been studied [74, 92], and even its mechanism is not clear. This is the starting point of the work in this chapter.

In order to have the solitary wave, there should exist two energy minima in the two states (AF and F states) and a energy barrier between the two states must also exist [90, 91]. Li *et al.* [74] observed and characterized the propagating solitary waves in a AFLC cell. They assumed that the necessary condition for the generation of the solitary wave is to have the negative dielectric anisotropy, which is the mechanism to induce a synclinic local minimum in the interlayer potential energy. The initial state of the cells was also assumed such that the **c** directors of the even layers lie at $\phi = 0$, which are not affected by the applied voltage, while those of the odd layers are at $\phi = \pi$ and they transfer to the position of the even layers by the external field. In this definition, ϕ is the angle between the directors and x axis. The latter lies along the glass plate. Thus, in their model, the **c** directors are horizontally aligned (HAF) being perpendicular to the applied field. However, it has been reported experimentally [12, 33, 93, 94] and proven theoretically [83, 94] that the virgin chiral AF stage is uncoiled into the unwound AF state by a relatively low field, where the **c** directors are aligned vertically (VAF), that is, parallel to the field, and it turns into the F state at a sufficiently large field. This contradicts the basic assumption made by Li *et al.* [74]. Whether

the unwound AF state is a VAF or a HAF state is an important starting point for the solitary wave propagation to occur. If the unwound AF state is VAF state as already found [94], the solitary wave propagation cannot appear unless their model is altered, as shown here.

5.2 Experiment and discussion.

We used MC881 for the electro-optic measurements, which is an optically pure AFLC compound synthesized by Mitsui Gas company (Fig. 5.2). This material does not have SmC^* phase. The phase sequence is Iso. (120^oC) SmA (112.5^oC) Sm$C_A{}^*$. To check the direction of the **c** director in the intermediate unwound state, we measured the retardation with increasing field by using spectroscopy. The light transmitted through the cell placed in between the crossed polarizers as a function of the wavelength can be expressed as:

$$T = A\sin^2\left(\frac{\pi d\Delta n_{\text{eff}}}{\lambda}\right) + B, \quad where \tag{5.1}$$

$$\Delta n_{\text{eff}}(\lambda) = k\frac{\lambda^2\lambda^{*2}}{\lambda^2 - \lambda^{*2}}. \tag{5.2}$$

Here, A is a scaling factor that depends on the orientation of the optical axis of the cell with respect to the polarizer and the intensity of the light source, d is the cell thickness, λ is the wavelength of light, Δn_{eff} is the effective birefringence and B is an offset signal. Through a fitting of the transmittance spectra, it is possible to obtain the value of the birefringence as a function of the applied field. To ensure a proper fitting, we must consider the dependence of Δn_{eff} on wavelength. The extended Cauchy equation [95] was used for the fitting of the data on the transmitted intensity as a function of the wavelength. Fig. 5.3 shows an example of the spectroscopic experimental data and the fitting results using Eq. 5.2. Fig. 5.4 shows the apparent tilt angle and the birefringence as a function of the applied field. In the lower part of Fig. 5.4, the increasing retardation at low

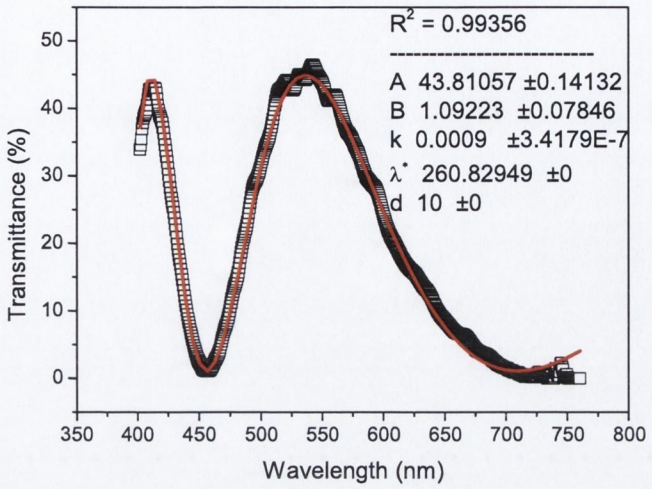

Figure 5.3: Spectroscopic data ($25\mu m$ planar cell, 40°C, 0V) and fitting result for birefringence.

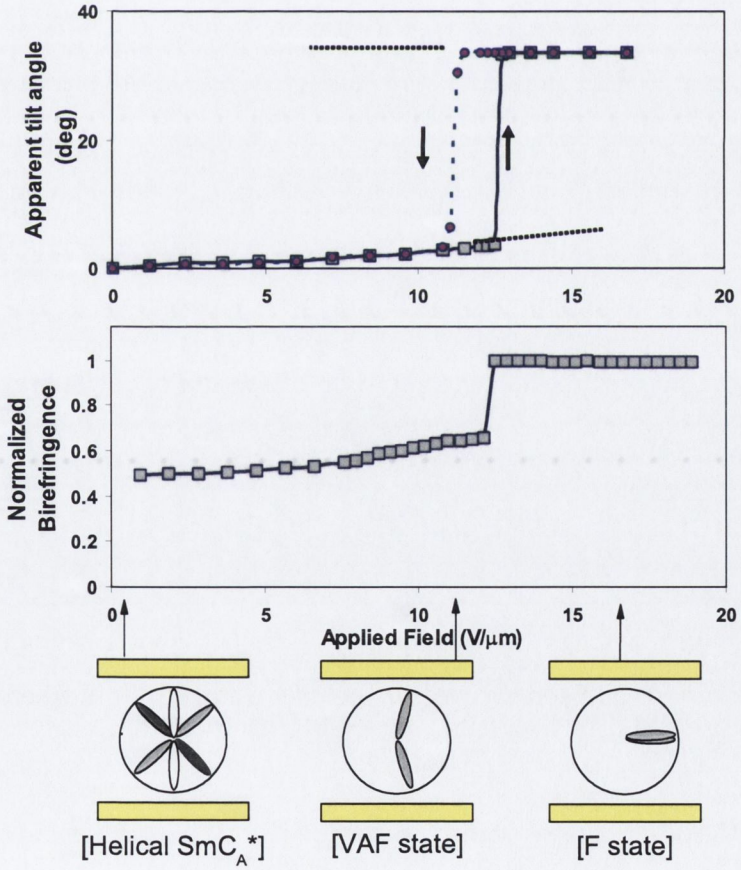

Figure 5.4: Apparent tilt angle (upper, $25\mu m$ planar cell) and retardation, Δnd (lower, $5\mu m$, planar cell) as a function of the applied field

voltages indicates that the **c** directors lie close to y axis, which is the VAF state shown in Fig. 5.2. The HAF state has a lower retardation than the virgin chiral antiferroelectric state. The increasing apparent tilt angle at low fields in Fig. 5.2 also leads to the same conclusion.

To model the solitary wave in the VAF state, we start with the free energy expression of an unwound helical limiting case. The free energy of ith layer can be written using the coordinate system and definitions of angles in Fig. 5.2 as

$$\begin{aligned} f_i &= \frac{K}{2} sin^2\theta (\frac{\partial \phi_i(x)}{\partial x})^2 - P_0 E cos\phi_i(x) - \frac{\Delta\epsilon'}{8\pi} sin^2\phi_i(x) E^2 + V(\Delta\phi(x)) \\ &\equiv \frac{K}{2} sin^2\theta (\frac{\partial \phi_i(x)}{\partial x})^2 + U(\phi_i(x), \Delta\phi(x)), \end{aligned} \tag{5.3}$$

Here, $V(\Delta\phi)$ is the interlayer interaction depending on the angle between the adjacent layers, and the effective dielectric anisotropy $\Delta\epsilon' = \Delta\epsilon sin^2\theta$. In Eq. 5.3, the first term of the equation is the elastic energy of the solitary wave, and the second and the third terms correspond to the coupling of the spontaneous polarization and the dielectric anisotropy with the applied field. The total potential energy $U(\phi_i(x), \Delta\phi(x))$ is defined as the sum of the interlayer interaction and the coupling with the applied field.

Corresponding to Eq. 5.3, the equation of motion of the solitary wave can be written as [74, 90]

$$I\frac{\partial^2\phi}{\partial t^2} + \gamma\frac{\partial\phi}{\partial t} - K'\frac{\partial^2\phi}{\partial x^2} = -\frac{dU(\phi_i, \Delta\phi)}{d\phi_i} \tag{5.4}$$

where I is the moment of inertia of a molecule and γ is the viscosity of the medium and $K' = Ksin^2\theta$. I can be neglected in the over-damped limit where γ is large, as is usually the case.

If only the dipolar interlayer interaction, ($V = V_0[cos(\phi_i - \phi_{i-1}) + cos(\phi_{i+1} - \phi_i)] = 2V_0 cos(2\phi)$) is considered as already assumed by Li *et al.* [74], the only

possible solitary wave solution of Eq. 5.4 can be found to be

$$\phi = 2tan^{-1}e^{d_1(x-v_1t)} \quad , \tag{5.5}$$

where $\phi \equiv \phi_i(x)$ and

$$d_1 = [-2(\frac{\Delta\epsilon'}{8\pi}E^2 + 2V_0)/K']^{\frac{1}{2}} \tag{5.6}$$

$$v_1 = \frac{PE}{\gamma d_1} \quad . \tag{5.7}$$

This solution does not correspond to the solitary wave for the AF-F transition usually observed in the AF cells, but does that of the transition from one F state to another F state at very large fields. Note that in the solitary wave solution [Eq. 5.5], directors change from $\phi = 0$ (for $x = -\infty$) to $\phi = \pi$ (for $x = +\infty$), that is, from $\Delta\phi = 0$ to $\Delta\phi = 2\pi$. To have a real value of d_1 in Eq. 5.6, the dielectric anisotropy should be nagative and the applied field, $E > 4\sqrt{-\pi V_0/\Delta\epsilon'}, (\sim 1.6 \times 10^3 statV/cm^{-1})$ $(> E_{th})$, which is quite a large field. Even though this solitary wave is physically possible, the moving speed (Eq. 5.7) is too fast to be observed in the usual microscopic experiment. Thus, with only the dipolar term present in the interlayer interaction, the solitary wave from the AF to F state cannot be attained irrespective of the sign of the dielectric anisotropy. This is due to the fact that the potential energy U is not a double well potential having the synclinic and the anticlinic minima. Note that the double well potential is required to obtain the solitary wave [90].

Now, we need to add the quadrupolar term in the interlayer interaction. The quadrupolar term was introduced in a phenomenological model of Landau expansion for AFLC by Orihara and Ishibashi [82], and an experimental evidence was suggested by Qian and Taylor [83] by observing the switching behavior in a AFLC cell. Link *et al.* [96] showed that even a pure achiral smectic-C liquid crystal has a double well potential energy having a synclinic minimum at a lower energy than an anticlinic minimum. Thus, it is reasonable to add the quadrupolar

term in the interlayer interactions.

$$\begin{aligned} V &= V_0(1+cos\Delta\phi) + V_0 b(1-cos2\Delta\phi) \\ &= V_0(1+cos2\phi_i) + V_0 b(1-cos4\phi_i) \end{aligned} \tag{5.8}$$

Here, the quadrupolar coefficient b is related to the relative depth of the synclinic minimum compared with that of the anticlinic minimum. The equation of motion (Eq. 5.4) can be rewritten as

$$\gamma\frac{\partial\phi}{\partial t} - K'\frac{\partial^2\phi}{\partial x^2} = -PEsin\phi + \Big(\frac{\Delta\epsilon'}{8\pi}E^2 + 2V_0\Big)sin2\phi - 4V_0 b sin4\phi \tag{5.9}$$

Here, I is ignored. Unfortunately, it is not easy to find the exact solution of this differential equation, but is obtained as an approximate solution of Eq. 5.9 as

$$\phi(x) \approx \frac{2}{\pi}\phi_0 tan^{-1}e^{d(x-vt)} \quad , \tag{5.10}$$

where ϕ_0 is the angle ϕ for $x \to \infty$, where the cell has the antiferroelectric domain, hence $2\phi_0 = \phi_{i+1} - \phi_i$. ϕ_0 depends on the applied field E, and $\delta\phi = \pi/2 - \phi_0$. Eq. 5.10 is plotted in the lower part of Fig. 5.1, where the **c** directors are highly distorted at the solitary wave and produces the high potential barrier, U, at the same position. The high energy barrier sustains the strong elastic restoring force by the distorted **c** directors. With a slight difference between the potential energies in F and AF states, the solitary wall moves and the F state enlarges with a consequential reduction in the size of the other state. Eq. 5.10 is the solution for ith layer and adjacent layer has an opposite sign of the angle of the **c** directors as seen in Figs. 5.1 and 5.2, so $\phi_{odd}(x) = -\phi_{even}(x)$. Here, we can find that the solitary wave in a layer is coupled with that of the adjacent layer, i.e., the solitary wave could propagate normal to the layer plane, though the speed is much slower than that along the x direction. On the other hand, in the conventional model [74], only the odd layers are supposed to have the solitary waves, and the even layers stay and act as obstacles to prevent the solitary wave propagation normal to the layers, and as a consequence, the solitary wave in each layer is independent of the

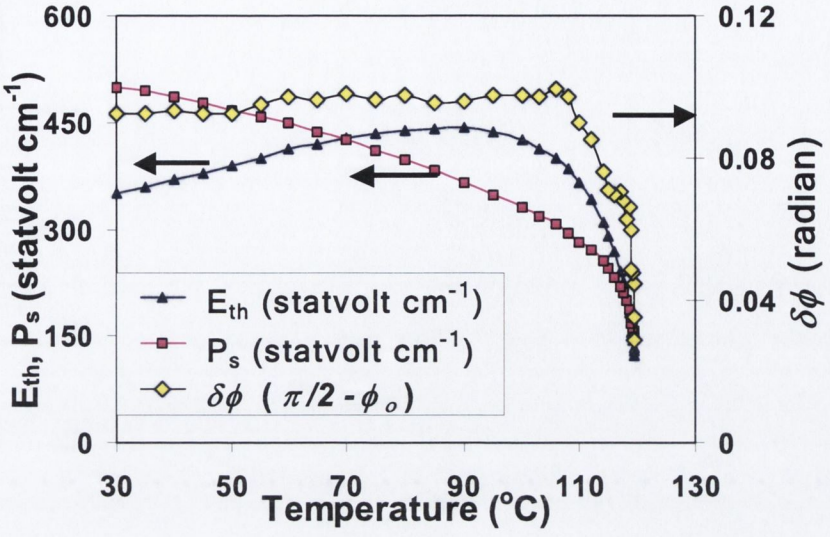

Figure 5.5: Measured P_s, E_{th} and $\delta\phi$ ($25\mu m$ planar cell)

others. Usually, the solitary wave has a finger-like shape and builds up as a bundle of rays, the width of which is more than several thousand times the thickness of a single layer and becomes thicker with time. The special shape of the solitary wave can be explained by the proposed model as a coupling between the solitary waves in the adjacent layers.

The necessary condition for the differential Eq. 5.9 to have a real solution can be found by analyzing the total potential energy U. To have the solitary wave, $\partial U/\partial\phi = 0$ and $\partial^2 U/\partial\phi^2 > 0$ should be satisfied at $\phi = \phi_0$ (anticlinic minimum) and 0 (synclinic minimum). This is the same condition for having the first order transition between the AF and the field induced F states, and the details were already studied by Qian and Taylor [83]. By ignoring the dielectric anisotropic term, we can find that when $b > 1/20$, the potential energy U has a double well potential near the critical field (E_{th}) and the cell could exhibit a solitary wave, and when $b > 1/4$, the potential energy U has a double well potential even at the zero field. Thus, the solitary wave does not originate from the dielectric anisotropy, but does from the quadruloar term of the interlayer interaction.

From the condition $\partial U/\partial\phi = 0$ at $\phi = \phi_0$, we can find $\delta\phi(= \pi/2 - \phi_0) \ll 1$:

$$\delta\phi \approx \frac{PE}{4V_0(4b+1) + \frac{\Delta\epsilon'}{4\pi}E^2} \tag{5.11}$$

Since $\Delta\epsilon'/(4\pi)E^2$ is smaller than $4V_0(4b+1)$, $\delta\phi$ related to the apparent tilt angle increases linearly with the applied field according to Eq. 5.11, which accords well with the experimental results shown in Fig. (see also 5.4).

When the applied field = E_{th}, where the solitary wave velocity is zero, the potential energy at the two minima should be equal to each other.

$$U(E = E_{th}, \phi = 0) = U(E = E_{th}, \phi = \phi_0') \tag{5.12}$$

By using $\partial U/\partial\phi = 0$ at the two minima and Eq. 5.12, we can find b, V_0 and E_{th}.

$$V_0 = \frac{3\cos\phi_0' + 2}{4(\cos\phi_0' + 1)^2} PE_{th} - \frac{\Delta\epsilon'}{16\pi}E_{th}^2, \tag{5.13}$$

$$b = \frac{PE_{th}}{16V_0\cos\phi_0'(\cos\phi_0' + 1)^2}, \tag{5.14}$$

$$E_{th} = \frac{16V_0 b\cos\phi_0'(\cos\phi_0' + 1)^2}{P}, \tag{5.15}$$

where $\phi_0' = \phi_0(E = E_{th}$. ϕ_0' can be obtained by $\phi_0' = \cos^{-1}(\tan\theta'/\tan\theta)$, where θ' is the apparent tilt angle at E_{th} and θ is the tilt angle of the director from the layer normal.

Fig. 5.5 shows the measured values of P_S, E_{th} and $\delta\phi(E = E_{th})$ using a planar cell of 25 μm thickness. Using both homeotropically and planar-aligned cells, we measured $\Delta\epsilon \simeq -0.7$ in SmC_A* phase. The upper graph in Fig. 5.6 gives calculated V_0 and b from the measured results. It shows that V_0 increases with decreasing temperature and is saturated at low temperatures. Meanwhile, the quadrupole coefficient b is almost constant over a wide range of temperatures and increases dramatically near the transition temperature to SmA. This means that the synclinic minimum gets closer to the anticlinic minimum as the temperature

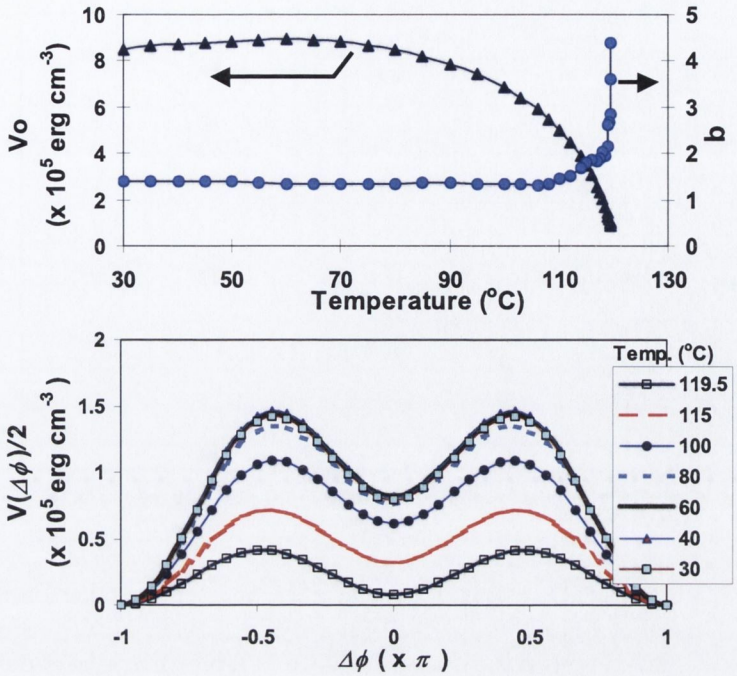

Figure 5.6: Calculated V_0 and b (upper graph), and interlayer interaction energy as a function of $\Delta\phi$ (lower graph).

approaches the transition temperature even though the barrier potential between them remains reasonably high as shown in the lower part of Fig. 5.6.

By putting the approximate solution Eq. 5.10 into the differential Eq. 5.9 and using the measured values of V_0, b, we can find the velocity (v) and the width parameter (d) of the solitary wave as function of the applied field as shown in Fig. 5.7. Here, v and d are determined by fitting two equations in both sides of Eq. 5.9, and the coefficient of determination, R^2 for the fitting at each electric field is higher than 0.999, which means that Eq. 5.10 is quite an accurate approximation for the solution of the differential equation. In this simulation, we assumed that $K = 10^{-6}$ dyne and $\gamma = 5.0$ poise so as to match the simulation results with the experimental results. The velocity of the solitary wave shows a linear dependence as function of the applied field near E_{th}.

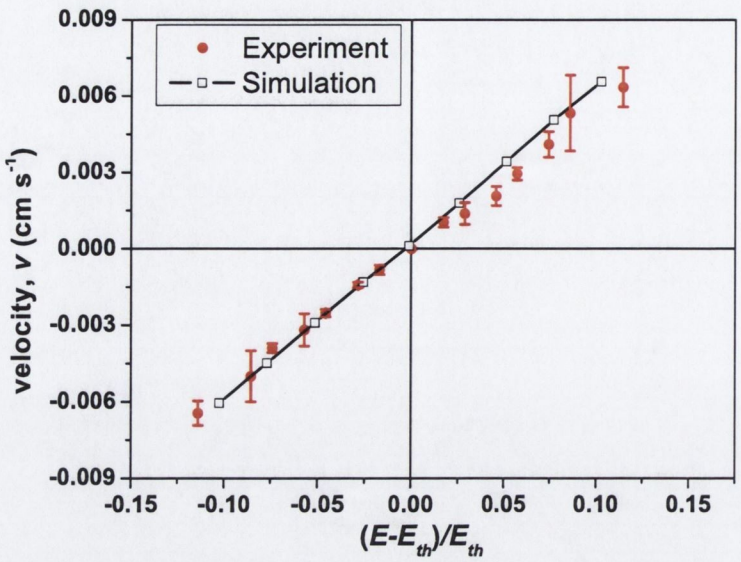

Figure 5.7: Measured velocity of the solitary wave and simulation result by using Eqs. 5.9 and 5.10 ($25\mu m$ planar cell, $50°C$). Simulation parameter: $\gamma = 5$ poise, $K = 10^{-6}$ dyne. Error bars denote the standard deviation over ten measurements for each data point.

5.3 Conclusion

The conventional model [74] for the solitary wave in the switching of the SmC_A^* to SmC^* states explains well the basic mechanism for the solitary wave propagation in the AFLC cells, but due to its over simplified nature, it gives several incorrect conclusions: the solitary wave is due to the negative dielectric anisotropy, and the pretransitional effect cannot be explained, and the solitary wave in each layer is separated from the neighboring one.

Our model based on the transition from the VAF to the unwound ferroelectric state can reasonably explain all of the observations: the solitary wave is due to the quadrupolar term in the interlayer interaction but is not related with the sign of the dielectric anisotropy, and the pretransitinal effect always exists, and the solitary wave of each layer affects the neighboring layers and can propagate normal to the layers. The solitary wave builds up like a bundle of rays giving it the shape of a finger as observed, which can be explained in our model.

We predict the generation of a new type of a solitary wave due to a negative dielectric anisotropy when a very large square shaped field is applied, even though its detection may not be easy. We calculate, V_0, and the quadrupolar coefficient, b, of the interlayer interaction in a pure AFLC. Surprisingly, the results show that even the pure AFLC not having SmC^* phase has a deep synclinic minimum since the quadrupolar coefficient $b \simeq 1.37$ is almost the same ($b \simeq 1.34$) for a commercial AFLC mixture (Chisso, CS4001) having SmC^* phase [86]. Moreover b, increases exponentially near the transition. This means that the antiferroelectric coupling becomes weaker near the transition temperature to the SmA phase.

Chapter 6

Dynamic Mechanism of SmC_A*–SmC* Phase Transition due to Solitary Wave Propagation.

"In this chapter, *the temperature induced solitary waves is reported, and the mechanism of the SmC_A*–SmC* Phase Transition is investigated based on the non-homogeneous model based on the solitary wave propagation.* "

6.1 SmC_A*–SmC* Phase Transition and the interlayer interactions.

Liquid crystals have played an important role in clarifying the various aspects of phase transitions in condensed matter physics due to the existence of a variety of phases. In this Letter, we report an important characteristic feature of

the temperature-induced phase transition between the SmC_A^* and SmC^* phases for the first time and also clarify the nature of the phase transition. We observe the temperature-induced solitary wave propagation that brings about the SmC_A^*–SmC^* phase transition and find from the observations that SmC^* free energy minimum persists in the entire SmC_A^* temperature range. At the same time significant supercooling is not observed at the transition. Based on the knowledge that the established tilted smectic structure almost completely suppresses the azimuthal-angular thermal motion of liquid crystalline molecules, it is simply expected that the free energy barrier hinders the transition from the local SmC^* minimum to the global SmC_A^* minimum even below the critical temperature. As actually observed here, however, the elastically coupled liquid crystalline molecular motions overcome the free energy barrier by forming propagating solitary waves [90].

Tilted smectic phases have a multi-layered structure that usually consists of a number of single-molecular layers. The average molecular direction in a layer, *i.e.* the in-layer director, is slanted from the layer normal by the tilt angle θ, which is constant over all layers, and is represented as $\mathbf{n}_i = (n_{ix}, n_{iy}, n_{iz}) = (\sin\theta\cos\varphi_i, \sin\theta\sin\varphi_i, \cos\theta)$ for the i-th layer in the coordinate system shown in Fig. 6.1. The azimuthal angle difference, ϕ ($\equiv \varphi_{i+1} - \varphi_i$), between the two neighboring layers can be either synclinic (*i.e.* $\phi \sim 0$) or anticlinic (*i.e.* $\phi \sim \pi$) as in ferroelectric SmC^* and antiferroelectric SmC_A^* in chiral smectic liquid crystals [8, 10]. Hence, the transitions between these phases occur through a change of ϕ between $\phi \sim 0$ and $\phi \sim \pi$. The phase transitions between the tilted smectic phases have been explained using various phenomenological models, most of which are based on Landau-de Gennes theory. The first phenomenological model regarding the SmC_A^*–SmC^* phase transition was suggested by Orihara and Ishibashi [82]. They introduced a modified director vector, $\xi_i = (-n_{iy}n_{iz}, n_{ix}n_{iz}) = \sin\theta\cos\theta(-\sin\varphi_i, \cos\varphi_i)$, and chose $\xi_s = (\xi_i + \xi_{i+1})/2$ and $\xi_a = (\xi_i - \xi_{i+1})/2$ for the order parameters in the Landau-de Gennes theory. Here, ξ_s and ξ_a are maximized at the synclinic and the anticlinic orderings, respectively. They allowed the variation of θ as well as of φ from layer to layer, but the variation of θ has been ruled out by the successive experimental observations [97]. Consequently, the free

energy suggested by Orihara *et al.* simply becomes a function of ϕ ($\equiv \varphi_{i+1} - \varphi_i$) at a fixed temperature as

$$\begin{aligned} f &= \alpha_a\xi_a^2 + \alpha_s\xi_s^2 + \beta_a\xi_a^4 + \beta_s\xi_s^4 + \gamma\xi_a^2\xi_s^2 \\ &= A(\alpha_s + \alpha_a) + (A^2/2)(3\beta_s + 3\beta_a + \gamma) \\ &\quad +\{A(\alpha_s - \alpha_a) + 2A^2(\beta_s - \beta_a)\}\cos\phi \\ &\quad +(A^2/2)(\beta_s + \beta_a - \gamma)\cos 2\phi \\ &\equiv C + D\cos\phi - Q\cos 2\phi, \end{aligned} \tag{6.1}$$

where $A(\equiv \{\sin^2(2\theta)\}/8)$, C, D and Q are constants at a fixed temperature. Thus, the free energy for the SmC_A^*–SmC^* phase transition can be expressed as the interlayer interaction energy between the neighboring layers consisting of the dipolar ($\propto \cos\phi$) and the quadrupolar ($\propto \cos 2\phi$) terms. This is naturally expected from the nature of the transitions between SmC_A^* and SmC^* described in the introductory paragraph. Recent phenomenological models basically include these terms, and these are added to other terms [50, 65, 98, 99]. In fact, this interlayer interaction energy form has been suggested intuitively, and used in analyzing the electric-field-induced SmC_A^*–SmC^* switching [83, 84, 100], though not used for explaining the phase transition.

Figure 6.1 shows a comparison of the two methods: (a) the weakly first order transition described by Landau-de Gennes theory and (b) the interlayer interaction described by Eq. (6.1). The free energy difference Δ and the barrier height H between the SmC_A^* and SmC^* minima illustrated in Fig. 6.1 are calculated by using Eq. (6.1),

$$\Delta = 2D, \; H = \frac{D^2}{8Q} + 2Q + |D| \tag{6.2}$$

Recently, we devised and reported a new method for determining D and Q experimentally in the antiferroelectric cell [84]. During the field-induced switching in the antiferroelectric cell, the solitary wave propagates as Li *et al.* [74] actually observed and Song *et al.* modeled appropriately [84]. The model allows us to

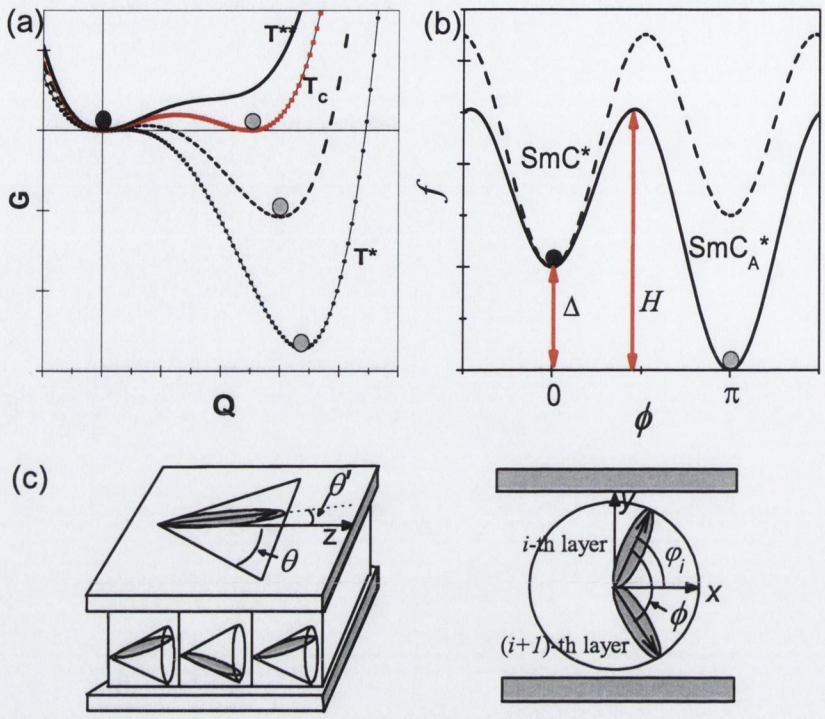

Figure 6.1: (a) The Landau-de Gennes free energy G as a function of the order parameter Q at different temperatures. (b) The free energy f as a function of the relative angle between the adjacent layers ϕ in SmC_A* (solid line) and in SmC* (dashed line). (c) Schematics of a planar antiferroelectric cell, where the triangle on top of glass is the projection of the smectic cone. The apparent tilt angle, θ', under an application of electric fields is distinguished from the phase tilt angle θ, where the molecules are aligned vertically. [84, 100]

measure D and Q. Here, the method is briefly explained. The free energy of a cell having a solitary wave propagating along the x axis under the application of an electric field E can be obtained by adding the elastic energy of the soliton and the coupling energy of the spontaneous polarization P_s with E into Eq. (6.1) as

$$f' = K' \left(\frac{\partial \varphi_i}{\partial x} \right)^2 - P_s E \cos\phi + D \cos\phi \qquad (6.3)$$
$$-Q \cos 2\phi + C \equiv K' \left(\frac{\partial \varphi_i}{\partial x} \right)^2 + U(\phi),$$

where the effective elastic coefficient $K' = K \sin^2(\theta)/2$, and the total potential energy $U(\phi)$ is the sum of the interlayer interaction and the electric coupling energy. The first and second terms represent elastic and electric coupling energies,

respectively. The kinetics of the soliton is governed by the total potential energy U. To have the solitary wave, U should have two energy minima, where $\phi = 0$ for the synclinic minimum and $\phi \approx \pi$ for the anticlinic minimum. At the threshold field, $E_{\rm th}$, the solitary wave has a zero velocity, and the potential energy at the two minima becomes the same. Hence,

$$U(E = E_{\rm th}, \phi = 0) = U(E = E_{\rm th}, \phi = \phi_{\rm th}) \tag{6.4}$$

$$\left(\frac{\partial U}{\partial \phi}\right)_{\phi=0} = \left(\frac{\partial U}{\partial \phi}\right)_{\phi=\phi_{\rm th}} = 0 \tag{6.5}$$

where $\phi_{\rm th}$ is the value of ϕ at $E = E_{\rm th}$. From Eqs. (6.4) and (6.5), we can find that

$$D = \frac{3\cos(\phi_{\rm th}/2) + 2}{4\left\{\cos(\phi_{\rm th}/2) + 1\right\}^2} P_{\rm s} E_{\rm th} \tag{6.6}$$

$$Q = \frac{1}{16\cos(\phi_{\rm th}/2)\left\{\cos(\phi_{\rm th}/2) + 1\right\}^2} P_{\rm s} E_{\rm th} \,. \tag{6.7}$$

We can determine $\phi_{\rm th} = \pi - 2\sin^{-1}(\tan\theta'/\tan\theta)$ by measuring the apparent tilt angle θ' at $E_{\rm th}$ and the phase tilt angle θ shown in Fig. 6.1. Hence, D and Q are determined experimentally.

6.2 Experiments and discussion.

The compounds used are MC-813 and MC-881 synthesized by Mitsubishi Gas Chemical Company, Inc. (MGC) [51]. The phase sequence of MC-813 is Cry. (38°C) SmC_A^* (73°C) SmC^* (81°C) SmA (85°C) I. Having a wide temperature range of SmC_A^* and SmC^*, MC-813 is particularly suited for demonstrating the phenomenon under consideration. For comparison, MC-881 ((b) in Fig. 6.2) is used, the phase sequence of which is SmC_A^* (112.5°C) SmA (120°C) Iso. MC-881 does not exhibit SmC^* and hence the SmC_A^*-SmC^* phase transition; it is suitable for drawing a comparison with MC-813.

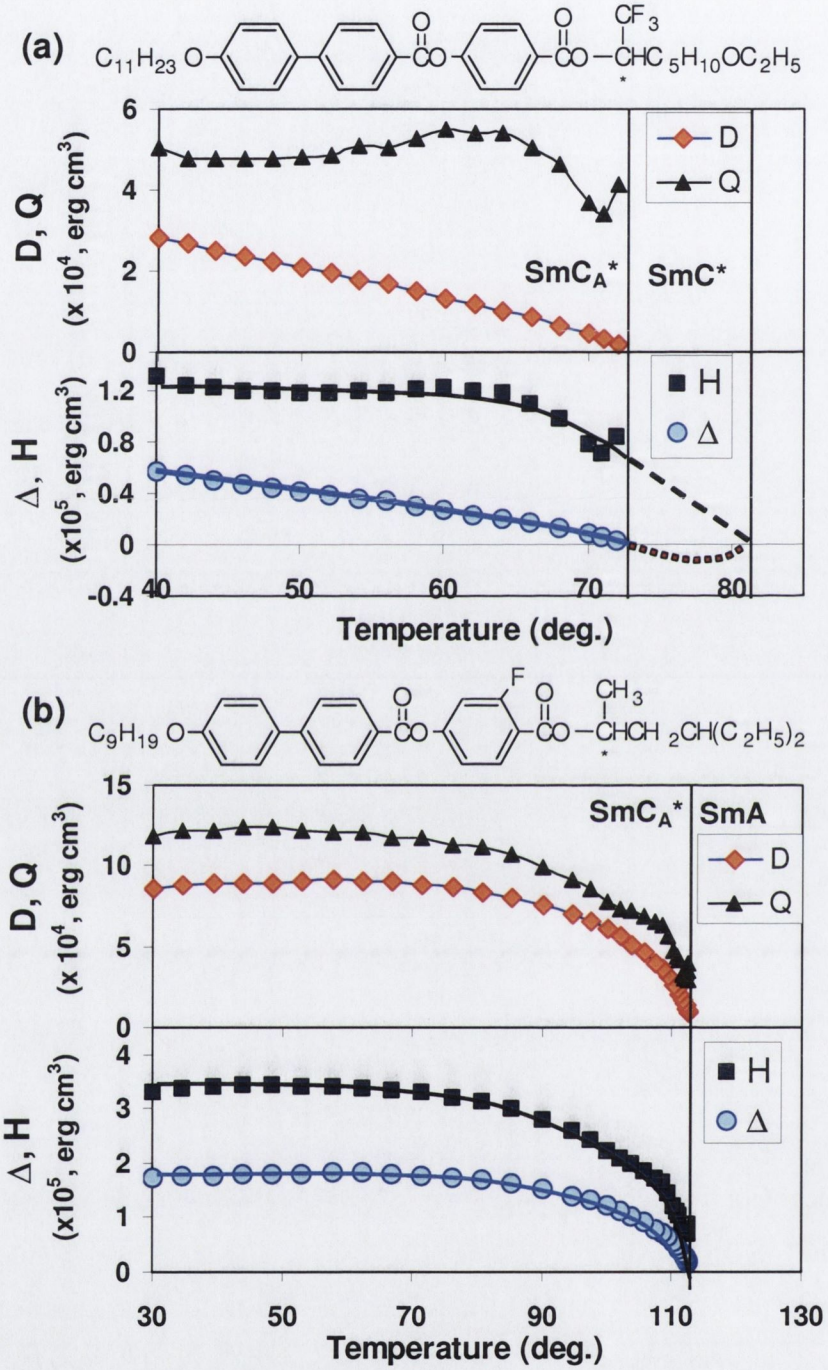

Figure 6.2: Experimental results; (a) MC-813 and (b) MC-881. D and Q are plotted in upper part of each compound and Δ and H are plotted in lower part of each compound. The experimental data of MC881 are taken from reference [84].

Figure 6.2 shows D, Q, Δ and H calculated from P_s, E_{th}, θ and θ'. These were measured in a homogeneously aligned 25 μm thick cell for MC-813 and data for MC881 were taken from our previous paper [84]. The parameters D, Q, Δ and H must become zero at the phase transition temperature to SmA as is actually confirmed in MC-881 and anticipated by extrapolation (the dashed and dotted lines of Fig. 6.2(a)) in MC-813. This is not clear in MC-813 where we could not obtain Δ and H in SmC^*. However, simple extrapolation indicates that Δ varies gradually and changes its sign at the SmC_A^*–SmC^* transition temperature, which is the same behavior as in the Landau-de Gennes theory for the weakly first order phase transition. On the other hand, H has large positive value over the entire temperature range of smectic-C phases, which exhibits a striking contrast to the weakly first phase transition frequently encountered in liquid crystals and treated by the Landau-de Gennes theory [2, 101], where we define two additional characteristic temperatures T^* and T^{**} close to the critical temperature T_c as shown in Fig. 6.1. On cooling, T^* is the limit of metastability of the high temperature phase; its free energy still shows a local minimum though it is not a global minimum for $T^* < T < T_c$. The limit of metastability of the low temperature phase occurs at T^{**} where the secondary minimum disappears on heating. The obtained large H implies that the free energy has always two minima separated by the barrier H in the entire temperature range of SmC_A^* and SmC^*. The free energy does not have T^* and T^{**} illustrated in Fig. 6.1 under the Landau-de Gennes theory for the first order phase transition. Hence, very large supercooling and superheating could be expected, or SmC_A* may not appear at all due to the high energy barrier between the synclinic and the anticlinic minima while cooling. However, the supercooling or superheating observed at the SmC_A^*–SmC^* phase transition is actually less than a few degrees if the effects due to the substrate interfaces are minimized.

A fundamental question arises: How does the phase transition overcome the free energy barrier between the two states, and why is the supercooling or superheating not large? The solitary wave propagation [90], which is a consecutive transition of one state to another state as dominoes, can give a clue for answering

the question. The solitary wave in itself is quite an interesting physical phenomenon. This is a solution of a non-linear equation, with a property that energy is transmitted in a localized way, and occurs in diverse phenomena in physics such as in ocean as Tsunami, string theory as D-branes, and biology where these occur as Davidoff solution for modeling ATP. In liquid crystals, the solitary waves were observed in the nematic-SmA transition [102] and in the switching of the surface stabilized ferroelectric liquid crystal cell [103] and in the switching of the SmC_A^* cell [74].

Likewise, in the temperature-induced phase transition under consideration where Δ varies gradually to zero and H remains still large, the temperature-induced solitary wave propagation is naturally expected. To explain the solitary wave, we start from Eq. (6.3) by inserting $E = 0$, because we are considering the intrinsic phase transition but not the field induced switching. The corresponding Euler-Lagrange equation for the solitary wave is written as [84, 90]

$$\gamma \frac{\partial \phi}{\partial t} - K' \frac{\partial^2 \phi}{\partial x^2} = -\frac{dU(\phi)}{d\phi} = D \sin \phi - 2Q \sin 2\phi \ . \tag{6.8}$$

The physically interesting solution of Eq. (6.8) is

$$\phi(x) = \tan^{-1} e^{-(x-vt)/d} \ , \quad \text{where} \tag{6.9}$$

$$d = \frac{1}{4}\sqrt{\frac{K'}{Q}} \simeq \frac{1}{2\sqrt{2}}\sqrt{\frac{K'}{H}} \tag{6.10}$$

$$v = \frac{4dD}{\gamma} = \frac{2d\Delta}{\gamma} \simeq \frac{s_0}{\sqrt{2}\gamma}\sqrt{\frac{K'}{H}}(T_c - T) \ , \tag{6.11}$$

where γ is the viscosity of the medium, d and v are the width and the speed of the solitary wave. Here we use linear approximation for Δ near T_c so that $\Delta \simeq s_0(T_c - T)$, where s_0 is the slope of Δ. The width of the solitary wave is inversely proportional to $\sqrt{H}$; the velocity of the solitary wave, also inversely proportional to $\sqrt{H}$, is proportional to $T_c - T$ and hence changes its sign at the phase transition temperature.

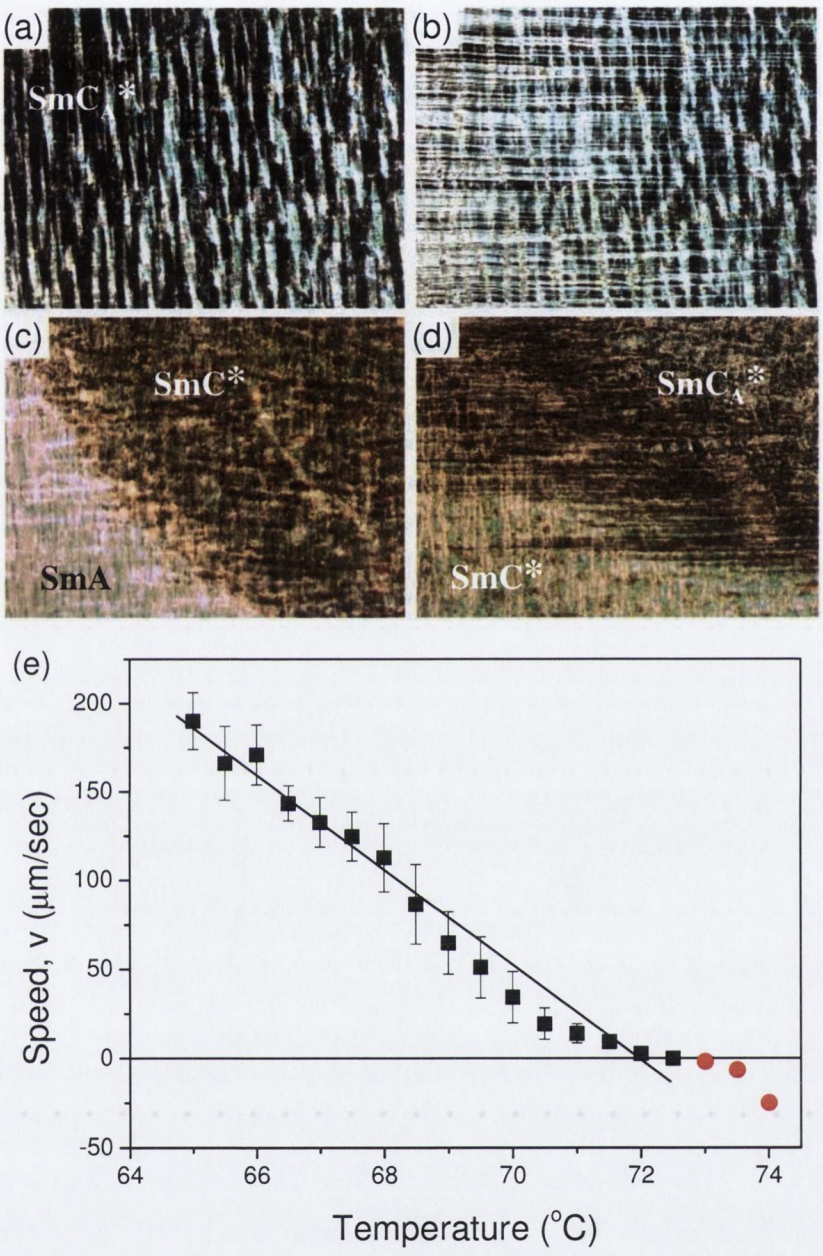

Figure 6.3: Microscopic images in an isothermal cell ((a), (b)) and in a temperature gradient cell ((c), (d)) under two polarizers, the angle between which was selected for the best images to distingush . (a) image was taken immediately after heating the cell slightly higher than T_c and (b) image was taken after about 10 seconds. (c) and (d) were taken at the SmC*-SmA transition and the AF-F transition respectively, where temperature difference between left bottom to right top is about 1.3°C. (e) is the velocity of the solitary wave as function of temperature.

For observations of the solitary wave, we made a 25 μm thick homogeneously aligned (planar) cell of MC-813. This large cell thickness avoids the excessive surface effect from the alignment layer. Fig. 6.3 (a) and (b) show the temperature induced solitary waves, which are observed for the first time as the temperature-induced SmC_A^*–SmC^* phase transition. The cell was kept at 71°C while in SmC_A^*. Then we increased the temperature to 73.5°C, which is slightly higher than T_c. When the temperature reaches this value, the first image (a) in Fig. 6.3 is taken, where it is still at SmC_A^*. The solitary waves, which consist of a number of lines parallel to the layer plane, start to propagate as shown in Fig. 6.3(b). The solitary waves propagate in the reverse direction when the temperature is decreased below the transition temperature, as expected from Eq. (6.11). Next, we made a temperature gradient cell by inserting a thin insulator between the heater and one of the sides of the cell. The temperature difference across the two edges in the microscopic images is found to be ~1.3°C. As shown in Fig. 6.3 (a) and (b), the boundary of SmA–SmC^* transition gives a good accord with the isothermal lines. However, the boundary of the SmC_A^*–SmC^* transition runs zigzag, which is of similar shape observed in the electric-field-induced solitary wave [74, 84]. The measured velocity of the solitary wave is given in Fig. 6.3(e). For $T < T_c$, velocity is measured at zero field by first inducing the SmC^* domain by applying the field, and then turning it off. However, for $T > T_c$, neither the SmC_A^* domain nor the domain walls can be obtained. Therefore, by heating the cell quickly from just below to slightly above T_c, the velocity of the domain wall is measured. As shown in Fig. 6.3, the measured velocity of the solitary wave shows rather linear dependence with temperature. The slight mismatch near the phase transition temperature may be caused by the frictional effect of surfaces, which is beyond our discussion here and remains to be clarified in future work.

To summarize, we experimentally obtain the free energy difference Δ and the barrier height H between SmC_A^* and SmC^* minima. It is of double well shape in the entire range of temperatures of the SmC_A^* phase, which is a surprising and interesting phenomenon. The transition occurs only through a non-homogeneous

process, *i.e.* the solitary wave propagation overcomes the high free energy barrier. The mechanism is applicable not only for the SmC_A^*–SmC^* transition but may also be applicable for the phase transitions between all the smectic C variant phases [50]. It means that the intrinsic phase transitions between these phases are actually strong first order transitions, but the propagating solitary waves make these transitions to have the properties of weakly first order. We observe the propagating solitary waves through a microscope, and measure the speed as a function of temperature. Basically, the solitary wave can arise from defects or imperfect boundaries. Therefore, if we make a cell that satisfies the perfect condition of no imperfections, we may observe very large supercooling and may even cool down the cell to the crystalline phase without observing SmC_A^*. We can also explain a strong dependence of the phase transition temperature on the cell thickness.

Chapter 7

Solitary Wave Propagation in Surface Stabilized Ferroelectric Liquid Crystal Cells.

"In this chapter, *the solitary wave propagation in SSFLC cells caused by the surface anchoring of alignment layers is investigated for different conditions of alignment on the two opposite surfaces. It is reported that The polar anchoring energy difference (Δw_p) between the alignment layers can be calculated by measuring E_c, and Δw_p depends on the rubbing condition and on the material of the alignment layer.* "

7.1 Introduction to the solitary wave in SSFLC cells.

Nematic liquid crystal displays (LCDs) have revolutionized the display industry. However these displays suffer from major drawbacks such as: the poor

image quality of fast moving objects due to slow response time and their limited viewing angle. Ferroelectric liquid crystals (FLCs), which respond by an interaction of the electric field with the spontaneous polarization (P_s), are reported to overcome the slow response time as well as the problem of limited viewing angle. A surface stabilized ferroelectric liquid crystal [48, 104] cell has been one of the most promising methods in display applications using FLCs.

In SSFLC cells, usually two types of domains appear: up/down domains, where the polarization is directing upwards/downwards as shown in Fig. 7.2, or twisted domains where the polarization is twisted along the cell thickness direction. The boundaries of these domains move on the application of the electric field as shown in Fig. 7.2. The boundary movement is a solitary wave. The solitary wave in a SSFLC cell is not only an interesting phenomenon scientifically, but it also plays an important role in the switching property, a key factor that determines its applications. The solitary wave in a SSFLC cell was observed and studied by Handschy *et. al.* [103, 104] for the first time, and was investigated in detail using computer simulations by Maclennan *et. al.* [105], and it was suggested [106] that this can be used to improve the switching property in a SSFLC cell by determining the factors that control its propagation.

As shown in chapter 8, we can find a solitary wave in the electric-field induced antiferroelectric-ferroelectric (AF-F) switching in the SmC^*_A cells [34]. This is basically quite similar to the solitary waves in a SSFLC cell because the solitary waves in these cells are actually the elastically connected liquid crystal molecular motions. This induces a transition from one to the other state or domain. However, the behavior and the mechanisms are rather different. As reported in our previous paper, the solitary wave in the AF-F switching is caused by the interlayer interaction between the smectic layers. On the other hand, in SSFLC cells, the surface anchoring by the alignment layers is the origin of the solitary wave as are the appearance of the various domains. Hence, the surface condition is an essential part of the solitary wave in SSFLC cells, which, however, has rarely been studied so far.

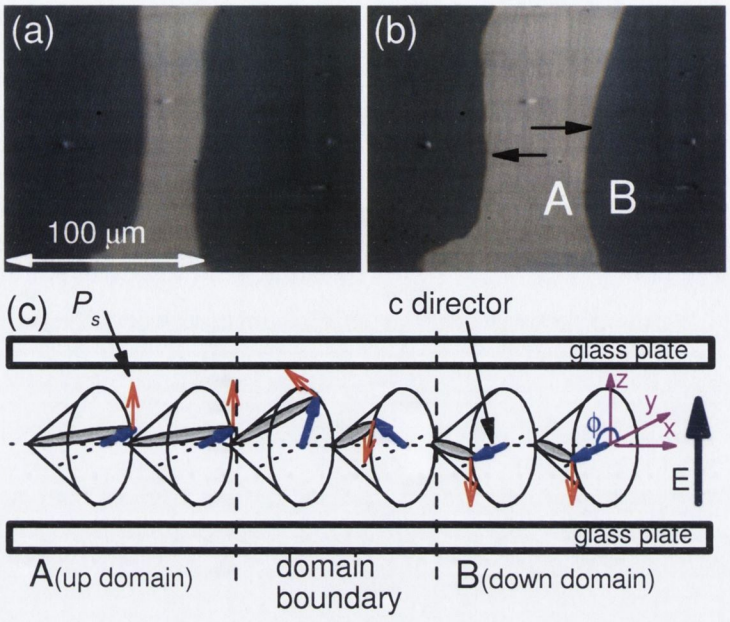

Figure 7.1: Microscopy for the solitary wave in a SSFLC; (b) picture was taken 3 seconds after taking (a), the schematics for the solitary wave and up/down domains and boundary (c). The directors can move on a cone, which is the necessary condition that the layer thickness does not change during switching. Smectic layers are perpendicular to glass plates.

In this chapter, we characterize the solitary wave in a SSFLC cell under the various surface conditions including asymmetric alignment layers. The asymmetric alignment structures in liquid crystal cells are intentionally designed to produce better alignment [107] or to have special cell structures using the hybrid alignment technique [71]. These also happen to appear as an unintentional side-effect caused by the different surface conditions for the two plates such as in TFT LCD (Thin Film Transistor Liquid Crystal Display), where a TFT circuit embedded on one plate and a color filter on the other make the surface morphology rather different.

7.2 Model for the solitary waves in SSFLC cells.

Handschy *et.al.* [103, 104] characterized the solitary wave in SSFLC cells theoretically including the director distortions varying along the cell thickness direction and also along the cell plate direction. However, a simplification in the

director distribution could make the calculation easier, and allow us to investigate the various aspects of the propagating solitary wave itself.

Here, we assume that the director is uniform along the thickness direction, which is usually assumed in the up and down domains of SSFLC cells by neglecting a slight distortion near the surfaces, and we only consider the distortion of the director along the direction parallel to the glass plate, which simplifies the solitary wave to be a one-dimensional problem. First, we will consider the surface anchoring energy per unit surface area usually written as [108]

$$\begin{aligned} W &= w_0 + (-w_{p1}\cos\phi_1 + w_{p2}\cos\phi_2) \\ &\quad -(w_{n1}\cos^2\phi_1 + w_{n2}\cos^2\phi_2), \end{aligned} \tag{7.1}$$

where ϕ is the azimuthal angle of the $\mathbf{c}$ director at surfaces, and w_0, w_p and w_n are ϕ independent, ϕ dependent polar and non-polar coefficients of anchoring energy respectively. Note that $w_p \propto \cos\phi$ since it distinguishes the direction of polarization, while $w_n \propto \cos^2\phi$ since it only concerns the relative angle of the director from the surface. The subscribes 1 and 2 represent the two surfaces. As we assume that the director is uniform along the cell thickness, $\phi_1 = \phi_2 \equiv \phi$ in the up/down domains, and the anchoring energy is reduced as

$$\begin{aligned} W(\phi) &= w_0 + (w_{p2} - w_{p1})\cos\phi - (w_{n1} + w_{n2})\cos^2\phi \\ &\equiv w_0 + \Delta w_p \cos\phi - 2\bar{w}_n \cos^2\phi, \end{aligned} \tag{7.2}$$

where $\Delta w_p \equiv (w_{p2} - w_{p1})$ is the polar anchoring energy difference between the two surfaces, and $\bar{w}_n \equiv (w_{n1} + w_{n2})/2$ is the average non-polar anchoring energy.

Therefore, the free energy can be expressed as

$$\begin{aligned} F &= \int \left[K' \left(\frac{\partial \phi(x)}{\partial x} \right)^2 - P_s E \cos \phi(x) \right] dV + \int W(\phi) dA \\ &= \int \left[K' \left(\frac{\partial \phi(x)}{\partial x} \right)^2 - P_s E \cos \phi(x) + \frac{W(\phi(x))}{l} \right] dV \\ &\equiv \int \left[K' \left(\frac{\partial \phi(x)}{\partial x} \right)^2 + U(\phi(x)) \right] dV, \end{aligned} \tag{7.3}$$

where $U(\phi(x)) \equiv w_0/l - (P_s E - \Delta w_p/l)\cos\phi - 2\bar{w}_n/l \cos^2\phi$, and the effective elastic coefficent $K' \equiv K \sin^2 \theta/2$, and l is cell thickness. The first term in Eq. 7.3 is the elastic distortion energy of the solitary wave, the second term is the coupling energy of the polarization with the field and the last term is the anchoring energy.

Corresponding to Eq. 7.3, the equation of motion of the solitary wave can be written as [74, 90, 91]

$$\gamma \frac{\partial \phi}{\partial t} - K' \frac{\partial^2 \phi}{\partial x^2} = -\frac{dU(\phi)}{d\phi} \tag{7.4}$$

where γ is the viscosity of the medium.

The solitary wave solution of Eq. 7.4 can be found to be

$$\phi(x) = 2tan^{-1} e^{(x-vt)/d}, \text{ where} \tag{7.5}$$

$$d = \frac{1}{2}\sqrt{\frac{K'l}{\bar{w}_n}} \tag{7.6}$$

$$v = \left(E - \frac{\Delta w_p}{l P_s} \right) \frac{P_s}{2\gamma} \sqrt{\frac{K'l}{\bar{w}_n}} \, . \tag{7.7}$$

Here d and v represent the width and the speed of the solitary wave, respectively. Thus, the critical field E_c, where the speed of the solitary wave becomes zero, can be expressed as

$$E_c = \Delta w_p/(l P_s). \tag{7.8}$$

Table 7.1: Surface conditions for each cells, and experimentally obtained Δw_p; For the strong rubbing condition, the surface was rubbed 4 times with the same rubbing strength as the weak rubbing process.

Code.	Surface 1	Surface 2	Δw_p (J/m^2)
SR-SR	strong rubbing	strong rubbing	0
SR-WR	strong rubbing	weak rubbing	2.64×10^{-5}
SR-NR	strong rubbing	no rubbing	3.80×10^{-5}
SR-ITO	strong rubbing	no alignment layer	4.38×10^{-5}

E_c is zero when $w_{p1} = w_{p2}$, but is not zero under the asymmetric alignment condition.

7.3 Experimental results and discussion.

For the observations of the solitary wave, FLC mixture, Felix0018 synthesized by HOECHST AG Company was used. 2 μm thickness cells using two indium tin oxide (ITO) glass plates coated with RN-1175 (Nissan Chemical Co.) were prepared. The surfaces of the alignment layer were rubbed with a commercial rubbing machine (EHC Co. Ltd., RM-50), and four types of cells as shown in Table 7.1 were prepared.

For the AF-F switching, the antiferroelectric SmC^*_A state is stable at low fields and the ferroelectric state is stable at high fields. Since both states are independent of the sign of the applied field, the speed (v') of the solitary wave corresponding to the domain moving between the two states depends on the absolute value of the applied field $|E|$, hence $v'(E) = v'(-E)$. On the application of rectangular shape ac field, the domain boundary does not oscillate but moves with a constant velocity. On the other hand, the solitary wave occurring at the boundary of the up and the down domains in the SSFLC cell depends on the sign of the applied field, because the directions of P_s in both domains are opposite and P_s favors aligning parallel to the applied field. One domain enlarges at the expense of a reduction in the size of the second domain for positive fields, but the domain size reduces for negative fields. Hence, on the application of the rectangular shape

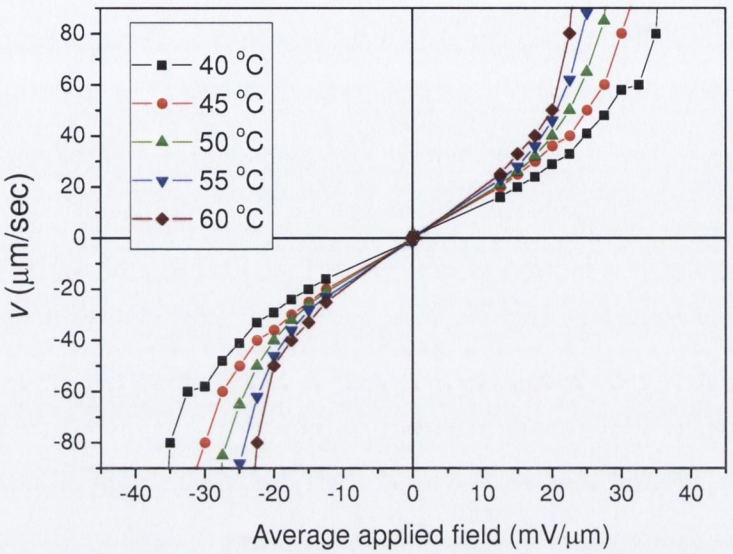

Figure 7.2: The velocity of the solitary wave for a cell (SR-SR) having symmetric alignment layer at various temperatures.

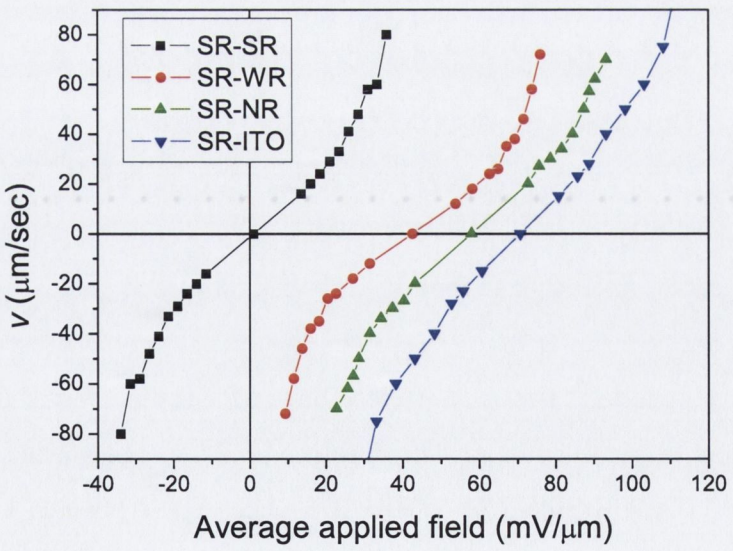

Figure 7.3: The velocity of the solitary wave for various conditions of the alignment layers.

ac field, the domain boundary oscillates corresponding to the applied field. Therefore, a dc field can better be used to observe the domain movement. When a dc electric field is applied to the cell, the boundaries of the domains propagate along one direction, but the speed of solitary wave decreases with time rather quickly. This is not an intrinsic property of the solitary wave, but is due to a reduction in the field across the cell. This is caused by the ionic impurities that accumulate close to the two surfaces. This problem is solved by applying a triangular-waveform of electric signal at 10 Hz having a dc off-set voltage. The domain boundaries oscillated as the applied field, and the off-set voltage was controlled to keep the average velocity of the boundary motion to be zero. The off-set field, where the average velocity of the solitary wave becomes zero, is actually E_c. This is measured just after the voltage is applied to avoid problem due to the accumulation of ionic impurities close to the surfaces of the cell. The off-set voltage increases with time as the ionic impurities accumulate. A trivial calculation shows that the velocity of the solitary wave = (width of the oscillating boundary) $\times$ $2f$, where f is the frequency of the ac part of the applied field.

The velocity (v) of the solitary wave in a usual SSFLC cell having symmetric alignment layers (SR-SR cell in Table 7.1) was measured for different temperatures as shown in Fig 7.2. v almost linearly increases with increasing field at low fields and diverges at large fields. At large fields, one state transfers to the second state simultaneously in the entire area, and v could therefore be not be measured. The behavior of the solitary wave for the cells having asymmetric alignment layers, also plotted in Fig. 7.3, are rather different. The critical electric field E_c is not zero in these cells, and E_c varies with the surface condition, which accords with Eq. 7.8 derived in our model. As Δw_p between the two layers increases, E_c increases, which can be confirmed by the measured values of E_c for these cells. The values of E_c are found that SR-SR < SR-WR < SR-NR < SR-NP, which accords with the intuitively expected order for the differences between the two surfaces. We can calculate the polar anchoring energy difference Δw_p from the experimental results by using Eq. 7.8. The values of the calculated Δw_p for each cell are listed in Table 7.1.

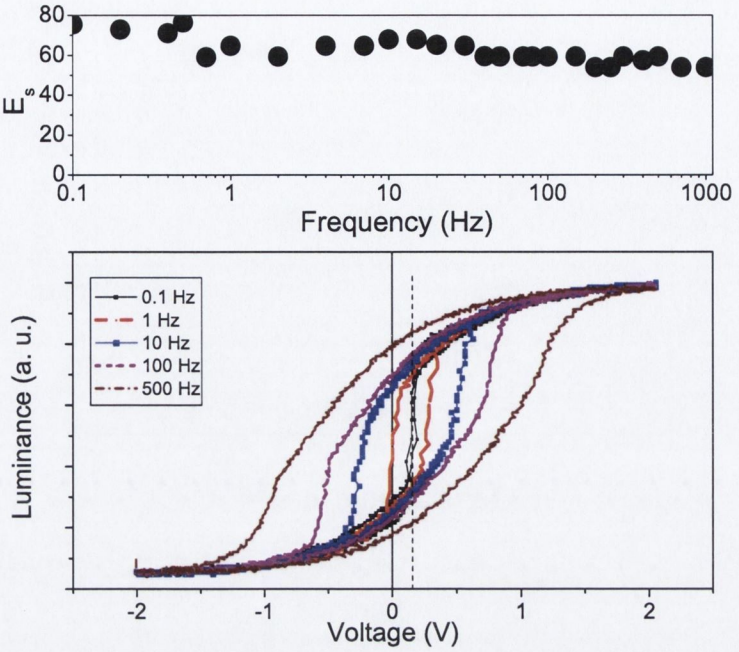

Figure 7.4: Optical transmittance vs. applied field under the cross polarizers (lower part), where the angles of the cell with polarizers are controlled to have the symmetric luminance curve, and the E_s as a function of the frequency of the applied field.

E_c varies considerably when measured at different points of the cells. For example, E_c in SR-NR cell was observed varying from 70 mV to 110mV from point to point. This implies that the rubbing uniformity is not perfect for these cells. To find the average E_c over a wide area of the cell, we measured the optical transmittance with applying triangular wave form electric field under cross polarizers. As shown in Fig. 7.4, E_s, which is the field at the symmetric position of the hysteresis curve, shifts from zero. E_s is almost independent of the frequency of the applied field and shows only a slight decrease at large fields. Actually, the measured E_s was found to be almost the same as E_c obtained by observing the solitary wave. This can easily be understood. The free energies of both domains are the same at E_c, which is the usual property of the solitary wave, and the symmetric field E_s is actually the average transition field between the up and down domains, where the free energy of the up and down domains should be the same. We reasonably conclude that $E_c = E_s$.

We measured E_s, which is an average value over the observed area of a

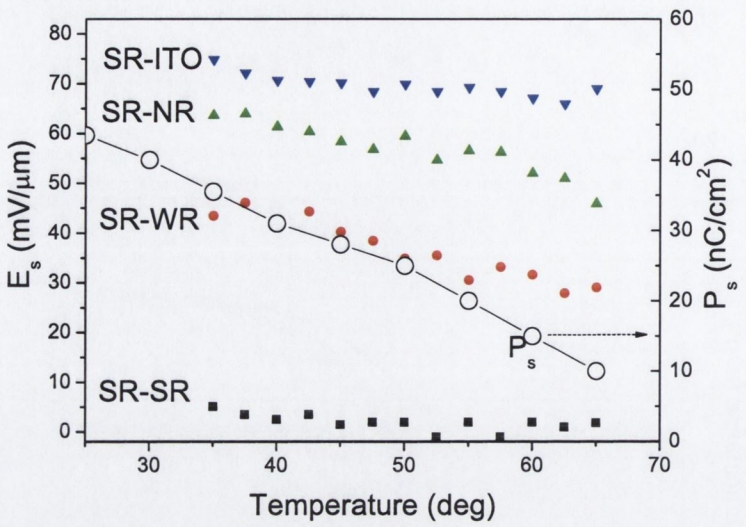

Figure 7.5: E_s as a function of temperature for the various conditions of alignment layer.

cell and has less error compared with E_c obtained through the observation on the solitary wave. As shown in Fig. 7.5, E_s is almost constant with temperature. This was confirmed by observing E_c as well (data not shown). This is a rather surprising result, because E_c is proportional to P_s, which keeps increasing with decreasing temperature as shown in Fig. 7.5 (open circle points). Note that $E_c \propto \Delta w_p / P_s$. To have constant E_c over a wide temperature range, Δw_p should also be proportional to P_s. This implies that the polar anchoring energy coefficient w_p actually depends on P_s, and the polar anchoring energy W_p can be expressed as $W_p \propto (\vec{P}_s \cdot \hat{s})$, where $\hat{s}$ is a unit vector normal to the surface of the plate.

We have modeled the solitary waves in SSFLC cells having asymmetric alignment layers, and carried out experiments, and these accord with the model. We showed that by observing the solitary wave in SSFLC cells, the polar anchoring energy difference can be obtained. We also found that the polar anchoring energy may also depend on P_s.

Part. IV

Interlayer interaction and The stability of The subphases.

Chapter 8

Cell thickness dependence of the stability of chiral smectic-C phases

"In this chapter, *a theory for describing the cell thickness dependence of the stability of chiral smectic-C phases is suggested. The theory accords well with the experimental results*[1]. "

8.1 Theory for the cell thickness dependent stability of the smectic-C^* phases

Since antiferroelectric liquid crystals was discovered in 1989 by Chandani *et al.*, many new physical findings including various subphases have been reported.

[1]The experiment was carried out by U. Manna, and the experimental data were analyzed by U. Manna and the author. Theory and model were given by the author.

One of the most interesting topics about these is that since the free energy differences among these smectic-C phases are rather small [109], transitions or frustrations between these phases have been expected, and also have been observed under various external effects such as electric fields, cell thickness, and mixing ratio in the binary mixtures [12, 55, 56, 86, 110–113]. In this chapter, the cell thickness dependencies of the stability for the various smectic phases are considered in detail.

The field of surface physics is evolving to include not only the study of surfaces of single crystals in vacuum but also of solid interfaces in contact with liquids, high pressure gases and other solids [114]. These interface systems turn up in a host of applications such as electrochemistry and bio-physics. It has been known that surfaces and the confinement affect the liquid crystalline properties. The liquid crystal devices exploit the phenomenon of alignment by the surfaces [17]. It is also known that phase transitions of chiral smectic liquid crystals are controlled by confinements effects [115–119] and by their alignment [120]. However the results on the temperature range of SmC* variant phases have not so far been obtained in a systematic manner as a function of the cell thickness and these have not been explained by a theory that determines the stability of these phases. We theoretically analyze the effect of surfaces on the stability of these phases by considering the contribution of the anchoring energy and the distortion energy of the bulk liquid crystals induced by the surfaces in order to clarify as to how the transition temperatures depend on the cell thickness and as to how the temperature range of the some of the phases decreases rapidly with decreasing cell thickness and finally some of the phases are not observed for low cell thicknesses. We present experimental data on the dependence of the temperature range of SmC* variant phases of a prototype LC that exhibits SmC* variant phases as a function of the cell thickness in the range 3 to 80 μm. Theoretical results are found to agree with the experiments.

According to a recent phenomenological model for the free energy expression for the various smectic C phases [14, 109], the free energy is expressed as

$$\begin{aligned} VF_b = \sum_{i=1}^{N} \Big[\tilde{F}_0(\theta) - \tilde{a}\frac{\Delta T}{T^*}(cos\varphi_{i-1,i} + cos\varphi_{i,i+1}) - \widetilde{B} \\ (cos^2\varphi_{i-1,i} + cos^2\varphi i, i+1) + \frac{1}{2\chi}\{\mathbf{P}_i^2 + g(\mathbf{P}_i\mathbf{P}_{i+1} \\ +\mathbf{P}_i\mathbf{P}_{i-1})\} + c_s(\mathbf{P}_i\xi_{i+1}) + c_f cos\theta(\mathbf{P}_i\Delta\mathbf{n}_{i\pm1})\Big], \end{aligned} \tag{8.1}$$

where F_b is the free energy per unit volume, V is the volume of summation, and the second term on the right side is temperature dependent while all other terms are temperature independent. T^* is the transition temperature between the synclinic and anticlinic smectic C phases in the absence of any intermediate phases. $\Delta T = T - T^*$. The physical meaning of the second and the third terms of this phenomenological expression can be easily understood, even though the original mechanism is not so simple. The c-directors between neighboring layers are likely to be in one plane by positive $\widehat{B}$, *i.e*, the synclinic or anticlinic orderings, and as temperature increases, the ferroelectric configuration is favored by positive $\widetilde{a}$. Emelyanenko and Osipov suggested that the other terms, which are related the discrete spontaneous polarization, induce the various subphases.

Eq. 8.1 can be rewritten as

$$\begin{aligned} F_b &= T < -\frac{\widetilde{a}}{T^*}(cos\varphi_{i-1,i} + cos\varphi_{i,i+1}) > + F_O \\ &\equiv AT + F_O, \text{ where} \\ A &\equiv -\frac{\widetilde{a}}{T^*} < (cos\varphi_{i-1,i} + cos\varphi_{i,i+1}) > \\ &\equiv -A_0 < (cos\varphi_{i-1,i} + cos\varphi_{i,i+1}) > \end{aligned} \tag{8.2}$$

Here, F_O denotes the sum of all the other terms in Eq. 8.1 and is independent of temperature and dependent on the structure, polarization etc. <> is the average per unit volume.

In the square shaped cell having area S and thickness d, the total free energy can be written as

$$\begin{aligned} F_T &= SdF_b + 2SF_s \\ F_T/Sd \equiv F_t &= F_b + 2F_s/d \end{aligned} \tag{8.3}$$

Here, F_s is the free energy induced by unit surface, which includes the anchoring energy and the distortion energy of bulk liquid crystals induced by the surface. Combining Eq. 8.2 and 8.3, we get

$$F_t = AT + F_O + 2F_s/d \tag{8.4}$$

Let us consider the phase transition between phases 1 and 2 having $q_T = q_1$ (lower temperature phase) and $q_T = q_2$ (higher temperature phase) respectively. At the bulk transition temperature T_c without surface effect, the bulk free energies of two phases are the same. Hence

$$A_{q1}T_c + F_{O,q1} = A_{q2}T_c + F_{O,q2} \tag{8.5}$$

New transition temperature, T considering the surface effect can be found as

$$\begin{aligned} &A_{q1}T + F_{O,q1} + 2F_{s,q1}/d \\ &= A_{q2}T + F_{O,q2} + 2F_{s,q2}/d \end{aligned} \tag{8.6}$$

From Eq. 8.5 and 8.6, we can determine the transition temperature depending on the surface effect, given by:

$$T = T_c - \frac{2(F_{s,q1} - F_{s,q2})}{d(A_{q1} - A_{q2})} = T_c - \frac{2\Delta F_{s,(q1,q2)}}{\Delta A_{q1,q2}} \frac{1}{d} \tag{8.7}$$

Thus, we see that the transition temperature is inversely proportional to the cell thickness, and its coefficient depends on the differences of the free energy (ΔA) and the surface energy (ΔF_s).

Eq. 8.7 is quite simple, but it gives a clear physical understanding about the thickness dependence of the transition temperature. The bulk transition temperature T_c is determined by Eq. 8.5, where F_O contains various complex interlayer interactions and varies according to models, and by using the measured T_c, we can avoid the rather controversial calculation process containing F_O. By assigning phase 1 as lower temperature phase, ΔA is always positive. Therefore, the sign of the coefficient of the last term in Eq. 8.7 is determined by ΔF_s. If ΔF_s is positive, that is, the surface energy of phase 1 is higher than that of phase 2, the transition temperature decreases with decreasing cell thickness. On the contrary, if ΔF_s is negative, that is, the surface energy of phase 1 is lower than that of phase 2, the transition temperature increases with decreasing cell thickness.

A can be found from Eq. 8.2 for the transitions among SmC^*, Sm$C^*_A(1/2)$, Sm$C^*_A(1/3)$ and SmC^*_A phases. However, for the transitions among SmA^*, SmC^*_α and SmC^*, the first term in Eq. 8.1 contributes to the phase transition dominantly. That is, near the SmA^*-SmC^* transition, the tilt angle θ changes sharply with temperature, and the free energy is mostly governed by the tilt angle dependent term. Note that usual Landau expansion for the second-order SmA^* to SmC^* transition is described as $F_{AC} = f_0 + a_0(T - T_{AC})\theta^2 + a_4\theta^4 + ...$ Thus, for the transitions among SmA^*, SmC^*_α and SmC^*, $A \equiv a_0\theta^2$. Here, a_0 is supposed to be much higher than A_0, because the energy difference between SmA^* and SmC^* is roughly 10^3 order higher than the energy difference between SmC^* and SmC^*_A [109]. Therefore, in Eq. 8.7, ΔA for the transitions among SmA^*, SmC^*_α and SmC^* is much higher than those among SmC^*, Sm$C^*_A(1/2)$, Sm$C^*_A(1/3)$ and SmC^*_A. This means that the transition temperature between SmA^*, SmC^*_α and SmC^* is insensitive to the cell thickness.

Now, we shall consider the surface energy. We assume that the phase transition occurs in all liquid crystals including surface area. This assumption seems

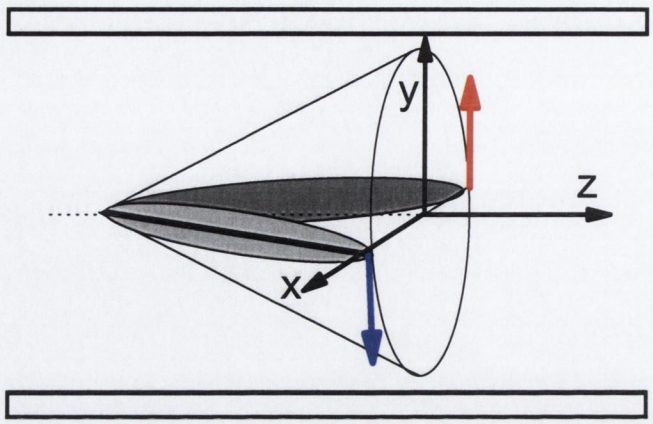

Figure 8.1: Cell Structure, φ is the angle between director and x axis. Spontaneous polarization directing downward is colored blue, and that directing upward is colored red. The same colors for the spontaneous polarization is used in Fig. 8.2.

reasonable, because the supercooling or superheating effect is observed usually and is stronger as the thickness decreases, implying that the supercooling is induced by the anchoring effect of the surfaces and the phase transitions occur close to the surface.

The surface energy induces a distortion in the bulk liquid crystals as well, which should be considered in determining F_s . So, F_s can be written as

$$\begin{aligned} F_s &= W_s + E_h + E_l \\ &= W_s + \frac{1}{S}\int \left[K_1 \left(\frac{d\overline{\varphi}}{dz} - \overline{\varphi}_0 \right)^2 + K_2 \left(\frac{d\overline{\varphi}}{dy} \right)^2 \right] dV, \end{aligned} \tag{8.8}$$

where W_s, E_l and E_h having the dimensions of energy per unit area are the surface anchoring energy, the inlayer distortion energy and the helical distortion energy, respectively. $\overline{\varphi}$ is the angle of the last layer of a single period in each phase, *i.e* $\overline{\varphi}$ is the angle of the every forth layer, the every third layer and the even layer in $\mathrm{Sm}C^*_A(1/2)$, $\mathrm{Sm}C^*_A(1/3)$ and $\mathrm{Sm}C^*_A$ phases respectively. For $\mathrm{Sm}C^*$, $\overline{\varphi} = \varphi$. $\overline{\varphi}_0$ is the wave vector ($= 2\pi/p$, where p =pitch). Thus, F_s can be separated to three different types of energy; surface anchoring energy W_s, the distortion energy of helix $d\overline{\varphi}/dz$ and the in-layer distortion along thickness direction $d\overline{\varphi}/dy$. These are actually coupled, and it is not so simple to estimate the total energy exactly. So,

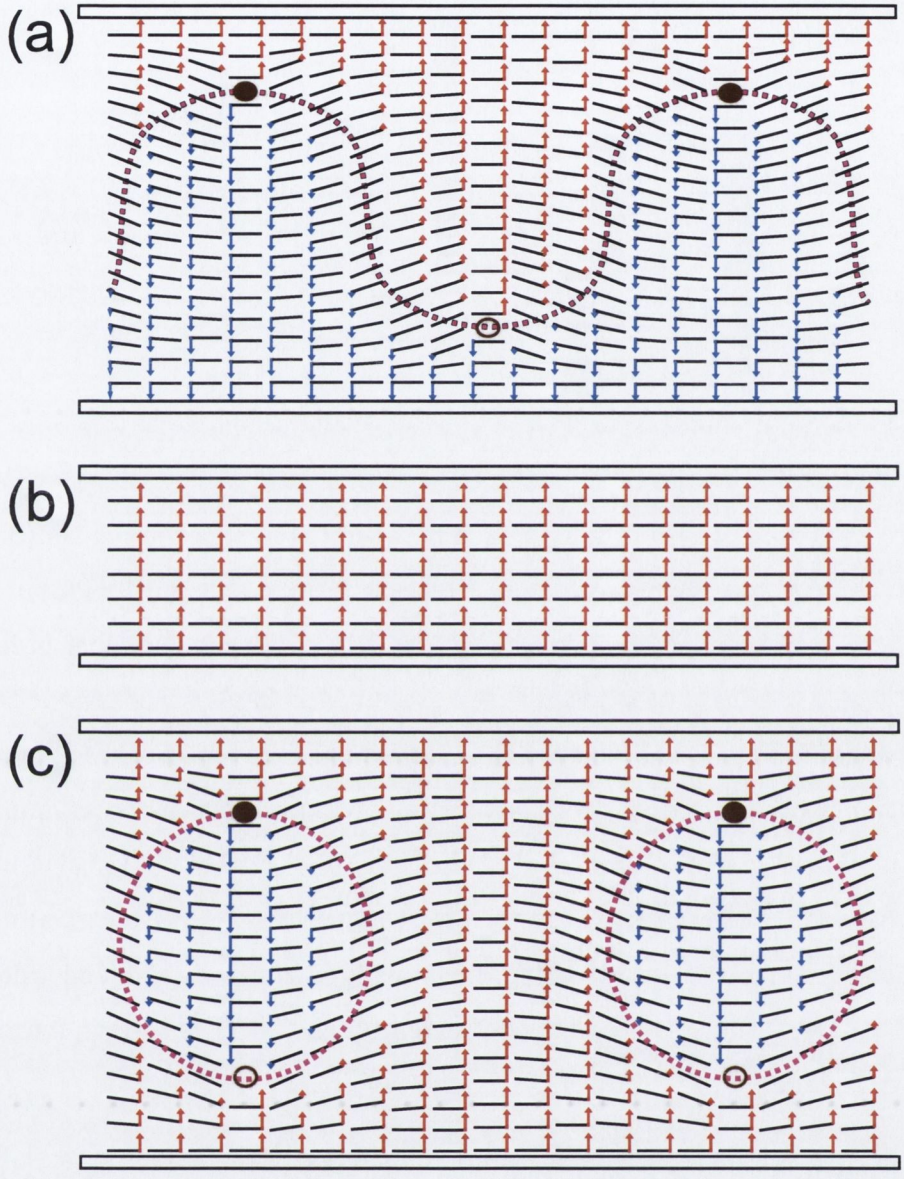

Figure 8.2: Schematic diagram for director distribution in smectic C phases. Red and blue arrows denote the spontaneous polarizations, the black lines are directors projected on the $y-z$ plane, purple dot lines denote the directors having $\overline{\varphi} = \pi/2$ or $-\pi/2$, and the black solid and open circles are the defect lines parallel to x axis. (a) is the director distribution for thick non-symmetric phases cell, where surface anchoring energy is minimized by forming symmetric alignment in both surfaces. (b) is for thin non-symmetric phases cell, where asymmetric alignment appears. (c) is for thick symmetric phases cell. For thin symmetric phases cell, the helical structure disappears in (c). This plot is based on the work by Brunet and Williams [121] and by Glogarova *et.al.* [122]

we need to simplify it.

The surface anchoring energy W_s can be written as

$$W_s = -w_1(cos\varphi_1 - cos\varphi_2) - w_2(cos^2\varphi_1 + cos^2\varphi_2), \tag{8.9}$$

where w_1, w_2 are the polar and the non-polar coefficients respectively, and φ_1, φ_2 are the angle at surface 1 and surface 2 respectively. When w_2 is sufficiently large, φ_1 and φ_2 should be 0 or π.

The director distribution in the cell is plotted schematically in Fig. 8.2, which is based on the work by Brunet and Williams [121] and by Glogarova *et.al.* [122]. We need to recognize the difference between the symmetric phases (SmC^*_A and SmC$^*_A$(1/2)) and the non-symmetric phases (SmC^* and SmC$^*_A$(1/3)). The symmetric phases such as SmC^*_A and SmC$^*_A$(1/2) have the same number of layers for $\varphi = 0$ and for $\varphi = \pi$, while the non-symmetric phases such as SmC^* and SmC$^*_A$(1/3) phase have a different number of layers for $\varphi = 0$ and for $\varphi = \pi$. This means that the residual spontaneous polarization exists in the asymmetric phases, and it is canceled out in the symmetric phases. Therefore,in the symmetric phases, the polar anchoring energy is not affected by whether $\overline{\varphi} = 0$ or π, but in the non-symmetric phases, the polar anchoring energy strongly depends on whether $\overline{\varphi} = 0$ or π. Thus, the $\overline{\varphi}$ is determined differently whether it is the symmetric or asymmetric phase.

We shall consider firstly the asymmetric phases (SmC^* and SmC$^*_A$(1/3)). The in-layer distortion energy is approximately $E_l \sim K_1(\overline{\varphi}_1 - \overline{\varphi}_2)^2/d^2 \times Sd/S = K_1(\overline{\varphi}_1 - \overline{\varphi}_2)^2/d$, when the distortion along y axis is uniform. Since it is inversely proportional to the cell thickness d, when the thickness is large, the in-layer distortion energy is rather small, and the minimum F_s is determined by minimizing W_s. To minimize W_s, the asymmetric alignment state as shown in Fig. 8.2 (a) should be obtained, that is, $\overline{\varphi}_1 - \overline{\varphi}_2 = \pi$. Therefore, the in-layer distortion energy can be expressed as $E_l \sim K_1\pi^2/d$ for thick cells. On the other hand, when the thickness is low, the in-layer distortion increases, and the minimum energy is determined to have minimum inlayer distortion energy. The minimum inlayer distortion energy

is obtained in the uniform states, where $\overline{\varphi}_1$ is the same as $\overline{\varphi}_2$ as shown in Fig. 8.2 (b), and $E_l \sim 0$ for thin cells. Thus, for the asymmetric phases, there exists a critical thickness ($d_{c,qT}$), at which the liquid crystal distribution transit from Fig. 8.2 (a) to (b) state. At the critical thickness ($d_{c,qT}$), the inlayer distorting energy is the same as the polar anchoring energy differences between the twist state and the uniform state. The anchoring energy difference of SmC^* is $2w_1$, and that of SmC_A(1/3) is $2/3w_1$. Therefore,

$$\begin{aligned} \text{for Sm}C^* : \quad & E_l = \pi^2 K_2/d, && \text{when } d > d_{c,1}, \\ & E_l = 0 && \text{when } d \leqq d_{c,1}, \qquad (8.10) \\ & d_{c,1} = \pi^2 K_2/(2w_1), \end{aligned}$$

$$\begin{aligned} \text{for Sm}C_A^*(1/3) : \quad & E_l = \pi^2 K_2/d, && \text{when } d > d_{c,1/3}, \\ & E_l = 0 && \text{when } d \leqq d_{c,1/3}, \qquad (8.11) \\ & d_{c,1/3} = 3\pi^2 K_2/(2w_1), \end{aligned}$$

Thus, the critical thickness of SmC_A(1/3) is around three times thicker than that of SmC^*.

Now, we will consider the helical deformation energy, which is also linked with the inlayer deformation energy, and contains defect lines as shown in 8.2 (a) and (c). The complexity of the deformation of the directors makes it difficult to calculate the helical deformation energy E_h directly. However, we can obtain E_h approximately by using a few assumptions. When the cell is thin, the inlayer distortion energy is too large to sustain the helical structure, hence the helical structures disappear and a uniform state is obtained. In the uniform state, the helical distortion energy becomes $E_h \sim K_1 d\overline{\varphi}_0^2$ per unit cell area from Eq. 8.8. As the cell thickness increase, an deformed helical structure appears from the center area and enlarges with increasing cell thickness. From this states, the helical distorting energy may not increase with increasing cell thickness, since the helical structure in the center area has zero helical distortion energy. Therefore, the helical distortion energy in large cell thickness can be expressed as $E_h \sim K_1 d_h \overline{\varphi}_0^2$,

Table 8.1: A and F_s for lower temperature smectic C phases.

	A	F_s(Thin cell)	F_s(Thick cell)
SmC^*	$-2A_0$	$-2w_2 + K_1\overline{\varphi}_{0,1}^2 d$	$-2(w_1+w_2) + d_h K_1 \overline{\varphi}_{0,1}^2 + \pi^2 K_2/d$
Sm$C_A^*(1/2)$	0	$-2w_2 + K_1\overline{\varphi}_{0,1/2}^2 d$	$-2w_2 + d_h K_1 \overline{\varphi}_{0,1/2}^2$
Sm$C_A^*(1/3)$	$2/3A_0$	$-2w_2 + K_1\overline{\varphi}_{0,1/3}^2 d$	$-2(w_1/3+w_2) + d_h K_1 \overline{\varphi}_{0,1/3}^2 + \pi^2 K_2/d$
SmC_A^*	$2A_0$	$-2w_2 + K_1\overline{\varphi}_{0,0}^2 d$	$-2w_2 + d_h K_1 \overline{\varphi}_{0,0}^2$

Table 8.2: A and F_s for higher temperature smectic C phases. the values in ()s is approximated ones for simulation.

	A	F_s
SmA^*	0	$-2w_2$
SmC_α^*	$a_0\theta_\alpha^2 (\approx 1000A_0)$	$-2(w_1+w_2) + d_h K_1 \overline{\varphi}_{0,\alpha}^2 + \pi^2 K_2/d$
SmC^*	$a_0\theta_{ferro}^2 (\approx 1300A_0)$	$-2(w_1+w_2) + d_h K_1 \overline{\varphi}_{0,1}^2 + \pi^2 K_2/d$

where d_h is another critical cell thickness indicating the change from the non-helical structure to the helical structure.

For the symmetric phases, W_s does not depend on the direction of $\overline{\varphi}$, so the minimum energy state is determined to have a minimum inlayer distortion energy in all thickness range as shown in Fig. 8.2 (c). Therefore, the inlayer distortion energy is ignored. A and F_s for lower temperature smectic C phases are listed in Table 8.1.

Usually, the typical domains of surface stabilized ferroelectric state, up and down domains appears around 2 to 4μm thickness in SmC^*. So, we shall assume that the critical thickness of SmC^* and Sm$C_A(1/3)$ are 3μm and 9μm respectively. For SmC_α^* phase, $\overline{\varphi}_{0,\alpha}$ is very large, so the F_s is mostly governed by $\overline{\varphi}_{0,\alpha}$. The period of a pitch in SmC_α^* is just a few layers, while that in SmC^* is around a few 100 layers. We shall assume that F_s of the SmC_α^* phase is around 50 times of F_s of SmC^* for simulation. And a_0 is assumed to be 1000 times higher than A_0 based on the simple free energy comparison in reference [109]. Based this model, we can summarize A and F_s as shown in Table 8.1 and 8.2.

Fig. 8.3 represents the simulation result under the condition: $w_1/A_0 = 7 \times 10^7 m$. Here, we need to mention that this simulation is for understanding the qualitative behavior of the stability of various smectic C phases in the function

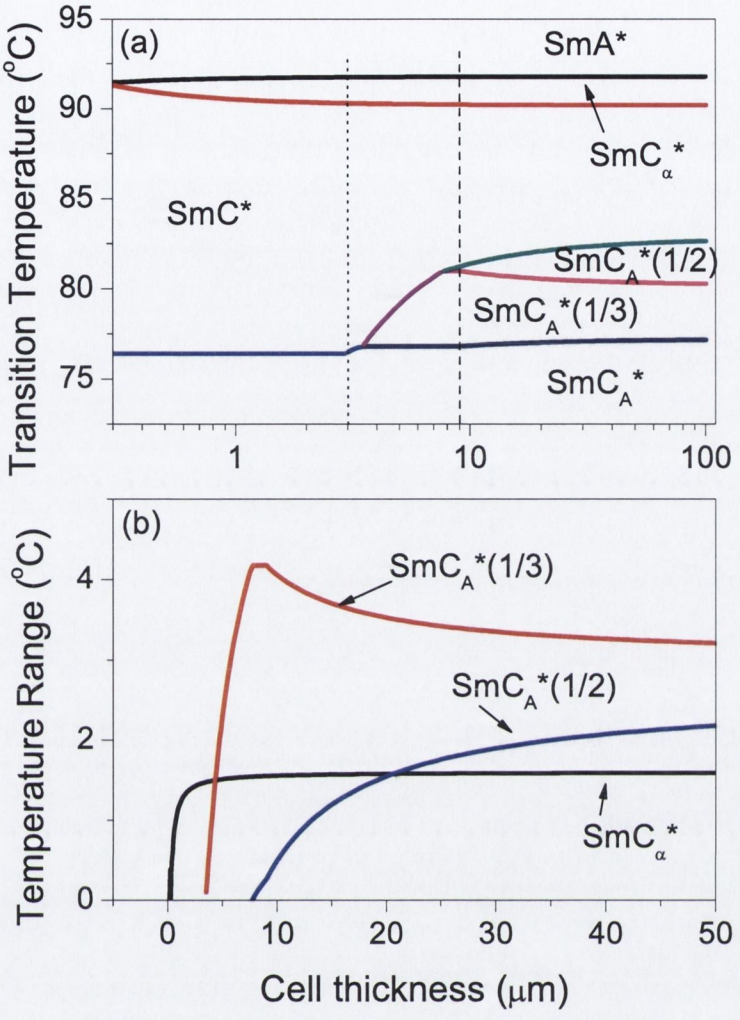

Figure 8.3: Example of simulation; Thick lines are the transition temperature.

of thickness, but it is not adequate to determine the accurate transition temperature because significant simplification has been taken during calculating F_s, and A is just phenomenological coefficient and not exactly calculated or measured one. However, the simulation results are in good agreement with the experimental results considering the significant simplification. A different factor between the experiment and the theory is that the experiment was carried out by cooling the sample and the data contains the super-cooling effect, while the theory is based on the actual transition temperature not considering the super-cooling effect. Therefore, as the thickness of cell becomes thinner, the experimentally measured transition temperature becomes lower due to the super-cooling effect.

From the simulation, we can find a few important points: *i)* $SmC^*_A(1/3)$ is more stable than $SmC^*_A(1/2)$ under the surface effect. This is due to that $SmC^*_A(1/2)$ has the highest anchoring energy among neighboring phases. *ii)* The instability is mostly due to the polar anchoring energy. *iii)* The SmC_α is rather stable, though the surface energy of that is high, and the transition temperatures between higher temperature phases are rather insensible by the surface effect. This is due to the temperature dependent coefficient of the free energy is high. *iv)* The temperature range of $SmC^*_A(1/3)$ is rather constant up to the thickness $SmC^*_A(1/2)$ exists. Once $SmC^*_A(1/2)$ disappears, the temperature range of $SmC^*_A(1/3)$ decreases rapidly with decreasing thickness. This is not so obvious in experimental results, but similar two step stability is perceived.

8.2 Comparison between experimental and simulation results.

The compound 12OF1M7, which has also been named as AS-573 was extensively studied so far to investigate the ferrielectric subphases with high q_T parameter [81], the relaxation processes in antiferroelectric liquid crystals [78], and the field-induced phase transitions in an antiferroelectric liquid crystal [123]. The existence of the SmC^*_α phase in 12OF1M7 was confirmed using dielectric, pyroelectric [124] and optical reflectivity measurement [57].

We present a more systematic, and precise experimental data[2] of the dependence of the stability of the smectic-C phases on different cell thickness varying from 3 μm to 80 μm. To find the phase transition tempeatrues, dielectric response for each cell thickness was measured and analyzed in detail.

Fig. 8.4$(a-b)$ shows the experimental results of the dependence of the transition temperature of the phases and of temperature range for which the Sm-C_α*, Sm-C_A*$(1/2)$ and Sm-C_A*$(1/3)$ phases are stable on the cell thickness varying from

[2]This experiment was done by U. Manna.

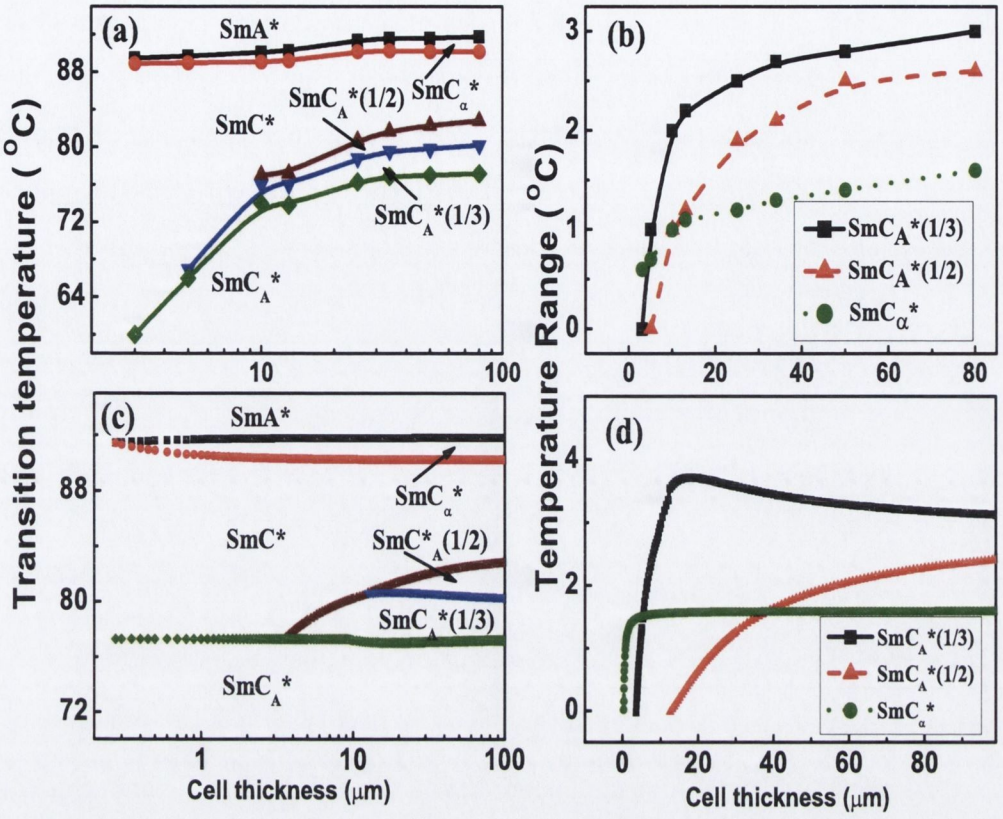

Figure 8.4: Comparison of experimental (a,b) and simulation results (c,d). The dependence of the (*a*) transition temperature of the phases and (*b*) temperature range for which the Sm-C_α*, Sm-C_A*(1/2) and Sm-C_A*(1/3) phases are stable on cell thickness varying from 3 to 80 μm. $(c-d)$ The simulation result under the condition: w_1/A_0=1.05 $\times$ $10^7 m$ and $c_1 = c_2$.

3 to 80 μm. We see that the transition temperatures of almost all the phases show a decreasing trend with decreasing cell thickness. We observe that on reducing the cell thickness, the Sm-C_A*(1/2) phase disappeares before the Sm-C_A*(1/3) phase, whereas the Sm-C_α* phase is rather stable. We see that for the cell thickness of approximately above 9 μm, the temperature range of the phases does not vary to a large extent, while for lower cell thicknesses, the temperature range of the phases decrease rapidly with decreasing cell thickness and for about 3 μm cell thickness the Sm-C_A*(1/2) and Sm-C_A*(1/3) phases totally disappear. Fig. 8.4$(c-d)$ represents the simulation result under the condition: w_1/A_0=1.05 $\times$ $10^7 m$ and $c_1 = c_2$. Here, we need to mention that this simulation is for understanding the qualitative behavior of the stability of various smectic-C^* phases as a function of thickness,

but it is not adequate to determine the transition temperatures accurately because significant simplification has been taken during calculating F_s, and A is just phenomenological coefficient and not exactly calculated or measured one. However, the simulation results are in good agreement with the experimental results considering the significant simplification. A different factor between the experiment and the theory is that the experiment was carried out during cooling of the sample and the data contains the super-cooling effect, while the theory is based on the actual transition temperatures while neglecting the super-cooling effect. Therefore, as the thickness of cell becomes thinner, the experimentally measured transition temperatures get lower due to the super-cooling effect.

8.3 Conclusion

The stability of the Sm-C_α*, Sm-C_A*(1/2), Sm-C_A*(1/3) and Sm-C_A* phase is investigated by finding the transition temperature of the phases and the temperature range for which the phases are stable by varying cell thickness experimentally in a systematic and precise way. From the theoretical analysis, we can explain the experimental observations as follows: *i)* Sm-C_A*(1/3) is more stable than Sm-C_A*(1/2) under the surface effect. This is due to that Sm-C_A*(1/2) has the highest anchoring energy compared to neighboring phases. *ii)* The instability is mostly due to the polar anchoring energy. *iii)* The Sm-C_α* is rather stable, though the surface energy of this is high, and the transition temperatures between higher temperature phases are rather unaffected by the surfaces. This arises from the higher temperature dependent coefficient of the free energy. *iv)* The temperature range of Sm-C_A*(1/3) is rather constant up to the thickness to which Sm-C_A*(1/2) exists. Once Sm-C_A*(1/2) disappears, the temperature range of Sm-C_A*(1/3) decreases rapidly with decreasing thickness. This is not so obvious in experimental results, but a similar two step stability is perceived.

Chapter 9

Gradual phase transition between the SmC_A^* and SmC^* phase and the thresholdless antiferroelectricity; influences by confinement and binary mixture

"In this chapter, *so-called the frustration between SmC_A^* and SmC^* phases is investigated. The phenomenon is revealed to be actually coexistence of SmC_A^* and SmC^* phases induced by suppression of phase transtion between them."*

9.1 Introduction to the thresholdless antiferroelectricity

Antiferroelectric liquid crystals (AFLCs) show the tristable switching, which is the electric-field-induced phase transition from antiferroelectric anticlinic SmC_A^*

to ferroelectric synclinic SmC^* and usually has characteristic dc threshold and hysteresis [10]. On the contrary to these usual behaviors, "thresholdless antiferroelectricity" was suggested [55]: In two apparently AFLC mixtures designated later as the Inui (Tokyo) and the Mitsui mixtures, respectively, the thresholdless, hysteresis-free, V-shaped switching was actually induced by an applied electric field [56, 125] and attracted many researchers' interest for the application to gray-scale displays [126–130]. Two mechanisms have been anticipated for the thresholdless switching in AFLCs: A continuous change of the azimuthal angle difference ϕ from the anticlinic to synclinic ordering [83, 86, 110, 111, 131], and Langevin-like alignment characterized by the randomized azimuthal angle φ from layer to layer due to the reduced correlation [55, 56, 112, 113, 132, 133]. Here, $\phi = \varphi_{i+1} - \varphi_i$ and φ_i is the azimuthal angle of the tilting direction for i-th layer. The continuous change of ϕ indicates that the free energy plotted as a function of ϕ has only a single minimum at any given applied electric field, and the angle $\phi_{\min}$ corresponding to the minimum energy decreases from anticlinic ($\phi_{\min} \approx \pi$) to synclinic ($\phi_{\min} \approx 0$) gradually with increasing the applied filed. In other words, the antiferroelectric state evolves to the ferroelectric state continuously. On the other hand, the Langevin-like alignment presupposes that the energy difference between the two energy minima corresponding to ferroelectric and antiferroelectric states have almost the same energy and the energy barrier between them also diminishes. As a result, any state of ϕ between synclinic and anticlinic orders can be excited thermally, and the frustrated state is obtained at zero field.

Because of the potential for gray-scale displays, Mitsubishi Gas Chemical Company, Inc. (MGC) and Mitsui Chemicals, Inc. were energetically developing liquid crystalline compounds and mixtures which show the V-shaped switching [51–53, 56, 125, 134]. MGC insisted that their developed compounds were FERRIELECTRIC by observing conoscopic figures with melatopes parallel to an applied electric field. However, a recent systematic and detailed study by Song *et al.* [37] has clearly revealed that their compounds were unambiguously ferroelectric. As the terminology "thresholdless antiferroelectricity" prevailed at that time in the liquid crystal display community, Mitsui Chemicals simply anticipated

that the compounds they developed for the V-shaped switching materials were in the bulk phase as antiferroelectric anticlinc SmC_A^* [134]. Taking account of the similarity in the chemical structure, however, Mitsui Chemicals' compounds must also be in their bulk phase as ferroelctric synclinic SmC^*, although no detailed study as Song *et al.* performed had yet been reported. It is now rather clear that ferroelectric liquid crystals with large spontaneous polarization can show the thresholdless V-shaped switching [85, 135–138]. In fact, there have been many reports that the Inui (Tokyo) mixture is ferroelectric but not antiferroelectric in the bulk [112, 113, 139, 140]. Quite recently Manjuladevi *et al.* also reported that ferroelectric liquid crystal materials with large spontaneous polarization and long helical pitch show the V-shaped switching [141]. Hence, the thresholdless V-shaped switchings observed in MGC and Mitsui compounds are actually the ferroelectric V-shaped switching.

Now, we can retrospectively remark that both companies adopted the same strategy of enhancing the frustration preparing their optimized binary mixture of antiferroelectric and "ferroelectric" liquid crystal compounds for the "thresholdless antiferroelectricity". In the temperature–concentration (T–x) phase diagram of their binary mixtures, the boundary between SmC_A^* and SmC^* is rather vertical and parallel to the ordinate temperature axis as contrasted with the ordinary ones which slant significantly. Near the critical concentration where the almost vertical boundary crosses the abscissa concentration axis, both SmC_A^* and SmC^* have nearly the same free energy and hence, the frustration is expected. Such a strategy seems to have been adopted from the beginning for the Mitsui as well as the Inui mixtures [56, 142]. Gorecka *et al.* and Pociecha *et al.* reported the frustration phenomenon in an intermediate range of concentrations for the binary mixtures using C12 and C13 compounds [143, 144]. They observed that the polar properties of the phase gradually evolve from antiferroelectric-like to ferroelectric-like over a wide range of temperatures. This continuous evolution of the polar character was suggested to arise from the frustration between the antiferroelectric and ferroelectric phases and the formation of clusters of both phases, which result from the weak dependence of the interlayer interactions on ϕ. The frustration was

anticipated to be influenced not only by the concentration of mixtures but also by the surface interactions or the electric field treatment. They also reported the observation of the thresholdless switching in the mixture.

In this way, though a real example for the intrinsic "thresholdless antiferroelectric" V-shaped switching has not been found so far, the research of the "thresholdless antiferroelectricity" actually gave rise to the ferroelectric V-shaped switching mode, which is still important for the applications and for the scientific understanding, and it also motivated the finding of the so-called frustration phenomenon observed in the binary mixtures by Gorecka *et al.* [143, 144]. In particular, the frustration phenomenon is still unclear in its characteristics and mechanism, and the frustration has much similarity with the thresholdless switching. The main purpose of this chapter is to clarify the so-called frustration phenomenon using mixtures of antiferroelectric MC881 and ferroelectric MC452, which were originally synthesized for the development of the "thresholdless antiferroelectricity" by MGC. The mechanism and the origin for the frustration phenomenon is investigated including the effects of the mixture ratio, the surface confinement and the applied field. We also re-examine the two mechanisms already suggested for the "thresholdless antiferroelectricity", that is, the continuous evolution of ϕ and the Langevin-like alignment. These investigations are carried out in view of the consideration that the interlayer interaction energy can provide answers for the various questions regarding the frustration phenomenon and the thresholdless antiferroelectricity. The super cooling phenomenon enhanced by surface confinement is also studied in detail. Finally, we also report clear experimental results supporting the ferroelectric V-shaped switching using the MGC compound, MC452.

9.2 Experiment

Samples used are the binary mixtures of antiferroelectric MC881 and ferroelectric MC452 compounds, and 12OF1M7. The chemical structures shown

in Appendix A. MC881 and MC452 were developed by MGC as the so-called "V-shaped switching materials" for gray-scale displays [51–53], and show simple phase sequences, I (122°C) SmA^* (114.5°C) SmC_A^* and I (107.2°C) SmC^*, respectively. In these references some of the mixtures as well as MC452 were considered as ferrielectric, for the melatopes in conoscopy emerges parallel to an applied electric field. As already pointed out in Introduction section, however, Song *et al.* have unambiguously identified them as ferroelectric [37]. Both homeotropically and homogeneously aligned cells of these samples were prepared using a Dow Corning silane coupling agent, 72% 3-(trimethoxysilyl)propyldimethyloctadecyl ammonium chloride and 28% methanol, and a Nissan Chemical aligning agent, RN1175, respectively. Various cell thicknesses, ranging from less than 1 μm through 100 μm, were used for performing the following experiments that are essential for advancing the subject.

We first obtained the bulk phase diagram in the MC881–MC452 binary mixture system using sufficiently thick cells. Phase boundaries were determined by analyzing dielectric responses, spectroscopical Bragg reflection observations, and birefringence measurements using a photo-elastic modulator (PEM). The dielectric measurements were carried out at a frequency of 1 kHz with an impedance analyzer (HP-4192A) using 25 μm homogeneous (planar) cells. As was actually used in the phase identification of a prototype antiferroelectric liquid crystal, MHPOBC [145], the soft mode in SmA and the Goldstone mode in SmC^* are helpful in determining the phase transition temperatures among isotropic, SmA, SmC^*, and SmC_A^* by observing the low frequency dielectric response. The Bragg reflection bands of 100 μm cells were also measured at an oblique incidence angle of 20° using a UV/visible-IR spectrophotometer (Perkin Elmer, Lambda 900). As is generally known now, SmC^* has the full-pitch helical periodicity and hence shows not only the characteristic reflection band (half-pitch band) but also the full-pitch band, whereas SmC_A^* with the half-pitch helical periodicity only gives the characteristic reflection band [146]. Since both the dielectric and spectroscopic measurements showed some complexities, suggesting the emergence of subphases between SmC^* and SmC_A^*, the electric field induced birefringence of 25 μm homeotropic cells

was studied to determine the electric field–temperature ($E - T$) phase diagram by using an experimental system using a photo-elastic modulator (PEM). The references [24, 25] described in detail the PEM-based setup for measuring the field-induced birefringence using homeotropic cells together with its effectiveness in identifying the subphases.

For better observation of the frustration effect, we studied the interface-induced destruction of the anticlinic antiferroelectric order in SmC^*_A by using sufficiently thin homogeneous cells. Phase boundaries were determined by analyzing dielectric responses at 1 kHz measured with the same apparatus as described above. Particular attention was paid to the thermal hysteresis effects, for the boundary critically depends not only on the cell thickness used but also on the cooling and the heating processes. We also studied switching characteristics by using 9 μm cells of several mixtures at 35°C, one of which was clearly located in the SmC^*_A region in the bulk phase diagram obtained above and showed a similar behavior to the so-called V-shaped switching. In order to clarify the cause for the emergence of thresholdless response to an applied electric field in the bulk SmC^*_A phase, we observed the texture of μm cells of MC452 (R-moiety) and its partially racemised mixture with MC536 (S-moiety) with an optical polarizing microscope (Olympus BX-52).

Then we tried to determine experimentally the free energy plot against the azimuthal angle difference between the adjacent smectic layers at various data points (specified by the concentration and temperature) in the SmC^*_A region of the above obtained binary mixture phase diagram. By assuming the uniaxial distribution of the molecular short axes as well as the perfect orientational and translational order, the free energy at a particular temperature can be written in a very simplified form as [147]

$$F = const + D\cos\phi - Q\cos 2\phi - P_s E\cos\phi, \tag{9.1}$$

where ϕ is the azimuthal angle difference of the in-layer directors between the adjacent layers and *const*, D, and Q are functions of the director tilt angle, and

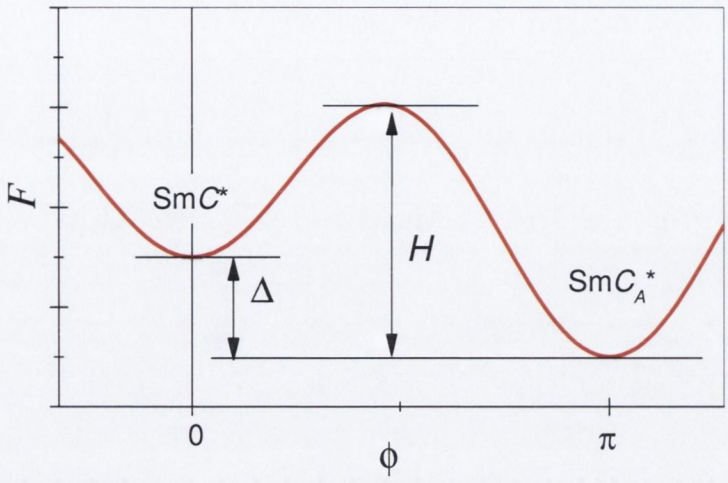

Figure 9.1: The interlayer interaction energy represented by Eq. (9.1). $Q/D = 2$.

P_s is the spontaneous polarization [50, 65]. The coefficients D and Q are given as functions of experimentally measurable quantities [84, 86, 148],

$$D = \frac{3\cos(\phi_{th}/2)+2}{4\{\cos(\phi_{th}/2)+1\}^2} P_s E_{th}, \tag{9.2}$$

$$Q = \frac{1}{16\cos(\phi_{th}/2)\{\cos(\phi_{th}/2)+1\}^2} P_s E_{th}. \tag{9.3}$$

Here E_{th} the critical field, and ϕ_{th} indicates the value of ϕ at $E = E_{th}$. The critical field E_{th} can be determined as a field where the solitary wave observed during the field-induced switching from SmC$_A^*$ to SmC* has zero speed [84, 86]. We can also determine $\phi_{th} = \pi - 2\sin^{-1}(\tan\Theta'/\tan\theta)$ by measuring the apparent tilt angle Θ' at E_{th} and the director tilt angle θ in the field-induced SmC*. The free energy difference Δ and the barrier height H between the SmC$_A^*$ and SmC* minima are calculated using Eq. (9.1),

$$\Delta = 2D,\ H = \frac{D^2}{8Q} + 2Q + |D|. \tag{9.4}$$

Figure 9.1 illustrates the free energy having the dipolar and the qudrupolar terms.

We also carried out various optical measurements using 12OF1M7 for clarifying the supercooling effect enhanced by the surface effect.

9.3 Results and Discussion

9.3.1 Phase diagram of MC881-MC452 binary mixture system and the gradual phase transition

Figure 9.2 shows the temperature–concentration ($T - x$) phase diagram in the binary mixture system of anticlinic antiferroelectric MC881 and synclinic ferroelectric MC452. In order to be free from any interface effects, it was obtained using 25–100 μm thick cells. The phase boundary neither depends on the cell thickness nor shows obvious thermal hysteresis, so far as using such thick cells. The boundary between the SmC_A^* and SmC^* is almost vertical and parallel to the temperature axis in the low temperature region as contrasted with the ordinary one which slants significantly [12]. In the molecular theory for the anticlinic smectic-C_A phase [65], SmC_A^* always becomes stable at low temperatures, and there should exist SmC_A^* at sufficiently low temperatures if the compound does not transit to other phases or is crystallized. Figure 9.2 clearly indicates that SmC_A^* could not exist as a low-temperature phase of SmC^* on the right side of the vertical boundary. This is a rather surprising result. We will discuss it in the next section. We shall designate the mixing ratio corresponding to the vertical line the critical mixing ratio R_c. The Sm$C_A^*(1/3)$ phase having 3-layer periodicity was observed over a narrow range of temperatures at the boundary. The existence of Sm$C_A^*(1/3)$ can be confirmed by PEM results shown in Fig. 9.3. In the temperature range corresponding to Sm$C_A^*(1/3)$, no selective reflection peak was observed in the visible/IR experiments upto a wavelength of 1.9 μm.

Another phase diagram was constructed by using dielectric measurement with thinner cells of 2 μm thickness. The experiments were carried out during both heating and cooling cycles. The obtained phase diagram is shown in Fig. 9.4. In thin cells, since the dielectric response changes gradually near the transition temperature, it not easy to decide the exact transition temperature, and so we determined the transition temperatures at the center of the gradually changing

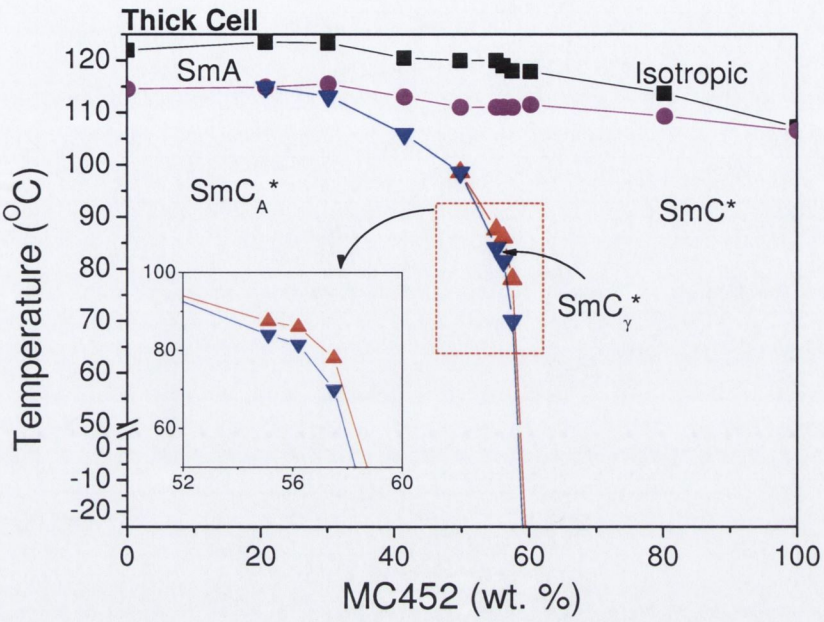

Figure 9.2: Bulk phase diagram of binary mixture system of MC881-MC452. The boundary between SmC^*_A and SmC^* becomes almost vertical parallel to the ordinate temperature unit below 70°C, so that we can define the critical concentration R_c. The mixture near R_c stably exists as smectics even at -25°C.

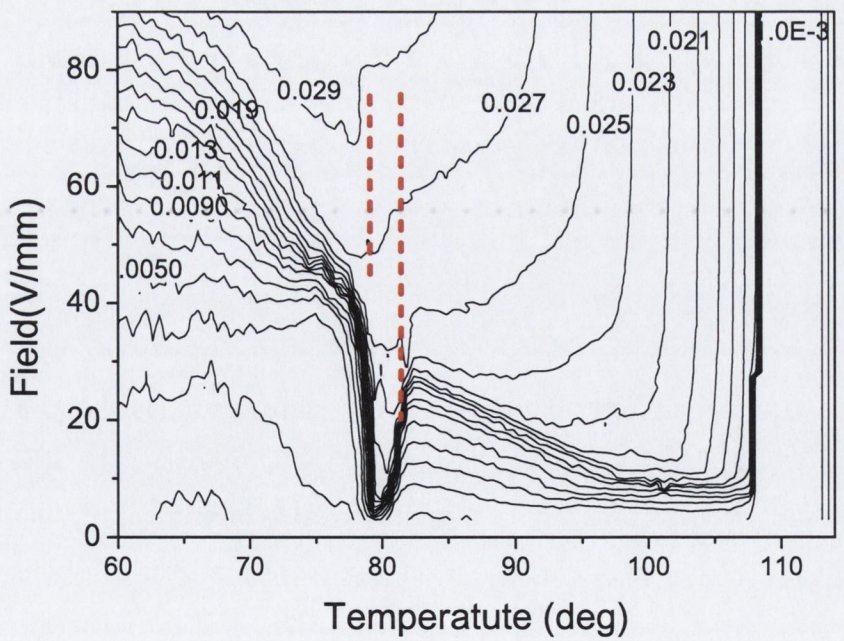

Figure 9.3: PEM data, indicating clearly the emergence of the subphase SmC^*_A(1/3).

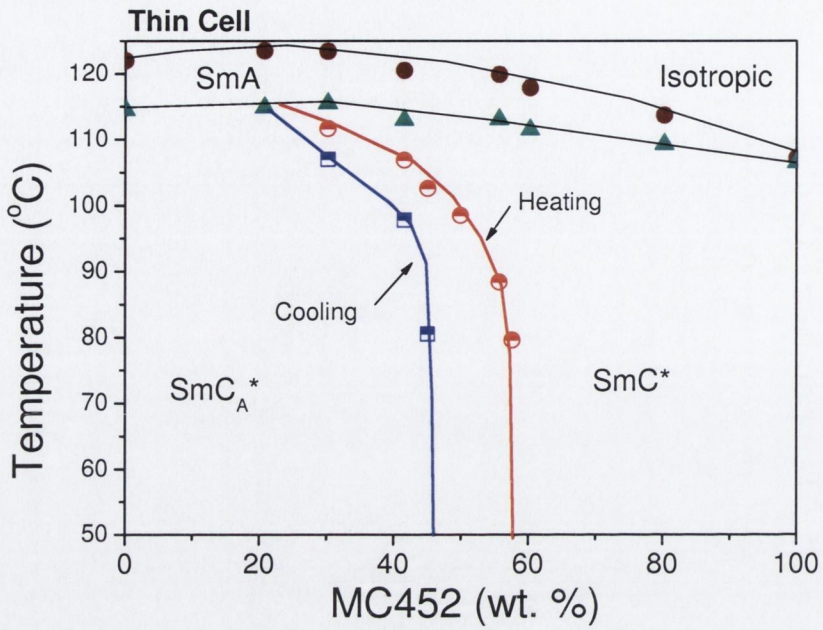

Figure 9.4: Phase diagram using 2μm thick cells and dielectric measurement.

dielectric response. In thin cells, the SmC^*-SmC^*_A transition temperatures obtained during cooling are much lower than those obtained during heating, that is, the super cooling and super-heating are significantly large. The super-cooling is so large near R_c that the transition is not detected during the cooling cycle. Since the super-cooling is not observed in the thick cells, we can see that the super-heating basically arises from the surface effects, but its mechanism has not been explained clearly so far.

Figure 9.5 shows the real part of the dielectric permittivity as a function of temperature in two thick cells and a thin cell using 40% and 55.5% MC452 mixtures in MC881. In the thick cell using 40% MC452 mixture, SmC^*–SmC^*_A the transition is clearly detected in a narrow temperature range, which is the common behavior observed at the phase transition. However, the transition is rather dull and unclear in the thin cell using the same mixture or in the thick cell using the 55.5% MC452 mixture. The dull curves of the dielectric response clearly show that the phase transition occurs gradually over a wide temperaure range. Both of the confinement by surfaces and the concentration of the binary mixtures result in the same effect in the phase transition, that is, the gradual transition,

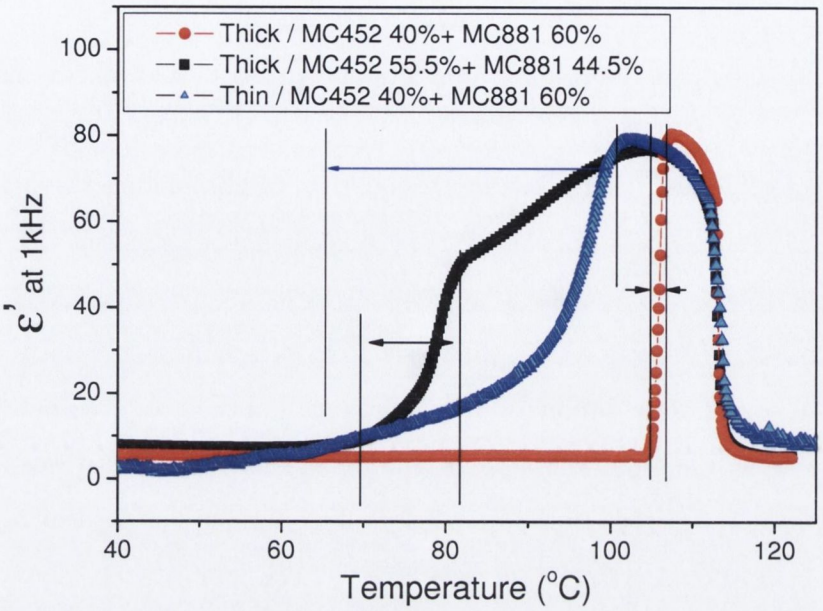

Figure 9.5: Real part of dielectric permittivity measured at 1kHz using various cell conditions. The cell conditions are given in the inset: "thin" and "thick" indicate about 2μm and 25μm thickness cells, respectively.

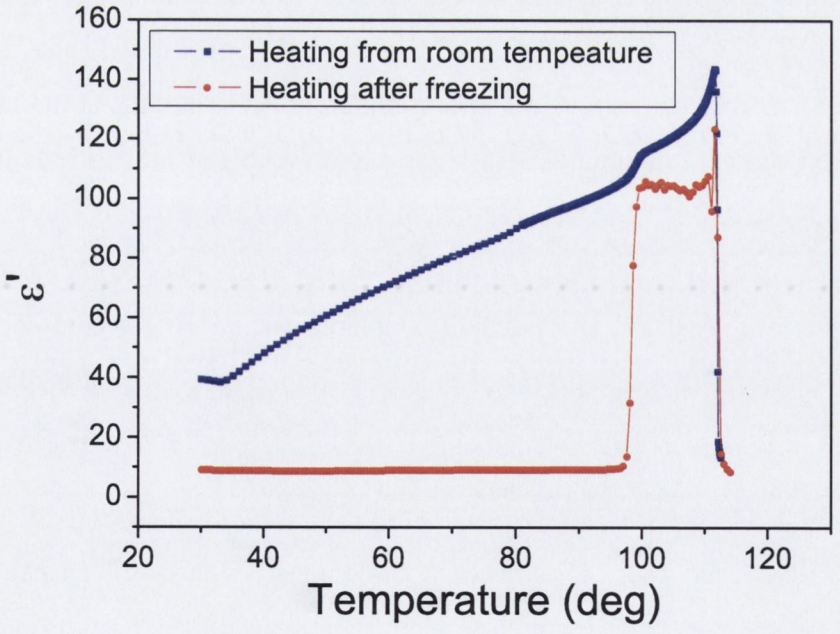

Figure 9.6: Real part of dielectric permittivity measured at 1kHz by using a 2μm thick cell and 50 % mixture. Blue square data points was obtained during heating a cell after keeping the cell in room temperature, and red circle data points was obtained during heating the cell after keeping at -5^oC for 2 hours.

which was already reported by Gorecka *et al.* [143, 144]

In order to find the origin of the gradual phase transition, we carried out another experiment as shown in Fig. 9.6, where two sets of the real part of the dielectric permittivity are plotted using the same cell with different thermal history. The dielectric response was obtained using a 2μm thick planar cell, 50% mixture at a frequency of 1 kHz. After filling the cell with the 50% mixture at isotropic temperature, the cell was cooled down to room temperature. Firstly, the blue square data points were obtained during heating from the room temperature. For the second experiment, the cell was cooled down again to -5°C and was kept for 2 hours. After then, the red circle data points were obtained during heating. A clear difference is detected as shown in Fig. 9.6. The cell kept at -5°C shows a sharp step near 98°C, which indicates the clear phase transition from SmC^*_A to SmC^* phases. However, for the other cell kept at room temperature, the transition is unclear. The dielectric response for the cell kept at -5°C is the typical behavior for the SmC^*_A–SmC^* transition. The dielectric response for the cell kept at room temperature is rather close to that to the behavior of the SmC^* phase except for a slight jump in ϵ' close to the transition temperature. This implied that the liquid crystal at room temperature is not in a completely synclinic nor anticlinic state, but this is a mixture involving both the synclinic and the anticlinic states. On heating, only a part of the cell experiences the phase transiton at the transition temperature, since the other part is already in the SmC^* phase. By keeping the cell at a low temperature, the partially synclinic state changes completely into anticlinic state, and the liquid crystal acquires the pure SmC^*_A phase. Therefore, in the area between the two vertical transition lines in the phase diagram shown in Fig. 9.4, the two phases can coexist simultaneously.

Gorecka *et al.* [143, 144] explained these phenomena as the frustration between the antiferroelectric and the ferroelectric phases and the formation of nano-size (smaller than visible wavelength) antiferro- and ferroelectric clusters. For supporting their model, they introduced the interlayer interaction between the neighboring layers as a simple term $f_i = A_1(\xi_i \cdot \xi_{i+1})$ by neglecting higher terms, where ξ_i represents the director vector of i-th layer. This interlayer interaction

energy can simply be represented as $f_i \propto A_1 \cos\phi$, which is the dipolar term in Eq. (9.1). Hence, when mixing appropriately an antiferroelectric and a ferroelectric liquid crystalline materials, the coefficient A_1 approaches zero and the interlayer interaction energy becomes independent of ϕ. They pointed out this weak ϕ correlation of the interlayer interaction as the origin of the frustration and the formation of the clusters. However, the quadrupolar term in the interlayer interaction in the antiferroelectric phase has widely been reported and it is known to play an important role in the switching of the antiferroelectric phase and the phase transition. Qian and Taylor [83] showed that the quadrupolar term actually determines the switching characteristics of an antiferroelectric cell, and Song *et al.* [40, 84] showed that the quadrupolar term prohibits the homogeneous phase transition and instead makes it possible for the solitary wave propagation to occur. The solitary wave propagation leads to a slow non-homogeneous process and is quite different from a homogeneous phase transition. Therefore, it is impossible to understand the phase transition perfectly without the quadrupolar term as was attempted by Gorecka et al.[143, 144].

9.3.2 Thresholdless antiferroelectric switching in the binary mixture

Though the effects of the application of an electric field on antiferroelectric cells is apparently different from that of the application of thermal energy, the electric field induced switching behavior quite resembles the temperature induced phase transition. This is because the electric field favors and induces the ferroelectric state as the thermal energy also does so. Note that the thresholdless switching with field is very similar to the gradual phase transition with temperature. Hence, investigating the field induced continuous switching is quite helpful to understand the temperature induced gradual phase transition.

We measured the apparent tilt angle Θ' as a function of the applied field using 9μm cell. Figure 9.7 shows the field dependence of the apparent tilt angle for the various mixing ratios. The experiments were carried out with increasing and

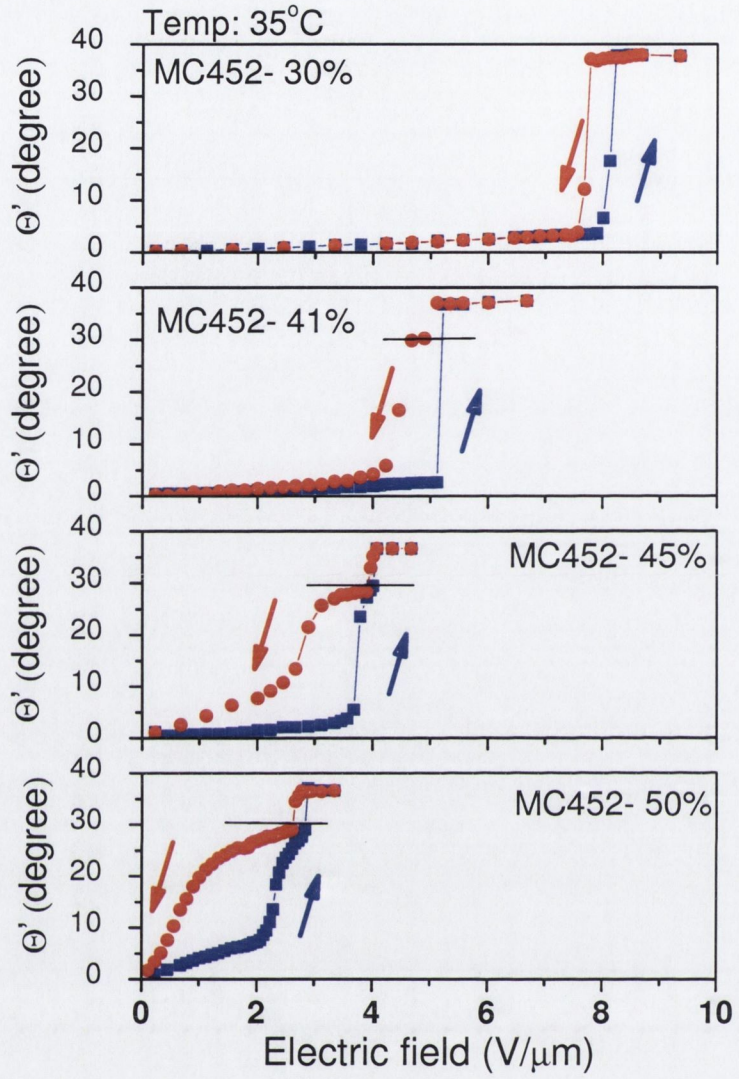

Figure 9.7: Apparent tilt angle Θ' as a function of the applied field for the various mixtures of MC452 in MC881 at 35 °C. Each measurement is carried out with the increasing and the decreasing fields as indicated by the arrows.

decreasing field at 35°C using 9μm planar cells. As the mixing ratio decreases, the threshold field for the transition from antiferroelectric (AF) to ferroelectric (F) state decreases. While the AF-F switching for 30% MC452 mixture shows a clear one step increase, which is a typical behavior of antiferroelectric materials, the AF-F switchings for the mxitures having higher mixing ratio of MC452 show a two-step increase and finally lead to a rather gradual increase as shown in Fig. 9.7. To identify the intermediate state at the two-step switching, we simulate the apparent tilt

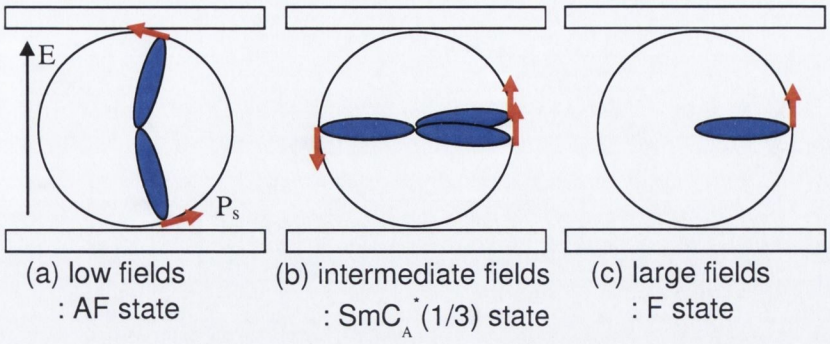

Figure 9.8: The relative orientation of the **c** directors at each step of the field induced transition. When $\theta = 37^o$, $n_o = 1.5$ and $n_e = 1.7$, $\Theta' = 30.4^o$ is found for SmC$_A^*$(1/3) state according to a simple simulation. The simulation result accords well with the experimental results shown in Fig. 9.7.

angle in SmC_A^*(1/2) structure shown in Fig. 9.8. The tilt angle θ of 40% mixture at 35°C is 37°. When $\theta = 37°$, $n_o = 1.5$ and $n_e = 1.7$, the apparent tilt angle Θ' for unwound SmC_A^*(1/2) state is found to be 30.4^o in our calculations, which is the same as Θ' found experimentally in the intermediate state. This implies that the intermediate state is the field induced SmC_A^*(1/2) state. This indicates that the field plays almost similar roles as those of the thermal energy. Note that the SmC$_A^*$(1/2) phase was observed between the SmC^* and the SmC_A^* phases in the phase sequence with temperature as shown in Figs. 9.2 and 9.3. Similarly, the SmC$_A^*$(1/2) state is observed in the intermediate range of field between the antiferroelectric and the field induced ferroelectric states [123, 149, 150]. As the mixing ratio decreases, the range of SmC$_A^*$(1/2) state is enlarged. Almost gradual increase of the apparent tilt angle is observed when the mixing ratio approaches the critical ratio R_c, but still it shows the two step increase.

The SmC$_A^*$(1/2) phase is not observed in thin cells. This may be because the stability of the SmC$_A^*$(1/2) phase is rather weak, and is easily suppressed by the surface energy. Similarly, a thiner cell may show a better continuous switching without the two step increase. We prepared two thin cells of 2μm thickness using 55% and 45% MC452 mixtures; 55% is close to the cirtical ratio ($R_c \approx 59\%$). In order to make the cells to be in the SmC_A^* phase, the cells was kept in -5°C for 15 hours. After heating the cell to room temperature, the apparent polarization

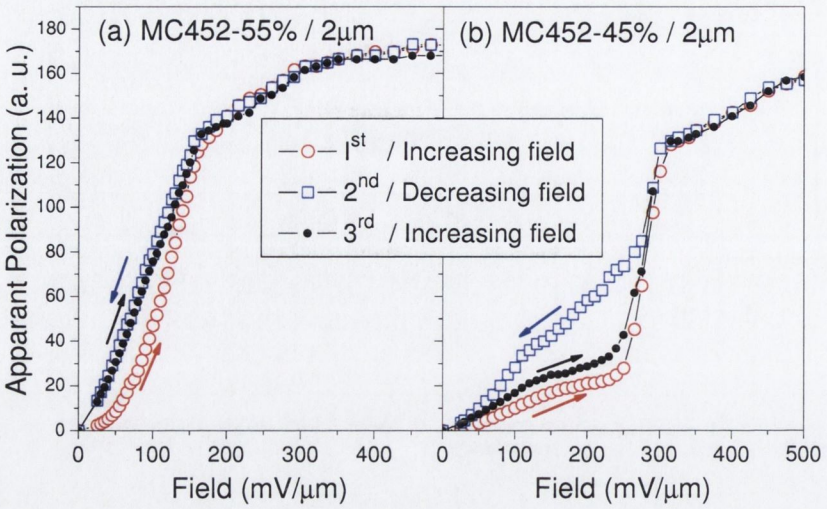

Figure 9.9: Apparent polarization as a function of applied field for $2\mu m$ thickness cells using (a) 55% MC452 mixture and (b) 45% MC452 mixture.

was measured with increasing and decreasing applied field as shown in Fig. 9.9. Three measurements were carried out for each cell: the first data were obtained with increasing field using the vergin cell, then the second data were obtained with decreasing field, and the third ones were measured with increasing field again. The 45% MC452 cell (Fig. 9.9(b)) shows a threshold field, which is the typical behavior of the antiferroelectric phase. The third data correspond similarly to the first one, which means that the field induced ferroelectric state easily returns to the initial antiferroelectric state when the field is removed. On the other hand, the 55% MC452 cell (Fig. 9.9(a)) shows a gradual increase of the polarization with increasing field, which is quite similar to the thresholdless antiferroelectricity. Since the virgin cell is the SmC^*_A phase, the continuous switching means that the antiferroelectric phase gradually tranforms to the field induced ferroelectric state. However, the third data is similar to the second data, but is different from the first one. This means that the field induced ferroelectric state does not return to the initial antiferroelectric state after removing the field. Hence, the third data is the switching of a ferroelectric cell, which means that the thresholdless antiferroelectricity is possible only for the first swing. After all, the thresholdless antiferroelectricity is possible as shown in Fig. 9.9(a), though the behavior is rather different from the conventional concept of the thresholdless antiferroelectric switching, because the

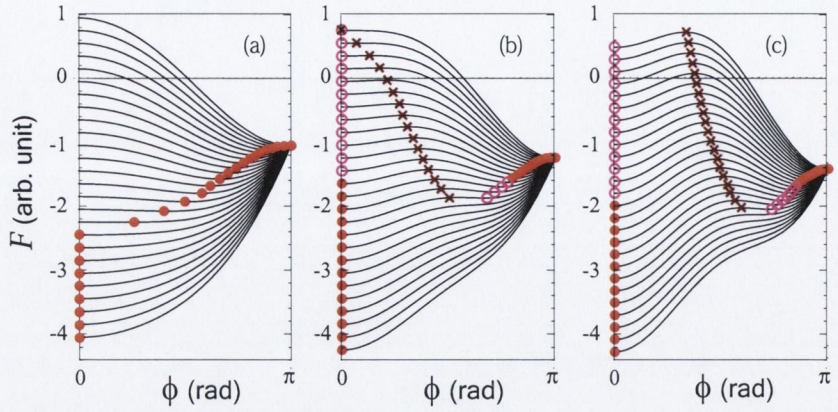

Figure 9.10: Free energy as a function of the azimuthal angle difference of the in-layer directors between the adjacent layers for various strengths of applied electric field calculated using Eq. (9.1). The values of parameters: (a) $Q/D = 0.05$, (b) $Q/D = 0.25$, and (c) $Q/D = 0.5$. The applied field increases from top ($E = 0$) to bottom line for each graph. Solid red circles are global minimum points, open pink circles are local minimum points, and brown crosses are the energy barrier between the two energy minima. For $Q/D \leq 0.05$, only a single minimum exists at any applied electric field, and for $Q/D > 0.25$, $\phi = 0$ is the local energy minimum even at zero field.

conventional switching is supposed to be used for applications and should occur at high frequencies as well, that is, the antiferroelectricity should recover quickly when turning the applied field off. Hence, the kind of thresholdless antiferroelectricity observed here is not useful for applications.

9.3.3 The mechanism of the frustration and the solitary waves

As pointed out by Qian and Talyor [83] and later by Parry-Jones and Elston [86], the interlayer interaction is the most crucial factor in determining the characteristics of the phase transition between the SmC_A^* and the SmC^*. Now, we will reexamine the two models suggested for the thresholdless antiferroelectric switching mode: the continuous evolution model and the Langevin-like model from the view point of the interlayer interaction energy. Based on the electrostatic dipolar interactions, Lee and Lee presented a geometrical model for the azimuthal angle change and gave the thresholdless criterion [110]. Qian and Talyor and more

recently Parry-Jones and Elston made a detailed analysis of the change in terms of the interlayer interaction energy as a function of the azimuthal angle difference between the adjacent layers at any given applied electric field [83, 86]. The continuous evolution can be achieved when the quadrupolar term is small enough as compared with the dipolar term, and the interlayer interaction has always one energy minimum. Figure 9.10 shows the free energy against ϕ at various applied fields for three parametric values of Q/D. When Q/D is large enough as shown in (c), the free energy have two energy minima at various applied fields, and the tristable switching is expected. However, when the quadrupolar term is very weak as shown in (a)($Q/D \leq 0.05$), the free energy plots have always a single energy minimum, and the continuous evolution is expected.

Therefore, if there exists such a material having very weak quadrupolar interlayer interaction term as compared to the dipolar term, the continuous evolution, that is, the thresholdless antiferroelectricity can be obtained even in a thick cell. However, all of the thresholdless switching in AFLC cells have so far been obtained in a thin cell, and most of these have been revealed as the ferroelectric V-shaped switching since the surface suppresses the antiferroelectricity as shown in the previous section. In the molecular theories, the synclinic ordering is favored by the isotropic dispersion attraction between the molecules and the steric energy between the layers, which are supposed to be most dominant interlayer interaction energies [65]. Therefore, the existence of the local minimum at the synclinic ordering is naturally expected even in the antiferroelectric phase, which also supports the presence of the significantly large quadrupolar term, as being actually measured in the following. In this way, though the continuous evolution is possible theoretically, an actual material having such physical properties may not exist. The Langevin-like alignment assumes the ϕ independent free energy, and randomized angle difference between the adjacent layers. This may be possible only when both the dipolar and the quadrupolar terms are close to zero. Using the same reason as explained above, the liquid crystalline material having the weak tilting direction correlation is also hard to realize.

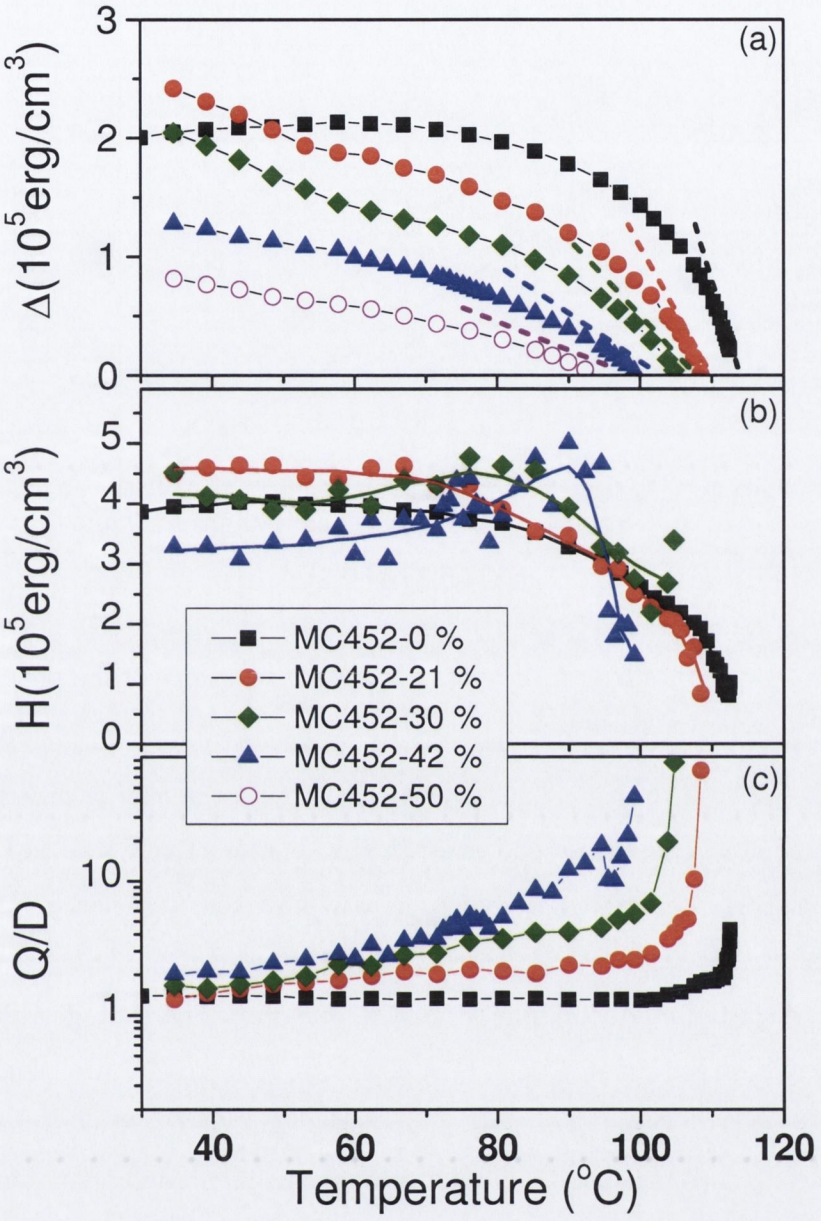

Figure 9.11: (a) Free energy difference between SmC^*_A and SmC^* minima, (b) its barrier height separating these, and (c) Q/D with temperautre.

We measured the actual interlayer interaction energy in the binary mixtures using the method explained in Section 9.2. Figure 9.11 shows the measured H, Δ and Q/D as a function of temperature for various ratios of mixtures using 25μm thickness planar cells. We can see that Q/D is always much larger than 0.25, which means that there exist always two energy minima. While H does not change much with the mixing ratio, Δ decreases with the increase in the

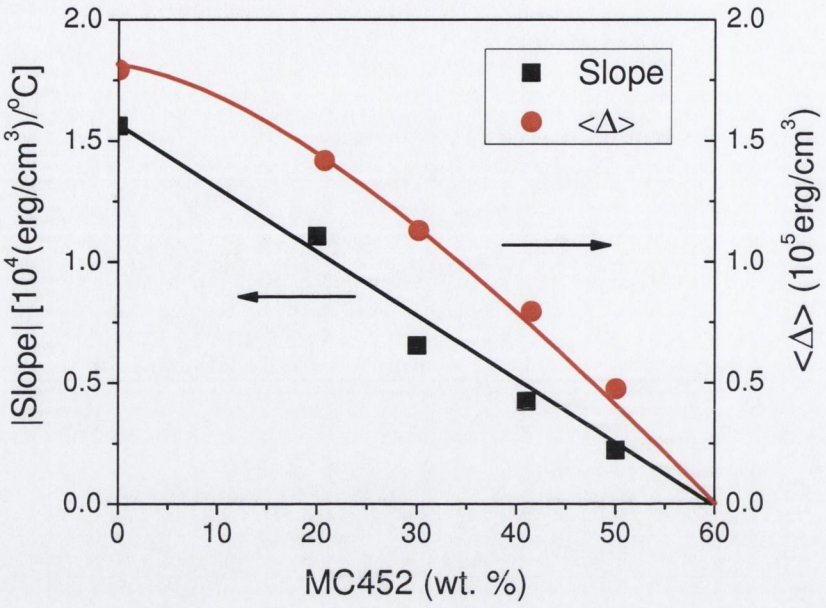

Figure 9.12: Averaged $\langle\Delta\rangle$ over the temperature range from $(T_c - 50)^oC$ to $(T_c - 10)^oC$ (upper), and the absolute value of the slope near T_c.

mixing ratio of MC452. Note that Δ and H represent the energy difference and the barrier height between the two energy minima, respectively. the two minima; each representing the stable state of a phase. Therefore, the large value of H implies that there exists the large energy barrier between the two phases. The trend of Δ with the concentration is quite interesting. The average values of Δ over the temperature range from $(T_c - 50)$°C to $(T_c - 10)$°C are plotted with the concentration in Fig. 9.12. $\langle\Delta\rangle$ approaches zero at R_c, which means that the energy difference between the anticlinic and synclinic orderings becomes zero. The experimental observation is quite understandable. Pure MC881, which is an antiferroelectic material, has the minimum free energy level in the anticlinic ordering. By adding MC452, which is a ferroelectric material, the free energy level in synclinic ordering decreases and Δ decreases. Since the synclinic and the anticlinic ordering have the same energy level close to the critical concentration R_c, Δ reduces to zero. Hence, we can conclude that by adding the ferroelectric material to the antiferroelectric one, the energy difference between the synclinic and the anticlinic orders reduces but the energy barrier between these is little influenced. Moreover, the slope of Δ with temperature depends on the concentration. The

doted line for each curve represents the slope of the curve near T_c in Fig. 9.11(a). The absolute values of the slope of the lines are plotted in Fig. 9.12, which shows that the slope also approaches zero as the mixing ratio gets closer to R_c.

Actually, we can explain the gradual phase transition phenomenon using the above measured interlayer interaction energy. In Chapter 5 and 6 [84], we showed that, when there exists an energy barrier between the ferroelectric and the antiferroelectric energy minima as in the binary mixtures under consideration, the only possible way for the phase transition to occur is a non-homogeneous process, *i.e.* the solitary wave propagation to overcome the energy barrier [40, 84]. Usually, the solitary wave starts from defects and its propagation is also influenced by the surface effects. The energy difference between the two phases, Δ, is the driving force for the solitary wave to propagate. Therefore, the phase transition strongly depends on the competition between the driving force by Δ and the frictional effect by surfaces and defects. When Δ is large, the driving force for the phase transition is so strong that the transition occurs very quickly. On the other hand, if Δ is small, the driving force is weak compared to the friction and in some part of the cell, the transition may successfully occur slowly but in the other part, the meta stable state remains and the two phases actually coexist. This explains why the coexistence of two phases appears near the critical concentration R_c, where the energy difference Δ is minimized as shown in Figs. 9.11 and 9.12. The slope of Δ with temperaure is the most important factor. As shown in Fig. 9.12, the slope approaches zero near the critical concentration. The slope means the temperature dependence of Δ, hence the low value of the slope means that Δ becomes weakly dependent to the temperature. On cooling, Δ experiences its sign reversal at the transition temperature T_c, and the anticlinic ordering, which was the meta-stable state at high temperatures, becomes the global stable state. On further cooling, Δ increases and the driving force for the solitary wave propagation increases. If the slope of Δ is large as the case for the large concentration of MC881, Δ increases quickly with decreasing temperature and the phase transition occurs rapidly in a narrow temperature range. However, if the slope of Δ is small as being near the critical concentration, Δ increases very

slowly with decreasing temperature and the driving force for the solitary wave to propagate is rather weak even when the temperature is much lower than T_c. Hence, large super cooling and at the same time rather dull phase transition are observed as shown in Figs. 9.4 and 9.5. The slope of Δ explains why the phase transition line between the SmC^*_A and the SmC^* phases in the phase diagram is vertical. The slope approaches zero at R_c: the zero slope means that the transition between SmC^* and SmC^*_A occurs almost at the same concentration over a wide range of temperatures, and the transition line in the phase diagram becomes vertical. The thresholdless antiferroelectricity shown in Fig. 9.9(a) is similarly explained. Moreover, the reason why the antiferroelectricity does not recover after removing the field is explained by the fact that Δ is small and the driving force for the solitary wave is too weak for the propagation to occur.

9.3.4 Surface effect: How does the interface induce the supercooling?

The super cooling effect also can be explained by the interlayer interaction having the double energy minima. In this section, the super-cooling phenomenon of the SmC^*–SmC^*_A phase transition is clarified.

The liquid crystal used is 12OF1M7. The chemical structure and the phase sequence are described in Appendix A.

Fig. 9.13 is the optical transmittance as a function of applied field for various cell thicknesses, where a 0.003 Hz triangular ac field was used. Since the frequency is quite low, this acts almost as a DC field. The tristable switching and the hysteresis characteristics shown in the figure are well known. Here, it should be noted that the hysteresis in the 1.6 μm thickness cell is the largest, while thicker cells have less hysteresis. It is worthy to recall the phase diagrams in Figs. 9.2 and 9.4. The supercooling in a thin cell is much larger than that in a thick cell. That is, the supercooling in the temperature coordinate corresponds to the hysteresis in the field coordinate. We can see that the surface effect influences

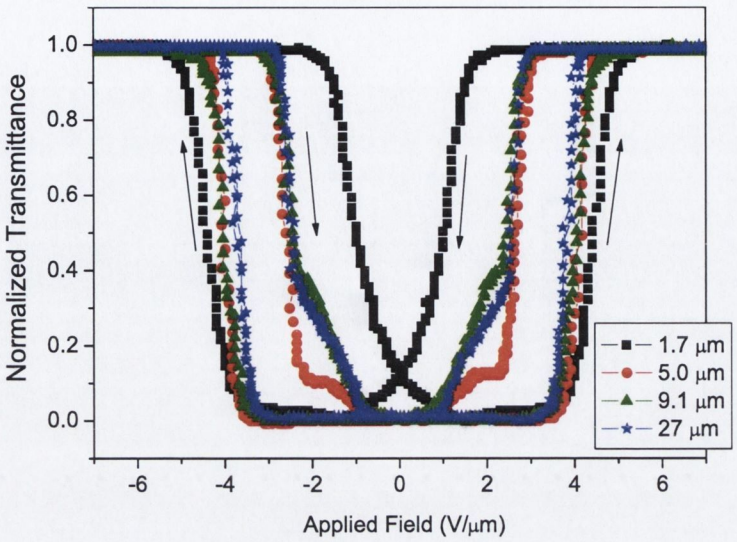

Figure 9.13: Transmittance as a function of the applied field for various cell thicknesses of 12OF1M7. The experiment was carried out using cross polarizers and a 3 mHz triangular field.

not only the phase transition temperature but also the field induced switching. In chapter 7 and chapter 8, we already showed that the phase transition is possible only through the solitary wave propagation.

Fig. 9.14 shows microscope images and the apparent tilt angle during the field induced phase transitions. A 9 μm thickness 12OF1M7 planar cell was prepared, and the apparent tilt angle was measured as a function of the applied field using a 30 Hz square shape field at 50°C. On increasing field, a direct transition from AF to F state appears, and on decreasing field, a two step transition similar to Fig. 9.7 was observed. When $\theta = 27°$, $n_e = 1.7$ and $n_o = 1.5$, the apparent tilt angle of the unwound Sm$C^*_A(1/3)$ is calculated as 14.7°, which exactly corresponds to the intermediate state on decreasing field in Fig.9.14. Therefore, the intermediate state is supposed to be the field induced Sm$C^*_A(1/3)$ state. At each step, microscopic images were recorded. As shown the images corresponding to the steps, the transition occurs through solitary wave propagations. That is, one small domain appears and the size of the domain increases with time. On cooling, the transition from the F state to the intermediate Sm$C^*_A(1/3)$ state and the transition from the intermediate state to the antiferroelectric state are also

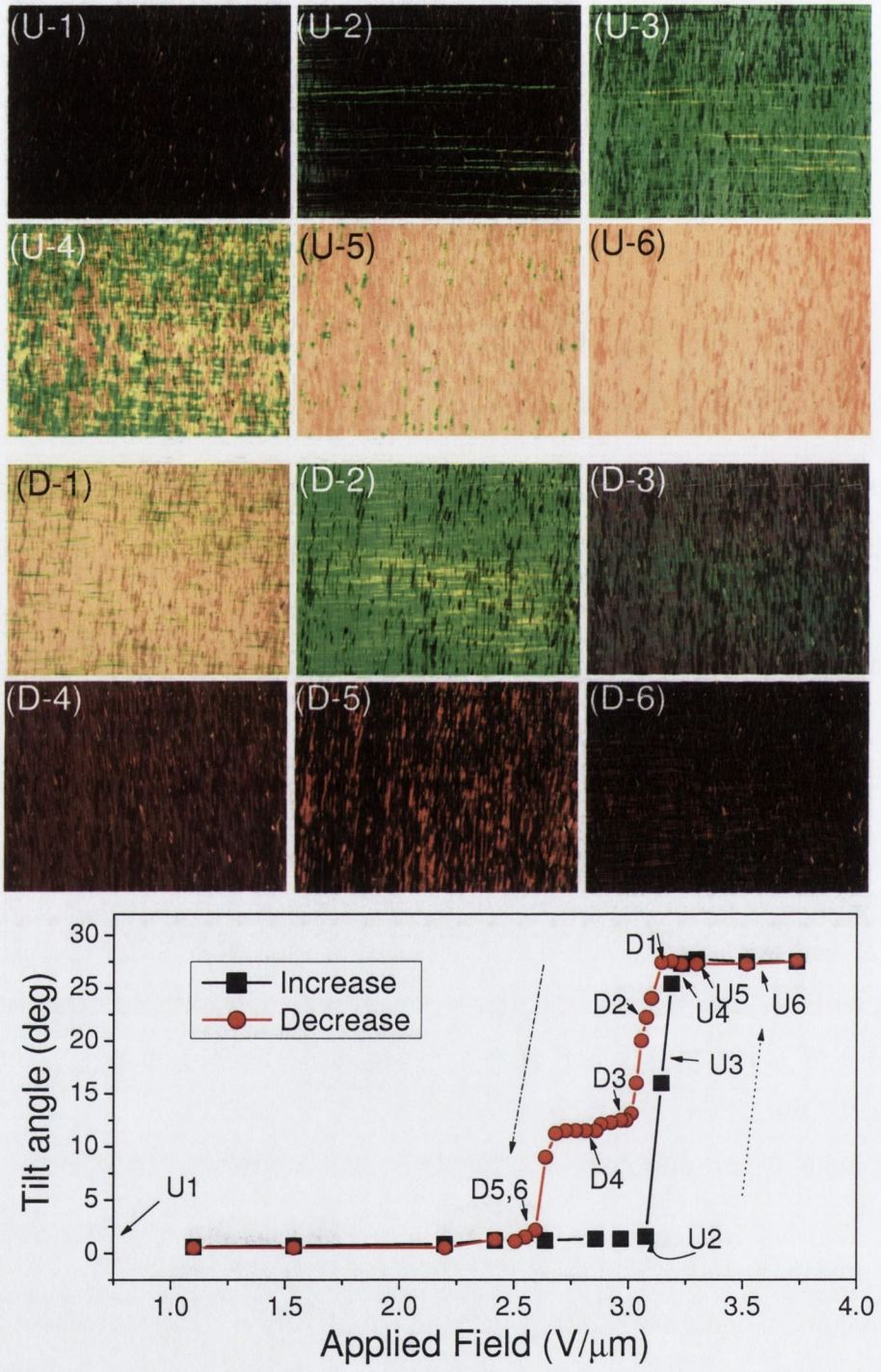

Figure 9.14: Microscpic images and apparent tilt angle as a function of the amplitude of the applied field for various cell thicknesses (12OF1M7) at 50°C. A 30Hz square wave field is applied.

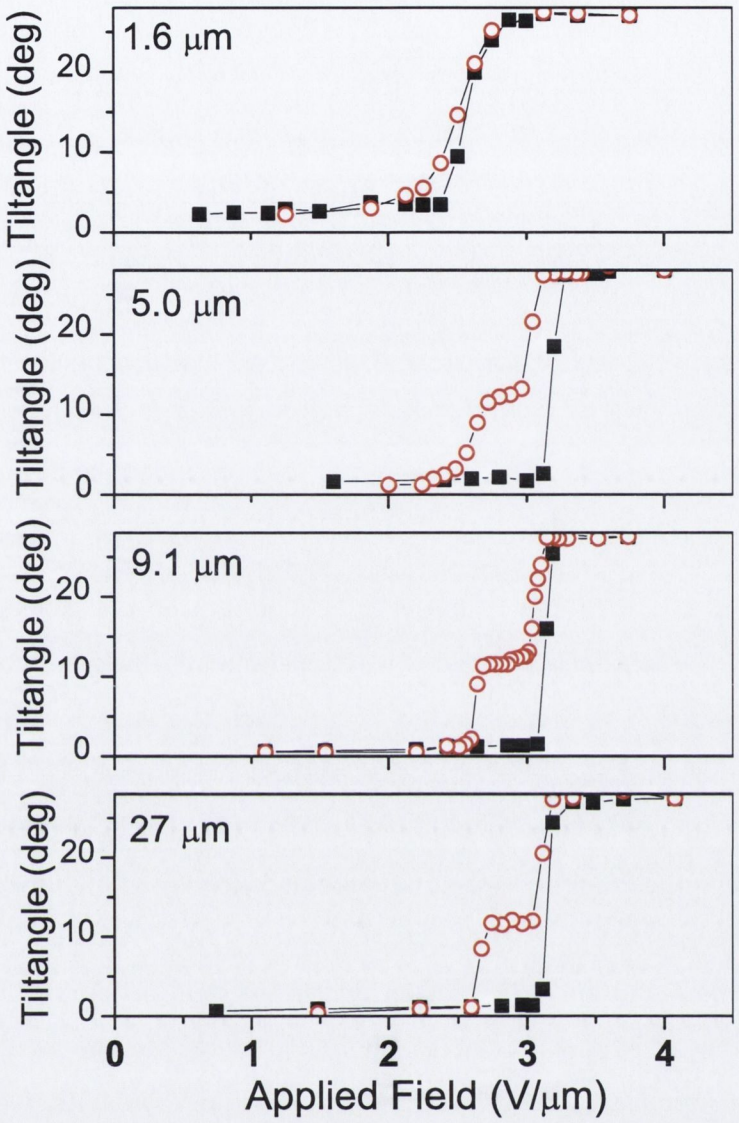

Figure 9.15: Apparent tilt angle as a function of the amplitude of the applied field for various cell thicknesses (12OF1M7) at 50°C. A 30Hz square wave field is applied.

accompanied by solitary wave propagations. This implies that each state including the intermediate state has its own local energy minimum, and also an energy barrier exists between the states. The transition from one state to the other should overcome the energy barrier between them, which is possible only through solitary wave propagation as explained in chapter 7 and 8. The microscopic images show additional information; during the AF-F transition on increasing field and the F-$SmC^*_A(1/3)$ state transition on decreasing field, two types of solitary waves occur.

U-1 image having dark color corresponds to AF state, and U-5 having orange color corresponds to F state, and between U-1 and U-5, U-3 having green color appears. Both of the transitions from U-1 to U-3 and from U-3 to U-5 are accompanied by the solitary waves shown in U-2 and U-4 images. On the transition from the F state to an intermediate state during decreasing field, the similar green color state (D-2) appears. Therefore, rather unstable additional state (U-3, D-2) different from the intermediate SmC^*_A(1/3) state (D-4) exists. The identification of the U-3 or D-2 is not dealt with here, but is surely interesting. Anyway, the solitary wave always appears in the field induced phase(or state) transition, confirming that the phase transition occurs always through the solitary wave propagation.

Therefore, if there exist some obstacles preventing the generation or the propagation of the solitary wave, the phase transition and the field induced AF–F switching are suppressed. Note that, even though another state may be the global energy minimum, without the propagation of the solitary wave, the liquid crystal cell will stay in the other meta stable state. The critical field E_c, where the free energies of AF and F states become the same, is found to be about 3.1 V/μm for the 9 μm cell as shown in Fig. 9.14, but the actual transition occurs at 4.0 V/μm on increasing field and at 2.2 V/μm on decreasing field as shown in Fig. 9.13. We can find that it requires a certain minimum energy for the solitary wave to generate and to propagate, and the energy required increases with decreasing cell thickness, which implies that the interface necessitates the energy. Therefore, the surface effect of the alignment layer acts as an obstacle and prevents the formation and propagation of solitary wave. This is the mechanism of the large supercooling effect and the large hysteresis in a thin cell.

To investigate the suppression of the solitary wave, similar tristable switching experiments were carried out using 30 Hz square wave shape electric fields in cells of various thicknesses, and the results are plotted in Fig. 9.15, which contains a few important points.

Firstly, the large hysteresis observed in Fig. 9.13 becomes very small even in the thinest cell. The only difference between the two experiments is that the applied field in Fig. 9.13 is close to dc field, while that in Fig. 9.15 is ac field. This means

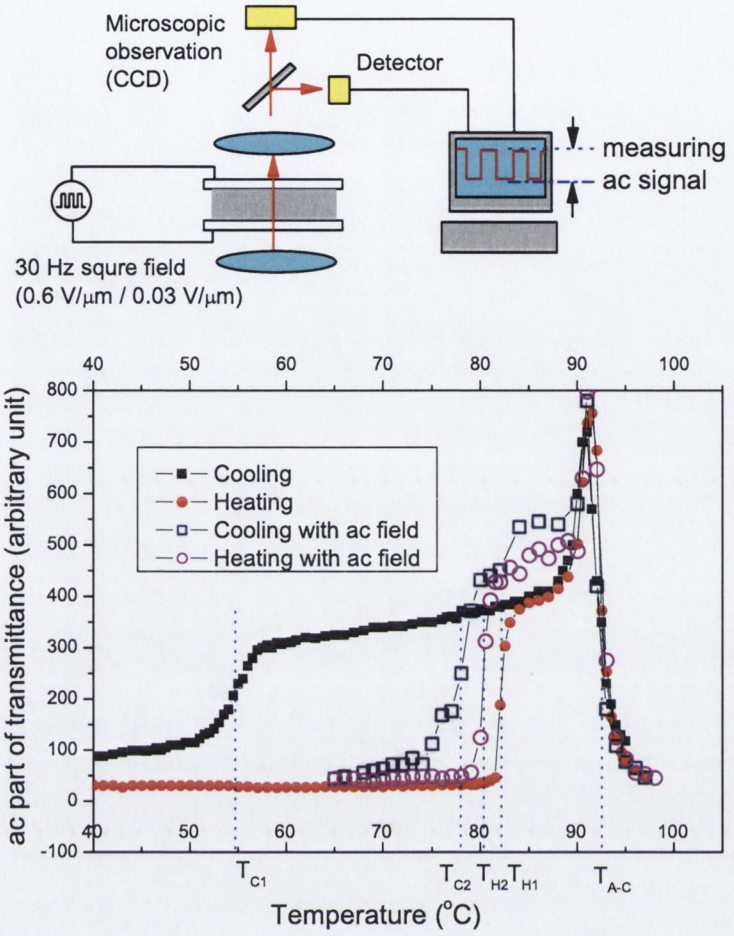

Figure 9.16: The ac part of the transmittance on weak ac field (30Hz, 0.03V/μm) as a function of temperature (1.6μm thickness, 12OF1M7). T_{C1} and T_{H1} were obtained during cooling/heating without field respectively, and T_{C2} and T_{H2} were obtained during cooling/heating with 0.6V/μm field

that the 30 Hz ac fields enhance the generation and the propagation of the solitary waves. This can be easily understood intuitively. 30 Hz ac fields makes the liquid crystal molecules reorient corresponding to the applied fields, and the vibration overcomes the suppression energy required by the surface effect.

Secondly, the critical field E_c is found to inversely depend on the cell thickness, *i.e.* the thinnest cell has the smallest E_c. This is already predicted by the model suggested in chapter 10. The effect of the surface is to make the ferroelectric synclinic order more stable, and so, it causes the transition temperature to decrease. Similarly, the surface effect makes the critical field E_c decrease as shown in Fig.

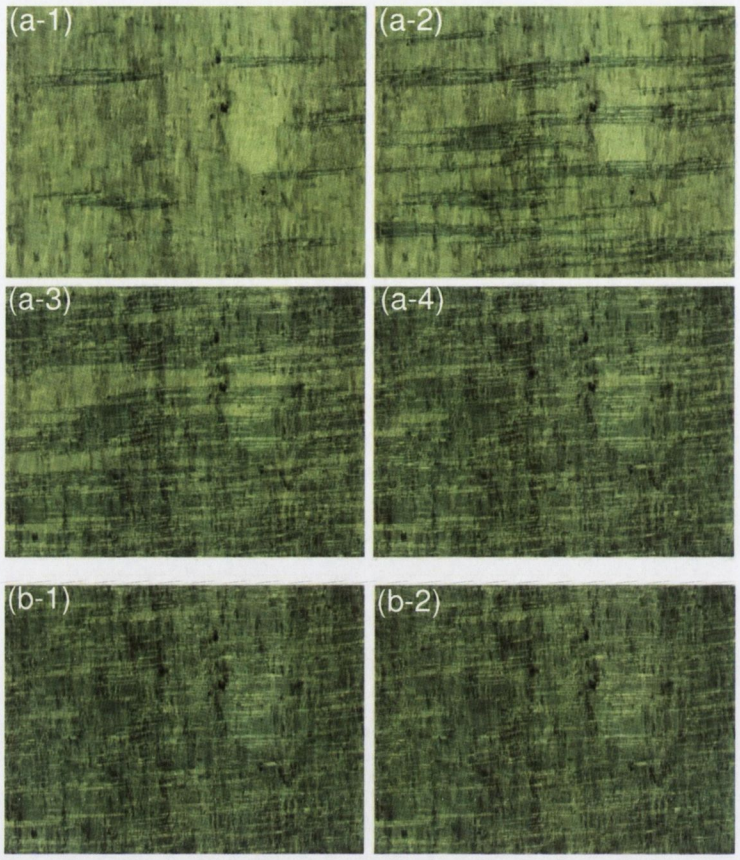

Figure 9.17: Microscopic images during the cooling experiment without ac field (solid square shaped points) shown in Fig. 9.16. (a)-1,2,3 and 4 were taken at 58, 56, 54, 50°C, respectively. (b)-1 and 2 were taken at 45°C promptly and after 5 minutes, respectively.

9.13.

Thirdly, the intermediate Sm$C^*_A(1/2)$ state becomes unstable as the cell thickness decreases. This is quite similar to the cell thickness dependence of the transition temperature of sub phases explained in chapter 10.

These phenomena need to be investigated in detail, but here, we only focus on the first phenomenon. That is, the ac square field helps the solitary wave appear and reduces the hysteresis significantly. If the same mechanism can be applied to the temperature induced phase transition, we can control the large supercooling phenomena by applying similar ac fields. For this, we carried out an optical measurement, for which the experimental setup is shown in the upper part of Fig. 9.16. A 1.6 μm thin cell containing 12OF1M7 is used. The cell is placed between

the two crossed polarizers and makes an angle of 22.5° with the polarizer. For inducing motion of the liquid crystalline molecules, a very weak (0.03 V/μm) 30 Hz square wave field is applied, and the ac part of the transmittance is measured. The SmC^* phase shows a very sensitive response to the weak field due to the strong Goldstone mode, but the SmC^*_A phase does not. Therefore, there is a clear contrast between two phases as shown in Fig. 9.16. This method is rather similar to the dielectric measurements, but it has a few advantages compared to these. The optical signal can be recalculated into the birefringence, and the experiments can be carried out with simultaneous direct microscopic observation. At very low frequencies such as 30 Hz, the ionic effect, which sometimes causes serious noise in dielectric measurements, is negligible.

The first experiment was carried out with only the weak signal field (30Hz 0.03V/μm square wave field) applied on cooling and heating. T_{A-C} in Fig. 9.16 is the phase transition between SmA^* and SmC^*, and T_{C1} and T_{H1} indicate the transition between SmC^* and SmC^*_A on cooling and heating respectively. As shown in Fig. 9.16, there is a very large supercooling effect which accords well with the results given in Fig. 9.4. Figure 9.17 shows microscope images recorded during the first cooling experiment, where (a)-1, 2, 3 and 4 were taken at 58, 56, 54, 50°C, respectively, while (b)-1 and 2 were taken at 45°C promptly and after 5 minutes, respectively. The images show that the phase transition occurs through the propagation of solitary waves as explained in chapter 6. However, the solitary waves appear over a wide temperature range in contrast to the case of a thick cell. Image (b) shows that even at 45°C, the SmC^* domains still persist. This implies that the surface suppresses the propagation of the solitary wave.

In the second experiment, a larger 30Hz 0.6V/μm square wave field was applied to the cell during cooling and heating. Only during measurement, was the applied field replaced with the weak signal field (0.03V/μm). Surprisingly, the supercooling effect was significantly reduced as shown in Fig. 9.16, where T_{C2} and T_{H2} indicate the transition temperature on cooling and heating respectively. This experimental result shows that an applied ac field assists the solitary wave to overcome its suppression by the surface effect in the thin cell.

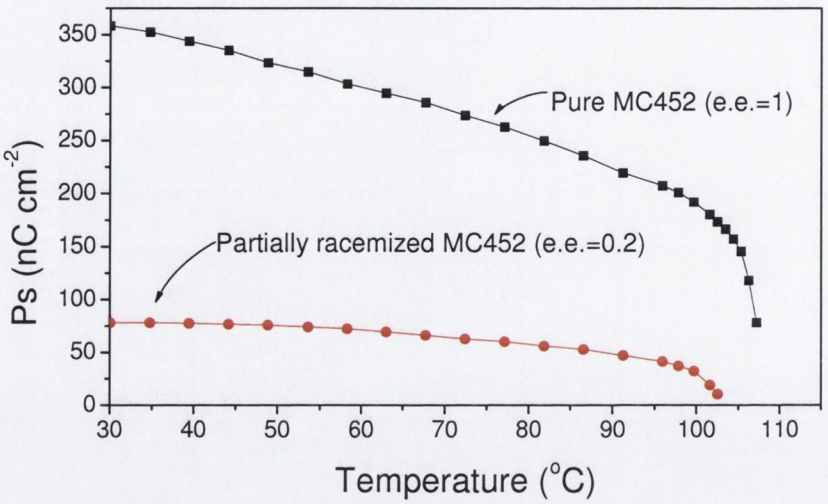

Figure 9.18: Spontaneous polarization of MC452 and its partially racemised mixture having e.e.=0.2, where e.e.=([R]-[S])/([R]+[S]).

These experimental results clearly show that the surface suppresses the generation and the propagation of the solitary wave, and thus, it produces the supercooling in the temperature induced AF–F transition and the hysteresis in the AF–F switching. The effect is more pronounced when the energy difference between the two states is small. Therefore, the largest supercooling appears near the critical mixing ratio R_c in the binary mixture.

9.3.5 Possible ferroelectric V-shaped switching in very thin cells of bulk antiferroelectric mixtures with nearly critical concentrations

In this way, the coexistence of the SmC^*_A and the SmC^* phases over a wide temperature range is explained by the suppression of the solitary waves. So far, various phenomenological theories regarding SmC^*_A–SmC^* transition have been suggested, but these models deal with only the static free energy minimum but not the dynamic process of the phase transition. These models have provided valuable information for finding the phase having the minimized free energy at given temperature and the phase sequence with temperature, but these are not applicable to explaining as to how the phase transition occurs at the transition

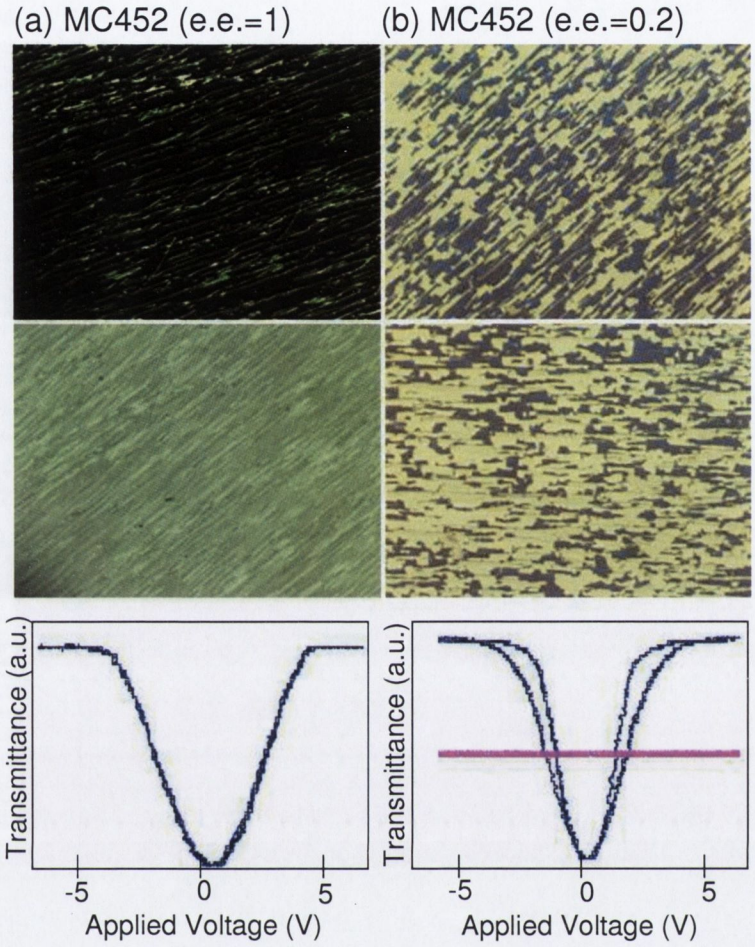

Figure 9.19: Nominally optically pure S moiety MC452 (e.e.= 1) shows a single domain with its extinguishing direction parallel to the smectic layer normal in a cell of thickness about 1μm (a), while its partially racemised mixture with R moiety has two domains (b). The switching characteristic also shows the difference. The red horizontal line in the switching graph (b) is the optical transmittance when turning the applied field off, which is due to the domains.

temperature. This is why it has widely been believed that the phase transition may simply occur when the minimum free energy shifts from one phase to another phase. However, our investigation for the dynamic process of the phase transition shows that the transition is not simple and the process can be easily suppressed. The terminology "frustration" seemed to be chosen due to the belief that the transition may rather simply occur, and as a result, the coexistence of the two phases is regarded as the frustration state, which means the both phases can be excited thermally and these easily transformed each other due to a small energy

difference between the two phases. However, as explained above, the coexistence of the two phases is actually caused by the suppression of the phase transition. The suppression is more effective when the energy difference between the two phases is small and the friction by the surface is strong, hence the coexistence and the gradual transition appear near the intermediate concentration and furthermore in a thin cell. Thus, the gradual phase transition or the so-called frustration phenomenon can be explained clearly by the suppression mechanism.

When the cell becomes really thin, e.g. 1 μm or less in thickness, so that the surface effects favoring ferroelectricity prevail in the whole sample, the surface stabilized ferroelectric states, in particular, the twisted ones, may possibly be produced even in the bulk antiferroelectric mixtures. This is particularly easy to occur when the mixture concentration is close to the critical one R_c. Note that the surfaces are more or less polar and force the spontaneous polarization in each layer to direct outwards or inwards. Depending on the polarity of the surfaces and the sign of spontaneous polarization of the sample mixture smectics, there exist two kinds of twisted states, TR1 and TR2, or TL1 and TL2 [151]. When the spontaneous polarization is large, an elastic constant concerning the **c**-director bend deformation apparently becomes very large because of the considerable bulk polarization charges, $\rho_P = -\mathrm{div}\mathbf{P}_s$, caused by the deformation [135, 136]. Therefore, the directors tend to be parallel to each other in planes vertical to the substrate plates to avoid any deformed structure so that the twisted regions become extremely thin and finally diminish; consequently, the complete extinction direction of the cell is observed along the smectic layer normal as contrasted with the ordinary twisted states. Mottram and Elston [131] reported a detailed theoretical investigation into the effects of polar anchoring which induces ferroelectric ordering close to the cell surfaces, in a liquid crystal cell containing an atiferroelectric liquid crystalline material. Experimentally, in fact, the V-shaped switching is almost observed in a 2 μm cell of the binary mixture with a concentration of MC452 close to R_c as shown in Fig. 9.9.

Although we have not yet performed any detailed switching experiment near the critical concentration region, we have observed the ferroelectric V-shaped

switching in the ferroelectric component of the binary mixture system here studied, MC452. Here we show the rather direct evidence for the relation between the switching characteristics and the polarization. We used nominally optically pure MC452 and a partially racemized R (MC452) and S (MC536) mixture of enantiomeric excess 60%. The racemized mixture has about 20% polarization of the pure material as seen in Fig. 9.18. The sign of polarization in MC452 is negative. The textures observed under crossed polarizers are given in Fig. 9.19. The pure MC452 cell shows a single domain, the extinction direction of which is along the smectic layer normal, whereas the *e.e.* = 60% cell shows two domains, which are the twisted surface stabilized states, TR1 and TR2. The substrate surfaces coated with RN-1175 apparently force spontaneous polarization to point outward. The lower part of Fig. 9.19 illustrates the response to a 0.1Hz triangular waveform electric field. It is of excellent V-shaped switching character and becomes sufficiently dark at $E = 0$ in the pure MC452 cell. When the field is turned off, it still becomes dark. On the other hand, the *e.e.* = 60% cell does not become sufficiently dark at $E = 0$ and shows some hysteresis; when the field is turned off, it is not dark naturally, for there exist the two domains. The in-plane directors are apparently aligned parallel to the plane normal to the smectic layer and vertical to the substrate plates, although the standard deviation is rather large $\sigma = 17.5°$, since our cell preparation technology was not good as seen in Fig. 9.19. The distribution becomes sharper at the tip of "V", as has been noticed in the early stages of investigation [152]. Similar experimental investigations in the antiferroelectric binary mixtures near the critical concentration R_c are interesting future problems to be studied.

9.4 Conclusions

We have investigated the gradual phase transition observed at intermediate concentrations of the binary mixtures of MC452 and MC881. These materials were originally synthesized for observing the thresholdless antiferroelectricity to

be used in displays. The similar phenomenon of gradual phase transition was reported by Gorecka et al. for the first time, but it was not clearly clarified mostly due to a poor understanding about the interlayer interactions at that time and in particular by their neglect of the quadrupolar term. We measured the interlayer interaction energy directly by varying concentration of the binary mixtures by using a method that was developed for measuring the interlayer interaction energy. The experimental results show that the energy difference Δ between the SmC^* and SmC^*_A phases and the slope of Δ decreases with increasing ratio of the ferroelectric material in the mixtures, but the energy barrier between the two phases remains large. The results are rather different from the assumption made by Gorecka *et al.* of neglecting the quadrupolar term, that is, the quadrupolar term was assumed to be zero. The experimental results allow us to understand the mechanism of the gradual phase transition observed in the material in the intermediate concentration in the thin cell. In the binary mixtures, the phase transition occurs through the solitary wave propagation, and the solitary wave propagation can be easily prohibited by the friction of the surface effects. When Δ is small, the solitary wave propagation is easily suppressed and some part of the cell remains in the meta-stable phase even after the temperature crosses the phase transition temperature. By changing the temperature further, the phase transition occurs gradually via the boundary propagation. Hence the two phases coexist over a wide range of temperatures. Since the gradual phase transition is similar to the phenomenon of thresholdless antiferroelectric switching in the sense that one state transits to the other state gradually, the thresholdless switching is naturally expected to arise from the same mechanism as for the gradual phase transition. Actually, we observed the thresholdless switching near the critical concentration using a thick cell. The mechanism is the same as the gradual phase transition, that is the suppression of the solitary wave propagation. This is different from the conventional models: the continuous evolution of ϕ and the Langevin-like alignment. We remark that the switching speed is too slow to use in applications. We also provide a better evidence for supporting the polarization steepness model for observing the ferroelectric V-shaped switching.

Chapter 10

The SmC_A^*(1/3) - SmC^* Liquid Crystal Phase Sequence Reversal

"In this chapter, *a theory for describing the cell thickness dependence of the stability of chiral smectic-C phases is suggested. The theory accords well with the experimental results.* "

10.1 Phase sequence reversal.

Discover of aniferroelectricity [10] in liquid crystals led to the intensive research activities into the detailed study of SmC_A^*, which results in the identification of various ferrielectric subphases (SmC_A^*(1/2) and SmC_A^*(1/3)) in the temperature range between SmC_A^* and SmC^* phases [12]. Investigations on chiral smectic phases are not only of interest from the view point of practical applications but also from basic science: to study the molecular interactions.

The apperance of these subphases can be understood as a result of the competition between the antiferroelectric and ferroelectric interactions in adjacent

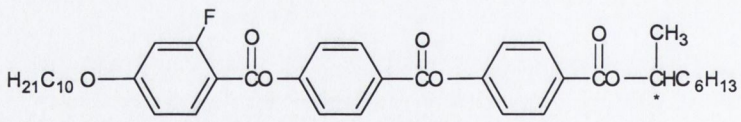

Figure 10.1: Chemical structure of 10OHF.

smectic layers, which stabilizes the SmC_A^* and the SmC^* phases. This competition produces various ferrielectric subphases with a different sequence of AF and F orderings among the smectic layers and are observed only in the chiral systems, in the temperature range where the free energy of synclinic ferroelectic and anticlinic antiferroelectric interactions are almost equal [51, 143]. These subphases are characterized by so-called short-pitch periodicity. Detailed experimental study and the theoretical model describing the intermolecular interaction results in the conclusion that liquid crystal sample exhibit the phase sequence SmA- SmC_α^* - SmC^*- Sm$C_A^*(1/3)$- Sm$C_A^*(1/2)$- SmC_A^* on decreasing the temperature. In some systems some phase may be missing, but if they exist they will always appear in the same phase sequence upon cooling. The SmC_A^* is the lowest temperature phase. The SmC_A^* and the subphases Sm$C_A^*(1/2)$, Sm$C_A^*(1/3)$ show 2- 3- and 4- layer periodic structures respectively. The SmC_α^* phase was reported to have temperature-dependent periodicity varying from 5 to 8 layers and is similar to the SmC^* but having a very short helical pitch [153, 154]. In addition to this well-established phase sequence, other ferrielectric subphase with longer short pitch periodicity and existence of the two kind of the SmC_α^* phases were also reported [24].

Faye et.al [155] have observed the unusual phase sequence in chiral non-symmetric dimesogen 10BB5BBB8*; When a sample was cooled slowly, the Sm$C_A^*(1/2)$ phase appeared in the narrow temperature range between SmC_α^* and SmC^*. Later Laux et. al [156] also reported the unusual phase SmC^*-Sm$C_A^*(1/2)$-SmC_α^* sequence in the 10HF. On a free surface drop, they observed Sm$C_A^*(1/2)$ above SmC^*, where the temperature range of the Sm$C_A^*(1/2)$ phase was about 2°C in heating and about 11°C on cooling. Recently Wang et.al [157] reported the same phase sequence reversal in 10OHF by null transmission ellipsometry and in the

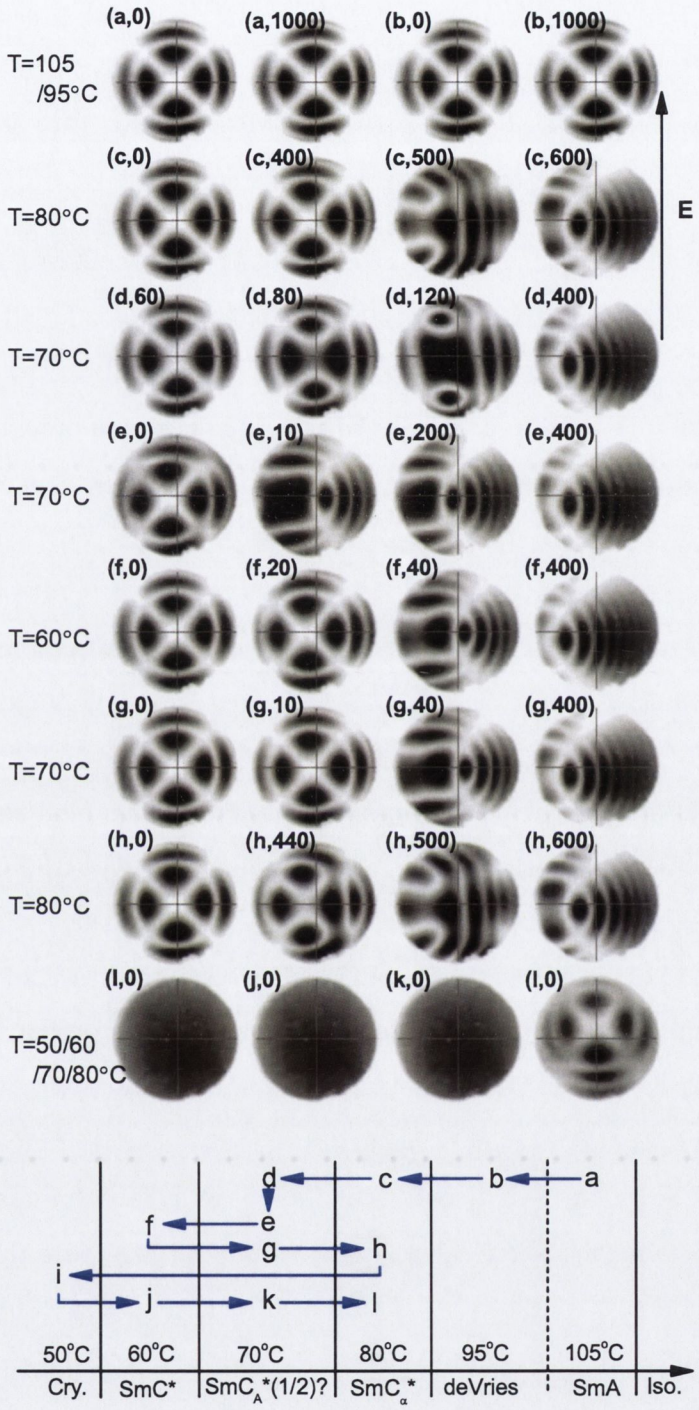

Figure 10.2: Conoscopy as a function of temperature and applied filed (1Hz, rectangular wave fields). Experiments were carried out as following orders: (a) 105°C (SmA) → (b)95°C (de Vries SmA) → (c)80°C (SmC^*_α) → (d) 70°C (Sm$C^*_A(1/2)$) → (e)70°C (SmC^*) → (f) 60°C (SmC^*) → (g) 70°C (SmC^*) → (h)80°C (SmC^*_α) → (i)50°C (Cr) → (j)60°C (Cr) → (k)70°C (Cr) → (l)80°C (SmC^*_α). The numbers in each image represents the amplitude of the applied field (V/mm).

binary mixtures with 9OTBBB1M7 by employing both null transmission ellipsometry and resonant X-ray diffraction. Sandhya *et al.* reconfirmed the phase sequence reversal [158]. Figure 10.1 shows the chemical structure of 10OHF, and its phase sequence is shown in the lower part of Fig. 10.2.

Conoscopic measurement, where thick homeotropic cells are used, is useful to analyze the bulk properties of liquid crystal, since it can rule out the possibility of the surface effect playing any role in the results obtained by using planar cell measurements. A homeotropic cell of 75μm thickness was prepared and conoscopic measurement was carried out with the temperature sequence plotted in Fig. 10.2. At each temperature, the conoscopic images were recorded at various applied fields. Images (a) and (b) in Fig. 10.2 show typical behaviors of SmA phase. Even though in de Vries SmA the molecules are tilted, the random distribution leads to a uniaxial overall symmetry. So, the conoscopy couldn't distinguish de Vries (b) and conventional (a) SmA phases. Images (c) and (h) shows the typical behaviors of SmC^*_α where the unwinding of helix requires relatively high fields and the intermediate state shows high negative biaxiality with the increasing tilt angle [33]. Images (e), (f) and (g) are one of the typical behavior of the SmC^* phase [34, 51]. The unwinding of the SmC^* phase has no threshold and increase of the voltage shifts the center of the image in the direction perpendicular to the applied field and the center continues on shifting in this direction with an increase in voltage. This is such a typical behavior of a ferroelectric SmC^* phase [34]. Image (d) has a slight threshold (note that the image at 60 V/mm is the same as the state at 0V/mm) and show a biaxiality without tilting (note that the image at 80V/mm has no tilt but has a biaxiality and the image at 120V/mm shows very high biaxiality but the tilt angle of this is very low) and the optical plane is parallel to the direction of the field. This is the typical signature of a Sm$C^*_A(1/2)$ phase [31, 51]. However, once the phase is completely unwound by applying fields and becomes ferroelectric SmC^* phase, it retains there (e) even after turning off the fields, unless it is cooled from SmC^*_α again. If the sample is heated from low temperature phase, SmC^*, it shows the behavior of SmC^* (g) at the temperature 70°C where Sm$C^*_A(1/2)$ would have normally appeared under the cooling cycle.

Note that image (e) shows initially rapid unwinding compared to that of the image (g). This is because image (e) was recorded just after removing the field *i.e*, just after taking the image (d). Usually, after applying the field in a homeotropic cell of SmC^* phase and turning off the field, the sample does not return to a perfectly coiled initial helical structure, but it contains defects or disclination lines. The disclination lines imply that the helical fractures that have occurred during the helical unwinding process persist after the field has been removed. Especially, in this material, we think that the energy difference between the synclinic and anticlinic states is somewhat lower than in the usual ferroelectric materials, and more disclination lines can persist easily after turning off the field. Therefore, the state (e, 0) at zero field is not a perfect helical structure, but a slightly distorted helix. We observed the slightly tilted image of (e, 0) compared with other images at zero field. The slightly distorted helical structure can easily be unwounded by applying the field. This makes a slight difference in the images. On the other hand, (g) is obtained by heating the cell slowly from 60°C with an almost perfect helical structure. When it is heated from crystalline it melts to SmC^*_α phase indicating the absence of SmC^* and Sm$C^*_A(1/2)$ phases (images i-l) in heating mode. Eventhough the conoscopic figures at Sm$C^*_A(1/2)$ phase shows similar behaviour of ferriphase there is some difference. It is not like usual Sm$C^*_A(1/2)$ phase which is reported in the literature [51]. The melatopes are not perpendicular to the field which is observed usually in Sm$C^*_A(1/2)$ phase. We are observing the behavior similar to that of Sm$C^*_A(1/3)$. The difference of the melatopes between the Sm$C^*_A(1/2)$ and the Sm$C^*_A(1/3)$ phases is induced by the residual spontaneous polarization. In the Sm$C^*_A(1/2)$, the residual polarization is canceled out by the symmetric structure of the Sm$C^*_A(1/2)$ as the case in the SmC^*_A phase, and the melatopes in the usual Sm$C^*_A(1/2)$ phase are perpendicular to the field [51]. Whereas, in the Sm$C^*_A(1/3)$, there exists a large residual polarization, and the melatopes becomes parallel to the field [51]. The metastable phase observed in conoscopic measurement at 70°C was confirmed to be a Sm$C^*_A(1/2)$ instead to Sm$C^*_A(1/3)$ by many [157, 158], as explained above.

There may be two reasons for this behavior. First reason is the flipping of

the molecules occurred thermally owing to the defects. Miyachi *et al.* [159] observed the disordered and fluctuating feature in laser diffraction of the Sm$C_A^*(1/2)$ phase. They explained this behaviour by flipping of the synclinic molecules. This will create an effective in-plane spontaneous polarization perpendicular to the tilt plane. Such flipping of the molecule may easily occur thermally, because it does not change the number of the anticlinc (A) and synclinc (F) orderings of adjacent layers. The consecutive molecular arrangement of a unit cell ASASASAS... may become ASSAASAS.... The energy difference between these two molecular arrangements is very small, but the latter has an effective spontaneous polarization. This means that flip of the **c** directors of only one of the layers has given rise to this changed structure. The unit cell on the average has periodicity of four layers because such a defect may occur only in one out of say 100 layers. This flipping of molecules in some parts of the smectic layers may be caused by the soliton-like wave motion. This will cause both the static and dynamic distortions in the helicoidal structure. It may not be possible to observe such a defect even using resonant x-rays. The second reason may be the Sm$C_A^*(1/2)$ phase existing at high temperature is unusual and metastable, i.e, the stability of the Sm$C_A^*(1/2)$ phase is rather weak compared with the normal low temperature Sm$C_A^*(1/2)$ phase. The conscopic image obtained at 70 °C has a small tilt angle but a large biaxiality. Moreover, a slight threshold appears. The low threshold is a characteristic of Sm$C_A^*(1/2)$ but not of Sm$C_A^*(1/3)$ phase. Therefore we conclude that phase under consideration is Sm$C_A^*(1/2)$. However, the observed direction of the melatopes is parallel to the applied field. The direction of the melatopes is determined by the residual polarization. In Sm$C_A^*(1/2)$ phase, the spontaneous polarization of each layer is almost canceled out by the opposite direction of the neighbouring polarization, and a small residual polarization is almost parallel to the **c** director as shown in a schematic Fig. 10.3(a) However, when the symmetric balance is broken, that is, when one of the polarization vectors is larger than the other, the melatopes rotate as shown in Fig. 10.3(b). This may give rise to a disturbed structure for Sm$C_A^*(1/2)$ phase as is observed here.

We came to the conclusion that the high temperature phase is 4-layer

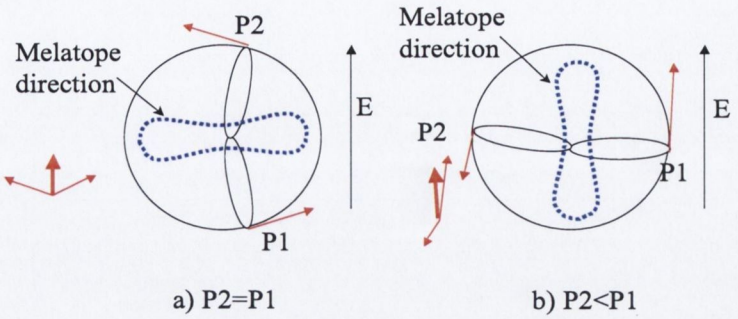

Figure 10.3: Schematic diagram illustrating the dependence of directions of melatopes on the residual polarization for (a) P2=P1 and (b) P2<P1.

phase and exhibits the phase sequence SmC^*_α – Sm$C^*_A(1/2)$ – SmC^* in cooling mode. Summarizing we find that both high temperature Sm$C^*_A(1/2)$ phase and low temperature SmC^* phase is monotropic and high temperature Sm$C^*_A(1/2)$ is metastable i.e once the sample is transformed to SmC^* phase on application of electric field or cooling to the SmC^* phase, it retains there and it does not come back to original state on removal of the field or heating from SmC^* phase, unless it is cooled from SmC^*_α phase again.

To improve the stability of the Sm$C^*_A(1/2)$ phase we have studied the binary mixture of 10OHF with C9. Fig. 10.4(a)[1] shows the temperature dependent dielectric permittivity for 1kHz done in cooling mode for a different concentration of C9 with 10OHF (quantified by the value of the parameter X; for example X=10 is 10wt% of C9 in 10OHF). It has been observed that the range of the Sm$C^*_A(1/2)$ phase increases with the concentration of C9. The range of low temperature SmC* phase also increases initially, upto X=25 mixture, then it starts to decrease and finally for X=55 mixture the SmC^* phase disappears. Hence there is no phase sequence reversal for X=55. When sample is heated from the SmC^* phase, the high temperature Sm$C^*_A(1/2)$ phase does not exist in heating mode for X=0, as we discussed earlier. But it exists even for X=10 and the range increases with the concentration of C9 (see Fig. 10.4(b)). It has been observed that the range of Sm$C^*_A(1/2)$ phase is smaller compared to that in cooling mode. When the sample

[1] All experiments shown in Fig. 10.4 were carried out by Dr. K.L.Sandhya.

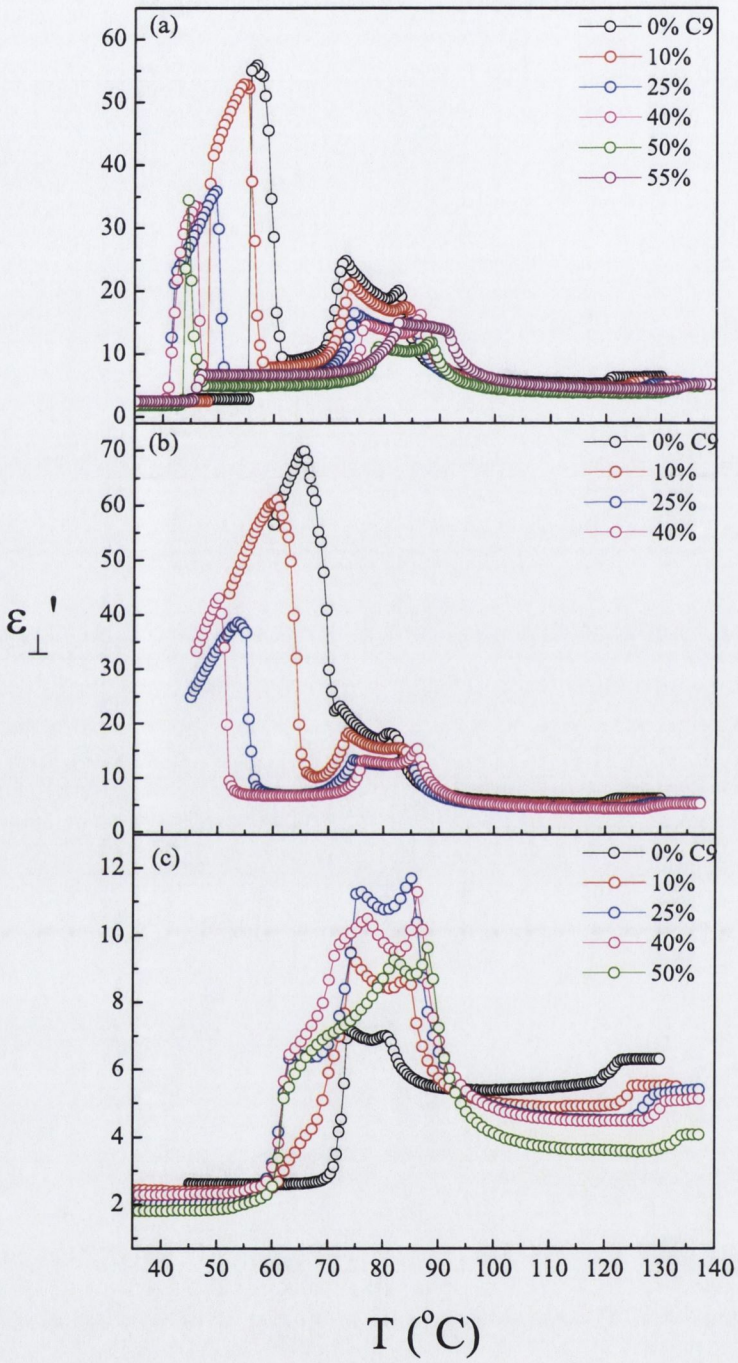

Figure 10.4: (These data were obtained by Dr. K.L.Sandhya.)Temperature dependence of dielectric permittivity for 1kHz in (a) cooling (b) heating from low temperature SmC^* phase and (c) heating from Crystalline for different mixtures.

is heated from the crystalline the low temperature does not exist even for the mixture (Fig. 10.4(c)) and hence the SmC^* phase is monotropic.

Thus, the reversal of the phase sequence has been observed many times, but a proper theory has not been suggested so far.

10.2 Simple phenomenological description for the phase sequence reversal.

At present state, it is not easy to give a clear theoretical model for explaining the phase sequence reversal, but it may be worthy to have a brief glance about this. After the first phenomenological theory for the phase transitions among the SmC phases was suggested by Orihara and Ishibashi [82], various phenomenological theories have been suggested to accommodate as many experimental results as possible as explained in the previous chapter. Though the details of the phenomenological models vary, a few terms, especially governing the SmA^* - SmC^* phase transition and the SmC^* -SmC_A^* transition are quite similar. Let us start from the phenomenological model suggested by Emelyanenko and Osipov [14, 65].

$$VF_b = \sum_{i=1}^{N} \Big[\tilde{F}_0(\theta) - \tilde{a}\frac{\Delta T}{T^*}(cos\varphi_{i-1,i} + cos\varphi_{i,i+1}) - \widetilde{B} \\ (cos^2\varphi_{i-1,i} + cos^2\varphi i, i+1) + \frac{1}{2\chi}\{\mathbf{P}_i^2 + g(\mathbf{P}_i\mathbf{P}_{i+1} \\ +\mathbf{P}_i\mathbf{P}_{i-1})\} + c_s(\mathbf{P}_i\xi_{i+1}) + c_f cos\theta(\mathbf{P}_i\Delta\mathbf{n}_{i\pm1})\Big], \tag{10.1}$$

where $\tilde{F}_0(\theta)$ is the tilt angle dependent free energy part governing the non-tilted to tilted phase transition, that is the SmA^* – SmC^* phase transition, and the second and third terms are designed for expressing the synclinic phase to the anticlinic phase transitions, that is the SmC^* – SmC_A^* transition. T^* is the transition temperature between the synclinic and anticlinic smectic C phases in the absence of any intermediate phases. $\Delta T = T - T^*$. The first three terms commonly appear in the most phenomenological model in slightly different forms. The other terms

in Eq. 10.1 are the spontaneous polarization terms including the flexoelectric polarization, which is believed to govern the generation of sub-phases between SmC^* and SmC^*_A in the model. While the last four terms are different and are model dependent and sometimes controversial, the meaning of which are not explained here as these are not concerned with a problem of the phase reversal. The first three terms are rather clear in physical meaning and these appear in slightly different forms in the various phenomenological models based on Landau free energy expansion.

The physical meaning of the second and the third terms of this phenomenological expression can be easily understood, even though the origin of the parameters is not simple to find. The **c**-directors between neighboring layers are likely to be in one plane by positive $\tilde{B}$ (that is, synclinic or anticlinic orderings), and as temperature increase, the ferroelectric configuration is favored by positive $\tilde{a}\Delta T/T^*$. In most compounds and mixtures studied so far, the ferroelectric phase has been observed at a higher temperature than antiferroelectric phase. For this reason, $\tilde{a}$ is assumed to be always positive. Note that ΔT is positive for higher temperatures and is negative at lower temperatures than temperature T^*, and as a result, if $\tilde{a}$ is positive, the ferroelectric configuration is stable in a high temperature range. On the contrary, if $\tilde{a}$ is negative, this is stable over a low temperature range. In this way, the phase sequence between the synclinic and anticlinic phases is determined by the coefficient $\tilde{a}$.

Physically, coefficients $\tilde{a}$ and $\tilde{B}$ may be originated from the steric and the van der Waals interactions between nearest layers [99]. Both the steric and the van der Waals interactions contribute to positive $\tilde{B}$, and so, undoubtedly, $\tilde{B}$ is positive. Osipov et.al. [65, 109] suggested that the positive $\tilde{a}$ arises from the anisotropic dipole-dipole dispersion interaction, where the steric energy is rather independent to the temperature while the instant dipole-dipole interaction between two neighboring layers strongly depends on the temperature. According to their model, $\tilde{a}$ should be positive and the phase sequence reversal may not appear. However, the observations of the phase sequence reversal imply that $\tilde{a}$ is actually negative in these particular materials. It is surely not a usual case, but a negative

value of $\tilde{a}$ may be possible, though a clear theoretical model cannot be present at this state.

We suggest that the steric energy is also strongly temperature dependent, extremely large at low temperatures and it reduces to a low value with increase in temperature. The instant transverse dipole-dipole interaction energy continues to dominate at higher temperatures. We suggest that the temperature dependence of the steric energy gives rise to negative $\tilde{a}$, i.e., synclinic is favored at low temperatures and anticlinic at high temperatures. This can give rise to the phase reversal sequence observed here.

The importance of the steric term was verified experimentally by Lee and Lim [160]. In the paper, the antiferroelectric phase is induced by adding a dopant, which reduces the steric energy by acting as a lubricant material. This implies that the steric energy strongly depends on the surface morphology of layers, and so, it is very difficult to describe the strength and the dependency with temperature accurately with a simple molecular model given by Osipov and Fukuda [109], where the dependency of the steric energy with temperature is simply ignored. Song *et al.* [84] measured the interlayer interaction as function of temperature in an antiferroelectric material, where the energy difference (Δ) between the synclinic and anticlinic positions increases and saturates quickly with decreasing temperature, whereas the spontaneous polarization keeps increasing with decreasing temperature for an entire temperature range. The measured energy difference Δ even shows a slight decrease at low temperatures. The increasing spontaneous polarization with the decreasing temperature implies that the molecular order parameter and the steric energy may keep increasing with the decreasing temperature, and the steric energy could induce the saturation and even decrease in Δ with the decreasing temperature. This result also shows that the steric energy is temperature dependent and could significantly contribute to the phase reversed behavior as has been experimentally observed here. At higher temperatures the steric energy may indeed be negligible.

Thus, in some materials, $\tilde{a}$ may be negative due to a strong contribution by the steric energy. In this case, ferroelectric phase presents at low temperature, and antiferroelectric phase exists at large temperature. Hence, by the negative value of $\tilde{a}$, the phase sequence reversal is expected. On addition of the material exhibiting antiferroelectric phase, favours the high temperature AF phase and hence in the binary mixture the range of AF phase not only increases significantly but also becomes stable.

Part. V

Interlayer interaction and Unwinding process in the SmC^* phase.

Chapter 11

Mechanism of field induced unwinding of SmC^* helix.

"In this chapter, *the mechanism of the field induced helical unwinding in the SmC* phase is investigated. New model based on the helical fracture is suggested and various physical properties are interpreted by using the new model. "*

11.1 Topological problem in the helical unwinding

The mechanism of unwinding of a helical structure is common to many areas in soft condensed matter physics and in biology. To complete the unwinding of the helical structure, two problems should be solved. The first one is that the twisting force, which induces the helical structure, should be overcome. For that, an external force usually applies on the helix to untwist it. The external force may depend on the energy difference between the coiled state and the unwound state. The helical unwinding in the SmC^* phase has been dealt with mostly in

this view point, that is, how large is the twisting force of the initial helix of the SmC^* phase. The other problem to be solved is a topological problem. In a helix having m nodes, one end has $2\pi m$ phase difference from the other end of the helix. To obtain the unwound state, the phase difference between two ends should be overcome. This problem is rather similar to disentangling a tangled string. Though this topological problem is an essential part in the helix unwinding, this problem has been commonly ignored.

Three mechanisms can be conceived to solve this topological problem. The first one is found in the unwinding of the helical structure of DNA in biology. The super twisted helix of DNA is unwound with the addition of enzymes called topoisomerases which fracture the helix selectively, and then reconnecting it for duplication and reproduction [161]. The animate nature has developed the helical fracturing technique for its evolution. Thus, the break in the helical structure into segments is an easy and an efficient method for solving the topological problem. The second mechanism is found in the conventional model for the helical unwinding of the cholesteric and the SmC^* phases, where the end molecules of the helix makes numerous turns for an unwinding process to be completed. This model is called as the diverging pitch model. Especially, this model was well-established in the cholesteric liquid crystals. The third one was suggested by Glogarova *et al.* [122] in the thin planar cells of the SmC^* liquid crystals. When the pitch is rather similar to the cell thickness, the liquid crystals in the center part of the cell have a helical structure, while those near the surfaces have the surface induced unwound structure. With applying field, the unwound part of the surface area enlarges by a loss of the helical area in the center part.

Figure 11.1 shows the schematics for the first and the second methods, that is, the helical fracture method (a) and the diverging pitch method (b). In the helical fracture method, the helix is divided into several segments, and it can reach the unwound state easily. In the diverging pitch model, the end point (blue circle) should rotate as many turns as the number of nodes. The third method (for details, see reference [122]) is quite clever method to avoid the complicate topological problem, but this method is possible only for thin cells and long pitch

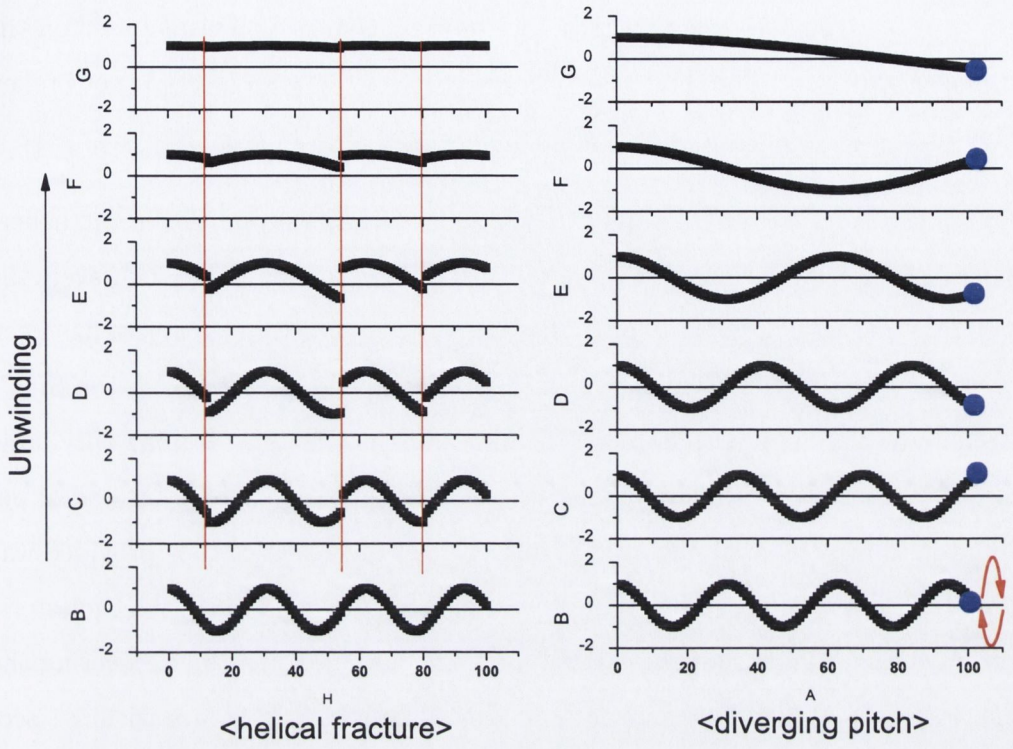

Figure 11.1: Schematics for the helical fracture (a) and the diverging pitch (b). In the helical fracture method, the helix is divided into several segments, and it can reach the unwound state easily. In the diverging pitch model, the end point (blue circle) should rotate many turns.

materials. Our interest is in the bulk property in the helical unwinding process but not the surface induced effect. For example, in thick planar cells using quite short helical pitch materials, or homeotropic cells, the third method is not suitable. Therefore, the intrinsic method for solving the topological problem in the helical unwinding is required.

The helical unwinding in FLCs brought about by the application of an external electric field has a similar topological problem to that of DNA, but has been explained differently, as described above. In 1977, Meyer [162] gave a model for the field-induced unwinding process of the helix in SmC^*, analogous to that in cholesteric liquid crystals also proposed by him [163]. The continuity of directors along the normal to layers is not broken during the unwinding process because the unwinding occurs through the pitch diverging, that is, the pitch increases with an increase in the applied field and finally it diverges to infinity at the critical

field E_c, where the helix is completely unwound [2, 164–167]. This is based on the continuum approximation, and the synclinic ordering between layers is not broken at any layers and at any applied field.

This diverging pitch model explains well the basic properties of the helical unwindings and is supported by a few experimental results [168]. However, the unwinding mechanism in the SmC^* phase based on the diverging model has been occasionally suspected. Cladis *et al.* [169] reported that the helix in the SmC^* phase may not reach to the completely unwound state though applying very large field. They insisted that many highly distorted 2π solitons [1] appear instead of being unwound fully by applying a field [169]. One of the evidence they provided was the contrast between the unwinding process of the SmC^* phase and the cholesteric liquid crystals. When the field is turned off, the time required for recovering the initial state is much different in both phases. The recovery occurs within 1 second in the SmC^* phase, but it takes about 1–10 minutes in the cholesteric liquid crystals. This implies that the unwinding mechanisms of the two liquid crystalline phases may be different. However, later, their highly distorted soliton model was denied experimentally by Maclennan *et al.* [170].

As shown in the previous chapters, the angle difference between two adjacent **c** director can transit from the synclinic to the anticlinic by an electric field or temperature, which means that the interlayer interaction cannot be explained fully by the continuum approximation. Moreover, it was reported that a number of helical fractures are produced by a relatively low field in some FLCs [34]. This is to state that the continuity of the helix can easily be broken, which is fundamentally different from the diverging pitch model. Thus, the helical unwinding in FLCs can be based either on the continuum theory or on a theory where the helix is fractured into smaller segments. If the helical unwinding in FLCs is based on the latter model, its mechanism for solving the topological problem becomes similar to that in DNA.

[1] Note that the 2π soliton is a different concept from the solitary waves and the 2π walls as being shown in the previous and this chapters. The 2π soliton forms along normal to layers.

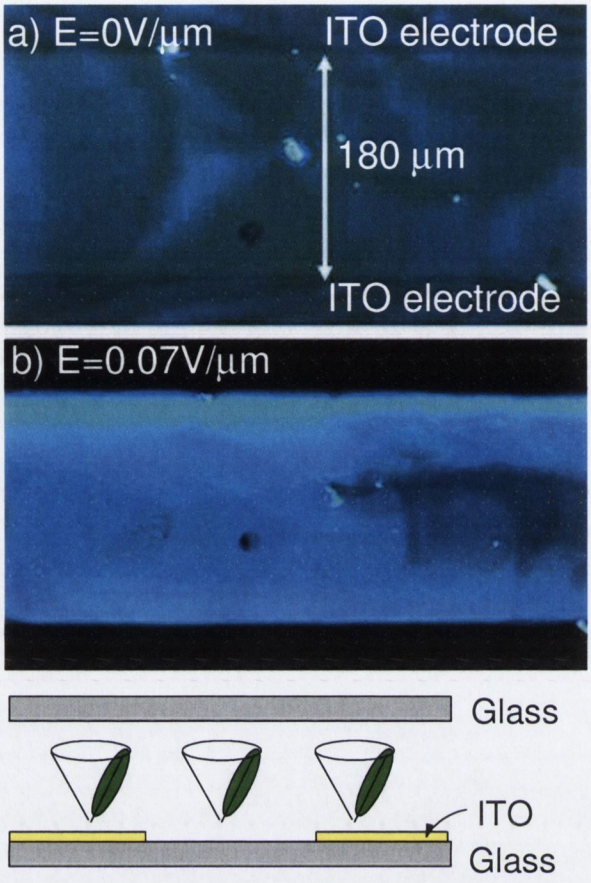

Figure 11.2: Microscopy for a thin homeotropic cell (d $\approx 7\mu$m, 88^oC) using 12OF1M7 without field (a) and with field (b).; From E $\approx$ 0.07V/μm (b), many domains indicating the helical fractures appear.; Schematic for the cell structure is shown in the lower part.

In this chapter, we propose a theory of the helical unwinding of SmC^* phase based on the model where the topological problem of the helical unwinding is solved by the helical fractures, and explains the experimental observations of dielectric response as a function of the bias field, which cannot be explained by the diverging pitch model. Basically, we do not deny the conventional diverging pitch model, which is still valid for some experimental conditions and materials [168]. However, we intend to expand the understanding of the various phenomena occurring during the helical unwinding, some of which does not follow the conventional model.

Recently, Krueger *et.al.* [171] reported that the helical pitch in various FLC materials does not change during the helical unwinding in planar cells in contrast

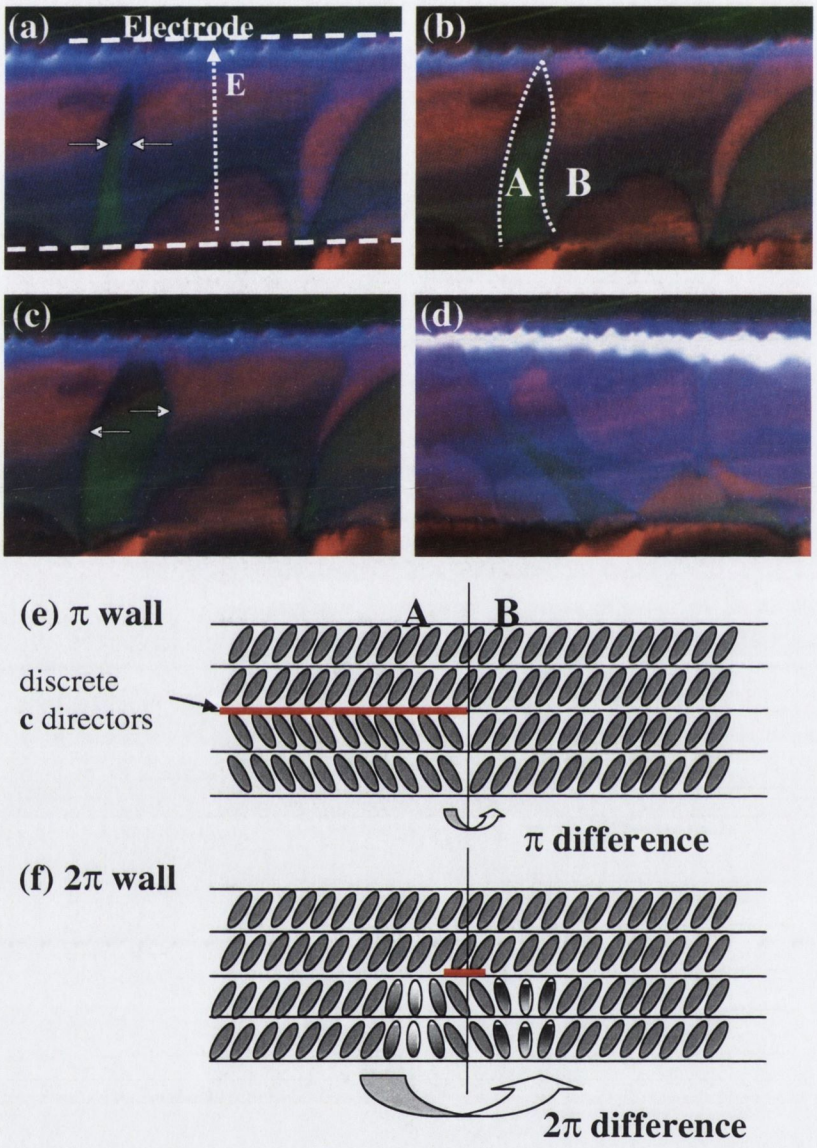

Figure 11.3: Micrographs (×200) of a thin homeotropic cell (1.5 μm) using MHPOOCBC at 70 °C.; Fields applied are (a) 28 V/mm, (b) 30 V/mm, (c) 32 V/mm, and (d) 42 V/mm. The domain walls move toward the direction of the arrows in images (a) and (c), but they remain stationary in image (b). (e) is a schematic diagram for the domain wall between areas A and B in image (b) (π wall-single dark line). This is also schematics for the helical fractures. π walls always are accompanied by discrete **c** directors, that is, helical fractures. (f) is a schematic diagram for 2π wall (2 dark lines).

to a few earlier observations [168] on DOBAMBC and similar compounds. They explained the phenomenon by using earlier models where the surface effect with disclination lines on surface is large enough to prevent helix from diverging [122], and that the relaxation frequency of the helical unwinding is too low to be detected in usual experiments [165]. Anyway, they proved the fact that the pitch does not diverge in planar cells in most FLCs. In a thin cell using a material having long helical pitches, the stationary helical pitch can be easily understood through the third method suggested by Glogarova et al. [122], but when the pitch $\ll$ the cell thickness, the unwinding process is not understood. Without pitch diverging, the break of helix should exist during the unwinding process as is in the unwinding of DNA.

We carried out microscopic observation with increasing fields using 12OF1M7 (Kingston Chemicals Hull, UK) and a thin homeotropic cell (cell thickness d $\approx$ 7μm) to minimize the surface effect. The cell structure, which is shown in Fig. 11.2, is designed to minimize the surface effect, where the homeotropic alignment is applied and so, the smectic layer is parallel to the glass plates. Moreover, thin ITO electrodes are used instead of wall electrodes, so no surfaces, which could generate the surface induced unwound part as is in a thin planar cell, exist. We find that many domains occur for $E \approx 0.07\text{V}/\mu\text{m}$ as shown in Fig. 11.2(b). The domain walls have single sharp lines indicating that these are π walls and accompany with the helical fractures as shown in Fig. 11.3(e) [34, 96, 172, 173]. The domain walls, which are observed in free standing films or homeotropic cells, are usually 2π or π walls. These are stabilized at the synclinic or the anticlinic minimum state. 2π walls have a double dark line under cross polarizers (sometimes 4 dark lines) and there is no difference in the relative angles of two adjacent layers ($\Delta\phi$) between the two domains separated by the walls, which means that 2π walls need not to be accompanied by the discrete **c** directors as shown in Fig. 11.3(f). On the other hand, less than 2π walls, one example of which is a π wall, have a single dark line (it can rarely be a double line) and are always accompanied by the discrete **c** directors, because $\Delta\phi$ between two domains separated by the walls are

different, which means at least one of the two domains has a discrete **c** director [96] as shown in Fig. 11.3(e).

We carried out the same microscopic observation using a thiner cell (d $\approx$ 1.5μm) with MHPOOCBC, where only 3–4 helical pitches locates in the cell. MHPOOCBC has very sensitive optical rotary power to the wavelength of light in the visible range, so despites of the thin cell thickness, the domain boundaries are well-distinguished as shown in Fig. 11.3. At zero field, a few 2π walls are observed. To check the domain boundaries are the π walls, we applied fields. The 2π walls separate into two π walls by the field. The clearly different color between domains A and B indicates the slightly distorted helical structure. Note that the optical rotary power is very sensitive to the helical structure. The domains overlapped but their boundaries did not appear to interfere with each other. This shows that the boundaries of domains are located in different layers. As explained above, the π walls always accompany with the discrete **c** director shown in the schematic (e) in Fig. 11.3. Thus, we can see that the low field generates the discrete **c** director, which induces the about a half pitch unwinding of the helix, which induces the different color in both domains.

Spectroscopic experiment using a thick homeotropic cell (d $\approx$ 100μm) was carried out to find the field dependence of the pitch. Figure 11.4 shows the results, where surprisingly, the selective reflection peak λ ($p \approx \lambda$/n, n is a refractive index) shows a step-like increase at the field the helical fractures occur as shown in the lower part of Fig. 11.4. When E= 0.07 - 0.1 V/μm, many propagating domain walls are observed in microscopy and the peak is not observed in spectroscopy (see the upper part of Fig. 11.4). At large fields, the peak is broad and multi-peaked, and disappears with a further increase in the field (Fig. 11.4). This observation clearly shows that the helical unwinding occurs through the helical fractures but not the pitch diverging. The applied field increases the stress on the helix, and the stress is released by the helix getting fractured through the domain wall propagation. Here, the helical pitch increases with the helical fractures, because each π wall propagation reduces the helix by half a turn. This is fundamentally different

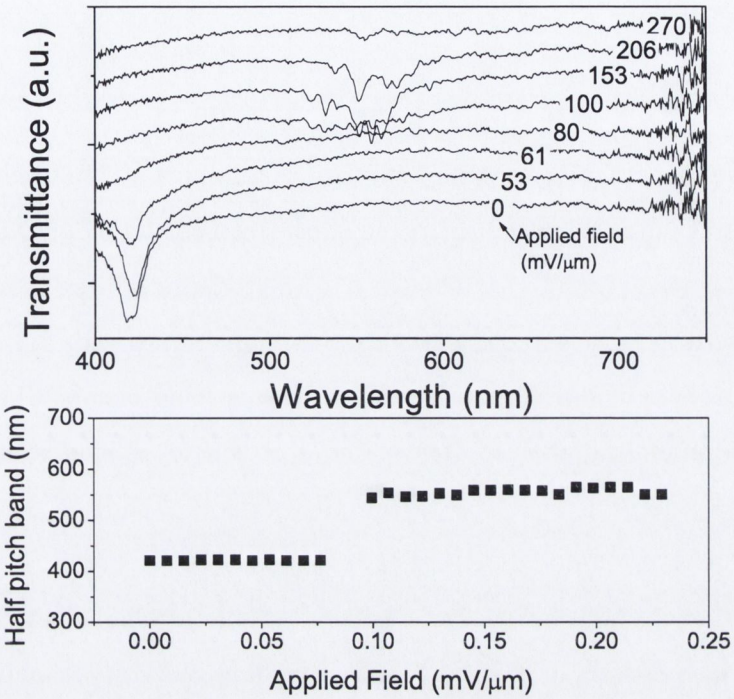

Figure 11.4: Visible spectroscopy for various applied fields (a) and the selective reflection peak with increasing fields (b) for a thick homeotropic cell (d $\approx 100\mu$m, space between two metal wall electrodes $\approx 500\mu$m). It shows a step-like increase at the field where the helical fracture occurs.

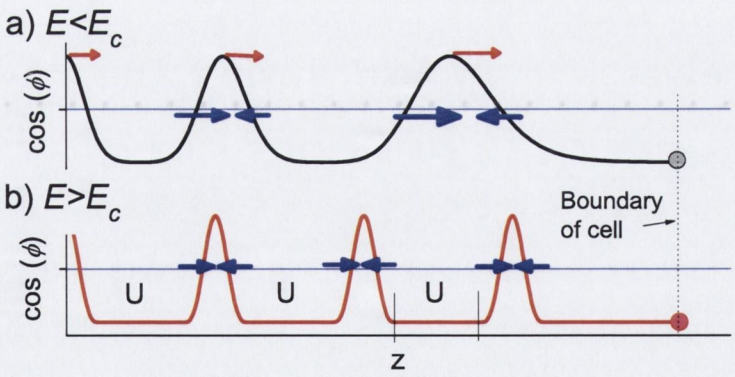

Figure 11.5: Schematics for the diverging force of the pitch. In the diverging pitch model, when $E < E_c$ (a), the unbalanced elastic forces at 2π solitons makes the elastically connected 2π solitons diverging to the cell boundary, but when $E > E_c$ (b), the unwound parts between 2π solitons isolates 2π solitons and no diverging force exists..

from a continuous increase in the helical pitch expected from the diverging pitch model.

A break in helix gives rise to a different possibility for explaining the helical unwinding. We can introduce a completely unwound apart (U) between the highly deformed parts called as 2π soliton [2] as shown in Fig. 11.5(b). Note that the completely unwound part (U) cannot exist in the diverging pitch model, because it makes the soliton isolate and it prevents the pitch from diverging. This can be easily understood by considering why the pitch diverging occurs. The diverging force arises from the unbalanced elastic forces of the 2π soliton so as to reduce the total elastic energy (Fig. 11.5(a)), but the horizontal shift of the isolated 2π wall does not reduce the total free energy (Fig. 11.5(b)). Therefore, the isolated soliton cannot have a diverging force normal to the applied field. Urbanc *et. al.*'s rigorous calculation [165] based on the diverging pitch model shows that the relaxation frequency of the pitch divergence converges to zero at E_c, which means that the diverging force disappears when $E > E_c$, where the unwound part (U) appears. The appearance of the unwound part (U) plays a quite important role in the various physical properties during the unwinding process. In the next section, the dielectric response with applied field is considered.

11.2 Dielectric response during the unwinding process.

Using the diverging pitch model, the dielectric response of the SmC^* phase with DC bias voltage was already studied by Urbanc *et.al.* [164, 165]. However, the theoretical prediction does not directly accord with the experimental results such as the dielectric strength ($\Delta\epsilon_G$) and the relaxation frequency (f_G) for the Goldstone mode and the effective polarization along electric field ($\langle P_E \rangle$). These properties have theoretically been predicted to have a sudden change near E_c. However, all the experimental results [116, 119, 122, 174–176] given so far have shown that these parameters do change gradually and finally reach saturation.

For the bias DC field dependences of the $\Delta\epsilon_G$ and f_G, a threshold voltage at a much lower field than E_c has been observed experimentally [119], which cannot be explained by the diverging pitch model.

In addition, some of the experimental observations based on the diverging pitch model have incorrectly been explained. The relaxation frequency of the Goldstone mode in SmC^* is known to increase with DC bias field. This is regarded as a typical property of SmC^* [116, 174–176]. Pfeiffer *et.al.* [174] suggested that the phenomenon may arise from an increase in the elastic constant of the highly deformed helix. Usually, the restoring force $F_{re.}$ for an elastomer on which this model is based is nonlinear in the regime of a large displacement x, that is, $F_{re.} = -x(\kappa_0 + \kappa_1 x^2 + ...)$. As a result, the effective elastic constant can increase with a larger displacement x; a typical property of a practical elastomer. However we surmise that the elastic energy does not correctly represent the interlayer interactions in SmC^*. It has already been proven that the interlayer interaction is based on the Landau expansion which has both dipolar and quadrupolar terms [14, 82, 84]. As a consequence of this form of interaction energy, the effective elastic constant with angular distortion $\Delta\phi$ will decrease rather than increase for a larger angular distortion . $\Delta\phi$ is the angle between the **c** directors of the two neighboring layers. Since $F_{re.} \approx -A\sin(\Delta\phi) - B\sin(2\Delta\phi) \approx -\Delta\phi[A+2B-\{(A+8B)/6\}\Delta\phi^2+...]$. It is therefore questionable whether SmC^* helix could have the property of a practical elastomer as assumed by Pfeiffer *et.al.* [174] in explaining the field dependence of the frequency of Goldstone mode in this phase.

Here, we explain the experimental observations based on the helical fractures, where the pitch divergence is not essential. We fix the pitch independent of the bias field and we consider the completely unwound parts between the highly deformed parts. We first need to find a function for the distorted helical structure caused by the bias voltage. We start from the well known free energy expression

and the corresponding Euler-Lagrange equation in the static case [162].

$$f = \int \left[\frac{K}{2} \left(\frac{d\phi}{dz} - q \right)^2 - P_s E \cos\phi \right] dz, \tag{11.1}$$

$$K \frac{d^2\phi}{dz^2} - P_s E \sin\phi = 0, \tag{11.2}$$

where the wave vector $q(= 2\pi/p$, where p is pitch) is adopted to produce a helical structure at zero field.

We derive an analytical expression using an assumption of the fixed pitch and introducing the completely unwound part in the helix. Using the Fourier expansion, we write the expression for the dependence of the azimuthal angle as a function of the distance along the layer normal

$$\phi(z) = qz + \sum_{i=0,1,\ldots} \phi_i \sin[(i+1)qz], \tag{11.3}$$

where ϕ_i's are the Fourier coefficients. To estimate the dielectric strength as function of the applied field, a simplified form of the director distribution function is required. We shall use up to the second term of the Fourier expansion at low fields ($E < E_t$). At high fields ($E > E_t$), some part of the helix is unwound completely, and the other part is highly distorted as shown in Fig. 11.6. Therefore, we divide the unwinding process into two stages: low and high fields, separated by a transition field E_t.

i) low fields ($E < E_t$)

$$\phi_l(z) \simeq qz - \phi_0 \sin(qz), \quad \textit{where } \phi_0 < 1, \tag{11.4}$$

ii) high fields ($E > E_t$)

$$\begin{aligned} \phi_h(z) &\simeq \rho(z - z_0) - \sin[\rho(z - z_0)], \\ &\qquad for\ z_0 < z < (p - z_0), \\ \phi_h(z) &= 0, \qquad for\ z < z_0\ or\ z > (p - z_0), \end{aligned} \tag{11.5}$$

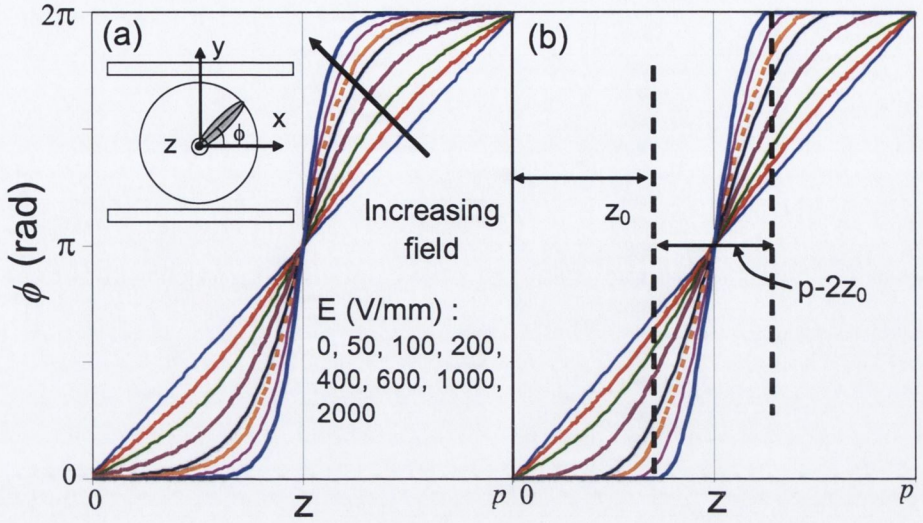

Figure 11.6: Director distributions for different DC fields. (a) simulating Eq. 11.1 directly. (b) simplified ϕ of Eq. 11.4 and 11.5. z_0 and $p - 2z_0$ are plotted for $E = 2$ kV/mm. Simulation conditions: $P_s = 100$ nC/cm^2, $K = 10^{-7}$ dyn, $p = 400$ nm and 1 layer $= 4$ nm. ϕ is defined in the inset of Fig. 11.6(a)

where $\rho = 2\pi/(p - 2z_0)$, that is, $z_0 = p/2 - \pi/\rho$.

From Eqs. 11.2, 11.4 and 11.5, we can find ϕ_0, ρ and E_t as

$$\phi_0 \simeq \frac{P_s E}{Kq^2}\left[1 + \frac{1}{2}\left(\frac{P_s E}{Kq^2}\right)^2\right]. \tag{11.6}$$

$$\rho \simeq \sqrt{\frac{5P_s E}{4K}}, \quad E_t \simeq \frac{4Kq^2}{5P_s}. \tag{11.7}$$

Surprisingly, E_t is found to have similar dependencies on the various parameters as $E_c = \pi^2 Kq^2/(16P_s)$ obtained by Meyer [162]. This will be discussed later.

To verify the simplified director distribution functions Eqs. 11.4 and 11.5, we compare the two director distributions by simulating from the free energy Eq. 11.1 and by simulating the simplified Eqs. 11.4 and 11.5. As shown in Fig. 11.6, two distributions agree with each other. This confirms the validity of the simplified distributions.

Corresponding to Eq. 11.1, Euler-Lagrange equation for the motion of **c** director by a weak ac field is written as

$$\gamma\frac{\partial\phi}{\partial t} - K\frac{\partial^2\phi}{\partial z^2} + P_s E\sin\phi = 0, \tag{11.8}$$

where γ is the viscosity of the medium. The applied field and ϕ_l under the low field case are written as

$$E = E_{\rm dc} + \delta E = E_{\rm dc} + \delta E_t e^{jwt}, \tag{11.9}$$

$$\phi_l(z) \simeq qz - \phi_0\sin(qz) - \delta\phi_0\sin(qz)e^{jwt}. \tag{11.10}$$

By using Eq. 11.9 and 11.10, Eq. 11.8 can be rewritten as

$$\begin{aligned}&\Big[-jw\gamma\delta\phi_0 - Kq^2\delta\phi_0 + P_s\delta E_t\{1-\phi_0\cos(qz)\}\Big]e^{jwt}\\ &-\phi_0 Kq^2 + P_s E_{\rm dc}\{1-\phi_0\cos(qz)\} = 0,\end{aligned} \tag{11.11}$$

where the time dependent and independent terms should be zero independently. Thus, we can obtain $\delta\phi_0$ as

$$\delta\phi_0 = \frac{\phi_0\delta E_t/E_{\rm dc}}{1+jw\gamma/(Kq^2)} \tag{11.12}$$

The dielectric susceptibility can be obtained

$$\chi = \frac{d\langle P_E\rangle}{dE} = \frac{\partial\langle P_E\rangle}{\partial\delta E}, \tag{11.13}$$

where P_E is the component of P_s parallel to the applied field, and $P_E = P_s\cos\phi$.

$$\begin{aligned}\langle P_E\rangle_l &= P_s\left[\frac{\phi_0}{2} - \frac{\phi_0^3}{16}\right] + P_s\left[\frac{1}{2} - \frac{3\phi_0^2}{16}\right]\delta\phi_0 e^{jwt}\\ &\quad -P_s\left[\frac{3}{16}\phi_0\right]\delta\phi_0^2 e^{j2wt} + \ldots\end{aligned} \tag{11.14}$$

$$\chi \simeq \left(\frac{1}{2} - \frac{3}{16}\phi_0^2\right)\frac{P_s\phi_0}{E_{\rm dc}(1+jw\gamma/(Kq^2))} \tag{11.15}$$

From Eqs. 11.13,11.14, and on assuming that $\chi = (\epsilon_0\Delta\epsilon_G)/[1+jw/(2\pi f_G)]$, where

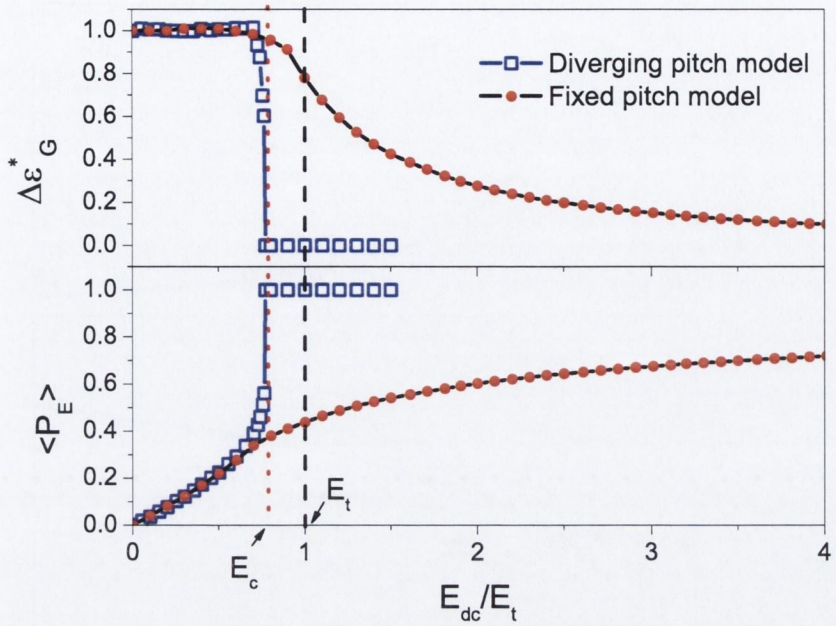

Figure 11.7: Plots for the normalized $\Delta\epsilon^*_G = Kq^2\Delta\epsilon_G/P_s^2$, and the normalized $\langle P_E \rangle$ expected for fixed and diverging pitch models [164].

$\Delta\epsilon_G$ and f_G are the dielectric strength and the relaxation frequency of the Goldstone mode, we find $\Delta\epsilon_{G,l}$ and $f_{G,l}$ at low fields as

$$\Delta\epsilon_{G,l} = \frac{P_s}{\epsilon_0 E_{\rm dc}}\left(\frac{1}{2}\phi_0 - \frac{3}{16}\phi_0^3\right), \tag{11.16}$$

$$\simeq \frac{P_s A}{\epsilon_0}\left(\frac{1}{2} + \frac{A^2}{16}E_{\rm dc}^2 - \frac{9A^4}{32}E_{\rm dc}^4\right), \tag{11.17}$$

$$where\ A \equiv P_s/(Kq^2),$$

$$f_{G,l} = \frac{Kq^2}{2\pi\gamma} \tag{11.18}$$

As shown in Eqs. 11.17 and 11.18, the relaxation frequency of the Goldstone mode does not depend on the dc bias at low fields, while the dielectric strength decreases slightly with the DC bias.

For the dielectric response at high fields, we can use Eq. 11.5 for the director distribution. The unwound part of the helix ($\phi = 0$) does not contribute to the dielectric response, so we need only to consider the distorted part. We shall use $z' \equiv z - z_0$. Then, ϕ under high applied fields is written as $\phi_h(z) \simeq \rho z' - \sin(\rho z') -$

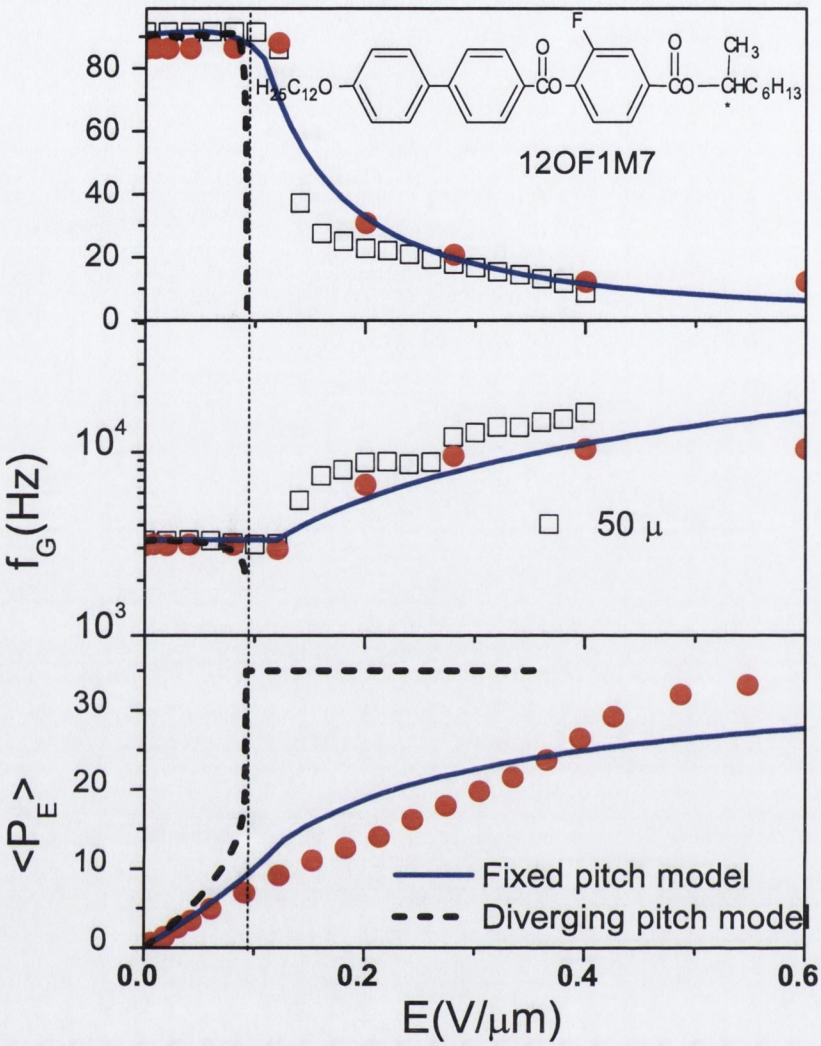

Figure 11.8: Experimental data for 12OF1M7 ($50\mu m$ and $25\mu m$ planar cells) and simulation results for the fixed and diverging pitch models. (Simulation conditions selected for the best fitted curves.)

$\delta\phi_0 \sin(\rho z')e^{jwt}$. Following the similar procedure as for low fields, we obtain

$$\phi_h(z) \simeq \rho z' - \sin(\rho z') - \delta\phi_0 \sin(\rho z')e^{jwt}. \tag{11.19}$$

Following the similar procedure as for low fields, we obtain

$$\begin{aligned}\langle P_E \rangle_h &= \frac{2z_0 P_s}{p} + \frac{(p-2z_0)P_s}{p}\left[\frac{7}{16} + \frac{5}{16}\delta\phi_0 e^{jwt}\right] \\ &= P_s\left[1 - \frac{9q}{16\rho} + \frac{5q}{16\rho}\delta\phi_0 e^{jwt}\right], \qquad (11.20)\end{aligned}$$

$$\Delta\epsilon_{G,h} = \frac{5qP_s}{16\epsilon_0\rho E_{\rm dc}} = \frac{5q}{8\epsilon_0}\sqrt{\frac{KP_s}{5E_{\rm dc}^3}}, \qquad (11.21)$$

$$f_{G,h} = \frac{K\rho^2}{2\pi\gamma} = \frac{5P_s E_{\rm dc}}{8\pi\gamma}, \qquad (11.22)$$

In Eq. 11.20, the term $(p-2z_0)/p$ shows that only the distorted part of the helix can contribute to the dielectric response. Thus, both the dielectric strength and the relaxation frequency are found to depend strongly on the amplitude of the DC bias at large fields. However, the mechanism does not arise from the nonlinearity of K, but from an increase in the effective wave vector ρ. That is, the high bias field increases z_0 and reduces the effective pitch $(p-2z_0)$, which in turn increases the relaxation frequency.

The DC bias dependence of normalized dielectric strength and the normalized macroscopic spontaneous polarization are plotted in Fig. 11.7, where those simulated from the diverging pitch model are also plotted for comparison [164]. Fig. 11.7 shows clear differences between the two models; E_c in the diverging pitch is lower than E_t in the fixed pitch model; $\Delta\epsilon_G$ and $\langle P_E \rangle$ change suddenly at E_c in diverging pitch model while those in the fixed pitch model change gradually. In the latter model, it is difficult to estimate E_c' for complete unwinding, much larger than E_c, because the non-homogeneous unwinding process, i.e. the solitary waves [34, 84] is the most important factor to decide the E_c'. Moreover, physical properties changes gradually near E_c' and so, it is not easy to find the critical field exactly.

The DC bias dependencies of $\Delta\epsilon_G$, f_G and $\langle P_E \rangle$ are compared with experimental data in Fig. 11.8 (see [167, 177] for the experimental method for $\langle P_E \rangle$). The experimental data was measured using 12μm thickness planar cell and 12OF1M7 (Kingston Chemicals Hull, UK) at a temperature 2°C below from SmC^*-SmA^*

transition. As shown in Fig. 11.8, the experimental results agree with those predicted by our model in spite of even using simplified ϕ functions. It shows also clear differences between the two models; $\Delta\epsilon_G$, f_G and $\langle P_E \rangle$ change suddenly at E_c in the diverging pitch model, while those in the fixed pitch model change gradually. Moreover, additional threshold voltage, which we cannot find in the diverging pitch model, is found experimentally and explained by the fixed pitch model. The dielectric response for the Goldstone mode and the effective polarization with DC bias voltage is also explained. According to Fig. 11.8, E_c found in the diverging pitch model is underestimated. This can be easily understood; in this model, the completely unwound part (U) is not allowed, and E_c is the same as the field, at which U part could appear for very large values of helical pitch. However, if the pitch does not diverge, U part should appear, and the unwound state of all helical structure can be obtained at a much larger field than E_c. The fixed pitch model is not suitable to estimate E_c' for complete unwinding, because it depends strongly on the quadrupolar term of the interlayer interaction energy, which we did not consider in Eq. 11.1, and the non-homogeneous unwinding process, i.e. the solitary waves or the domain walls propagation [34, 84]. Moreover, physical properties changes gradually near E_c' and so, it is not easy to find the exact critical field even experimentally.

E_t and E_c are compared with the experimental data in Fig. 11.9. Using Eq. 11.3 at $E_{\rm dc} = 0$, $E_t = 2P_s/(5\epsilon_0\Delta\epsilon_G)$ and $E_c = \pi^2 P_s/(32\epsilon_0\Delta\epsilon_G)$, and so E_t and E_c can be obtained by using measured P_s and $\Delta\epsilon_G$. We obtained the experimental data for ZL4655-000 and Felix-SCE9 from references [175, 176]. As shown in Fig. 11.9, the experimental E_t agree with their theoretical values based on the fixed pitch model, but the experimental E_c are about 7 times larger than their theoretical values based on the diverging pitch model. This clearly shows that the experimental results cannot be explained by the diverging pitch model.

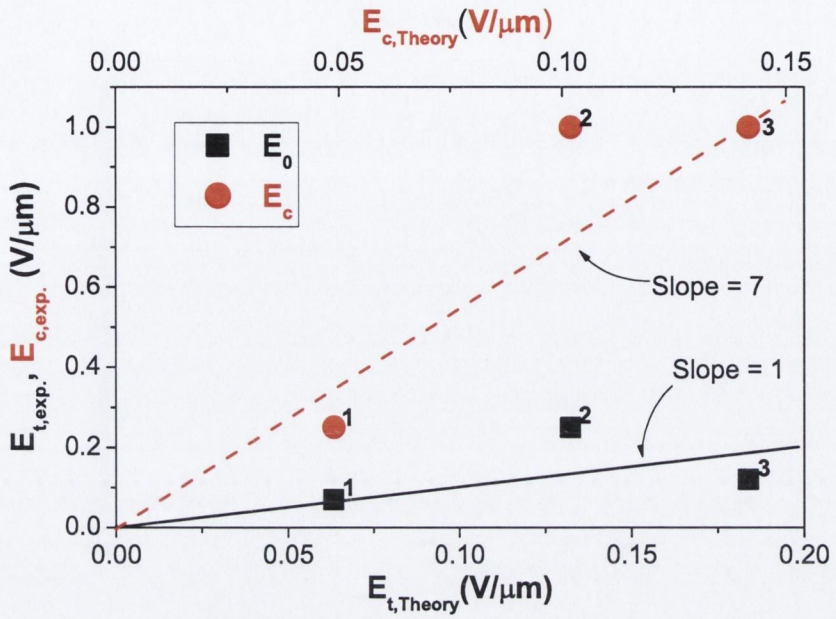

Figure 11.9: Plots of theoretical E_t (lower x axis) and E_c (upper x axis), and experimental E_t and E_c (y axis). Points 1 and 2 are for ZL4655-000 and Felix-SCE9 from results in reference [175] and [176] respectively, and points 3 are for 12OF1M7.

11.3 Conclusion and Future works.

As pointed out by Krueger *et.al.*, the pitch divergence is interrupted by the surface effects and by the slow and weak diverging force [122, 165, 171], hence the ideal pitch divergence may be possible only under rather limited conditions. Therefore, in usual experimental conditions such as usual planar cells, the fixed pitch model with a broken continuity of the helix may be commonly observed. This can be confirmed by the fact that none of the dielectric permittivity reported so far follows the expected one from the conventional pitch diverging model. Based on the helical fracture model, theoretical models for the dielectric strength and frequency of the Goldstone mode, and the effective polarization are suggested and are confirmed to agree with the experimental results. In the diverging pitch model, the critical field E_c for a complete unwinding is accompanied with sharp changes in the physical properties. However, the fixed pitch model implies that E_c may not be a distinct field since the physical parameters reach saturated values gradually. Electro-optical measurements on the unwinding process support it [34].

However, the model for the dielectric permittivity is not completed, because it does not include the helical fracture effectively, which may influence the dielectric permittivity and produce a step-like change. In the future, we need to extend this model to include the helical fracture and the non-homogeneous domain wall propagation.

Chapter 12

Interlayer interactions and the dependence of biaxiality of SmC^* on electric field in the helical unwinding process.

"In this chapter, *the unwinding process of pure and racemized mixtures of MHPOOCBC is investigated by using conoscopy. Pure MHPOOCBC shows a large positive biaxiality, which cannot be explained by ordinarily distorted helical structure. We explain the phenomena arises from the helical fractures.* "

12.1 Introduction

In this chapter, we have focused on the field induced unwinding process [2, 35, 36, 94, 162, 166] in the chiral smectic-C phase (SmC^*). During the unwinding process, some **c** directors in the adjacent layers are found to experience a change

from synclinic again to synclinic through an anticlinic order with the adjacent layer, that is, from $\Delta\phi = 0$ to $\Delta\phi = 2\pi$ as being presented in this chapter. By observing the unwinding process and defects, we may be able to understand the interlayer interactions.

Suwa *et al.* [35, 36] used conoscopy to investigate the unwinding process in MHPOBC and a short-pitch chiral smectic mixture, and they found two different types of unwinding behaviors having negative and positive biaxiality during the intermediate unwinding process. They suggested that the high positive biaxiality is quite an unexpected result and can be attained under a special distribution of the directors, a set of discrete **c** directors. However, they could not explain successfully the mechanism as to how such special distributions are obtained. We used a conoscopic method with tilted cells [33, 37], which gives an improved observable range of biaxiality and of the tilt angle. We found various unwinding behaviors in MHPOOCBC and its racemized mixtures depending on the racemization ratio and the temperature. Pure MHPOOCBC and mixtures with large enantiomeric excess (e.e) show large positive biaxiality during the intermediate unwinding process whereas the mixtures with low e.e. show negative biaxiality during the early stages of the unwinding process. Microscopic observations showed the various behaviors are due to the discontinuous **c** directors, that is, the helical fracture suggested in Chapter 11.

The aim of this chapter is to confirm the helical fracture model in the helical unwinding process of the ferroelectric phase, to explain the emergence of the various unwinding behaviors by the new model, and to estimate the azimuthal angle dependent interlayer interaction energy in the ferroelectric phase.

12.2 Experiments and results

The LC samples used are MHPOOCBC ((1-methylheptyloxycarbonyl)phenyl-4′-carboctyloxy-biphenyl-4-carboxylate), whose structure is shown in Fig. 12.1,

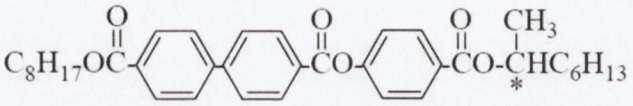

Figure 12.1: Chemical structure of MHPOOCBC ((1-methylheptyloxycarbonyl)phenyl-4′-carboctyloxy-biphenyl-4-carboxylate) (SmC^*_γ 42^oC SmC^* 87^oC SmA [12]). Pure MHPOOCBC and its racemic mixtures (e.e. = 0.3, 0.7) were used for experiments.

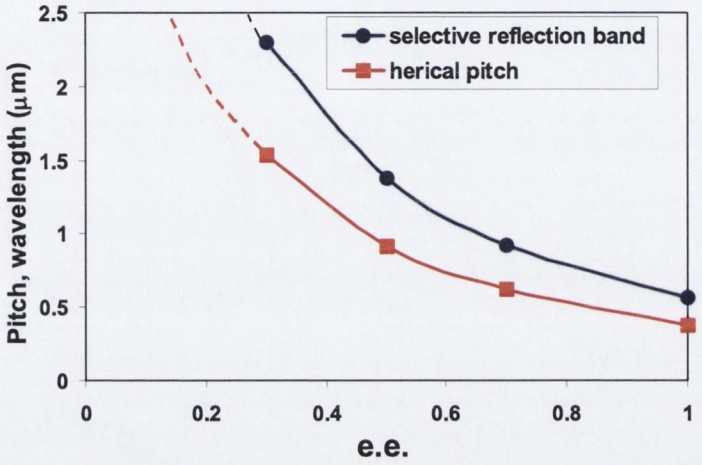

Figure 12.2: Helical pitch as function of the e.e. value of the MHPOOCBC racemic mixtures (80^oC). Dashed lines show extrapolation of the experimental data.

and its racemic mixtures, whose racemization ratio or the enantiomeric excess ratio (e.e.) defined as $(R-S)/(R+S)$ are 0.3, 0.7. Pure MHPOOCBC has a wide temperature range of the SmC^* phase and of SmC_γ* phase at low temperatures [12]. Homeotropically aligned cells having 100 - 150 μm thicknesses were prepared by using two ITO glass plates coated with a silane coupling agent. Biaxiality was studied by conoscopy with a tilted cell explained in Chapter 2 [33, 37].

The obtained conoscopic images were analyzed to get the biaxiality (n_Y - n_X) and the tilt angle (θ), where the Z axis is parallel to the long axis of the refractive index ellipsoid, the X and Z axes are in the tilt plane and the Y axis is perpendicular to the tilt plane. The racemic mixtures of MHPOOCBC having e.e values of 1.0 (pure MHPOOCBC), 0.7 and 0.3 have the pitch values varing from about 360 - 400nm, 580 - 640nm and 1490 - 1570nm respectively as seen in

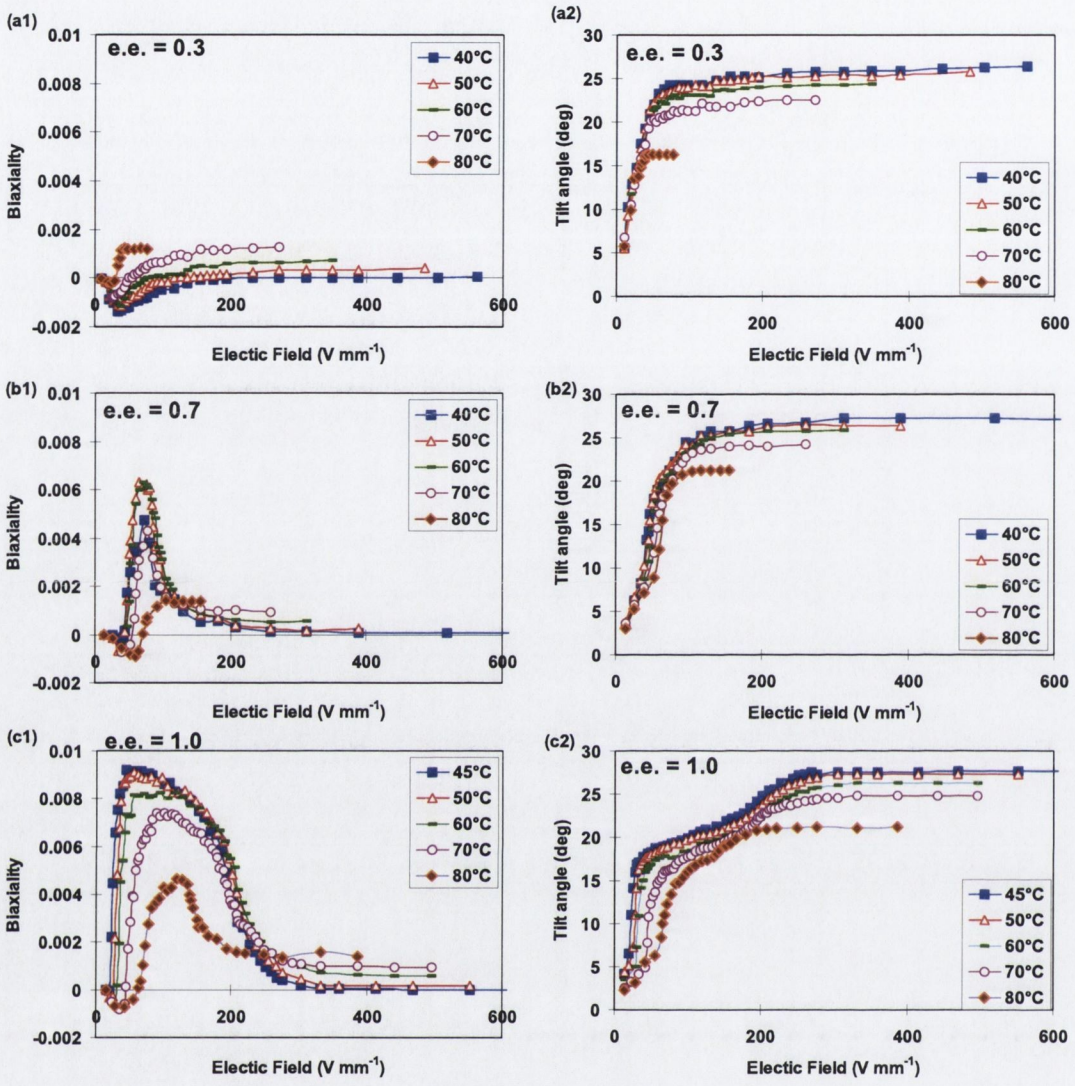

Figure 12.3: Results of the conoscopic measurements; left hand side: plots of the biaxiality $(n_Y - n_X)$ vs. voltage, right hand side: plots of the tilt angle vs. voltage at various temperatures, (a) e.e.=0.3, (b) e.e.=0.7, (c) e.e.=1 (here, the enantiomeric excess (e.e.)=$(R-S)/(R+S)$)

Fig. 12.2. (Here, we assumed $n_{lc} = 1.5$, which is needed for deducing the pitch from the selective reflection band). Thus, the pitch of the mixture of e.e = 0.3 is about three times longer than the wavelength of light. As explained in Chapter 2, the single-biaxiality approximation is valid up to roughly 7 times longer pitch than the wavelength, and the cell having e.e value of 0.3 also could be regarded as a single biaxial plate approximately. Our analysis is based on this approximation.

Figure 12.3 shows the experimental results of conoscopy. The graphs on the left hand side are the plots of the biaxiality, and ones on the right are those for the tilt angle for the optically pure MHPOOCBC and its racemized mixtures. The results are shown for e.e. values of 0.3, 0.7 and 1 in Fig. 12.3a, 12.3b and 12.3c, respectively. Mixture (a) (e.e.=0.3) shows negative biaxiality in the intermediate state of unwinding, while two others (e.e.=0.7, 1.0) show large positive biaxiality. The trend depends on the temperature as well, as seen in mixtures (b) and (c); the curve for 80^oC in (b1) shows the same trend as those in (a1). Similarly, a large positive biaxiality value decreases with temperature in (c1). The tilt angle graphs show interesting behaviors as well. The tilt angle of mixture in (a2) increases continuously with the applied voltage, but pure MHPOOCBC (c2) has a two step increase corresponding to the increasing and the decreasing parts of the biaxiality curve. Mixture (b) shows an intermediate trend. As Suwa *et al.* [35, 36] has correctly pointed out, the negative biaxiality observed in mixture (a) is well-explained by the conventional unwinding process, but the positive biaxiality in pure MHPOOCBC can't be explained by a conventional model, details of which will be described in the next section.

The helical fracture or the discrete **c** director explained in Chapter 11 can lead to this special unwinding process. We examined micrographs to obtain a better understanding for the relation between the helical fracture and the conoscopic data. Figures 12.4 and 12.5 show the microscopic images of 15 μm homeotropic cells using the pure (e.e.=1.0) and the racemized MHPOOCBC (e.e.=0.3) taken under crossed polarizers (the polarizer directions are parallel and perpendicular to the direction of the applied field), where temperature was 70^oC and 1 Hz AC square voltage was applied. It may be better first to examine the cell with a racemized mixture, which is rather closer to a general case (Fig. 12.5). The homeotropic cell with such a mixture had a uniform single domain in the SmA^* phase (texture is not shown here) and in the SmC^* phase. Under a field of 36 V/mm (image (b1) in Fig. 12.5), the cell is still uniform, and at 54 V/mm (image (b2)), a few domains start to appear from the edges of the electrode. At the same applied voltage, the tilt angle in the plot almost reaches a saturation level. The number

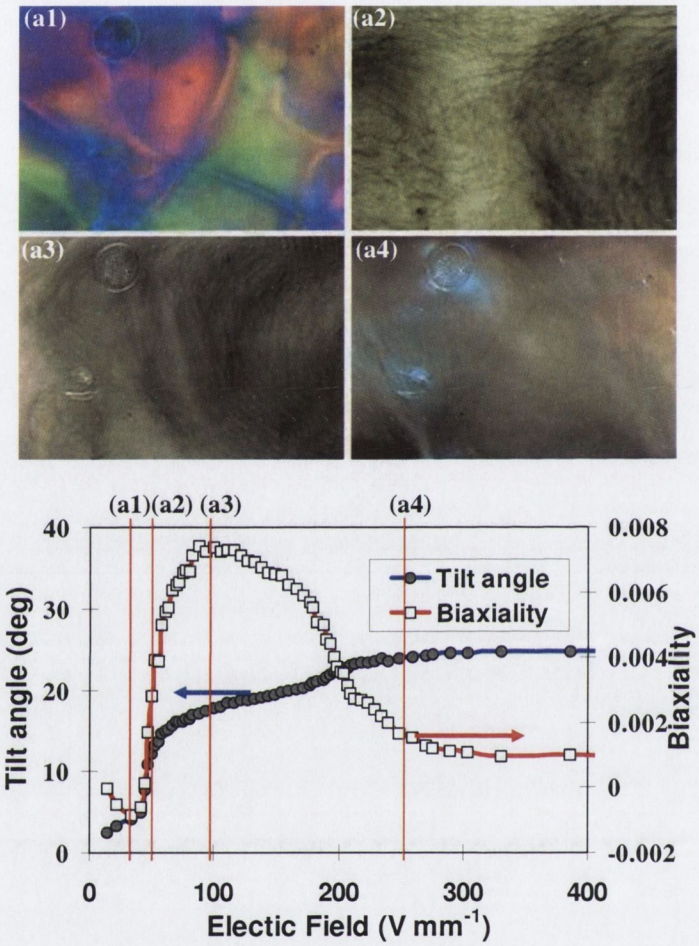

Figure 12.4: Micrographs (× 200) of a homeotropic cell with pure MHPOOCBC at 70^oC in SmC^* phase; (a1) 40 V/mm; (a2) 50 V/mm; (a3) 100 V/mm; (a4) 250 V/mm. The graph shown in the lower part is the biaxiality and the tilt angle corresponding to the fields for each microscopic image. The graph is from Fig. 12.3. The exposure time was adjusted for capturing the best quality of the images. The red and green colors in the image (a) are induced by the optical rotary power, which is very sensitive to the helical structure when the pitch is similar to the wavelength of the light for observation.

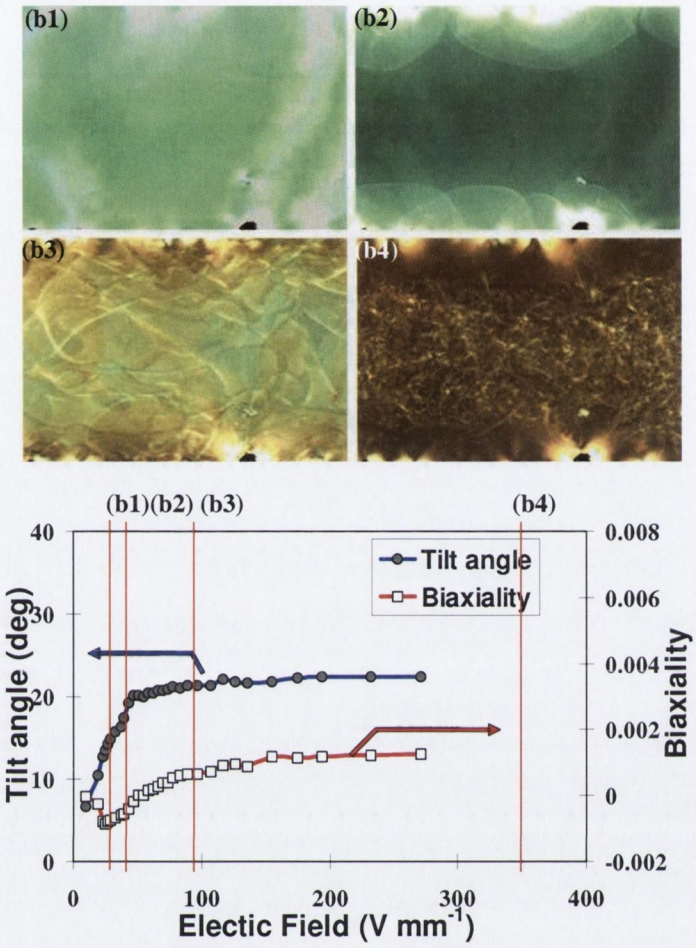

Figure 12.5: Micrographs (× 200) of a homeotropic cell with racemized MHPOOCBC (e.e.=0.3) at 70^oC; (b1) 36 V/mm; (b2) 54V/mm; (b3) 107 V/mm; (b4) 375 V/mm

of domains increased with applied voltage (image (b3)) and started to disappear from the same edges (image (b4)), which is in the unwound state. The domain walls have a single dark line, which means that the lines are accompanied by the discrete **c** directors, that is, the helical fracture. Here, the domain walls appeared for a significantly larger voltage close to the critical voltage for the unwound state. Therefore, the discrete **c** director does not affect the field dependence of the biaxiality shown in Fig. 12.3. Note that the field dependence of the biaxiality of the mixture (a) in Fig. 12.3 follows the conventional unwinding process, as explained by Suwa *et al.* [35, 36].

The cell with the pure MHPOOCBC in Fig. 12.4 showed a different behavior. In the pure MHPOOCBC, SmA phase did not show any domains (not shown here), but several domains emerged when the cell is cooled down from SmA to SmC^* phase ((a1) image in Fig. 12.4). The color is due to a slightly different helical structure for each domain, because the pitch is close to the green wavelength and the optical rotary power is very sensitive to the helical structure when the incident light has a wavelength close to the pitch of the helix. The domain boundaries have two dark lines indicating that the domains are the 2π domains walls. The domain boundaries were moved by applying electric field but the number of them did not change under an applied field of less than 40 V/mm (image (a1)). However, the number of domains increased suddenly near 50 V/mm (image (a2)) which corresponds to a field for a sudden rise in the biaxiality, and the generated domain walls have a single dark line indicating that the domains accompany with the discrete **c** directors. The number of domains continued to increase with the applied voltage (images (a3) and (a4)), but the domain boundaries got blurred. The domains finally disappeared at larger voltages, which indicates that the cell has finally reached the unwound state. Through the microscopic observations of pure MHPOOCBC, we can notice that the helical fracture is clearly related with the special behavior of the bias field dependence of the biaxiality for pure MHPOOCBC, because so many domains were generated at the same field at which a sudden rise in the biaxiality happened. Moreover, the field is much lower than the critical field required for a complete unwinding of the helix. According to the conventional pitch diverging model based on the continuum approximation, such a discrete **c** directors cannot appear, since it requires too large energy.

We present an additional evidence for the helical fracture. We measured the dielectric permittivity with increasing applied electric field using 25μm thickness cells. Figure 12.6 shows the results, where the cells show two low frequency relaxation processes. The square red data set corresponds to the conventional Goldstone mode, and the other relaxation process has much lower relaxation frequency. We can see that the dielectric strength of the new process for pure MHPOCBC increases sharply near 50mV/μm, which corresponds to the field for the appearance

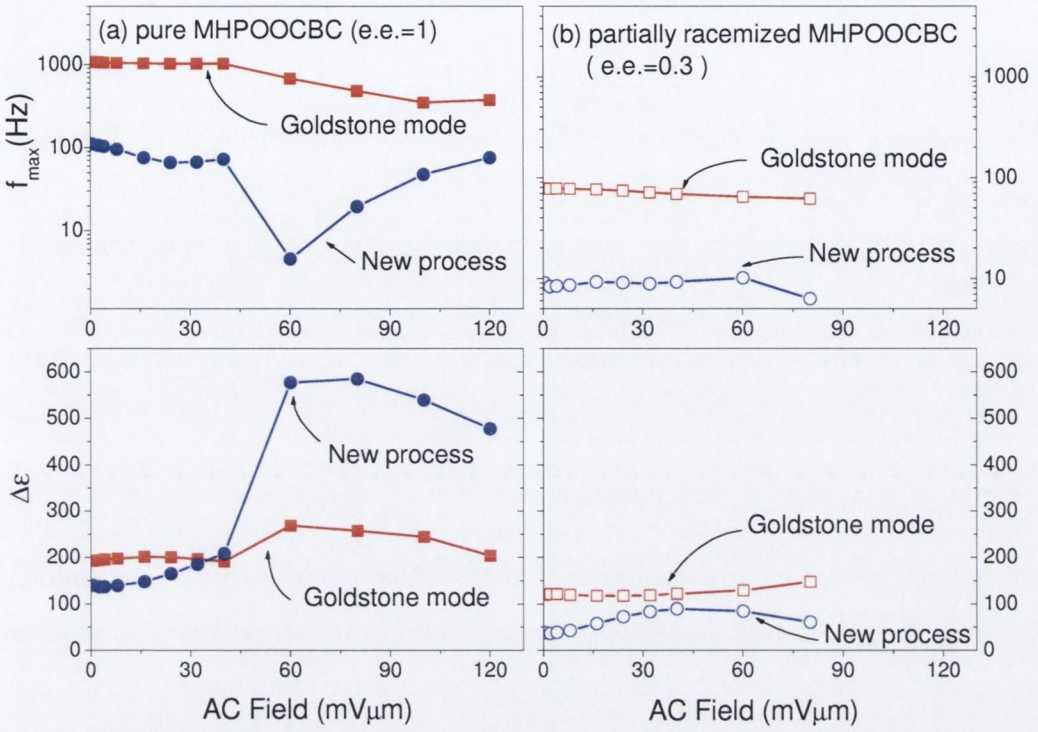

Figure 12.6: Dielectric permittivity with the increasing field using 25μm thickness homogeneous cells for (a) pure MHPOOCBC, and (b) partially racemized MHPOOCBC (e.e.=0.3) at 60°C; the upper parts are the maximum resonance frequency for each process (f_{max}) and the lower parts are the dielectric strength ($\Delta\epsilon$).

of the sudden domain walls. The same process is obtained even in the partially racemized MHPOOCBC, but the strength is very weak, and does not show any sudden jump. Hence, we can conclude that the new relaxation process arises from the helical fracture. The helical fracture mode exists even at zero field. This can be explained by assuming that the helical fractures occurring by applied field do not disappear even after turning the field off in the planar cell due to the surface effect. The helical fracture mode may occur due to the motions of each helical segments. Since the unit of the fluctuation is bulky, the process may have much lower relaxation frequency than that of Goldstone mode as being observed here. More detailed studies have not carried out yet, but we can see that the helical fractures affect the dielectric response as well as the optical response.

Thus, we can reconfirm that the helical unwinding occurs through the helical fracture as being modeled in the previous chapter. Also, we can see that the helical fracture strongly depends on the racemic ratio of the material. For pure MHPOOCBC, it occurs at earlier state, while it occurs at the later state of the helical unwinding process for the racemized one. However, in this state, the mechanism of the helical fractures is not clear. Undoubtedly, the solitary waves and the double well interlayer interaction encourage the generation and the propagation of the domain walls [84]. The quadrupolar coefficient of the interlayer interaction may induce the generation of the domains [84, 96]. However, since the solitary wave usually starts to propagate from defects, the sudden generation of the numerous domain walls at a particular field is not explained intuitively. The sudden appearance of the domain walls gives the impression that there could be another mechanism inducing the helical fracture. Moreover, after removing fields, the cell returned to the original state very quickly. The fast recovery is rather difficult to explain by only the quadrupolar term of the interlayer interaction energy.

Here, we suggest another possibility where a narrow energy well presents in the synclinic position of the interlayer interaction. It was proven that the presence of the narrow energy well can make the helical fracture to occur from uniform helix without defects (for details, see the Appendix in the reference [34]).

12.3 Simulation based on the narrow energy well model

In the helical unwinding process of chiral smectic phases, the angular dependent free energy of N smectic layers can simply be written in the following form

$$F = \sum_{i=1}^{N} \left[U_{i,i+1}(\Delta\phi) + \frac{\Delta\epsilon' E^2}{8\pi} \cos^2\phi_i - PE\cos\phi_i \right] \tag{12.1}$$

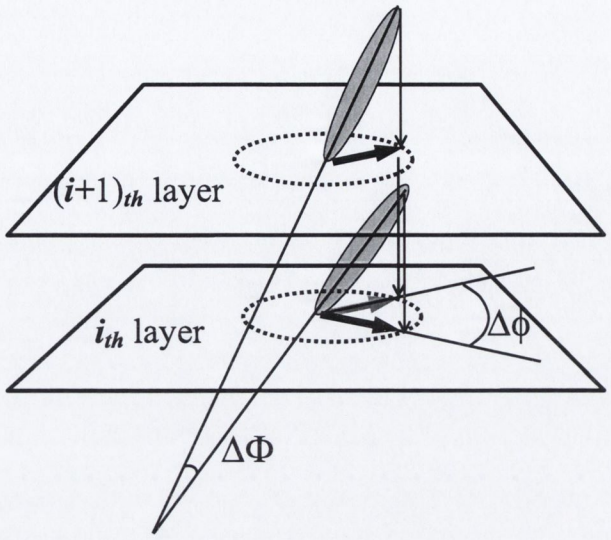

Figure 12.7: The angle between the two **c** directors ($\Delta\phi$) and the angle between the two directors (($\Delta\Phi$)) in Eq. 12.3.

where $U_{i,i+1}(\Delta\phi_{i,i-1})$ denotes the interlayer interactions of i_{th} layer with $(i+1)_{th}$ layer as a function of the relative angle $\Delta\phi$ between the two adjacent layers, and the two other terms are the interactions of the dielectric anisotropy ($\Delta\epsilon' = \Delta\epsilon \sin^2\theta$) and the spontaneous polarization (P) of the layers with the applied field, respectively. By adopting the continuum approximation in the interlayer interaction, the $U_{i,i+1}$ can be expressed as a usual elastic distortion energy and Eq. 12.1 can be written as [2, 162]

$$F = \int \{\frac{K}{2}(\frac{d\phi}{dz} - \phi_0')^2 + \frac{\Delta\epsilon' E^2}{8\pi}\cos^2\phi - PE\cos\phi\}dz \qquad (12.2)$$

where the wave vector $\phi_0'(= 2\pi/pitch)$ is adopted to produce an initial helical structure at zero field, and the discrete summation can be replaced by integration in the continuum approximation. The term for the dielectric coupling is commonly ignored because of its relatively small contribution to the total free energy. Equation 12.2 is the starting point of the conventional helical pitch diverging model [2, 35, 36, 94, 162, 164–167].

When the interlayer interactions in smectic phases are considered, a discrete rather than a continuous model gives a more general solution [25, 109]. Moreover,

the elastic form of energy in Eq. 12.2 used **c** directors instead of the molecular directors of liquid crystals and so it is discontinuous at $\Delta\phi_{i,i+1}=\pi$ as seen in Fig. 12.8, which is surely not realistic. It is quite natural to use the molecular directors for considering the elastic distortion energy. As illustrated in Fig. 12.7, when the tilt angle is θ and the angle difference between the **c** directors of two neighboring layers is $\Delta\phi$, the actual angle($\Delta\Phi$) between the two molecular directors can be written as

$$\Delta\Phi = 2\sin^{-1}(\sin\theta\ \sin\frac{\Delta\phi}{2}) \simeq 2\theta\sin(\frac{\Delta\phi}{2}) \tag{12.3}$$

This approximation is valid if the tilt angle is not too large. The conventional elastic energy between the i_{th} and $(i+1)_{th}$ layers can be written as

$$U_{i,i+1} = \frac{2K}{d^2}\theta^2\sin^2(\frac{\Delta\phi_{i,i+1}-\phi_0}{2}) = k(\theta)\sin^2(\frac{\Delta\phi_{i,i+1}-\phi_0}{2}) \tag{12.4}$$

where $k(\theta) = 2K\theta^2/d^2$ and K is a usual elastic constant($\sim$ 1 $\times 10^{-6}$dyne) and d is the thickness of a single layer ($\sim$ 4 $\times 10^{-7}$cm). ϕ_0 is the angle between the adjacent **c** directors at zero field. This equation is continuous near $\Delta\phi = \pi$. It follows the conventional continuum theory except for the discrete notation, and will give the same result in a calculation of the unwinding process.

Now, let us consider the narrow energy well in the synclinic position for explaining the helical fracture. How is such a narrow potential well physically possible? We need to reconsider the first part in Eq. 12.2, where the elastic energy part of this equation is taken from the nematic continuum theory. Meyer initially suggested Eq. 12.2 for the unwinding process of the cholesteric liquid crystals. This equation has been used to describe the unwinding process of SmC* phase of smectics without any modifications [2, 94, 162, 166] so far. Nevertheless the interlayer interactions are always present in the smectics. The curvature of the director in the nematic phase is continuous and smooth, and so the restoring force is proportional to the curvature strain, which is equivalent to the Hooke's law. However, in the smectic structure, the steric energy between the layers is not the same as that in a continuous medium but should relate to the surface-to-surface

interactions. Moreover, many other kinds of interlayer interactions different from the steric ones may also be involved. We can get some idea from the 'sawtooth model' suggested by Glaser and Clark [178] and later verified indirectly by Lee and Lim [160]. In the model, synclinic order is stabilized by the mesh of a set of sawteeth, so the steric energy becomes a minimum in the synclinic order, where the sawteeth represent the rough surface of the smectic layers consisting of the tilted terminal parts of molecules. The uneven surface in the model is supposed to be due to the out-of-layer displacements of molecules [55]. Their model suggests that the steric energy at the synclinic position is exceptionally larger than at other positions, which exactly corresponds to our experimental results. Based on the special steric energy concept described as 'sawtooth model', we can propose a simple intuitive energy form for the steric energy. The depth of the steric energy induced by meshing of the rough surfaces is expected to be proportional to the extent of meshing of the sawteeth with each other. The possibility of the energy having the shape of a Gaussian distribution looks plausible. That is, as the angle departs from the synclinic position, the extent for the surfaces to mesh with each other is likely to decrease exponentially on either sides of this position. Thus, we can modify Eq. 12.4 as follows;

$$U_{i,i+1} = k(\theta)\left[sin^2(\frac{\Delta\phi_{i,i+1} - \phi_0}{2}) - Ae^{-(\Delta\phi_{i,i+1}-\phi_0)^2/B}\right] \tag{12.5}$$

This elastic energy contains an expression for the Gaussian-shaped energy well in the synclinic order in addition to that of the conventional elastic energy, which is plotted in Fig. 12.8. The dimensionless parameters A and B control the depth and the width of the narrow energy well in the synclinic order.

Eq. 12.1 becomes;

$$\frac{F}{k(\theta)} = \sum_{i=1}^{N}\left[\sin^2(\frac{\Delta\phi_{i,i+1} - \phi_0}{2}) - Ae^{-(\Delta\phi_{i,i+1}-\phi_0)^2/B} - \frac{P}{k(\theta)}E\cos\phi_i\right] \tag{12.6}$$

where for convenience, both sides have been divided by $k(\theta)$.

Now, we will show that this intuitive interlayer interaction energy actually

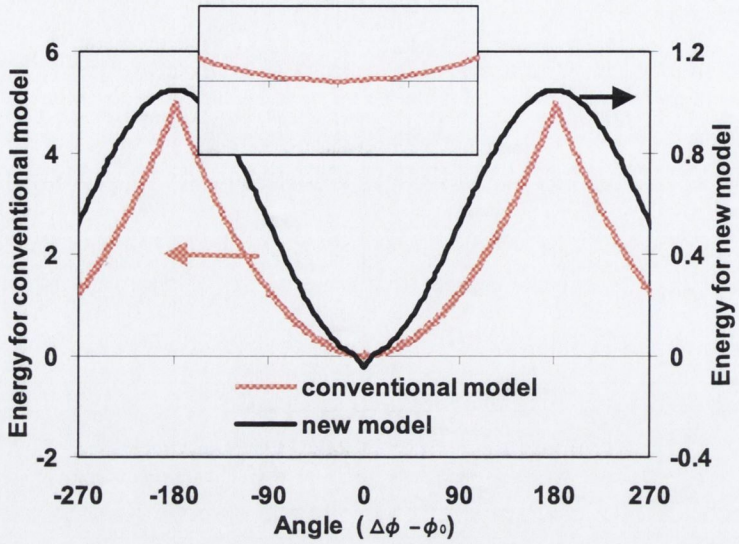

Figure 12.8: Elastic energy between the adjacent layers using classical elastic energy term (Eq. 12.2) and using the new model (Eq. 12.5, A = 0.04, B = 0.01, θ=30^o), which contains a term for the energy well. The inset shows an expanded view close to the synclinic position. The classical elastic energy and new elastic energy are plotted as $U_{classic}\ d^2/K$ and $U_{new}\ d^2/K$, respectively.

explains the helical fracture very well. Eq. 12.6 is not easy to solve analytically, so we solve it numerically to obtain the **c** director distributions as a function of the applied field using the computer simulation. The initial condition for the simulation is a uniformly coiled state, and on increasing the applied field gradually, the director distributions for the minimum free energy were calculated. For simplification, only one pitch was considered. After acquiring the **c** director distributions, an optical simulation was carried out to obtain the biaxiality and the tilt angle. For the optical simulation, we used the average refractive index approximation suggested in Chapter 2.

To verify the effect of a narrow energy well, we carried out simulations by using the above process. The simulation conditions are as follows: the number of layers in a single pitch = 90, pitch = 360 nm, $P/k(\theta) = 1.8 \times 10^{-5}$ nC/dyne, B=0.01, tilt angle 25^o, $n_e = 1.7$ and $n_o = 1.5$. The conditions are selected to be similar to the properties of the pure MHPOOCBC for known parameters such as the number of layers in a pitch, tilt angle and the spontaneous polarization, but

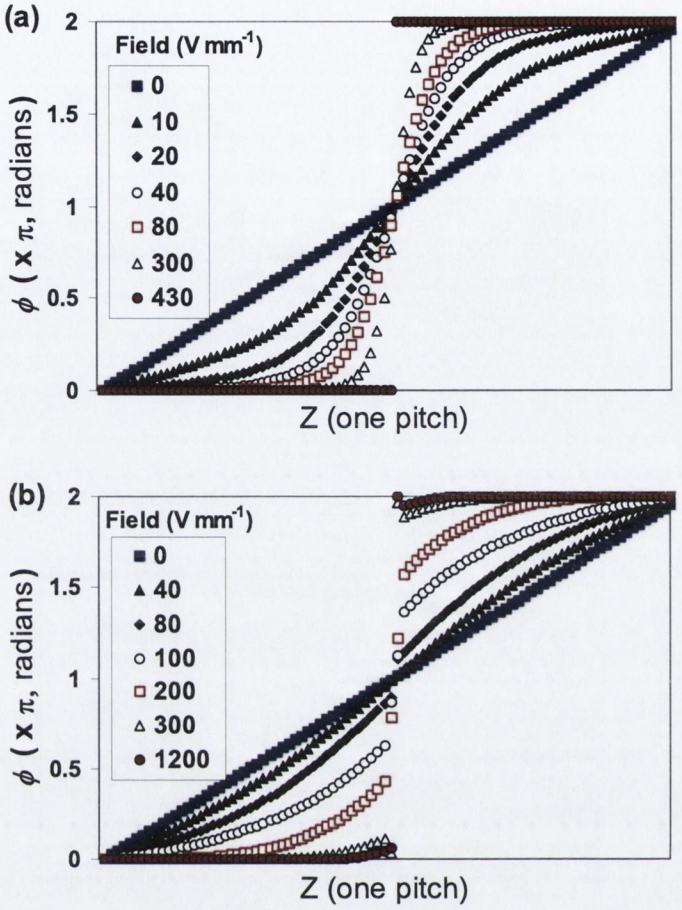

Figure 12.9: Simulation of directors vs. applied field, (a): conventional elastic energy (A = 0), (b): new model (A = 0.045). Simulation conditions: the number of layers in a pitch = 90, pitch = 360 nm, $P/k(\theta) = 1.8 \times 10^{-5}$ nC/dyne, B=0.01, tilt angle 25^o, n_e = 1.7 and n_o = 1.5.

for unknown parameters, we choose the general values for the smectics. Basically, all other parameters, except for A and B, do not sensitively affect the qualitative unwinding behavior.

The director distributions thus calculated are plotted in Fig. 12.9, which shows directions of the **c** directors for each layer in a single pitch. For $A = 0$, that is, for the classical elastic energy case, the **c** director orientations are continuous until the unwinding process is completed, while a discrete **c** director jump appears at relatively low fields when $A = 0.045$. As seen in this simulation, the narrow energy well generates a discrete **c** director distribution during the unwinding of the

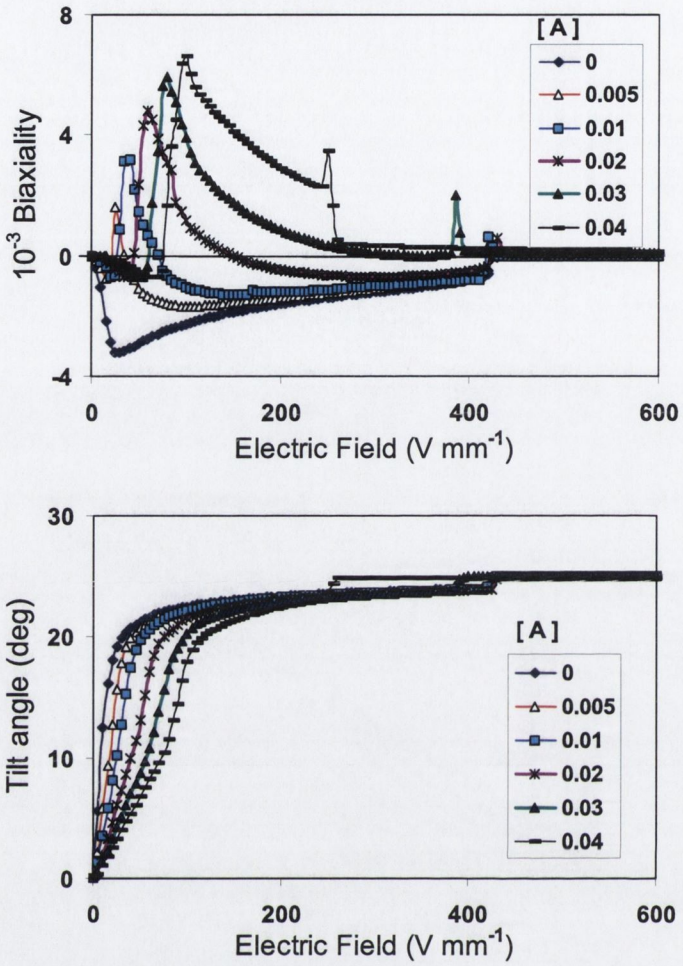

Figure 12.10: Simulation results for the biaxiality (a) and the tilt-angle (b) using new model with the parameter A being varied. Simulation conditions: same as those in Fig. 12.9.

helix. Figure 12.10 shows the results of the optical simulation. For $A = 0$, it shows negative biaxiality at low voltages and saturates to the unwound state, which is similar to the results of e.e.= 0.3 for a racemized mixture of MHPOOCBC. As the value of A is increased, the field dependence of the biaxiality becomes more like the results for e.e.= 0.7 of MHPOOCBC and finally those of the pure MHPOOCBC. Tilt angle results also show a similar behavior. As the value of A increases, a two step increase in the tilt angle appears, which is similar to the results for the pure MHPOOCBC.

From the two results in Fig. 12.9 and Fig. 12.10, we can see that the discrete **c** directors induce the high positive biaxiality. We should recall the microscopic

and conoscopic observations of the cells with racemized and pure MHPOOCBC. The cell with racemized MHPOOCBC showed domains near the saturation voltage whereas the cell with pure MHPOOCBC showed the same domains at quite low voltages. Likewise, the cell with racemized MHPOOCBC showed negative biaxiality at low voltages, but the cell with pure MHPOOCBC showed large positive biaxiality. These simulation results indicate that the cell with racemized MHPOOCBC has a shallow energy well whereas the cell with the pure MHPOOCBC has a deep one.

Now, we try to reproduce the experimental results by using our simulation. However, we may mention that this simulation has some limitations. Firstly, we did not consider the inlayer distortion and the solitary wave propagation in a layer, which may play a role in the unwinding process. Secondly, we assumed a perfectly uniform helical structure, but the real helical structure consists of many helical segments, each of which has a different length. The averaged spontaneous polarization of each segment is not zero so that each segment rotates even at very low fields. Lastly and the most importantly, the new energy model is quite a simplified intuitive model.

In spite of all those simplifications, the simulated biaxiality and the tilt angle dependencies on field shows a surprising similarity to the experimental results as seen in Fig. 12.11. Simulation conditions in the top graph are ($A = 0.001$, $B = 0.01$, $P/k = 0.4 \times 10^{-5}$ nC/dyne, the number of layers per pitch = 360, pitch = 1440 nm), middle ($A = 0.03$, $B = 0.01$, $P/k = 1.4 \times 10^{-5}$ nC/dyne, the number of layers per pitch = 180, pitch = 720 nm), lower ($A = 0.045$, $B = 0.01$, $P/k = 2.4 \times 10^{-5}$ nC/dyne, the number of layers per pitch = 90, pitch = 360 nm), and refractive indices are n_e=1.85, $n_{o1,o2}$= 1.5, 1.501 respectively.

These simulation results support the possibility that the various unwinding behaviors are due to the existence of a narrow energy well in the synclinic order, and the depth of the energy well depends on the enantiomeric excess ratio and the temperature. The higher the racemization ratio (that is, more pure), the deeper the energy well. This can easily be explained intuitively. The energy well

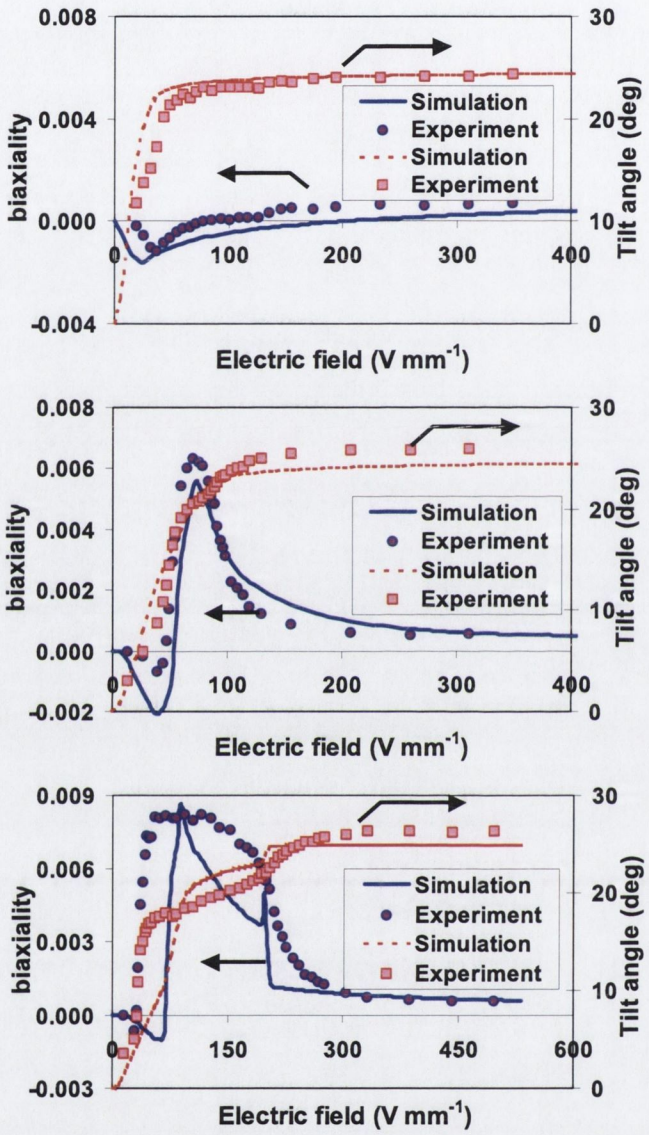

Figure 12.11: Comparison between the experimental data and the simulation; Experimental data: 60^oC, e.e.= 0.3, 0.7, 1.0 from the top, Simulation conditions: A = 0.001, 0.03 and 0.045, and P/k = 0.4, 1.4 and 2.4 $\times$ 10^{-5} nC/dyne, and pitch = 1440, 720 and 360 nm from the top of the figures, n_e=1.85, $n_{o1,o2}$= 1.5, 1.501, all other conditions are the same as those in Fig. 12.9, 12.10.

is located at $\Delta\phi - \phi_0 = 0$, that is, $\Delta\phi = \phi_0$, which generates helical structure. Intuitively, this helical structure is due to the chirality and this results in the terminal parts of molecules being slightly tilted away from the tilt plane. Opposite handed molecules may have oppositely tilted terminal parts and they disturb the mesh of two sawteeth. Therefore, by mixing the opposite handed molecules, we can decrease the depth of the narrow energy well. Temperature dependence can also be explained in a similar way. As temperature increases, thermal fluctuations become stronger and these consequently are neglected in a reduction of the depth of the energy well.

12.4 Conclusion

Based on the helical fracture model suggested in Chapter 11, the experimental results of conoscopy and dielectric measurement for pure and partially racemized mixtures of MHPOOCBC are interpreted. The field dependences of the biaxiality and the tilt angle show a rather suprising behaviors, that is, sudden jumps of the biaxiality and the tilt angle at a particular electric field, which cannot be explained by the conventional diverging pitch model. As Suwa *et al.* reported [36], the large biaxiality observed during the helical unwinding cannot be explained without discontinuous director distribution along normal to layers. The behaviors depend on the enantiomeric excess ratio of the material. The special behavior arises from the appearance of the helical fracture, which is confirmed by the microscopic observation. The helical fracture also produces a new dielectric process, which has a very low relaxation frequency. The detailed study for this relaxation process is not included in this thesis, and remains as a future work.

To explain the helical fracture phenomenon, we introduce a narrow energy well in the synclinic position. Surprisingly, the intuitive model explains well the conoscopic data as well as the helical fracture. Though we may need further experimental and theoretical evidences to confirm the existence of a narrow energy well in the synclinic position, it is clearly shown that the interlayer interaction is

the essential part of the helical unwinding process of the tilted smectic liquid crystalline materials and the interlayer interaction cannot be replaced by the simple continuum approximation.

Part. VI

Conclusion and Appendix.

Chapter 13

Conclusion and future works

13.1 Conclusion and Summary of this thesis

Undoubtedly, liquid crystals provide an attractive field of study for the various reasons; the variety of physical characteristics and phases, their great success in many applications, and their relevance to other fields such as biology and nanoscience. Their interesting properties mostly originate from the special shapes of liquid crystalline molecules and moderate intermolecular interactions, neither too strong nor too weak. The moderate intermolecular interactions enable liquid crystal phases with a flexibility in responding to moderate external forces. In nematic liquid crystals, the intermolecular interactions are not strong unlike those in the solid state, and the alignment of directors is easily distorted by the weak external fields. Elastic and viscous properties and order parameters *etc.* actually reflect the strength of the intermolecular interactions in nematic liquid crystals. The SmA^*

phase requires very large field to induce a significant switching behavior. This implies that the intermolecular interaction in the SmA^* phase is much stronger than that in the nematic liquid crystals. The strong interaction induces a special structure in smectic liquid crystals, *i.e.* the layered structure. The directional change of directors in the SmA^* phase accompanies the shrinkage of the layer thickness requiring large energy, and this makes the switching of the SmA^* phase difficult. However, a more flexible response to the external electric field reappears in lower temperature phases, smectic C phases. This can be explained by two facts; the emergence of a spontaneous polarization providing a strong couping with electric fields, and an easier azimuthal motion of layers.The azimuthal motion of molecules in the smectic C phases does not require a change of the layer thickness or large energy. Another reason for the easy azimuthal motion is that the interlayer interactions are much weaker than the intermolecular interactions forming the layered structure. This can be easily confirmed by observing the switching behavior of smectic C phases. An external electric field hardly influences the magnitude of spontaneous polarization in each layer, which implies that the electric field is too weak to affect the ordering of molecules in layers induced by the strong intermolecular interactions. However, the same external electric field induces a large change both in the interlayer ordering and in the residual polarization of a cell. This is the origin of the field induced AF-F switching behavior investigated in chapter 5. Therefore, while the intermolecular interaction is directly involved in the various electro-optic behaviors of nematic liquid crystals, the interlayer interaction, which basically originates from the intermolecular interaction as well, is a direct factor determining the electro-optic properties of smectic C phases.

In this way, the molecular interaction and the interlayer interaction are the most important factors determining the physical properties of liquid crystals, and in particular, the interlayer interaction provides a direct and simple way to explain the various physical phenomenon occurring in smectic C phases. However, the direct measurement of the interlayer interaction has rarely been reported so far due to experimental difficulties. In this thesis, a new method for measuring the interlayer interaction in smectic C phases is suggested based on the observation

of the solitary wave. Parry-Jones *et al.* [86] suggested a method to measure the interlayer interaction for the first time. However, their method is rather difficult to apply since their method requires to measure the dielectric strength as a function of dc field. Such measurements usually contain large errors. Moreover, all the other dielectric relaxation processes such as the molecular modes, ionic modes *etc.* were ignored, and these would also cause an error in the calculated interlayer interaction. By contrast, the method suggested in this thesis provides a simpler and more accurate way to determine the interlayer interaction. The new method allows us to understand the various phenomenon in smectic liquid crystals. Many of the new findings in this thesis are related to the method or to the interlayer interactions.

The new physical phenomenon reported in this thesis are summarised as follows:

• *Two kinds of temperature dependences of the biaxiality in the SmC* phase were found.*

This is related to the direction of the average molecular short axis in smectic layers. The molecular short axis refers to the shortest direction of the polarizability of the molecule, which is perpendicular to the central phenyl rings of molecules. In some liquid crystals, the average short axis is parallel to the tilt plane, and these materials show a decreasing biaxiality with increasing temperature. These materials have a positive P order parameter. On the other hand, in the other liquid crystals, the axis is perpendicular to the tilt plane, and these materials show an increasing biaxiality with increasing temperature. These materials have a negative P order parameter.

• *Temperature induced sign reversal of the biaxiality in the SmC* phase was found.*

This behaviour is also related to the direction of the average molecular short axis. The macroscopic biaxiality in the helically unwound state is determined by sum of the contributions of the P and C order parameters, which are related to the biased molecular short axis ordering and the anisotropic molecular long axis fluctuation, respectively. In the materials having a negaitive P order parameter, the contribution to the biaxiality by this negative P order parameter is maximized at low

tempertaures, and the macroscopic biaxiality is negative. At high temperature, the biaxiality becomes positive due to the relatively small contribution from the P order parameter. Therefore, the materials show a sign reversal of the biaxiality from negative to positive with increasing temperature.

• *Sign reversal of the dielectric anisotropy in SmA as functions of the frequency and the temperature was found.*

The sign reversal phenomena of the dielectric anisotropy as a function of the frequency is well known in some nematic liquid crystals known as dual frequency nematics. However, the same phenomena has not been reported to date in smectic liquid crystals. Moreover, the sign reversal occurs with temperature as well as the frequency in the SmA^* phase of a smectic liquid crystal. The phenomena arises from a collective dielectric relaxation process, the soft mode in the SmA^* phase.

• *The frequency of the antiferroelectric phase mode of the dielectric response was found to rapidly decrease by adding a ferroelectric liquid crystal to an antiferroelectric liquid crystal.*

This is assumed to be related to the interlayer interaction. That is, the antiferroelectric Landau coefficient α is reduced on adding the ferroelectric liquid crystal, the decreased α reduces the antiferroelectric coupling between the layers, and the frequency of the antiphase mode decreases.

• *The tendency of the biaxiality with applying field shows a strong dependency of mixing ratio of R and S.*

This dependency is related with the helical fracture occurring during the helical unwinding.

• *Temperature induced solitary wave propagation in the SmC_A^*-SmC^* phase transition.*

The solitary wave was found to occur during the SmC_A^*-SmC^* phase transition. The solitary wave provides the only way in which the transition can occur. This is found by measuring the interlayer interaction, which shows a double well shaped potential energy separated by a large energy barrier between the two minimum energy states in the entire temperature range of the smectic C phases. This shows

a striking contrast with the conventional weakly first order transition explained by the Landau-de Gennes energy expansion, where the double well shaped energy appears only in a narrow range of temperatures and also the supercooling/superheating phenomena corresponding to the double well potential appear. However, in the SmC_A^*-SmC^* phase transition, no significant supercooling/superheating is observed. It shows that the solitary wave is the only way for the transitions between the smectic C phases to occur.

• *The shift of the critical field E_c of the solitary wave in SSFLC cells using the asymmetric alignment layer.*

The solitary wave also occurs in SSFLC cells. The solitary wave in the SSFLC cells is induced by the surface anchoring energy. The critical field E_c, where the speed of the solitary wave becomes zero, depends on the polar anchoring energy difference between the two surfaces. This is measured experimentally and modeled theoretically.

• *The cell thickness dependence of the stability of chiral smectic C phases was investigated.*

As the cell thickness decreases, the phase transition temperature between smectic C phases shifts, and some sub phases even disappear. A theoretical model is suggested to explain this phenomenon, and the model accords well with the experimental results.

• *The coexistence of the antiferro- and ferroelectric states, which is commonly misunderstood as a frustration, was investigated.*

The stability of the antiferroelectric and the ferroelectric phases strongly depends not only on the surface confinement but also on the mixing ratio in the binary mixture. The measured interlayer interaction shows that the energy difference between the two states decreases as the mixing ratio in the binary mixture approaches a critical value. The small energy difference weakens the driving force for the generation and the propagation of the solitary wave, and the coexistence of the two phases occurs easily. The surface anchoring also interrupts the generation and the propagation of the solitary wave so that the coexistence of the phases occurs more easily in thin cells.

• *The phase sequence reversal phenomenon is explained theoretically based on experimental observations.*

This phenomenon can be dealt with by the interlayer interaction term.

• *Helical fractures occurred in the helical unwinding process of the SmC* phase.*

This is a rather surprising result, because the helical pitch diverging model had been considered to have explained the helical unwinding process almost perfectly. The helical pitch diverging model, which is based on the continuum approximation, shows a few limitations to explain various physical observations during the unwinding. The helical fractures actually occur, and shows that the continuity of c director along the normal to layer can be broken. That is, the angle difference ($\Delta\phi$) between the c directors of two adjacent layers can rupture from $\Delta\phi = 0$ to $\Delta\phi = \pi$ and again from $\Delta\phi = \pi$ to $\Delta\phi = 0$. The helical fracture is rather similar to the helical unwinding of DNA from a topological point of view.

• *Discontinuous increase of the helical pitch during the helical unwinding process.*

The helical fractures induce a discontinuous increase of the helical pitch.

New experimental methods developed for this thesis are as follows:

• The tilted conoscopic method has been developed.

• A new simulation method for estimating the molecular distribution through conoscopy is developed.

• A new method of measuring the interlayer interaction in the SmC_A^* phase is developed.

• A new method to measure the polar anchoring difference between the two surfaces in the cell is introduced by observing the solitary wave.

New theoretical models given in this thesis as summarized below:

• A new model is derived for describing the cell thickness dependence of the stability of the smectic-C phases.

• A new model is described for explaining the appearance of the solitary wave in the SmC_A^* phase.

• New models for explaining the SmC_A^*-SmC^* phase transition, and the continuous

evolution from the SmC_A^* to the SmC^* phase are provided.

• A new model is introduced for the helical unwinding process of the SmC^* phase based on the helical fractures.

• A new model is provided for explaining the dielectric response observed during the helical unwinding process.

13.2 Future work

Liquid crystals have a variety of special physical phenomena. The solitary wave, which is the subject of large part of this thesis, is one of these. Actually, several kinds of solitary waves exist in liquid crystal cells. They are associated with:

• Various temperature induced phase transitions

• Various field induced phase transitions

• Field induced domain wall propagation in SSFLC cells

• Field induced helical unwinding in thin planar cells

• Field induced helical fractures in ferroelectric cells

• π or 2π walls in ferroelectric or antiferroelectric films and cells

These solitary waves involve various physical properties. However, the solitary wave is not a homogeneous process, and it is not easy to deal with the bundle of the solitary waves occurring here and there in a cell, though a propagating single solitary wave can be modeled and simulated easily. For example, the solitary wave plays an important role in the helical unwinding process, but it is not easy to estimate when, where, how and in what number the solitary waves occur in the cell. This may depend on the surface or the boundary condition, the strength of applied fields, the density of defects etc. Therefore, we need a systematic method to deal effectively with such a non-homogeneous process. Such a method will provide better understanding concerning these complexities.

Another interesting fact is that examples of solitary waves are easily found in nature. Tsunami as an ocean wave, nerve signal propagation in biology and Morning Glory cloud in Australia *etc.* are examples. When we open a bag of crisps, we stretch the zig-zag shaped edge of the bag and the strong bag begins to tear easily. This is also a sort of solitary wave propagating in one direction, because the strong bondage of two adjacent polymer molecules in the bag is broken through a propagating localized wave, which overcomes the energy barrier between the chemically connected state and the separated states of the two molecules. A similar phenomena occurs in the cracks in rocks and stonework of buildings etc. It may be worth while to study the connection between these and solitary wave. A liquid crystal cell is the best conditions for studying the solitary wave, because the usual solitary waves existing in nature are difficult to control. As shown in this thesis, the study of the solitary wave assists the understanding of various physical phenomenon in liquid crystals. Moreover, the study of the waves in liquid crystals may also provide a possibility to figure out the properties of other solitary waves in nature.

It is also interesting to study the generation of various sub-phases and the phase sequence in terms of the interlayer interactions. As shown in Chapter 13, the interlayer interactions, especially the steric interaction may affect the phase sequence strongly, though it is not clear how this occurs. The most recent model for the generation of various smectic C variant phases is the discrete flexoelectric polarization model by Osipov *et. al.* [14, 65, 109]. It is well known that the flexoelectric effect is highly influenced by the steric interaction, which is one of the interlayer interactions. The measurement of the interlayer interaction can provide a clue for understanding the generation of the various smectic C variant phases.

Appendix A

A.1 Materials used for fabricating cells

Fig. A.1 shows the liquid crystal materials used in this thesis. The phase sequence shown in the figure may vary according to experimental conditions, material state, and experimental method.

MC815, MC884, MC452, MC536, MC514, MC881 and MC813 were synthesized by Mitsubishi Gas Chemical Company (MGC) in Japan, and MHPOOCBC and DOBAMBC were synthesized by Nissan Chemical Industries, LTD., in Japan. These materials were endowed to Prof. A. Fukuda and his co-workers for research purpose. 12OF1M7 was synthesized by Kingston Chemicals in Hull, UK. 3.b.5 was synthesized by prof. B. K. Sadashiva and his research group in C. V. Raman Avenue, Sadashivanagar, Bangalore 560 080, India. 10OHF was synthesized by prof. S. Kumar and his research group in Raman Research Institute, Bangalore, 560 080, India. Liquid crystal mixtures, the chemical structures of some of which are not known, were also used; Y102 (MGC), Felix0018 (HOECHST AG Company in Germany).

For alignment layers, RN-1175 and RN-1266 supplied by Nissan Chemical Co. in Japan were used for planar alignment, and a Dow Corning silane coupling agent (72%3-(trimethoxysilyl)propyldimethyloctadecyl-ammonium-chloride and 28% MeOH) and carboxylatochromium complexes (chromolane) were used for homeotropic cells.

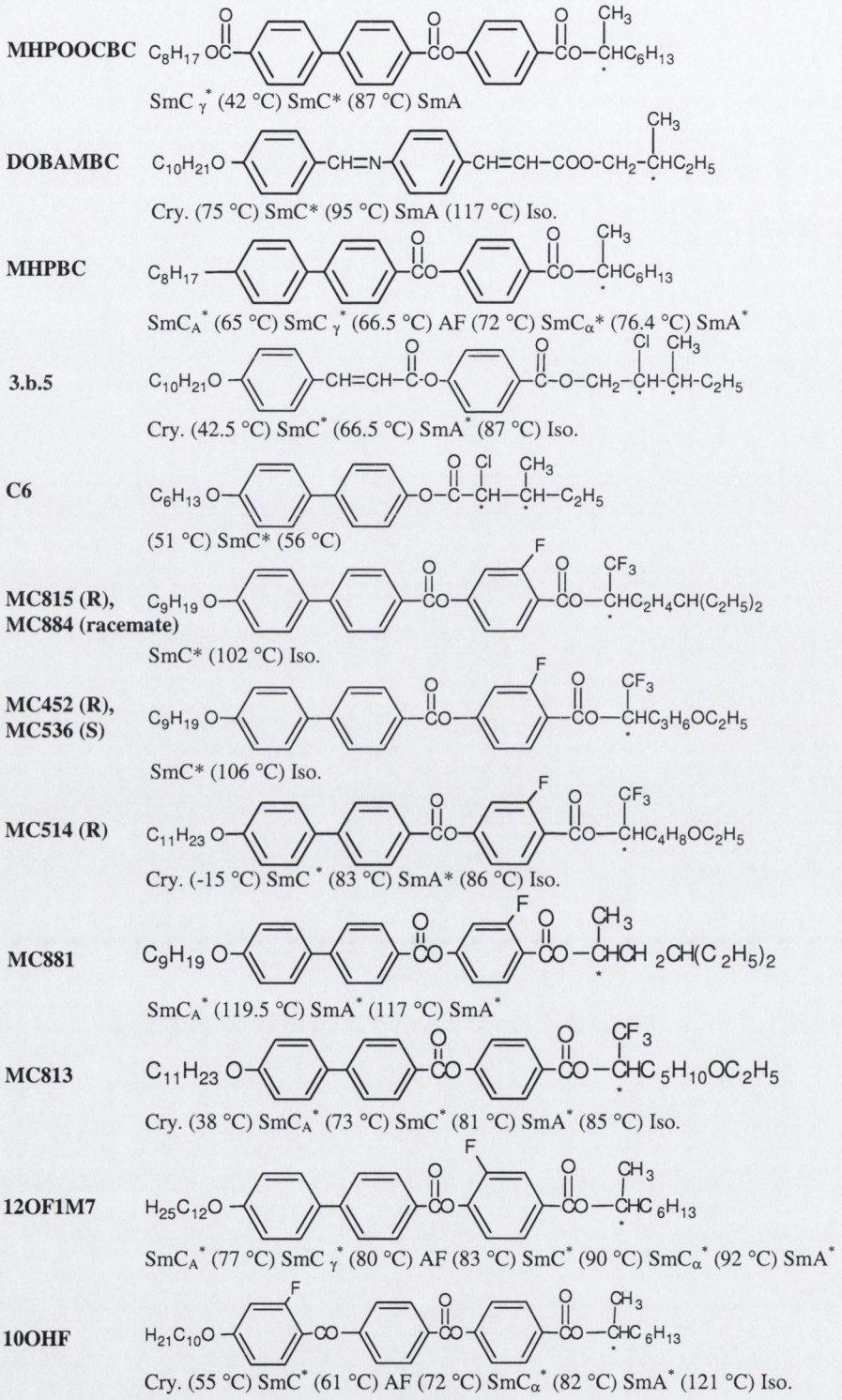

Figure A.1: Chemical structures and phase sequences of liquid crystal materials used in this thesis. Phase sequence could be measured slightly differently depending on experimental conditions, material state, and experimental method.

Commercial cells having 2, 5, 9 and 25 μm thickness were purchased from E. H. C Co., Ltd. in Japan, and were used for some measurements. For hand-made cells, either 0.7 mm thick glass coated with ITO (Indium Tin Oxide; 20$\Omega/\square$) or 1.1 mm thick glass coated ITO (100$\Omega/\square$) supplied by Prof. J. M. Oton in ETSI Telecomunicacion Ciudad Universitaria, Madrid, Spain, was used.

A.2 Apparatus

This section provides brief information about main instruments used in this thesis. For further details of concerning each instrument, refer to the linked web-site.

• **Optical Microscope:** Olympus BX-52 (Olympus Company), including the objective lens (Olympus, LM PlanFI, 50X / 0.5NA), the condenser (Instech, 0.65 NA), and Leica DFC480 (Leica, Digital camera for microscope)

- http://www.olympusfluoview.com/brochures/pdfs/bx52.pdf

- http://www.leica-microsystems.com/

• **Broadband dielectric spectrometer:** This system includes Alpha-A High Performance Modular Measurement System (Novocontrol GmbH, Impedance analyzer, $3\times10^{-5} - 2 \times 10^{7}$ Hz), Agilent 4291B RF Impedance/Material Analyzer (Agilent, $1 \times 10^{6} - 1.8 \times 10^{9}$ Hz) and Quatro Cryosystem (Novocontrol GmbH, temperature controller, $-160 - +400$°C). Analysis software, WINFIT (Novocontrol GmbH, software) is required.

- http://www.novocontrol.de/

- http://www.home.agilent.com/agilent/home.jspx

• **Optical Spectrometer:** Lambda 900 UV/VIS/NIR spectrometer (PerkinElmer, broadband high resolution spectrometer), and Avaspec-2048 (Avantes, fast fiber optic spectrometer).

- http://www.perkinelmer.com/default.htm

- http://www.avantes.com/

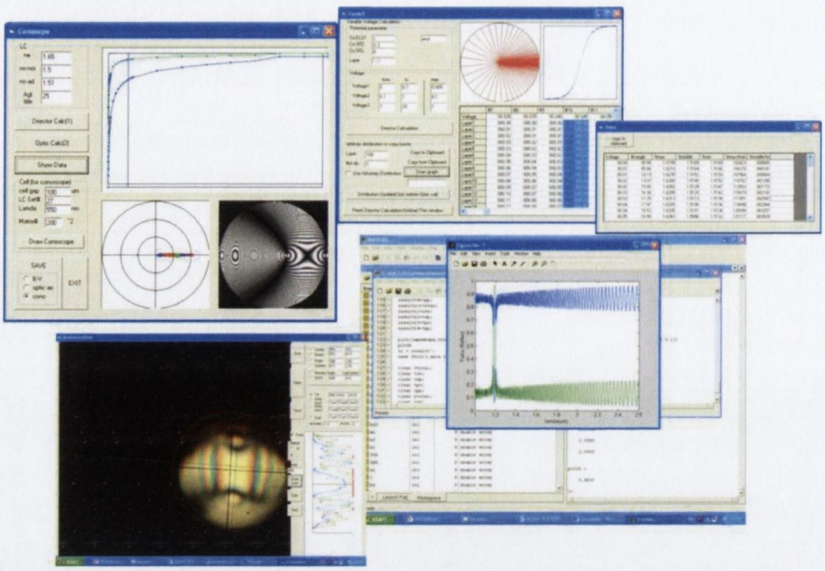

Figure A.2: Examples of Simulation Programs made by using Visual Basic or MatLab.

• **Photo-Elastic Modulator (PEM) system:** PEM modulator (HINDS Instruments)

- http://www.hindsinstruments.com/PEM_Components/products/default.aspx

- see also references [24, 25] for applications

A.3 Softwares

• **Visual Basic:** Microsoft Visual Studio V. 6.0 was used for analyzing conoscopic images automatically, simulating the unwinding process of helical structure, simulating the biaxiality of cell and conoscopic images etc.

• **MatLab:** MATLAB V. 6.1 was used for 4×4 matrix simulation, for example, conoscopic images and selective reflection etc.

• **Origin:** Origin 7.5 was used for analyzing experimental data, and for simple fitting simulation.

• **LaTex:** Miktex 2.7, Ghostscript 8.6, GSview, and TEXnicCenter were used for typesetting publications including this thesis.

Bibliography

[1] W. H. de Jeu. *Physical properties of Liquid Crystalline materials.* Gordon and Breach, New York, USA, 1980.

[2] P. G. de Gennes and J. Prost. *The physics of Liquid Crystals (2nd edition).* Oxford University Press, New York, USA, 1993.

[3] Edited by D. Demus, J. W. Goodby, G. W. Gray, H. W. Spiess, and V. Vill. *Handbook of Liquid Crystals, Vol. 1.* Wiley-VCH, Weinheim, Germany, 1998.

[4] S. T. Lagerwall. *Ferroelectric and Antiferroelectric Liquid Crystals.* Wiley-VCH, Weinheim, Germany, 1999.

[5] K. Merkel, A. Kocot, J. K. Vij, R. Korlacki, G. H. Mehl, and T. Meyer. *Phys. Rev. Lett.*, 93:237801, 2004.

[6] A. Saupe. *Mol. Cryst. Liq. Cryst.*, 1:527, 1966.

[7] D. A. Dunmur, D. A. Hitchen, and X.-Y. Hong. *Mol. Cryst. Liq. Cryst.*, 140:303, 1986.

[8] R. B. Meyer, L. Liebert, L. Strzelecki, and P. Keller. *J. Phys. Lett. (Paris)*, 36:L69, 1975.

[9] J. F. Nye. *Physical properties of Crystals.* Oxford University Press, Oxford, UK, 1957.

[10] A. D. L. Chandani, E. Gorecka, Y. Ouchi, H. Takezoe, and A. Fukuda. *Jpn. J. Appl. Phys.*, 28:L1265, 1989.

[11] T. Isozaki, T. Fujikawa, H. Takezoe, A. Fukuda, T. Hagiwara, Y. Suzuki, and I. Kawamura. *Jpn. J. Appl. Phys.*, 31:L1435, 1992.

[12] A. Fukuda, Y. Takanishi, T. Isozaki, K. Ishikawa, and H. Takezoe. *J. Mater. Chem.*, 4:997–1026, 1994.

[13] L. Landau. *Phys. Z. Sov. Union*, 11:26, 1937.

[14] A. V. Emelyanenko and M. A. Osipov. *Phys. Rev. E*, 68:051703, 2003.

[15] M. F. Vuks. *Opt. Spectrosk.*, 20:644, 1966.

[16] P. Yeh. *J. Opt. Soc. Am.*, 72:507, 1982.

[17] D. W. Berreman. *J. Opt. Soc. Am.*, 62:502, 1972.

[18] P. Yeh. *J. Opt. Soc. Am.*, 69:742–756, 1979.

[19] P. Yeh. *Optical Waves in Layered Media.* John Wiley & Sons, Inc., New York, 1988.

[20] I.-C. Khoo and S.-T. Wu. *Optics and Nonlinear Optics of Liquid Crystals.* World Scientific, Singapore, 1993.

[21] V. P. Panov. *Ph. D Thesis.* PhD thesis, Trinity College Dublin University, 2002.

[22] Y. Ouchi, T. Shingu, H. Takezoe, A. Fukuda, E. Kuze, M. Koga, and N. Goto. *Jpn. J. Appl. Phys.*, 23:L660, 1984.

[23] K. Hori. *Mol. Cryst. Liq. Cryst.*, 100:75, 1983.

[24] A. D. L. Chandani, N. M. Shtykov, V. P. Panov, A. V. Emelyanenko, A. Fukuda, and J. K. Vij. *Phys. Rev. E*, 72:041705, 2005.

[25] N. M. Shtykov, A. D. L. Chandani, A. V. Emelyanenko, A. Fukuda, , and J. K. Vij. *Phys. Rev. E*, 71:021711, 2005.

[26] F. Gouda, K. Skarp, and S. T. Lagerwall. *Ferroelectrics*, 113:165, 1991.

[27] A. Levstik, T. Carlsson, C. Filipic, I. Levstik, and B. Zeks. *Phys. Rev. Lett.*, 35:3527, 1987.

[28] N. Hayashi, T. Kato, T. Aoki, T. Ando, A. Fukuda, and S. S. Seomun. *Phys. Rev. Lett.*, 87:015701–1–4, 2001.

[29] One of the examples is CONOSCOPE manufactured by AUTRONIC-MELCHERS GmbH, Karlsruhe, Germany.

[30] Y. Galerne. *J. Phys. (Paris)*, 39:1311–1316, 1978.

[31] E. Gorecka, A. D. L. Chandani, Y. Ouchi, H. Takezoe, and A. Fukuda. *Jpn. J. Appl. Phys., Part 1*, 29:131–137, 1990.

[32] T. Fujikawa, K. Hiraoka, T. Isozaki, K. Kajikawa, H. Takezoe, and A. Fukuda. *Jpn. J. Appl. Phys.*, 32:985–988, 1993.

[33] J. K. Song, A. D. L. Chandani, O. E. Panarina, A. Fukuda, J. K. Vij, V. Goertz, and J. W. Goodby. *Ferroelectrics*, 344:41, 2006.

[34] J. K. Song, J. K. Vij, and I. Kobayashi. *Phys. Rev. E*, 75:051705, 2007.

[35] S. Suwa, H. Hoshi, Y. Takanishi, K. Ishikawa, H. Takezoe, and B. Zeks. *Jpn. J. Appl. Phys.*, 42:1335–1337, 2003.

[36] S. Suwa, Y. Takanishi, H. Hoshi, K. Ishikawa, and H. Takezoe. *Liq. Cryst.*, 30:499–505, 2003.

[37] J. K. Song, A. D. L. Chandani, A. Fukuda, J. K. Vij, I. Kobayashi, and A. V. Emelyanenko. *Phys. Rev. E*, 76:011709–1–13, 2007.

[38] M. Born and E. Wolf. *Principles of Optics.* Cambridge University Press, Cambridge, UK, 1999.

[39] J. Li and S. T. Wu. *J. Appl. Phys.*, 96:6253, 2004.

[40] J. K. Song, U. Manna, and J. K. Vij. *Europhys. Lett.*, 82:26003, 2008.

[41] I. Abdulhalim. *Appl. Opt.*, 46:2219, 2007.

[42] A. R. MacGregor. *J. Opt. Soc. Am. A*, 7:337–347, 1990.

[43] I. Abdulhalim. *J. Opt. A: Pure Appl. Opt.*, 1:646, 1999.

[44] M. A. Osipov and S. A. Pikin. *J. Phys. (Paris)*, 5:1–18, 1995.

[45] A. Saupe. *Mol. Cryst. Liq. Cryst.*, 7:59, 1969.

[46] T. R. Taylor, J. L. Fergason, and S. L. Arora. *Phys. Rev. Lett.*, 24(8): 359–362, 1970.

[47] T. R. Taylor, S. L. Arora, and J. L. Fergason. *Phys. Rev. Lett.*, 25:722–726, 1970.

[48] N. A. Clark and S. T. Lagerwall. *Appl. Phys. Lett.*, 36:899–901, 1980.

[49] P. M. Johnson, D. A. Olson, S. Pankratz, T. Nguyen, J. W. Goodby, M. Hird, and C. C. Huang. *Phys. Rev. Lett.*, 84:4870, 2000.

[50] A. V. Emelyanenko, A. Fukuda, and J. K. Vij. *Phys. Rev. E*, 74:011705, 2006.

[51] T. Matsumoto, A. Fukuda, M. Johno, Y. Motoyama, T. Yui, S. S. Seomun, and M. Yamashita. *J. Mater. Chem.*, 9:2051–2080, 1999.

[52] M. Takeuchi, K. Chao, T. Ando, T. Matsumoto, A. Fukuda, and M. Yamashita. *Ferroelectrics*, 246:1–20, 2000.

[53] Y. Yoshioka, M. Johno, T. Yui, and T. Matsumoto. *Euro. Pat. Appl.*, page EP1039329, 2000.

[54] D. W. Berreman. *Mol. Cryst. Liq. Cryst.*, 22:175, 1973.

[55] A. Fukuda. In *Proc. of the 5th International Display Research Conference (Oct,1995, Hamamatsu, Japan)*, Tokyo 105, Japan and California 92705-5421,USA, 1995. the Society for Information Display.

[56] S. Inui, N. Iimura, T. Suzuki, H. Iwane, K. Miyachi, Y. Takanishi, and A. Fukuda. *J. Mater. Chem.*, 6:671–673, 1996.

[57] V. P. Panov, B. K. McCoy, Z. Q. Liu, J. K. Vij, J. W. Goodby, and C. C. Huang. *Phys. Rev. E*, 74:011701, 2006.

[58] N. Isaert and J. Billard. *Mol. Cryst. Liq. Cryst.*, 38:1–18, 1977.

[59] A. A. Sigarev, J. K. Vij, A. Fukuda, B. Jin, and Y. Takanishi. *Mol. Cryst. Liq. Cryst.*, 311:97–109, 2004.

[60] W. G. Jang, C. S. Park, J. E. Maclennan, K. H. Kim, and N. A. Clark. *Ferroelectrics*, 180:213, 1996.

[61] K. H. Kim, K. Ishikawa, H. Takezoe, and A. Fukuda. *Phys. Rev. E*, 51:2166 – 2175, 1995.

[62] C. Zannoni. *The Molecular Physics of Liquid Crystals, Chapt. 3.* Academic Press, London, New York, San Francisco, 1979.

[63] H. E. J. Neugebauer. *Can. J. Phys.*, 32(1):1–8, 1954.

[64] H. S. Subramhanyam and D. Krishnamurti. *Mol. Cryst. Liq. Cryst.*, 22: 239–248, 1973.

[65] M. A. Osipov and A. Fukuda. *Phys. Rev. E*, 62:3724, 2000.

[66] J. Prost and R. Bruinsma. *Ferroelectrics*, 148:25, 1993.

[67] M. D. Ossowska-Chrusciel, R. Korlacki, A. Kocot, R. Wrzalik, J. Chrusciel, and S. Zalewski. *Phys. Rev. E*, 70:041705, 2004.

[68] A. M. Biradar, S. Wrobel, and W. Haase. *Phys. Rev. A*, 39:2693, 1989.

[69] E. P. Raynes and I. Shanks. *Electron. Lett.*, 10:114, 1974.

[70] M. Schadt. *Annu. Rev. Mater. Sci.*, 27:305, 1997.

[71] S. A. Jewell, T. S. Taphouse, and J. R. Sambles. *Appl. Phys. Lett.*, 87: 021106, 2005.

[72] S. A. Jewell and J. R. Sambles. *Phys. Rev. E*, 73:011706, 2006.

[73] D. Coates. *Mol. Cryst. Liq. Cryst.*, 49:83, 1978.

[74] J.-F. Li, X.-Y. Wang, E. Kangas, P. L. Taylor, C. Rosenblatt, Y. Suzuki, and P. E. Cladis. *Phys. Rev. B*, 52:R13075–R13078, 1995.

[75] S. Havriliak and S. Negami. *J. Polym. Sci.*, C14:99, 1966.

[76] G. Power, G. P. Johari, and J. K. Vij. *J. Chem. Phys.*, 119:435, 2003.

[77] K. Hiraoka, H. Takezoe, and A. Fukuda. *Ferroelectrics*, 147:13, 1993.

[78] Yu. P. Panarin, O. Kalinovskaya, and J. K. Vij. *Appl. Phys. Lett.*, 72:1667, 1998.

[79] M. Buivydas, F. Gouda, S. T. Lagerwall, and B. Stebler. *Liq. Cryst.*, 18: 879, 1995.

[80] J. K. Song, U. Manna, A. Fukuda, and J. K. Vij. *Appl. Phys. Lett.*, 91: 042907, 2007.

[81] Yu. P. Panarin, O. Kalinovskaya, J. K. Vij, and J. W. Goodby. *Phys. Rev. E*, 55:4345, 1997.

[82] H. Orihara and Y. Ishibashi. *Jap. J. Appl. Phys.*, 29:L115, 1990.

[83] T. Qian and P. L. Taylor. *Phys. Rev. E*, 60:2978 – 2984, 1999.

[84] J. K. Song, A. Fukuda, and J. K. Vij. *Phys. Rev. E*, 76:011708, 2007.

[85] A. D. L. Chandani, T. Hagiwara, Y. Suzuki, Y. Ouchi, H. Takezoe, and A. Fukuda. *Jpn. J. Appl. Phys.*, 27:L729–732, 1988.

[86] L. A. Parry-Jones and S. J. Elston. *Appl. Phys. Lett.*, 79:2097, 2001.

[87] R. Beccherelli, N. J. Mottram, and S. J. Elston. *Eur. Phys. J.: Appl. Phys.*, 9:247, 2000.

[88] Y. Yamada, N. Yamamoto, K. Mori, K. Nakamura, T. Hagiwara, Y. Suzuki, I. Kawamura, H. Orihara, and Y. Ishibashi. *Jpn. J. Appl. Phys., Part 2*, 29: 1757, 1990.

[89] N. Yamamoto, Y. Yamada, K. Mori, K. Nakamura, H. Orihara, Y. Ishibashi, Y. Suzuki, Y. Negi, and I. Kawamura. *Jpn. J. Appl. Phys., Part 2*, 30:2380, 1991.

[90] E. Magyari. *Phys. Rev. B*, 29:7082, 1984.

[91] L. Lei, S. Changqing, S. Juelian, P. M. Lam, and H. Yun. *Phys. Rev. Lett.*, 49:1335, 1982.

[92] X. Y. Wang and P. L. Taylor. *Phys. Rev. Lett.*, 76:640, 1996.

[93] M. Johno, A. D. L. Chandani, Y. Ouchi, H. Takezoe, A. Fukuda, M. Ichihashi, and K. Furukawa. *Jap. J. Appl. Phys.*, 28:L119, 1989.

[94] L. A. Parry-Jones and S. J. Elston. *Phys. Rev. E*, 63:050701(R), 2001.

[95] J. Li and S. T. Wu. *J. Appl. Phys.*, 95:896, 2004.

[96] D. R. Link, G. Natale, J. E. Maclennan, and N. A. Clark. *Phys. Rev. Lett.*, 83:3665, 1999.

[97] P. Cluzeau, H. T. Nguyen, C. Destrade, N. Isaert, P. Barois, and A. Babeau. *Mol. Cryst. Liq. Cryst.*, 260:69, 1995.

[98] A. Roy and N. V. Madhusudana. *Europhys. Lett.*, 36:221, 1996.

[99] M. Cepic and B. Zeks. *Phys. Rev. Lett.*, 87:085501, 2001.

[100] L. Parry-Jones, E. Kriezis, and S. Elston. *Jpn. J. Appl. Phys., Part 2*, 41: L1485, 2002.

[101] P.M. Chaikin and T. C. Lubensky. *Principles of Condensed Matter Physics, Chapt. 4*. Cambridge University Press, 1995.

[102] P. E. Cladis, W. van Saarloos, D. A. Huse, and J. S. Patel. *Phys. Rev. Lett.*, 62:1764, 1989.

[103] M. A. Handschy and N. A. Clark. *Appl. Phys. Lett.*, 41:39, 1982.

[104] M. A. Handschy and N. A. Clark. *Ferroelectrics*, 59:69, 1984.

[105] J. E. Maclennan, Q. Jiang, and N. A. Clark. *Phys. Rev. E*, 52:3904, 1995.

[106] D. C. Ulrich, M. J. Cherrill, and S. J. Elston. *Liq. Crys.*, 23:797, 1997.

[107] S. S. Seomun, T. Fukuda, A. Fukuda, J. G. Yoo, Yu. P. Panarin, and J. K. Vij. *J. Mater. Chem.*, 10:2791–2794, 2000.

[108] M. A. Handschy, N. A. Clark, and S. T. Lagerwall. *Phys. Rev. Lett.*, 51:471, 1983.

[109] M. A. Osipov, A. Fukuda, and H. Hakoi. *Mol. Cryst. Liq. Cryst.*, 402:9, 2003.

[110] S. D. Lee and J. H. Lee. In H. Uchiike, editor, *Proc. 4th Int. Display Research Conf. (Nov 19-21, Nagoya, Japan) - IDW prime97 -*, number LCT3-2, pages 69–72, Tokyo, Japan, 1997. SID Jpn. Chapt.

[111] H. Pauwels, B. Verweire, K. Dhave, and J. Fronier. *SID Symposium Digest*, 29:1175–1178, 1998.

[112] B. Park, S.-S. Seomun, M. Nakata, M. Takahashi, Y. Takanishi, K. Ishikawa, and H. Takezoe. *Jpn. J. Appl. Phys., Part 1*, 38:1474–1481, 1999.

[113] B. Park, M. Nakata, S. S. Seomun, Y. Takanishi, K. Ishikawa, and H. Takezoe. *Phys. Rev. E*, 59:R3815–R3818, 1999.

[114] G. A. Somorjai and J. Y. Park. *Physics Today*, October 2007:48, 2007.

[115] Yu. P. Panarin, C. Rosenblatt, and F. M. Aliev. *Phys. Rev. Lett.*, 81:2699, 1998.

[116] H. Xu, J. K. Vij, A. Rappaport, and N. A. Clark. *Phys. Rev. Lett.*, 79:249, 1997.

[117] Yu. P. Panarin, Y. P. Kalmykov, S. T. Mac Lughadha, H. Xu, and J. K. Vij. *Phys. Rev. E*, 50:4763, 1994.

[118] H. Moritake, N. Shigeno, M. Ozaki, and K. Yoshino. *Liq. Cryst.*, 14:1283, 1993.

[119] J. Lagerwall, P. Rudquist, S. Lagerwall, and B. Stebler. *Ferroelectrics*, 277: 239, 2002.

[120] W. Chen, M. B. Feller, and Y. R. Shen. *Phys. Rev. Lett.*, 63:2665, 1989.

[121] M. Brunet and E. Williams. *Ann. Phys.*, 3:237, 1977.

[122] M. Glogarova, J. Fousek, L. Lejcek, and J. Pavel. *Ferroelectrics*, 58:161, 1984.

[123] N. M. Shtykov, J. K. Vij, R. A. Lewis, M. Hird, and J. W. Goodby. *Phys. Rev. E*, 62:2279, 2000.

[124] N. M. Shtykov, J. K. Vij, V. P. Panov, R. A. Lewis, M. Hird, and J. W. Goodby. *J. Mater. Chem.*, 9:1383, 1999.

[125] C. Tanaka, T. Fujiyama, T. Maruyama, and S. Nishiyama. *Abstr. 21st Jpn. Liq. Cryst. Conf.*, 2C18:250–251, 1995.

[126] T. Yoshida, T. Tanaka, J. Ogura, H. Wakai, and H. Aoki. *SID Symposium Digest*, 28:841–844, 1997.

[127] R. Hasegawa, H. Fujiwara, H. Nagata, T. Saishu, R. IIda, Y. Hara, M. Akiyama, H. Okumura, and K. Takatoh. In *Proc. AM-LCD*, number AMp3-1, pages 119–122, Tokyo, Japan, 1997. Jpn. Soc. Appl. Phys., SID Jpn. Chapt.

[128] T. Verhulst. *Jpn. J. Appl. Phys., Part 1*, 36:720–729, 1997.

[129] M. Lu, K. H. Yang, and J. L. Sanford. *Ferroelectrics*, 246:163–173, 2000.

[130] L. K. M. Chan, P. Bartelous, P. W. H. Surguy, N. Flannigan, G. Swedenkras, C. Waldelof, M. Rampin, A. Vindigni, I. Underwood, D. G. Vass, M. I. Newsam, J. M. Oton, and X. Quintana. In Philip J. Bos, editor, *Proc. 20th Int. Display Research Conf. (Florida, Sept. 25–28, 2000)*, number P40, pages 261–264. Soc. Infomation Display, 2000.

[131] N. J. Mottram and S. J. Elston. *Phys. Rev. E*, 62:6787–6794, 2000.

[132] A. de Vries, A. Ekachai, and N. Spielberg. *Mol. Cryst. Liq. Cryst.*, 49(letters):143–152, 1979.

[133] N. A. Clark, T. Bellini, R.-F. Shao, D. Coleman, S. Bardon, and D. R. Link. *Appl. Phys. Lett.*, 80:4097–4099, 2002.

[134] Y. Hattori, T. Fujiyama, T. Maruyama, C. Tanaka, H. Hama, and S. Nishiyama. In *Proc. AM-LCD*, number LC p-1, pages 121–124, Tokyo, Japan, 1998. Jpn.Soc. Appl. Phys.

[135] M. Nakagawa and T. Akahane. *J. Phys. Soc. Jpn.*, 55:1516–1522, 1986.

[136] K. Okano. *Jpn. J. Appl. Phys.*, 25:L846–L847, 1986.

[137] N. A. Clark, D. Coleman, and J. E. Maclennan. *Liq. Cryst.*, 27:985–990, 2000.

[138] M. Copic, J. E. Maclennan, and N. A. Clark. *Phys. Rev. E*, 65:021708–1–9, 2002.

[139] P. Rudquist, J. P. F. Lagerwall, M. Buivydas, F. Gouda, S. T. Lagerwall, N. A. Clark, J. E. Maclennan, R. Shao, D. A. Coleman, S. Bardon, T. Bellini, D. R. Link, G. Natale, M. A. Glaser, D. M. Walba, and M. D. Wand X.-H. Chen. *J. Mater. Chem.*, 9:1257–1261, 1999.

[140] P. Rudquist, J. P. F. Lagerwall, M. Buivydas, F. Gouda, S. T. Lagerwall, D. M. Walba, and N. A. Clark. *SID Symposium Digest*, 30:409–411, 1999.

[141] V. Manjuladevi, Yu. P. Panarin, and J. K. Vij. *Appl. Phys. Lett.*, 91:052911–1–3, 2007.

[142] S. S. Seomun, T. Gouda, Y. Takanishi, K. Ishikawa, H. Takezoe, and A. Fukuda. *Liq. Cryst.*, 26:151–161, 1999.

[143] E. Gorecka, D. Pociecha, M. Glogarova, and J. Mieczkowski. *Phys. Rev. Lett.*, 81:2946–2949, 1998.

[144] D. Pociecha, M. Glogarova, E. Gorecka, and J. Mieczkowski. *Phys. Rev. E*, 61:6674–6677, 2000.

[145] K. Hiraoka, A. Taguchi, Y. Ouchi, H. Takezoe, and A. Fukuda. *Jpn. J. Appl. Phys., Part 2*, 29:L103, 1990.

[146] A. D. L. Chandani, Y. Ouchi, H. Takezoe, A. Fukuda, K. Terashima, K. Furukawa, and A. Kishi. *Jpn. J. Appl. Phys.*, 28:L1261, 1989.

[147] J. K. Song, A. Fukuda, and J. K. Vij. *Phys. Rev. Lett.*, (submitted), 2008.

[148] L. Parry-Jones and S. Elston. *Mol. Cryst. Liq. Cryst.*, 410:141–152, 2004.

[149] K. Hiraoka, Y. Takanishi, K. Skarp, H. Takezoe, and A. Fukuda. *Jpn. J. Appl. Phys., Part 2*, 30:L1819, 1991.

[150] S. Jaradat, P. D. Brimicombe, C. Southern, S. D. Siemianowski, E. DiMasi, M. Osipov, R. Pindak, and H. F. Gleeson. *Phys. Rev. E*, 77:010701(R), 2008.

[151] T. Shingu, T. Tsuchiya, Y. Ouchi, H. Takezoe, and A. Fukuda. *Jpn. J. Appl. Phys.*, 25:L206, 1986.

[152] S. S. Seomun, Y. Takanishi, K. Ishikawa, H. Takezoe, and A. Fukuda. *Jpn. J. Appl. Phys., Part 1*, 36:3586, 1997.

[153] Z. Q. Liu, B. K. McCoy, S. T. Wang, R. Pindak, W. Caliebe, P. Barois, P. Fernandes, H. T. Nguyen, C. S. Hsu, S. Wang, and C. C. Huang. *Phys. Rev. Lett.*, 99:077802, 2007.

[154] P. Mach, R. Pindak, A.-M. Levelut, P. Barois, H. T. Nguyen, C. C. Huang, and L. Furenlid. *Phys. Rev. Lett.*, 81:1015, 1998.

[155] V. Faye, A. Babeau, F. Placin, H. T. Nguyen, P. Barois, V. Laux, and N. Isaert. *Liq. Cryst.*, 21:485, 1996.

[156] V. Laux, N. Isaert, V. Faye, and H. T. Nguyen. *Liq. Cryst.*, 27:81, 2000.

[157] S. T. Wang, Z. Q. Liu, B. K. McCoy, R. Pindak, W. Caliebe, H. T. Nguyen, and C. C. Huang. *Phys. Rev. Lett.*, 96:097801, 2006.

[158] K. L. Sandhya, Yu. P. Panarin, U. Manna, J. K. Vij, and S. Kumar. *Phys, Rev. Lett.*, 98:219801, 2007.

[159] K. Miyachi, M. Kabe, K. Ishikawa, H. Takezoe, and A. Fukuda. *Ferroelectrics*, 147:147, 1993.

[160] J. H. Lee and T. K. Lim. *J. Appl. Phys.*, 98:094110, 2005.

[161] J. J. Champoux. *Annu. Rev. Biochem.*, 70:369, 2001.

[162] R. B. Meyer. Ferroelectric liquid crystals. *Mol. Cryst. Liq. Cryst.*, 40:33, 1977.

[163] R. B. Meyer. *Appl. Phys. Lett.*, 12:281, 1968.

[164] B. Urbanc, B. Zeks, and T. Carlsson. *Ferroelectrics*, 113:219, 1991.

[165] B. Urbanc and B. Zeks. *Phys. Rev. E*, 52:3892, 1995.

[166] N. Baytch, R. L. B. Selinger, J. V. Selinger, and R. Shashidhar. *Phys. Rev. E*, 68:041702, 2003.

[167] S. T. Lagerwall. *Ferroelectrics*, 301:15, 2004.

[168] S. A. Rozanski and W. Kuczynski. *Chem. Phys. Lett.*, 105:104, 1983.

[169] P. E. Cladis, H. R. Brand, and P. L. Finn. *Phys. Rev. A*, 28:512, 1983.

[170] J. E. Maclennan, M. A. Handschy, and N. A. Clark. *Phys. Rev. A*, 34:3554, 1986.

[171] M. Krueger and F. Giesselmann. *J. Appl. Phys.*, 101:094102, 2007.

[172] P. V. Dolganov, B. M. Bolotin, and A. Fukuda. *Phys. Rev. E*, 70:041708, 2004.

[173] R. Pindak, C. Y. Young, R. B. Meyer, and N. A. Clark. *Phys. Rev. Lett.*, 45:1193, 1980.

[174] M. Pfeiffer, S. Wrobel, L. A. Beresnev, and W. Haase. *Mol. Cryst. Liq. Cryst.*, 202:193, 1991.

[175] S. K. Kundu, K. Suzuki, and B. K. Chaudhuri. *Ferroelectrics*, 287:47, 2003.

[176] S. S. Roy, S. Kundu, N. Ghosh, T. P. Majumder, and S. K. Roy. *Mol. Cryst. Liq. Cryst.*, 328:161, 1999.

[177] J. Ruth, J. V. Selinger, and R. Shashidhar. *Appl. Phys. Lett.*, 65:1590, 1994.

[178] M. A. Glaser and N. A. Clark. *Phys. Rev. E*, 66:021711, 2002.